Optomechanics and Optical Packaging for Free-Space Optical Interconnects

Guillaume Charles Louis Boisset

Department of Electrical Engineering
McGill University
Montréal, Canada
February, 1998

A thesis submitted to the Faculty of Graduate Studies and research in partial fulfillment of the requirements of the degree of Doctor of Philosophy

0-612-44366-3

Abstract

Free-space optical interconnects (FSOIs) promise to deliver tremendous gains in connectivity and architectural freedom in future computing systems, especially at the backplane level. However, a critical hurdle that must be overcome for FSOIs to deliver on their promise is that of optical packaging. The objective of optical packaging in FSOIs is to implement an optical design within the specified alignment budget and support the associated optoelectronics. It is a multidisciplinary field combining aspects of mechanical, optical and electrical engineering. This thesis explores optical packaging issues for FSOIs such as: type of optical interconnect, impact of device technology, environmental effects, and fabrication issues. Approaches taken to address these issues in previous optical systems described in the literature are then studied; key points are the importance of improving diagnostic techniques and the benefits of microoptic/optoelectronic device integration. To further study these aspects, the optical packaging for a four-stage hybrid macrolens/lenslet FSOI backplane is designed, built, and characterized. A non-obtrusive, *in-situ* alignment diagnostic system which uses dedicated alignment beams running parallel to the main link is also designed, implemented and characterized. An analysis of optical crosstalk and signal-to-crosstalk ratio considerations due to misalignment is then presented and it is shown that crosstalk can be exploited to yield alignment diagnostic information at the expense of few additional components. A novel approach for simplifying prealignment of microoptics and optoelectronics during fabrication is then presented. This consists of using on-die reflective diffractive structures to generate reference marks for use during alignment and fabrication of integrated microoptic/optoelectronic packages. Future avenues of research are then discussed.

Résumé

Les interconnexions à optique à l'air libre (IOAL) sont jugées très prometteuses pour les systèmes informatiques de l'avenir car elles pourront augmenter la connectivité et offrir un plus grand champ d'action à l'architecture. surtout au niveau des plaques d'interconnexion arrière. Cependant un obstacle de taille à surmonter demeure l'empaquetage optique. dont le but est de réaliser une structure de support pour un design optique et les composantes optoélectroniques qui y sont associées. C'est un secteur de recherche multidisciplinaire faisant appel au génie mécanique ainsi qu'à l'optique et l'électronique. Cette thèse commence par décrire les facteurs qui ont une influence sur l'empaquetage optique. tels le type d'interconnexion optique. le choix des dispositifs optoélectroniques. les effets liés à l'environnement. et les problèmes de fabrication. Les moyens empruntés pour relever ces défis au cours de la réalisation d'autres systèmes optiques décrits ailleurs sont étudiés et deux éléments clés se révèlent : l'importance d'améliorer les mécanismes de diagnostic et les bénéfices qu'apporte l'intégration de l'optoélectronique et de la microoptique pendant l'empaquetage. La conception. la fabrication. et la caractérisation de l'empaquetage optique d'un système expérimental d'interconnexion de fond de chassis à base d'un système hybride micro/macro-optique sont présentées afin de permettre une étude plus approfondie des problèmes. Un système de diagnostic *in-situ* non-intrusif employant des faisceaux se propageant en parallèle aux faisceaux principaux de transfert de données est aussi décrit. Par la suite. une analyse des signaux croisés et du ratio signal-croisage est effectuée et il est démontré que le croisage des signaux peut être exploité à des fins de mesure d'alignement d'un système. et ce à un faible coût matériel. Suite à cette anlayse. une nouvelle technique pour simplifier le préalignement des composantes microoptiques et optoélectroniques est mise de l'avant. Celle-ci consiste à utiliser des structures réfléchissantes à diffraction qui sont situées à même le substrat optoélectronique pour produire des motifs lumineux simplifiant le préalignement et la fabrication d'empaquetage intégré. Une discussion portant sur les sujets futurs de recherche conclut le tout.

Acknowledgements

I wish to thank my advisor Dave Plant for his tireless support and encouragement over the course of this work. Dave was always there to give me the best guidance in theoretical, experimental and practical matters and led me to channel my work in the most productive manner. Most importantly, I am deeply indebted to Dave for the great trust he placed in me not only during the design and fabrication of the various backplane projects but also over the many years of lab construction, maintenance, and operation.

Encore un super merci à Dr. Brian Robertson for the critical help he gave me and for all that he taught me during our countless discussions in the lab and at the whiteboard. I thank Don Pavlasek for spending hours teaching me finer points of machining and fabrication, for leading me to an elegant solution in many mechanical designs and, along with Joe Boka, for repeatedly bailing me out when I needed pieces machined in a rush.

Many heartfelt thanks to everybody in the lab whom I had the honour and good fortune to work with over the years: Alain, Daniel, Danny, Dave, Dave, Eric, Fred, Lukas, Maddy, Marc, Marcos, Mike, Mike, Nam, Pritha, Rajiv, Wayne, and Yongsheng.

Many thanks to Scott Hinton who, half a decade ago, accepted me into the McGill Photonics Systems Group and opened many doors for me. Thanks to Rob Wodnicki and Kezia for their help, and to Kechang Song at McMaster University for his work on the MSMs. Thanks to Professor Frank Tooley for his advice, as well as to Professor Taghizadeh and George Smith. Thanks to Dr. Bill Robertson for the grating designs.

I wish to thank all staff at the Photonics Lab at the Naperville (Illinois) facilities of Bell Labs for the great kindness and professionalism they demonstrated during my three-day stay there.

Merci Séverine.

Finally, I dedicate this thesis to my parents for all the love, understanding, and support they gave me over the course of my studies at McGill.

The work described in this thesis was supported by the Nortel/NSERC industrial research chair in photonic systems, the Canadian Institute for Telecommunications Research and FCAR (comité B2-05). Multiple Phase Gratings were fabricated by the ARPA/Honeywell COOP production run.

The following five paragraphs are included as per McGill regulations.

Candidates have the option of including, as part of the thesis, the text of one or more papers submitted or to be submitted for publication, or the clearly-duplicated text of one or more published papers. These texts must be bound as an integral part of the thesis.

If this option is chosen, connecting texts that provide logical bridges between the different papers are mandatory. The thesis must be written in such a way that it is more than a mere collection of manuscripts: in other words, results of a series of papers must be integrated.

The thesis must still conform to all other requirements of the "Guidelines for Thesis Preparation". The thesis must include: A Table of Contents, an abstract in English and French, an introduction which clearly states the rationale and objectives of the study, a review of the literature, a final conclusion and summary, and a thorough bibliography or reference list.

Additional material must be provided where appropriate (e.g. in appendices) and in sufficient detail to allow a clear and precise judgement to be made of the importance and originality of the research reported in the thesis.

In the case of manuscripts co-authored by the candidate and others, the candidate is required to make an explicit statement in the thesis as to who contributed to such work and to what extent. Supervisors must attest to the accuracy of such statements at the doctoral oral defense. Since the task of the examiners is made more difficult in these cases, it is in the candidate's interest to make perfectly clear the responsibilities of all the authors of the co-authored papers.

ASSOCIATED PUBLICATIONS

The work reported in this thesis has been published or is being published in the form of the following papers.

Journal Articles

1 G. C. Boisset, D. R. Rolston, R. Iyer, Y. S. Liu, B. Robertson, D. Kabal, and D. V. Plant, "In-situ measurements of misalignment errors in free-space optical interconnects," submitted to *IEEE Journal of Lightwave Technology*, May, 1997, accepted January, 1998.

3 R. Iyer, Y.S. Liu, G.C. Boisset, D.J. Goodwill, W.M. Robertson, B. Robertson, M.H. Ayliffe, D. Kabal, F. Lacroix, and D.V. Plant, "Design, implementation, and characterization of an optical power supply spot array generator for a four stage free-space optical backplane", *Applied Optics*, 36, pp. 9230-9242 (1997).

4 G. C. Boisset, M. H. Ayliffe, B. Robertson, R. Iyer, Y. S. Liu, D. V. Plant, D. J. Goodwill, D. Kabal, and D. Pavlasek, "Optomechanics for a four-stage hybrid-SEED-based free-space optical backplane," *Applied Optics*, 36, pp. 7341-7358 (1997).

5 B. Robertson, Y. S. Liu, G. C. Boisset, M. R. Taghizadeh, and D. V. Plant, "In-situ interferometric alignment systems for the assembly of microchannel relay systems," *Applied Optics*, 36, pp. 9253-9260 (1997).

6 G. C. Boisset, B. Robertson, W. S. Hsiao, M. R. Taghizadeh, J. Simmons, K. Song, D. A. Thompson, and D. V. Plant, "On-Die Diffractive Structures for Alignment of Microlens Arrays to 2D OptoelectronicDevice Arrays," *IEEE Photonics Technology Letters*, 8, pp. 918-920 (1996).

7 D. V. Plant, B. Robertson, H. S. Hinton, M. H. Ayliffe, G. C. Boisset, W. Hsiao, D. Kabal, N. H. Kim, Y. S. Liu, M. R. Otazo, D. Pavlasek, A. Z. Shang, J. Simmons,

K. Chang, D. Thompson, and W. M. Robertson, "A 4x4 VCSEL/MSM Optical Backplane Demonstrator System," *Applied Optics*, 35, pp. 6365-6368 (1996).

8 D. V. Plant, B. Robertson, H. S. Hinton, W. M. Robertson, G. C. Boisset, N. H. Kim, Y. S. Liu, M. R. Otazo, D. R. Rolston, and A. Z. Shang, "An Optical Backplane Demonstrator System Based on FET-SEED Smart Pixel Arrays and Diffractive Lenslet Arrays, " *IEEE Photonics Technology Letters*,. 7, pp. 1057-1059 (1995).

Conference Proceedings

1 B. Robertson, Y.S.Liu, G.C.Boisset, M.H. Ayliffe, R. Iyer, D. Kabal, W. M. Robertson, H. S. Hinton, M. R. Taghizadeh, and D. V. Plant, "Michrochannel Interconnect Design Issues", Proceedings of the Microlens Arrays conference, European Optical Society, Topical Meetings Digest: 13, pp. 127-131 (1997)

2 D. N. Kabal, G. C. Boisset, D. R. Rolston, and D. V. Plant, "Packaging of two-dimensional smart pixel arrays." Proc.Summer Topical Meeting on Smat Pixels, Colorado, August 1996.

3 G. C. Boisset, B. Robertson, W. Hsiao, H. S. Hinton, and D. V. Plant, "Detection of x-y Misalignment Error Using Optical Crosstalk in a Lenslet-Array-Based Free-Space Optical Link, " Proc. OC'95, pp. 63-64.

4 B. Robertson, G.C. Boisset, H.S. Hinton, Y.S. Liu, N.H. Kim, R.M. Otazo, D. Pavlasek, D.V. Plant, D.R. Rolston, and W. M. Robertson, "Design of a Lenslet Array Based Free-Space Optical Backplane Demonstrator," Proceedings of the Optical Computing 1994 Conference, Inst.Phys. Conf. Ser. No. 139, pp.223-226.

Chapter 1: Introduction

Demand for computing power is increasing at an ever-higher rate in today's digital society. Moore's law, which states that chip performance doubles every 18-24 months, has held out for over thirty years and is expected to hold for the foreseeable future. However, transmitting information within computing systems is more problematic: interconnection throughput is not increasing as fast as chip performance is, which leads to a bottleneck. The way to increase interconnection throughput is to improve packaging techniques.

1.1 The Electronic Packaging Hierarchy

Proper engineering practice dictates that the best way to solve a complex problem is to break it into more manageable parts. To better attack the packaging problem, therefore, designers have broken down packaging into a hierarchy which is as follows[1] and which is shown in Figure 1.1. At every level of the hierarchy, the packaging serves to ensure high-speed interconnection between the sub-components. Other tasks played by packaging include protecting sub-components, dissipating thermal energy and distributing power.

- Level 1: chip carrier. This can be implemented using many different technologies such as dual in line pin (DIP) packages, ball grid arrays (BGAs), and plastic leaded chip carrier (PLCC), among many others.
- Level 2: printed circuit board (PCB), for chip-to-chip communication. Chip carriers are usually soldered onto the PCB. Technologies for implementing PCBs include flex film carrier, injection molded card, polymer filling and many others.
- Level 3: backplane, for board to board communication within a chassis
- Level 4: frame, which houses several chassis. Chassis-to-chassis interconnection is usually accomplished via high speed coaxial or fibre links.

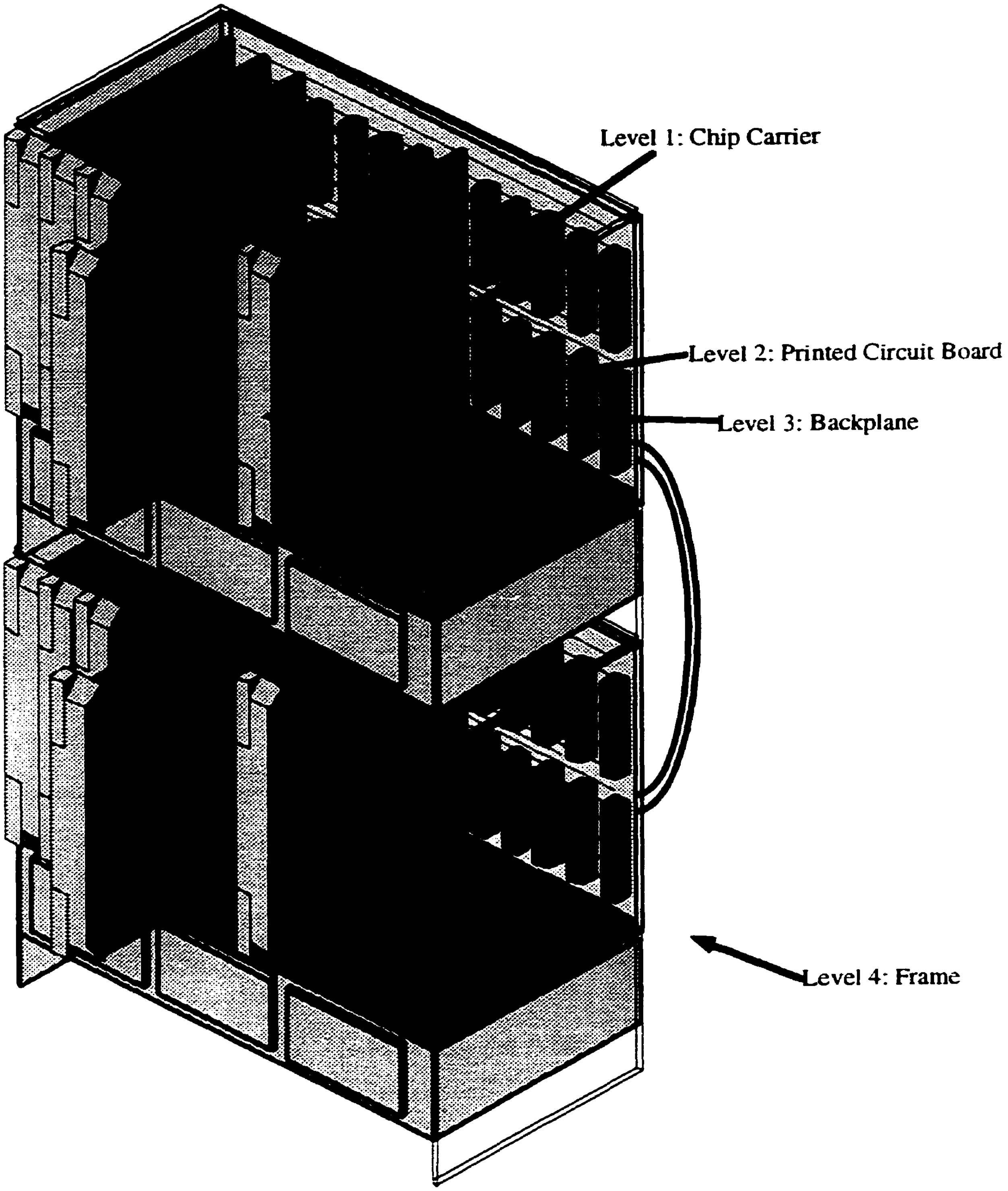

Figure 1.1: Electronic Packaging Hierarchy

The key, therefore, is to find where in the electrical packaging the bottlenecks are arising. Table 1.1 presents the Semiconductor Industry Association projections for silicon integrated circuits (ICs). Table 1.2 below that indicates the performance of various chip-carrier packaging technologies available today[2].

Year	Feature Size (microns)	Gates	On-Chip Clock (MHz)	Off-Chip Clock (MHz)	Pin-out Number (Rent's Rule)
1995	0.35	800K	200	100	980
1998	0.25	2M	350	175	1640
2001	0.18	5	500	250	2735
2004	0.12	10M	700	350	4026
2007	0.1	20M	1000	500	5928

Table 1.1: Semiconductor Industry Association projections for silicon ICs

Chip Carrier	Approx Bandwidth (Gbits/s)	Maximum I/O	Aggregate Bandwidth (Gbits/s)	Price (1 p.c.)	Supplier
DIP	0.1	50	5	\$5-20	Kyocera
QFP	1	150	150	\$15-50	Kyocera NTK
PGA (0.1" pin pitch)	0.4	400	160	\$15-50	Kyocera, NTK
LCC	2	156	312	\$15-50	Kyocera, NTK
BGA/LGA	1	600	600	N/A	Amkor, Kyocera

Table 1.2: Performance comparison of various chip carriers

Multiplying the pin-out number by the off-chip clock rate in Table 1.1 to get a maximum throughput requirement per IC, it can be seen that the 600 Gbits/s in Table 1.2 can accomodate can accomodate IC-PCB communication for at least the next few years. A similar analysis for chassis-to-chassis communication reveals that fibre links should be able to accomodate the demand.

The bottleneck is at the electrical backplane level.

1.2 Limitations of Electronic Backplanes

The primary advantage of a backplane is that it offers direct, cheap, and reliable multi-point, intra-chassis communication between any PCBs on the backplane without having to send data through an expensive switch elsewhere in the system. There exists a great body of work covering electronic backplane design issues. Table 1.3 overviews conventional and emerging electronic backplane approaches, which must be studied before optical backplanes can be considered.

APPROACH	BUS WIDTH (bits)	Clock (MHz)	MAX THROUGHPUT (Gbits/s)	NUMBER OF BOARDS	ENGINEERING COMMENTS
			CONVENTIONAL		
PCI/Compact PCI[3]	64	66	4.2	8	• PCI-PCI bridge chips needed for > 8 boards
Typical custom[4]	256	~75	20	15	• >12 layers • Signal:Ground = 4:1
			EMERGING		
Rambus[5]	64	500	32	5	•Variable current drive • single master for impedance reasons
Active impedance control[6,7]	64	600	40	5	• tunable termination • slew rate limited
Multi-serial bus [8,9]	>200	500	100	15	• multiple point-to-point • usually switch-based
Proprietary [10]	--	1000	100-500	10-20	• still in laboratory • possible EMI issues

Table 1.3: Conventional and emerging backplane approaches

Quite simply, Table 1.3, indicates that future backplanes will barely accomodate the data throughput demands of even one high performance (600 Gbits/s) chip on a PCB talking to another PCB, even with caching eliminating 90% of backplane accesses. This is the bottleneck for systems with high-performance and even mid-to-low performance requirements that often have several boards each with several CPUs and DSP chips in a chassis, in addition to many other memory and I/O PCBs. The backplane cannot keep up. The doubling of chip performance every two years just widens the gap.

Further comments on the table are as follows.

This table does not cover the conventional VME standard[11] which still dominates the medium performance (~640 Mbits/second) market today: the market for VME boards alone was greater than US$1.2 billion in 1996 and is still growing at 15% annually[12]. Recent developments include hybrid combinations such as the emerging VME320 approach which consists of a logical bus implemented by multiple serial lines converging to a common point then fanning out again with no regeneration–an electrical backplane equivalent to a star coupler. This technique reportedly allows for a 40 MHz clock on the backplane since distributed capacitances are eliminated and are effectively replaced by one large lumped capacitance located halfway down the trace[13]. This increases the total number of traces on the backplane, which can lead to higher fabrication costs.

As can be seen for emerging backplanes that are in current use (i.e. that have left the laboratory), the general trend indicates that board numbers tend to fall as overall throughput increases. The exception to this rule, namely multi-serial busses, could better be described as an overall architecture in which data is sent from board to board (on traces connected to just two boards) via switches residing within the system. Many reasons explain this phenomenon of fewer boards at higher speed: the two main reasons are given below.

First, adding boards and drivers adds capacitive loads to a backplane trace. This leads to a lower overall characteristic impedance, Z_o, on the trace, which reduces voltage swing for a given current drive and increases power consumption. Moreover, increasing the current sinking/sourcing capability of a driver will generally increase the capacitive load presented by the driver on the trace. This leads to a still lower Z_o. Attempts to overcome this problem, such as Backplane Transceiver Logic (BTL) on Futurebus+[14], ended in failure for different reasons ranging from insufficient slew rates on power supplies and annoying signal glitches to a general reluctance on the part of suppliers and users alike to invest time and money in a new untested technology.

Second, many high speed bus or backplane solutions position the master at one end of the trace[5], leaving only slaves everywhere else on the trace. This is done mainly because a driver at the end of a trace sees an impedance Z_o whereas a driver not at the end of a trace sees an impedance $Z_o/2$ (two impedances in parallel). Moreover, there are fewer complications associated with reflections if the master is at one end. As a result, there can be only two potential masters since a trace obviously has just two ends. Rambus even puts a termination resistor at one of the two ends, leaving only one master.

Another conclusion can be drawn from the table above. Active impedance control, while producing impressive results in both throughput improvement and especially power consumption, removes one of the key attractions of the traditional copper trace backplane, namely its reliability. The introduction on the trace of an active device in addition to the strict minimum required to drive a signal necessarily removes some reliability, which is effectively an added cost. If incremental increases in electronic backplane throughput come at the cost of additional active electronic devices, then optical backplanes, which promise tremendous (not incremental) increases in throughput at the cost of additional electro-optic devices, are a much better route.

Another issue not brought up in the table is that of the performance of electronic connectors. Connectors have an impact on the system by adding capacitance to the traces to which they are connected and adding inductance to the signal path. Moreover, connectors can contribute to crosstalk during signal transmission [15], and reducing this crosstalk can best be done by reducing the pin signal:ground ratio or increasing the pin pitch. Both solutions, however, reduce overall throughput.

In short, system designers do not have access to high-speed electrical backplanes.

1.3 The Promise of Free-Space Optical Interconnects

Free-space optical interconnects (FSOIs) promise to alleviate the transmission bottlenecks in the backplanes of high performance computing systems as the demand for information throughput between processing elements reaches ever higher. The reasons include the following[16, 17, 18]:

- greater spatial and temporal bandwidth yielding large throughput gains
- reduced electromagnetic interference (EMI) generation and susceptibility
- lower power dissipation
- lower skew, lower latency, and eliminated impedance mismatches
- potential for implementing new architectures

1.4 Optical Packaging to Enable Optical Interconnects

Many practical problems remain to be solved before FSOIs can deliver on their promise. Optoelectronic technology must improve so that devices can be made more reliable, receiver and transmitter designs must be made more efficient, optical designs have to be more efficient and optical packaging must be improved. However, comparing the level of sophistication of current smart pixels with their thousands of I/O [19] to that of current optical packaging which is still very bulky[20], a glaring discrepancy can be noted: smart pixel technology is much further ahead than optical packaging technology is. The lack of compact, cheap, and reliable optical packaging is slowing down the entire field: improving it would greatly hasten the arrival of commercial FSOIs. This is the reason why this thesis addresses optical packaging.

1.5 Organization of the Thesis

This thesis is organized as follows. Chapter 2 reviews issues and challenges in optical packaging for FSOIs. These include impact of device technology, environmental issues and fabrication concerns as well as the different types of optical interconnects. Given the challenges brought up in the previous chapter, chapter 3 covers the design, fabrication and characterization of optical packaging for a four-stage optical backplane implementing hybrid-SEED technology and a hybrid optical interconnect. This chapter underscores the importance of developing diagnostic techniques for FSOIs. Chapter 4 introduces a novel in-situ diagnostic technique involving higher-order alignment beams running parallel to the main link for alignment diagnostics. Chapter 5 introduces a more cost-efficient technique for diagnosting misalignment: optical crosstalk is used to deduce the alignment status of a FSOI. Chapter 6 develops novel packaging techniques to simplify fabrication and pre-alignment techniques for FSOIs.

1.6 Original Contributions

The original contributions presented by the author in this thesis are:

1) Design and fabrication of novel optomechanics for the first truly three-dimensional vertically-mounted multi-stage FSOI.
2) First extensive use of electronics and signal processing to characterize optomechanics for a FSOI.
3) First large-scale incorporation of *in-situ* diagnostic tools to help align and quantify performance of optical packaging within a FSOI.
4) Demonstration of the first system using optical crosstalk to monitor misalignment of a FSOI by designing and laying out detectors whose geometry is optimized to capture the greatest amount of diffracted power due to misalignment while optimizing the overall signal-to-crosstalk ratio (SXR). First calculation of adjacent channel SXR vs lateral misalignment for non-ideal diffractive lens.
5) First demonstration of reflective, diffractive, on-die features for alignment of microoptics to optoelectronics: first demonstration of the use of electrical signal lines to act as said diffractive alignment features, and calculation of effect of perturbations due to underlying metal traces on diffracted pattern.

Since the Photonic Systems Group is involved in multi-disciplinary research, a lot of work is done in teams and as such many people help each other out. For the work presented in this thesis, all under the inspired supervision of Professor Plant, the following people gave invaluable help. Dr. Brian Robertson was the first to tell me to consider diffractive effects in crosstalk and gave much insight in other countless discussions. Don Pavlasek spent hours going over fabrication considerations with me for the design and fabrication of phase II optomechanics. Of the hundreds of pieces for Phase II optomechanics, Mike Ayliffe designed scores of them including critical components such as the outer barrel. Dominic Goodwill and Rajiv Iyer also respectively designed and built most of the optical power supply. Yongsheng Liu helped out in optical matters. David Kabal laid out and supervised the fabrication of the printed circuit boards which featured signal traces for relaying electric alignment signals and helped in wirebonding. David Rolston laid out the large Si alignment detectors on the hybrid-SEED chip and managed to make available pin-outs for those signals. Discussions with Rob Wodnicki were fruitful for the silicon detectors. Dr. William Robertson (Middle Tennessee State University) optimized the fan-out grating design to supply higher orders for the alignment beams. Professor Taghizadeh at Heriot Watt University (Edinburgh, Scotland) fabricated the diffractive lenslets. Kechang Song (McMaster University, Hamilton, Canada) fabricated both MSM chips. Danny Birdie, Pritha Khurana, and Eric Bernier helped me take data at various times when I needed assistance. I never could have accomplished this thesis without all the above people and I sincerely thank them.

1.7 References

1 R. Tummala and E.J. Rymaszewski, Microelectronics Packaging Handbook, (Van Nostrand Reinhold, New York, 1989), pp. 7-60.

2 M. R. Otazo, "Packaging of two-dimensional optoelectronic device arrays for optical backplanes," M. Eng Thesis, McGill University, 1996.

3 J. Child, "Compact PCI builds momentum, attacks industrial applications," *Computer Design*, 35 (2), pp. 49-50 (1996).

4 H. W. Markstein, "Ensuring signal integrity in connectors, cables, and backplanes," *Electronic Packaging and Production*, pp. 61-69 (October 1996).

5 S. Nimmagadda, J. Dillon, and A. Moncayo, "A 533Mbits/sec/wire modular bus with single or double parallel termination," 1996 Electronic Components and Technology Conference, IEEE ref # 0-7803-3286-5/96, pp. 974-983.

6 "Active termination ups speed, cuts power use," *Computer Design*, 36 (3), p. 44 (1997).

7 S. Gogaert, M. Steyaert, and V. Peluso," 622 Mbit/s board-to-board link in 0.5 μm CMOS technology," IEEE 1995 Custom Integrated Circuits Conference, paper 22.6, pp. 447-450.

8 H. Högl, A. Kugel, J. Ludvig, R. Männer, K. H. Noffz, R. Zoz, " Enable ++: a general-purpose L2 trigger processor," 1995 IEEE Nuclear Science Symposium and Medical Imaging Conference Record, pp. 667-671.

9 J. R. Mashey, "From busses to modular, distributed crossbars, not all shared-memory systems are equal," Silicon Graphics Internal Report, available at www.sgi.com, (1996).

10 Personal private communication.

11 IEEE Standard 1014-1987 for a Versatile Backplane Bus: VMEbus.

12 "Worldwide Market for Merchant Computer Boards in Realtime and Embedded Applications", 1996 edition, Venture Development Corporation, as communicated by VME International Trade Association

13 J. Black, "A few words from the editor," *VMEbus Systems*, 14, (2), pp. 7-9 (April 1997).

14 IEEE Standard 896.2-1991, Futurebus+.

15 U. Walenhorst and A. Brenner. "High frequency characteristics of modular metric. high-density connector systems," Symposium Record. IEEE 1995 International Symposium on Electromagnetic Compatibility, pp. 483-489.

16 R. A. Nordin. F.J. Levi. R.N. Nottenburg. J. O'Gorman. T. Tanbun-Ek. and R. A. Logan, "A systems perspective on digital interconnections technology," *Journal of Lightwave Technology*. 10. pp. 811-827 (1992).

17 H. S. Hinton. An Introduction to Photonic Swicthing Fabrics. (Plenum Press. New York, 1993). pp. 4-15.

18 M.R. Feldman. S.C. Esener. C.C. Guest and S.H. Lee, "Comparison between optical and electrical interconnects based on power and speed considerations." *Applied Optics*. 27. pp. 1742-1751 (1988).

19 A. L. Lentine. D. J. Reiley. R. A. Novotny. R. L. Morrison. J. M. Sasian. M. G. Beckman, D. B. Buchholz. S. J. Hinterlong. T. J. Cloonan, G. W. Richards. and F. B. McCormick. "Asynchronous transfer mode distribution network by use of an optoelectronic VLSI switching chip." *Applied Optics*. 36. pp. 1804-1814 (1997).

20 G. C. Boisset. M. H. Ayliffe. B. Robertson. R. Iyer. Y. S. Liu. D. V. Plant. D. J. Goodwill. D. Kabal. and D. Pavlasek. "Optomechanics for a four-stage hybrid-self-electro-optic-device-based free-space optical backplane." *Applied Optics*. 36. pp. 7341-7358.

Chapter 2: Review of Optical Packaging for FSOIs

2.1 Introduction

Optomechanics is the discipline which consists of designing and fabricating reliable support structures for implementing optical designs. Optical packaging is a broader field which includes optomechanics but which also consists of integrating optoelectronic components and electronic packaging into complete systems. While the field of optomechanics has been studied for centuries [1] and is by now a well-established field with many excellent references [2.3.4.5.6], the field of optical packaging as applied to digital free-space optical interconnects (FSOIs) is relatively new[7].

The goal of this chapter is to review the principal optical packaging problems that have been overcome and others that will have to be overcome in order for FSOIs to work in industrial contexts. In other words. the key problems are introduced in this chapter: subsequent chapters describe research that was conducted to address the problems brought up in this review.

This chapter is divided as follows. Section 2.2 will cover the objectives that optical packaging must meet and the characteristics that it must have. Section 2.3 overviews the different types of optical interconnects used to implement FSOIs. Section 2.4 studies the impact of device technology on optical packaging. To help do so, two systems– one based on emitters and the other based on modulators – designed and fabricated at McGill will be considered. Section 2.5 covers environmental issues that affect FSOIs. Section 2.6 describes typical fabrication concerns that must be addressed. Section 2.7 presents an optical packaging hierarchy that has been adopted by optical packaging designers to better organize their task given the above concerns.

2.2 Optical Packaging Objective and Required Characteristics

2.2.1 Objective

The objective of optical packaging in FSOIs is to implement an optical design within the specified alignment budget and support the associated optoelectronics.

2.2.2 Required Characteristics

For FSOIs to leave the laboratory and gain widespread acceptance in industry. optical packaging should have the following characteristics :

- **Ruggedness**: This is by far the most important. Systems must remain aligned and functional over long periods of time. even when exposed to vibrations. shock, and environmental fluctuations. Many electronic and fibre optic applications today are compliant with standards describing expected ruggedness. ranging from civilian applications [8,9] to militaryones[10]. FSOI system will have to comply as well.
- **Ease of assembly and maintenance**: One cannot always have teams of highly trained researchers building and fixing systems one at a time. Reducing component count is one key simplification.
- **Low cost:** Recent estimates indicate that optoelectronic packaging costs represent 70-80% of total component cost in general optoelectronic systems[11], and are still high even in fibre-based links[12]. This is unacceptable. The costs must fall. Moreover. the total cost of operation, including maintenance as well as assembly. must be considered.
- **Small size and weight:** FSOIs must follow current packaging trends toward miniaturization [13].

- **Compatibility with existing plant infrastructure:** while not mandatory. compatibility with established standards [14] for mechanical structures in computing environments will help ensure a more rapid acceptance of FSOIs.

2.3 Types of Optical Interconnects

In FSOIs, the objective of an optical interconnect is to image arrays of beams from one plane to another. There are effectively four classes of interconnects used in FSOIs: these are shown respectively in Figure 2.1a through d [15].

a) macrolens-macrolens: From an optical packaging perspective, this is the simplest to design and align. As shown in Figure 2.1a, a relay (usually telecentric) is made up of two lenses. These systems have many drawbacks, however, since expensive and bulky multi-element compound lenses [16] often have to be built in order to obtain the high field of view necessary to image a beam array that may be several millimeters on a side. Moreover, most of the space-bandwidth product of the costly lens is wasted since the relayed beams occupy only a small part of the total image area.

b) lenslet-lenslet: to avoid using costly and inefficient compound macrolenses. interconnects can be implemented using just lenslets[17]. This implementation allows for very compact designs with simple optics. However, the maximum interconnect distance is limited unless non-telecentric systems are implemented [18, 19], but these are hard to align and still offer limited interconnect distances.

c) hybrid macrolens-lenslet: this approach combines the advantage of the high numerical aperture (NA) of lenslets with the longer distance relay capability of macrolenses. Moreover, the macrolenses do not have to be complex since they need only relay beams with low numerical apertures[20].

d) hybrid lenslet-minilens: this approach also uses lenslets with high NA to capture beams leaving a device plane. The minilens relay offers a greater flexibility of interconnect distances and implementation technology[21].

While not strictly free-space interconnects themselves, fibre ribbon interconnects are also of interest and sometimes play a role in FSOIs since many parallel computing and switching systems have used fibre bundles for bringing data into or out of a system[22,23,,24].

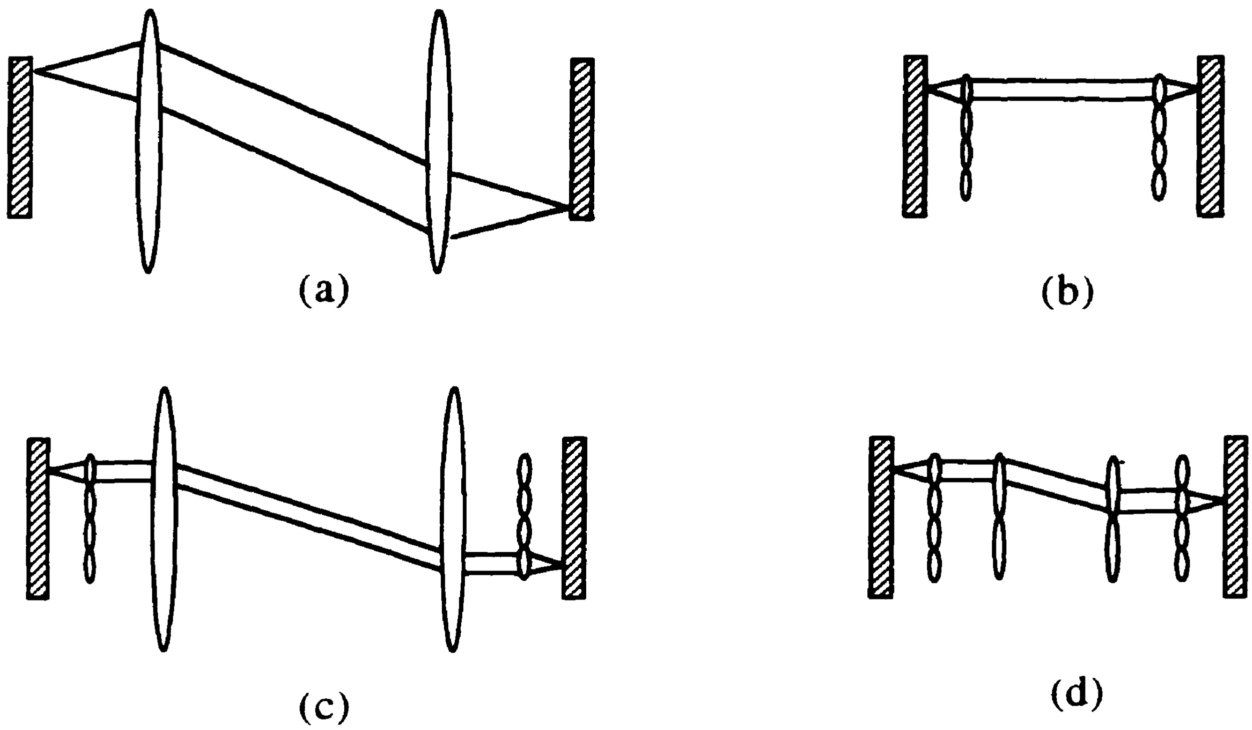

Figure 2.1: Different optical interconnect configurations a) macrolens-macrolens b) lenslet-lenslet c) hybrid macrolens-lenslet d) hybrid minilens-lenslet

2.4 Modulators vs Emitters: Impact of Optoelectronic Device Technology on Optical Packaging

From an optical packaging perspective, FSOIs can be divided into two categories: emitter-based and modulator-based. In emitter-based systems [25,26,27,,28,29], arrays of devices such as vertical cavity surface emitting lasers (VCSELs) directly generate the encoded beams of light which are sent to the next stage, as shown in Figure 2.2a. On the other hand, in modulator-based systems described to date, [30,31,32,33,34] an optical power supply (OPS) generates an array of optical power beams which are imaged onto an array of optical modulators at stage # 1: a typical setup is shown in Figure 2.2b. The modulated beam array must then be relayed to a detector array at stage # 2. There are thus two distinct alignment problems: first the array of optical power beams must be aligned onto the stage # 1 modulator array: second, the modulated beams must be aligned onto the detector array at stage #2. This is repeated as many times as there are stages in the system. In both approaches, beams of light with information encoded onto them are imaged from one stage to another. The fundamental difference between the two, as far as optical packaging is concerned, is that modulator-based interconnects are generally more complex for optical packaging designers since there is the additional step of aligning optical power supply beams onto modulators.

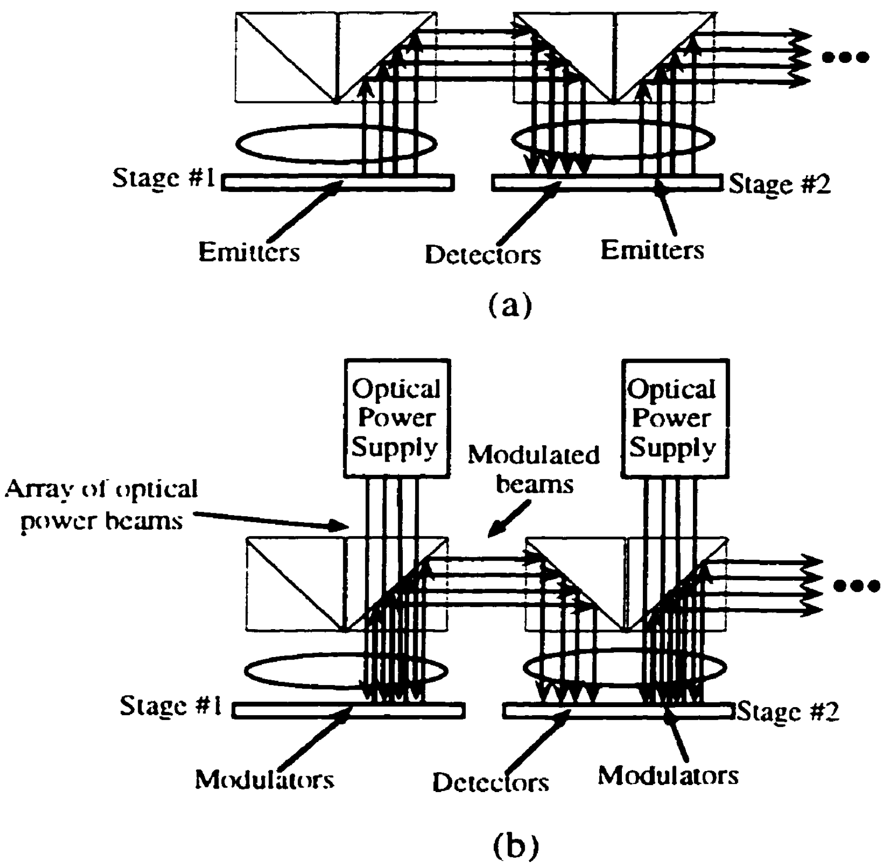

Figure 2.2: Optics for different device technologies a) emitter-based b) modulator-based

Broadly speaking, emitters can be divided into light emitting diodes (LEDs), edge emitting lasers, and surface emitting. Resonant cavity LEDs (also known as superluminescent LEDs) combine aspects of LEDs and lasers. LEDs are the cheapest and most reliable devices but they are inefficient, cannot be modulated beyond a few hundred MHz and the generated light is not very directional [35]. Edge-emitting lasers have been used for over a decade in long-haul fibre communication and experimental FSOI systems with edge emitting lasers have been demonstrated [28], but they are limited to 1D interconnects and so cannot match the throughput promise of 2D interconnects. Surface emitting lasers, led by VCSELs, are the most promising avenue of research right now. VCSELs can easily be fabricated into 2D arrays and offer low threshold currents, symmetric beam profiles, and wafer-scale testability, among many other qualities. Current challenges for VCSELs include polarization control [36] and attaching them [37] to or growing them [38] onto silicon integrated circuits in a way that does not negatively affect the above-mentionned superior VCSEL characteristics.

Modulator technologies include include the various SEED-based device families which are more advanced than emitters in terms of capability of attachment to silicon [39]. Liquid crystals, [40], exciton absorption reflection switches (EARS) [34], and others are also used [41].

In the following paragraphs, optical packaging design issues and constraints for emitter- and modulator-based systems will be studied by comparing an emitter-based system, a VCSEL-MSM system[27] and a modulator based one, the FET-SEED system[17], the optical packaging for both of which the author was largely responsible.

Obviously, comparing two systems that had vastly different architectures, design objectives, priorities, and budgets may be unjust. However, these systems were designed and built by essentially the same group of people within an 18 month time frame and have characteristics typical of their respective emitter and modulator classes and as such will serve well for the comparison. The FET SEED system is shown in Figure 2.3. the VCSEL-MSM system in Figure 2.4.

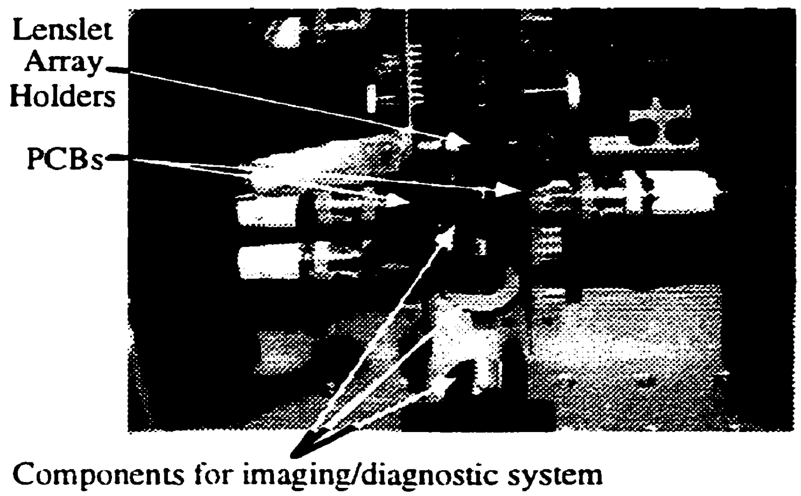

(a)

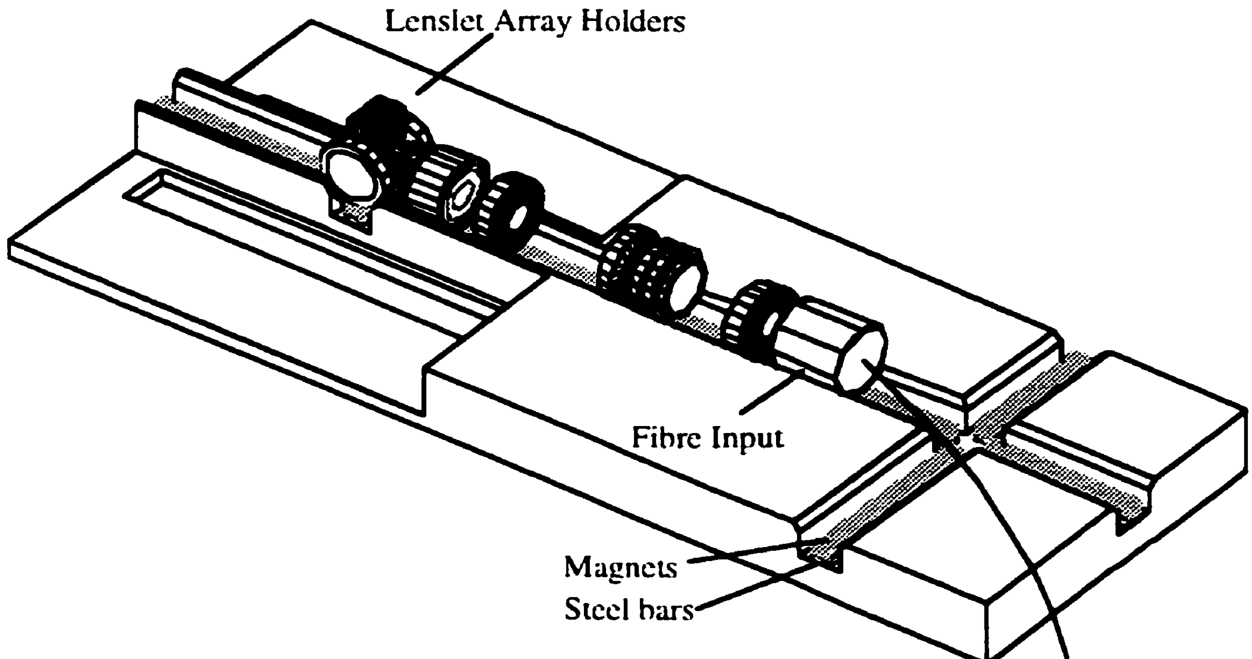

(b)

Figure 2.3: FET-SEED System a) Picture showing system with two PCBs and part of imaging/diagnostic system b) Diagram with PCBs and imaging/diagnostic system removed for clarity

(a)

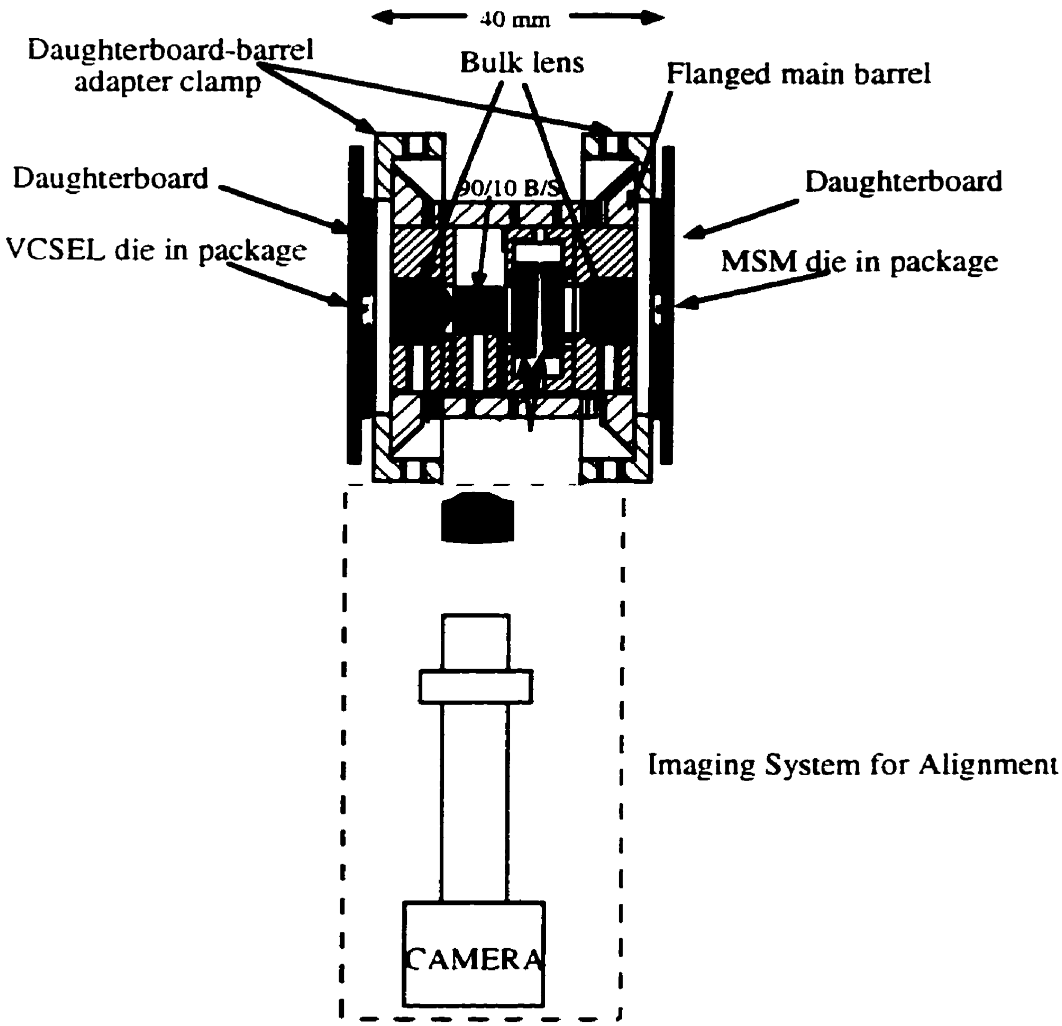

Figure 2.4: VCSEL-MSM system a) picture in chassis b) diagram showing imaging system

2.4.1 Divergence Angle

At either a modulator or emitter device window, the optical design is such that a beam waist is usually present (Gaussian beams are assumed). If w_o is the $1/e^2$ radius (a $2w_o$ diameter encircles 86% of the beam energy, a $3w_o$ radius encircles 99%) of the beam at the window, then the beam leaves the window with a full width $1/e^2$ max ($FWe^{-2}M$) divergence angle of θ in the far field, as shown in Figure 2.5, where θ is given by[42]:

$$2\theta = 2\frac{\lambda}{\pi w_O} \tag{1}$$

The VCSELs in the system had a nominal beam diameter at the window of $2w_o$=2.8μm($3w_o$=4.2μm), which gave a far field $FWe^{-2}M$ divergence angle of $2\theta_V = 22°$ (f/#=2.6). Given the VCSEL pitch of 125μm and the very high divergence angle, microoptics would have had to be 214 μm away from the devices to capture 99% of the light: this could have caused space constraints with the wirebonds on the device. Moreover, this would have imposed refractive lenslets since fabricating efficient diffractive lensets for such low f/# beams would have been expensive[43]. Given these constraints, it was decided to use the first type of interconnect described above, namely a macrolens-macrolens interconnect. This is a clear example of how the device technology, in conjunction with optical and packaging constraints, can dictate the type of optical interconnect implemented and impose a solution which may not be scalable. Previous systems incorporating VCSELs with lenslets have also encountered the problem of bondwires close to the microoptics[44]. It should be noted that problems of this nature can be overcome in part by using beam clustering[45], but this option requires control over the device layout, which is not always a possibility.

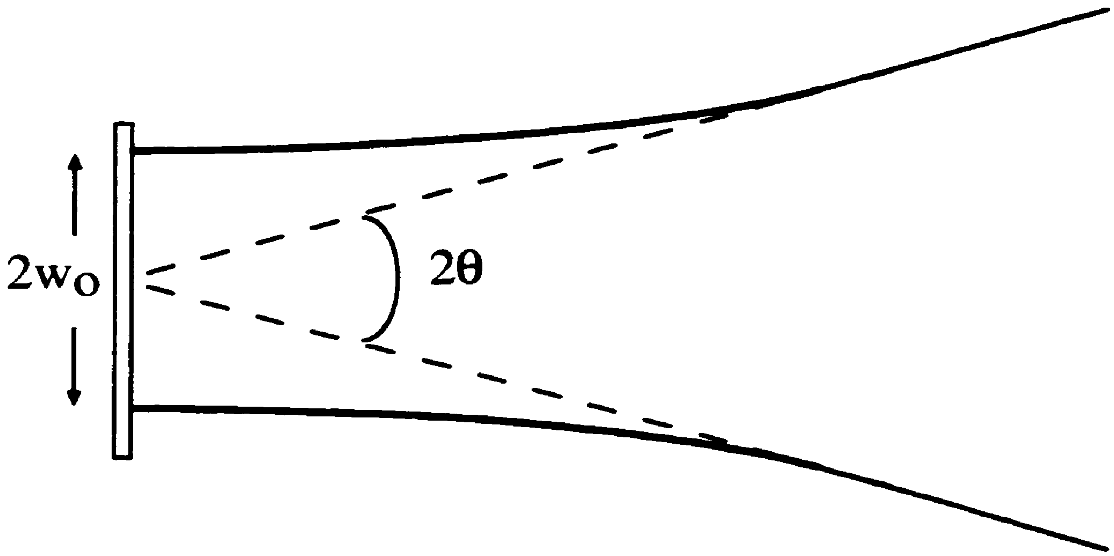

Figure 2.5: Far field divergence angle of an ideal Gaussian beam

Generally, modulator windows are bigger than emitter windows. As a result, the beam diameter w_o at the modulator window in equation (1) can be made bigger: this in turn reduces the divergence angle and thus increases the f/# of the beam leaving the smart pixel. This allows for more optical design freedom as can be seen from recent systems implementing FSOIs: for example, in these cases inexpensive diffractive microoptics can be placed close to the device windows in order to further reduce the numerical aperture of the beams. Afterwards, hybrid systems like the ones described above in section 2.3 can be used to relay the beams from one stage to another[46,47,48]. Demonstrators using just bulky macrolenses (the first type of interconnect described above in section 2.3) require more complex and expensive multi-element lenses[31,32] due to the large field of view requirements and low f/#s. The key point is that there is more flexibility allowed in the optical design because of the looser space constraints.

For example, the FET-SEED modulator windows were 25 μm x 25 μm, and the incident beams had a diameter of $2w_o$=13.3μm($3w_o$=20μm), which gave a divergence angle (FWe^{-2}M) of $2\theta_{=}$=2.32° (f/#=12.5) in the far field. This high f/# allowed for easy fabrication of high efficiency lenslets. Furthermore, the low divergence angle allowed for a focal length of 6.5 mm, placing the microoptics far from the optoelectronics.

2.4.2 Components

As shown in Figure 2.4, all the VCSEL-MSM optics, which consisted of two lenses, a pair of Risley Beam Steerers and a 90/10 beamsplitter were inserted into a flanged barrel which was then attached to daughterboard clamps mounted on their respective daughterboards. The barrel was 26.04 mm ± 20 μm long and was made of black anodized aluminium; the daughterboard spacing was 40 mm. The entire system was mounted in a standard 482.6 mm (19") 6U VME chassis. Mounting everything in a straightforward barrel was possible for this two-stage system because there is no OPS in an emitter-based system.

Most aggressive modulator-based FSOIs have used slotted baseplate approaches: relay components such as lenses and OPS components such as fan out gratings are mounted into circular magnetic steel cells which are placed on slotted baseplates. To hold the components in place, magnetic steel bars are bolted to the bottom of the slots and magnets are placed on the bars. The magnets then hold the magnetic steel cells securely in place. The FET-SEED system is a typical example, shown in Figure 2.3. Other techniques also use guide frame assemblies for a sturdier support of system optics [22, 49].

While at first glance the simplicity of the VCSEL-MSM system might seem to be an overwhelming advantage for emitter-based systems, the picture changes considerably for systems with more than two stages. As ca be seen in Figure 2.2, both modulator and emitter systems need additional components such as beamsplitters to relay beams to the next stage. The multi-stage modulator system is still more complex because of the alignment of the OPS, but multi-stage emitters nonetheless have considerable complexity[24] as well.

2.4.3 Alignment Tolerances

In the VCSEL-MSM interconnect, the tolereances were very loose. The spots incident on the detectors were nominally 5μm wide and the detectors were 50μm on a side.

As a result, the lateral alignment tolerance for <1% loss was ± 20μm in both x and y, and the system z alignment (defocus) tolerance was 85μm. Rotational (θ_z) and tilt (θ_x,θ_y) tolerance were both approximately 5°. Combinations of the above misalignments resulted in more than 1% loss. As a result of these loose tolerances, the system could be adjusted by hand, although an imaging setup through the 90/10 beamsplitter was necessary in order to see the detector windows on which the beams had to impinge. The corresponding modulator tolerances were tighter, with only ± 1μm in x-y lateral alignment tolerance, ±25μm in z and 0.25° in tilt and rotation, but that is because the windows were smaller[50]. Bigger windows would have yielded tolerances comparable to those of the VCSEL-MSM system.

The key number above is the tilt tolerance for the emitter. As can be seen in Figure 2.6, a beam incident on a modulator plane is reflected at an angle of 2β for a plane tilt of β whereas an emitter on the same plane would emit light with an angle of only β. As such, for otherwise equivalent systems, emitter tilt tolerances are twice as loose as those for modulators.

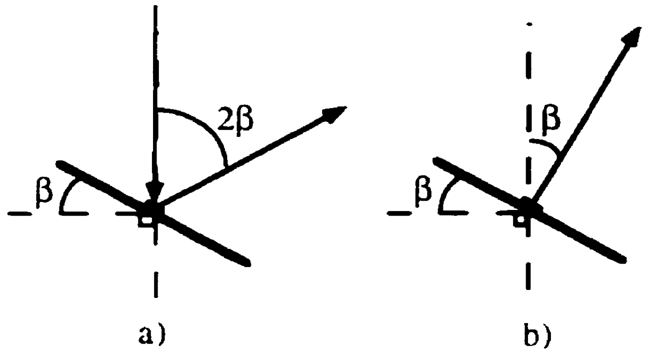

Figure 2.6: Impact of device plane tilt on angle of outgoing beam a) modulator b) emitter

2.4.4 Diagnostic

In order to assemble and align a system, the builders must have information about its current alignment status. The most common approach to gaining this information is to build an imaging system to image up the optical beams and their intended targets. These are shown in Figure 2.3 and Figure 2.4 for both respective systems. Although versatile and well engineered "periscope" imaging systems can be built to image hard-to-reach planes in an FSOI [31], imaging systems are generally unwieldy and bulky. For both systems, the imaging system is comparable in size to the actual FSOI. Even if diagnostic systems are not a permanent fixture and can be removed after assembly and diagnostic, FSOI systems must still leave room for diagnostic systems, reducing overall system density. Typical images obtained from an imaging system are shown in Figure 2.7.

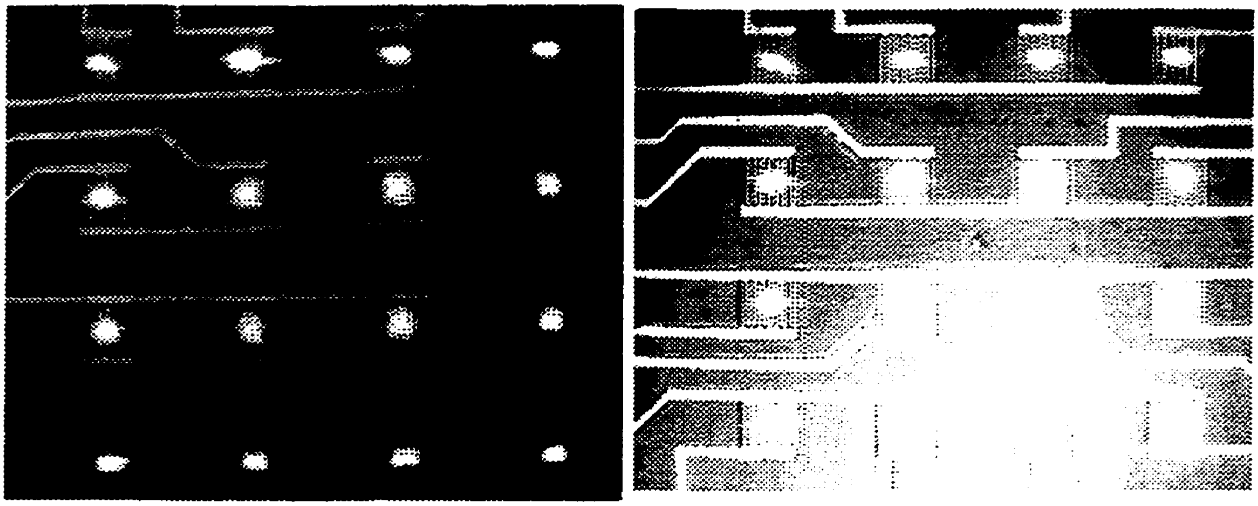

(a) (b)

Figure 2.7: Pictures of the illuminated MSMs in VCSEL-MSM system a) before drift-vibration test b) after test, three weeks later

After assembly, the VCSEL-MSM system was put through a vibration test in which it was exposed to a cooling fan for three weeks. As can be seen in the before and after views, the spots on the detectors did not move to within 2μm, which is the width of the MSM fingers–a convenient metric. The spots did not move after 30 consecutive insertions and extractions of the motherboards in the chassis. This characterization result is typical of those obtained using imaging systems: alignment measurements were obtained visually, and features on the chip were used to estimate quantitative values.

As shown above, using lenslets generally produces more compact systems, but imaging and alignment diagnostic are considerably more difficult. Much more time was spent aligning the FET-SEED system than the VCSEL-MSM system, in part because the imaging/diagnostic system for relaying the device image to the camera was much more elaborate. As was the case for the FET-SEED system, an imaging system for lenslet-based interconnects often must be of a hybrid nature, with lenslets and macrolenses needed to relay the image away from the main link and toward the camera. Since the main link consists of intricate and compact components which are carefully aligned, assembled, and interlocked, it is difficult to design optomechanics which can accept and align an insertable/removable hybrid imaging relay. Often, the designer is left in the untenable situation of having to build a diagnostic system for the diagnostic system.

As a result, given their complex nature yet vital role, alignment diagnostic systems are a very important field of research for FSOIs: two chapters of this thesis will be dedicated to the development of diagnostic systems that can generate useful alignment information while consuming minimal resources.

Modulator systems need more elaborate diagnostic systems since often the modulator plane and the detector plane must be monitored at the same time whereas only the detector plane need be monitored carefully for emitter systems.

2.4.5 Further Device Comments

Finally, it should be noted that modulators and emitters may be either one-sided or two-sided, the difference being whether the beams enter and leave from the same side of the optoelectronic device substrate (one-sided) or enter and leave from different sides, implying some form of through-the-substrate communication (two-sided). Most device technologies are one-sided, for reasons including enhanced contrast ratio, ease of device fabrication, and more effective heat sinking[51].

2.5 Environmental Issues

A realistic system must remain operational even when exposed to a harsh environment. Most electronic computing systems today are exposed to considerable thermal cycling as well as to mechanical vibrations originating from sources such as cooling fans blowing air and dust over components. As the power consumption of components increases in the future (recall that CMOS power consumption is linearly proportional to clock rate and transistor densities are constantly increasing), these environmental considerations will become ever more important and FSOIs will have to function effectively in these environments if they are to gain widespread acceptance. Moreover, diagnostic tools to quantify the optical misalignments, if any, caused by vibrations, shock, and thermal cycling will have to be developed.

This section describes the impact of adverse environmental conditions on advanced optical and electronic systems described in the literature and, more importantly, draws conclusions from published results that must be considered when designing FSOIs. Key conclusions will be shown to be the importance of diagnostics and the need to well understand phenomena such as thermal expansion in order to design practical solutions such as athermalization.

2.5.1 Vibration Isolation and Compensation

Maintaining optical performance independent of external vibration can be accomplished by using passive means (isolation), active means (compensation), or both.

Currently, the most advanced vibration isolation and compensation systems can be found in Laser Interferometer Gravity wave Observatory (LIGO) experiments. One of the most sophisticated LIGOs will detect gravity waves causing a differential path length difference of 1 attometre (10^{-18} m) over an interferometer consisting of two orthogonal, 4km long interferometer arms[52]. These systems generally use multiple cascaded passive vibration isolation systems consisting of metal springs and magnetic eddy current dampeners in addition to active control loops using feedback and piezoelectric actuators[53,54]. Extensive system characterization is performed in all LIGOs. An important lesson gained from studying such systems is the importance of developing effective measurement techniques to characterize the vibratory behaviour of optomechanical systems. This lesson is particularly relevant to FSOIs such as backplanes which are exposed to the vibrations of fans and shocks of component insertions and extractions. The next chapter covers the development of a vibration characterization scheme for diagnostic of a free-space backplane. Closely related to vibration compensation is the issue of adaptive optics, most often used to eliminate atmospheric distortion in ground-based telescopes [55]. While fascinating, very little of this is applicable to FSOIs.

Another technique for maintaining system operation in even the most difficult environments is to assemble the system using extremely stiff components all fastened together with no movement allowed. For example, the Mars Observer Laser Altimeter (MOLA) consisted of dozens of optical and optomechanical components. All the key components were painstakingly adjusted on the ground and when the system was finally aligned, glue was poured over all the key components, ensuring nothing was disturbed during the violent liftoff and trip to Mars[56]. Stiffeners have also been used to eliminate component movement in previous FSOI demonstrations [57] .For this technique to work, however, proper athermalization and material selection are paramount, as the next subsection indicates. This technique of gluing critical components once aligned was implemented in a system demonstrator described in the next chapter.

Finally, simple solutions such as mounting a FSOI system in a chassis using 1.91 cm rubber spheres have been implemented with success[22].

For the sake of comparison, a good hard disk drive today can withstand a shock of 200 Gs while operating or 500 Gs while in storage. This corresponds to a drop of half a metre onto a hard floor[58].

2.5.2 Thermal Effects

Thermal effects affect optical packaging in two different ways. The first effect, which is indirect, is the heat sinking required for optoelectronics which can affect optical packaging space constraints. The second impact, this one direct, is the effect of temperature changes on the optical packaging and the optics.

2.5.2.1 Chip Thermal Control

Smart Pixel chips generate heat, which must be removed. A typical smart pixel chip consists of CMOS circuitry which provides the intelligence, and receivers and emitters or modulators for the optical I/O. This analysis assumes that attaching emitters to a chip is as easy as attaching modulators, although this is not the case today. Assuming a chip in which the intelligence consumes 5W and which requires 1000 optical I/O channels each running at 622Mbit/s, the total on-chip power would be approximately 5+2.4=7.4W for a modulator-based solution and 5+10=15W for the emitter solution, using typical values for transceiver consumption for various technologies[15]. Removing this heat requires heat sinks, the size of which is a function of the required heat removal, air circulation and system layout. Typical heat sinks for the heat dissipation values given above can have dimensions of 63x80 x 26mm[59]. Using the optomechanics themselves as a heat spreader has been accomplished before [22,32] although this often only displaces the problem since, as the subsection below indicates, thermal flow can also affect optical packaging performance.

This discussion also indicates how all optical packaging issues are closely coupled. For example, reducing the size of required heat sinks to loosen optical packaging constraints can be accomplished by increasing fan speed, generally at the cost of higher vibrations or vibration frequencies closer to the resonant frequency of the system.

2.5.2.2 Athermalization of Optics and Optical Packaging

Temperature changes can bring about many changes in an optical interconnect: 1) the index of refraction, n, of glass or plastic changes with temperature, T. For example, $dn/dT=1.7\times10^{-6}$, and -105×10^{-6} for BK7 and acrylic respectively[60] 2) The size of a lens can increase with temperature, changing its surface curvature and as such its focal length 3) the optomechanics can expand with temperature, changing the spacing of the components 4) expansion of the components within their retaining rings can bring about strain which, if sufficiently large, can affect differently the ordinary and extraordinary indices of refraction, leading to birefringence and changes in polarization.

A straightforward approach is to actively maintain the entire system at a constant temperature, thus eliminating the problems. This approach has led to active cooling of baseplates with water exchangers, for example [31]. Another approach is to design the system such that the different thermal effects act in opposing ways, canceling each other out. A small design example illustrating one approach to athermalization is useful: in Figure 2.8, the lens must collimate the light from the source, which means the source always must be at the lens front focal plane. However, the lens focal length changes with temperature.

The focal length, f, of a thin lens is given by

$$1/f = (n-n_{air})(R_1-R_2) \tag{2}$$

where R_1 and R_2 are the radii of curvature of the two lens surfaces and the index of air is assumed to be unity. Differentiating with respect to temperature and rearranging gives x_f, the change in normalized focal length with temperature [60]:

$$x_f = \frac{1}{f}\frac{\mathrm{d}f}{\mathrm{d}t} = \alpha_g - \frac{\mathrm{d}n/\mathrm{d}t - n\mathrm{d}n_{air}/\mathrm{d}t}{n-1} \tag{3}$$

where α_g is the coefficient of thermal expansion of the glass (α_g=7.1μm/m/°C for BK7), and dn_{air}/dt = -0.964 . For BK7, x_f=0.98μm/m/°C. Therefore, designing a spacer made of material having a coefficient of thermal expansion α =0.98μm/m/°C will ensure athermalized proper collimation by keeping the correct distance between source and lens.

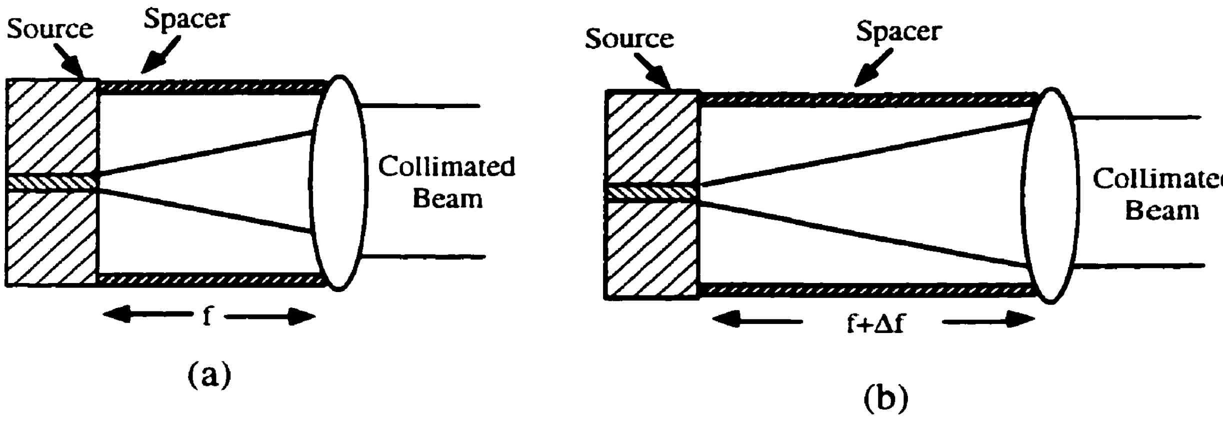

Figure 2.8: Example of athermalization a) at nominal temperature, T b) at T+ΔT, spacer expands by as much as focal length increases.

Other interesting athermalization solutions may not even involve optomechanics. For example, etching diffractive lenses onto refractive lenses can effectively athermalize a lens for a given wavelength over a given temperature range[61]. Multiple lens systems can also be athermalized using a combination of optical and optomechanical compensations [62].

The lesson learned from studying these solutions is that thermal effects are unavoidable but can be used to advantage: in the next chapter, a novel method for thermal-load lens mounting is presented which exploits thermal effects to simplify an optomechanical design.

2.5.3 Other Environmental Effects

Dust is a major problem for FSOIs. It can accumulate on microoptics and so block channels or scatter light. If it lands on optoelectronics, it can affect their performance and potentially block device optical windows. For systems featuring removable components such as backplanes, the problem is even worse as the system may not necessarily be sealed. It should be noted that electronics has studied the problems for years since even electronic connectors are affected by dust [63]. The most common solution for overcoming improper contacts caused by dust is "wipe"[64]. This is a mechanism in which an overhanging component in the female part of a connector rubs against a connector pin or finger as it is inserted. The longer the wipe effect or the harder the wiping action, the less dust is present and as such the better the contact. The wiping comes at a price, however. Longer wipe (i.e. longer pins and mating components) means higher inductance in the connector assembly [65] and high wipe increases the required insertion force. More significantly, at every insertion/extraction (I/E) cycle, small amounts of the expensive metal coating on the pins and fingers get – not surprisingly – "wiped" off: this is a principal reason why connectors have a limited number of I/E cycles. For example, a typical three-row gold-pinned backplane connector can only survive 200 I/E cycles[66].

The implications are clear: if electronics already has considerable problems with dust, then optical packaging designers have their work cut out for them. Moreover, electronic injection of signals into an optical backplane, as is done in the demonstrator system described in the next chapter, is also subject to dust problems.

Humidity also causes problems. Rust and bowing of printed circuit boards due to high humidity all lead to potential problems. Finally, electromagnetic interference, while incapable of affecting light beams, can affect the optoelectronics, as was noticed in our lab. An interesting way to help combat this would be to ground all metal optomechanics, especially if the optoelectronics are mounted on or near metal barrels and slugs.

2.6 Fabrication Considerations

No discussion on optical packaging is complete without covering fabrication aspects which must be considered at the design stage. While many textbooks are available for detailed discussions of general mechanical design principles [67,68] as well as for optomechanical design in particular,[2-6] experience is the best teacher. Below is a sampling of problems faced over the course of many optical backplane demonstrations which serves well to give an idea of fabrication challenges designers must overcome.

- **Making clamping points available**

A workpiece must generally be clamped down for machining, and the design must ensure clamping points for both initial fabrication and subsequent modifications.

The flanged barrel shown in Figure 2.4 is an insightful example. The flanged barrel would have been very awkward to hold during drilling of screw holes and milling of slots. It was thus decided to perform the machining as shown in Figure 2.9. To obtain the workpiece shown, a 33 mm diameter rod (the maximum outer diameter of the flanges) was turned and bored as per design. However, the original rod was chosen to be 30 mm longer than the 26 mm barrel length to facilitate clamping for the drilling and milling. As can be seen, the jaws of the chuck can clamp the workpiece with ease. Only after these operations had been performed was the 30 mm excess cut off.

This may have simplified clamping during fabrication, but when some holes and slots had to be reworked later, it was difficult to clamp the piece since clamping points were absent (the extra 30 mm having been cut off). Much time was lost for a simple post-production touch-up because clamping points were no longer available.

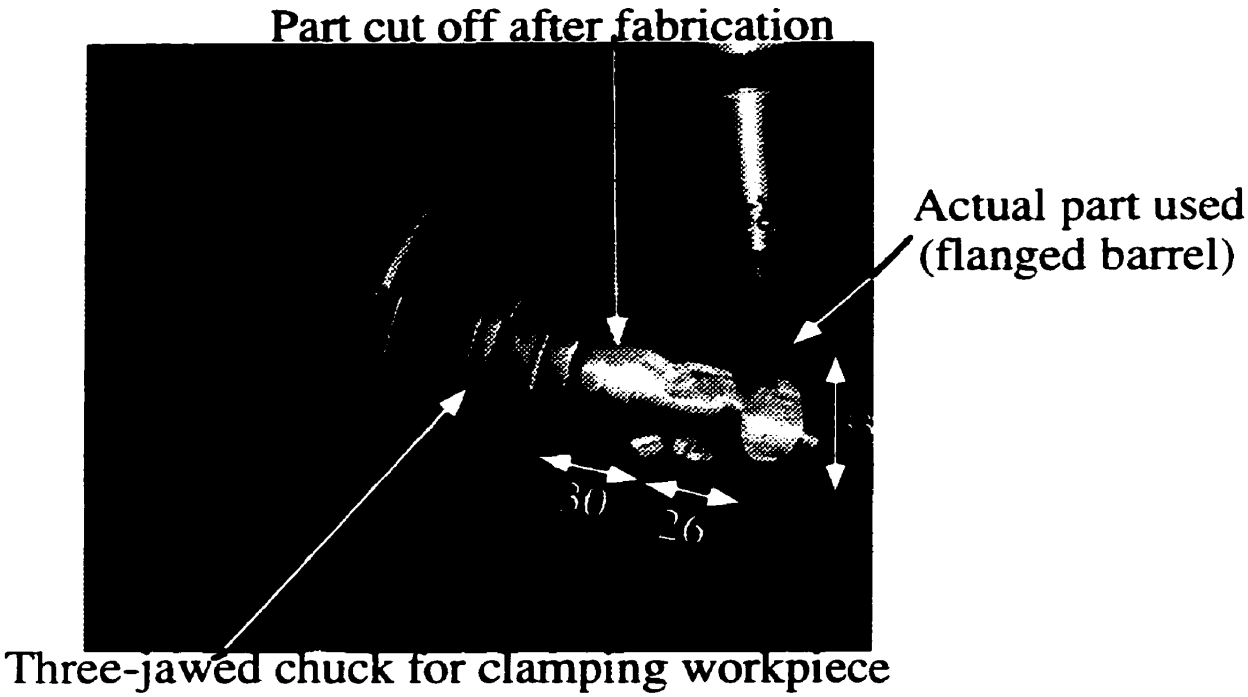

Figure 2.9: Barrel during machining held by three-jawed chuck

- **Minimizing additional features**

Every additional feature on every piece must be justified. Features added "just in case" often cause problems, especially at interfaces. The following example is typical.

During system assembly, the Risley Beam Steerers (RBSs) in the barrel of Figure 2.4 had to be rotated about the optical axis. Little holes were therefore drilled along the outer circumference of the cells holding the RBSs:a small hand tool could then be inserted into these holes to rotate the cell. It was originally thought that having more holes would make it easier to rotate the cell since it would make more holes accessible to the user, especially since the cell was located in a barrel offering limited access.

However, some holes caused many problems after the cell was anodized: at burrs around some holes, there was an accumulation of very hard anodized metal which eventually scraped against the barrel in which the cell was inserted, causing considerable damage. Reducing the number of holes to a more manageable value would have reduced the probability of damage due to an improperly deburred hole or slot. In fact. it was partly due to this type of damage that the rework and reclamping mentioned above had to be performed on the flanged barrel. These two examples further serve to show how different fabrication problems can affect and actually compound each other.

• **Minimizing clamping operations**

Every time a piece is clamped to or unclamped from a machine, the production process is halted. Additionally. repeated clamping operations introduce repeatability errors since the origin must be determined after every new clamping. Clamping operations. while unavoidable. should be minimized. An example of minimization is as follows.

A lot of five pieces called daughterboard holders – shown in Figure 2.10a– had to be machined. Each individual piece required three clamping operations just for the holes and slots: one for the features on the top. one for the bottom. and one for the side holes. For the five piece lot. this would have required 15 clamping operations.

Figure 2.10b shows a better design. In this case, all the operations on the top are performed in just one clamping. and similarly for the bottom. The workpiece is then cut and the side holes can be drilled on individual pieces. Total cost: 7 clamping operations. The fabrication was accelerated and the functionality of the finished pieces was unchanged.

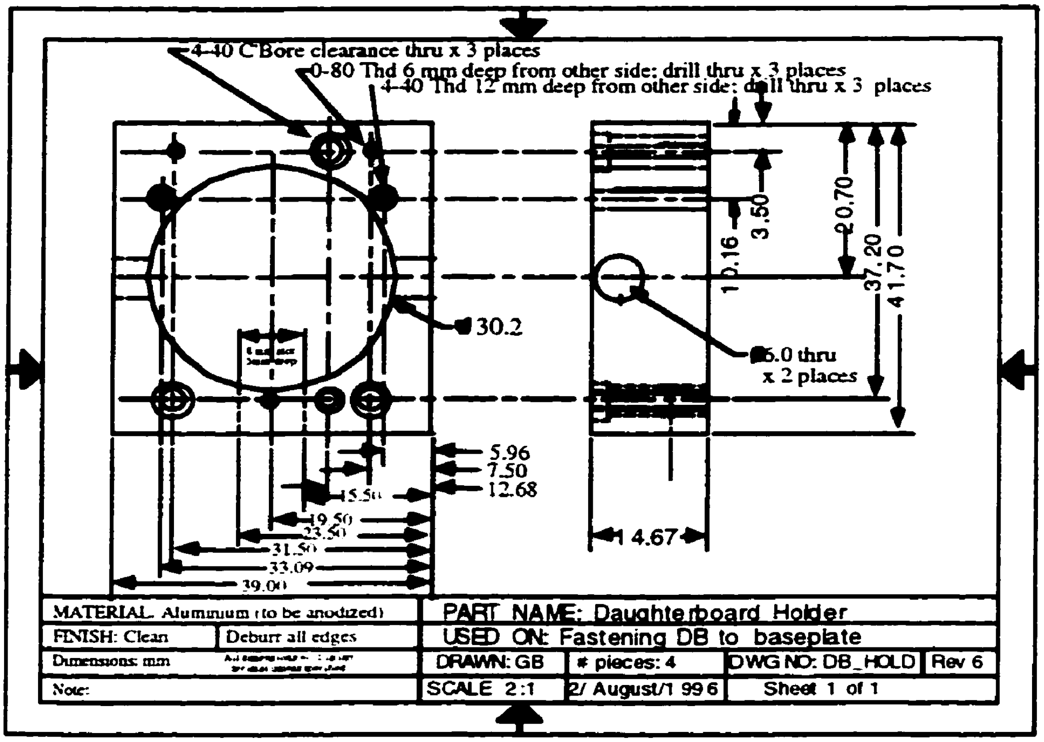

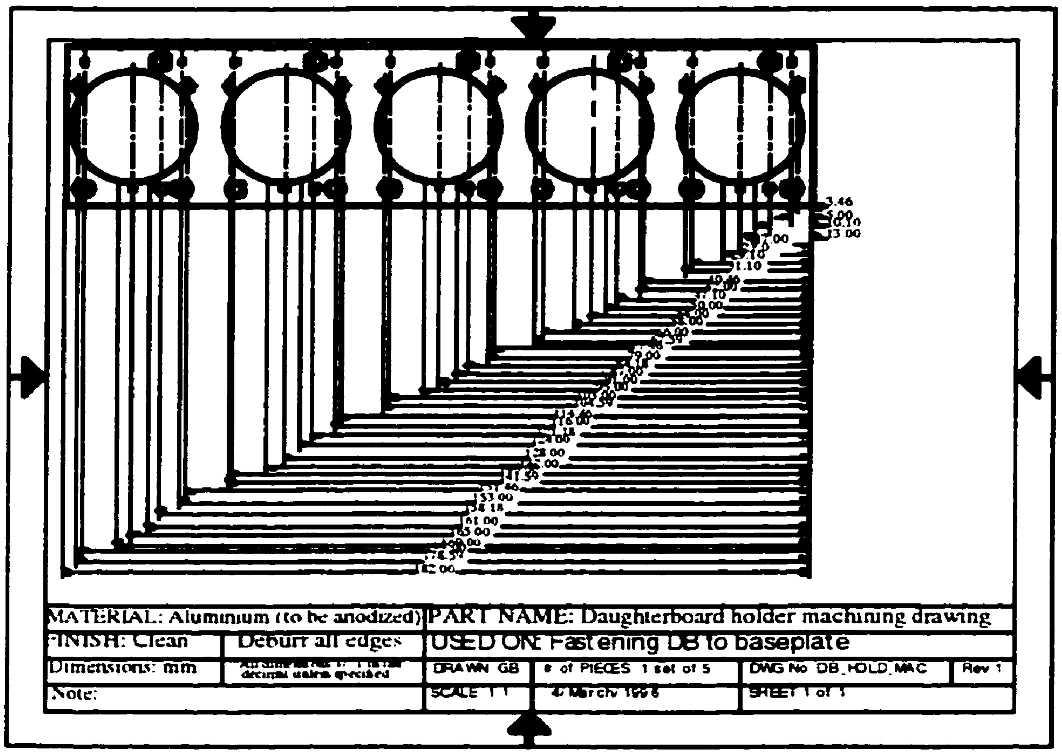

Figure 2.10: Drawing for daughterboard holders a) inefficient design b) more efficient (fewer clamping operations)

2.7 Integration Hierarchy

In order to better organize all the above characteristics and issues of interest. an optical packaging hierarchy analogous to the electronic packaging hierarchy can be adopted. Three levels are defined in this hierarchy, shown in Figure 2.11.

The third level is the overall system with chassis-to-chassis links. the most established level. This is mostly accomplished by fibre links. Considerable research into packaging of 1-D fibre arrays for medium haul (one to several hundreds of metres) has already taken place[69,70,71] and several products such as Motorola's Optobus™ and HP's Polo™ are on the market.

The second level is the chassis itself, with its stage-to-stage links for distances of up to 50 centimetres (the term module, defined below, could also be used instead of stage). The numerous FSOI demonstrator systems described in the references above [25-34] have implemented this level whereas fibre links have not yet convincingly demonstrated that they can deliver data over centimetre-scale distances in ways that are competitive with either electrical links or FSOIs. Typical examples of second level interconnects are the traditional barrel with lenses and prisms in the VCSEL-MSM system above.

The first level is the module level itself. A module is an optoelectronic device array integrated with its optical packaging support structure, often with microoptic components attached and aligned with respect to the device array. A module can represent an entity such as an MCM port or backplane port or switching node. Most recent demonstrated systems have tended in this direction of having sophisticated optical packaging for the device. This can take the form of slugs[31]. highly-engineered mounts and flexible boards within a frame assembly[22]. and integrated microoptics. among others.

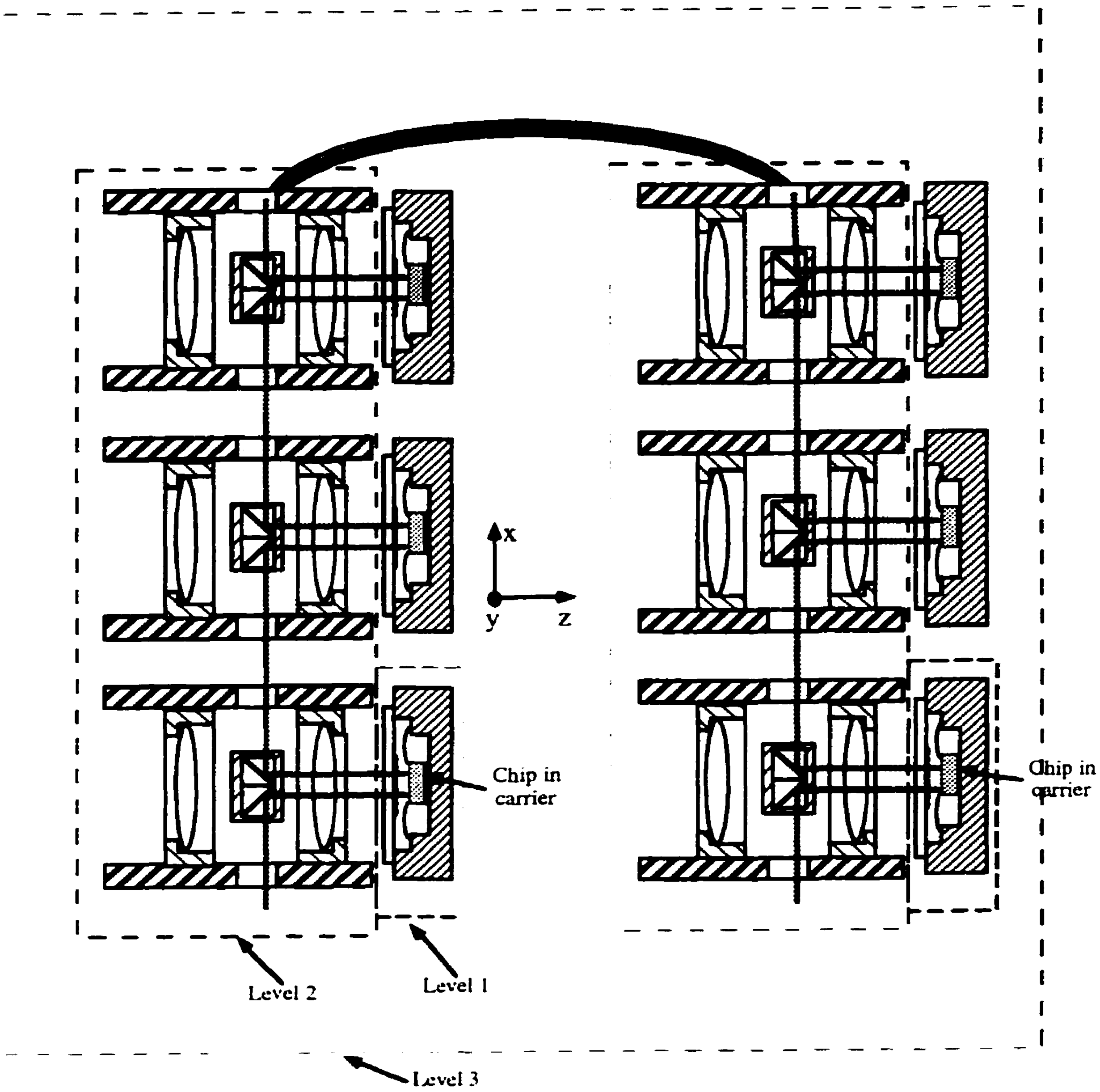

Figure 2.11: Optical packaging hierarchy

First level packaging integration of microoptics and optoelectronics is particularly promising since it offers tremendous advantages in terms of reduced size and loosened alignment tolerance in "upstream" parts of interconnect. A few calculations at this point are appropriate. The following assumptions are made: the beams at the lenslet array have a Gaussian irradiance distribution with diameter $3w_L$=125 µm, the lenslet focal length is f_μ=1 mm, the spot size at the detector is $3w_o$=20µm and the detector windows are 25 µm x

25 μm. In Figure 2.12a, the lenslets are not integrated to level 1 whereas in (b) they are integrated

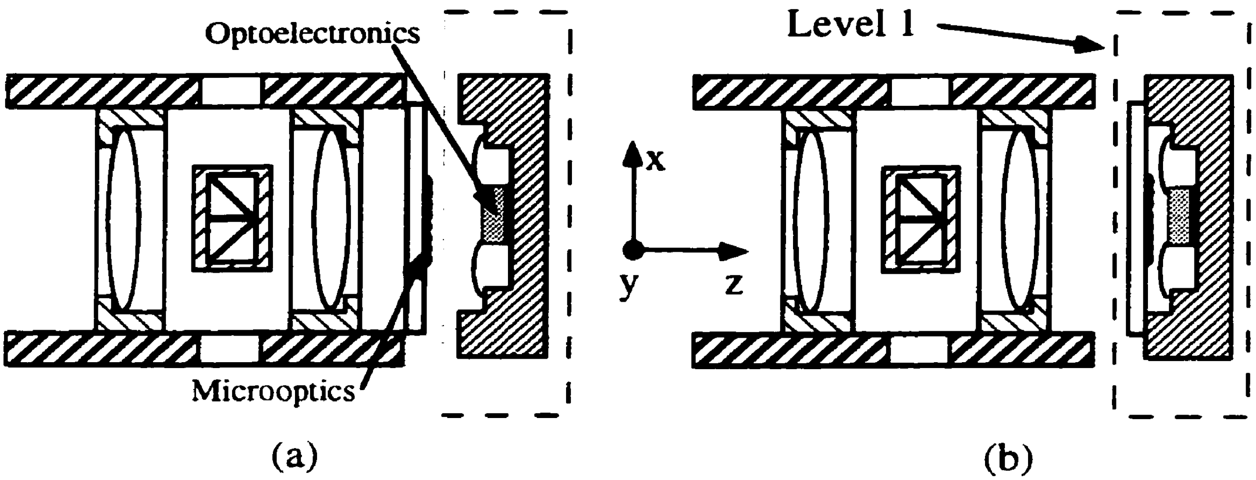

Figure 2.12: Packaging of level 1 a) microoptics not integrated to optoelectronics b) microoptics integrated

Now, when the system is built and a chip is inserted (or if for some reason the level 1 package has to be replaced because of a failure or for an upgrade), it is much easier to insert and align an integrated optoelectronic/lenslet package into the system than it is to insert and align just the chip. The graph in Figure 2.13 demonstrates this. In Figure 2.13a, the normalized coupling efficiency vs the lateral (x or y direction) misalignment of the level 1 package is plotted. For the integrated lenslet/optoelectronics option, a 25μm error still gives a 95% coupling efficiency whereas for the stand alone optoelectronics, coupling efficiency approaches zero (diffractive effects described in chapter 5 slightly change this but the conclusion still holds). Similarly for defocus (z misalignment) in (b), a 400μm misalignment will give near 100% efficiency for the integrated solution whereas the stand alone solution will have barely over 70% efficiency. Rotation (θ_z) can be represented as a lateral error varying over the array. On the other hand, as far as tilt (θ_x,θ_y) of the incomingbeam relative to the level 1 module is concerned, Figure 2.14 indicates that the less integrated solution (Figure 2.12a) may seem advantageous since the integrated lenslet changes the angle into a lateral error of $\Delta x_e = f_\mu \tan\theta_y$ at the detector: the efficiency is then similar to the one indicated by the dashed line in Figure 2.13a with $f_{\mu}\tan\theta_{y}$ replacing Δx_{e}. However, the converse is also true: a well fabricated module with no lateral error between the lenslet axis and centre of emitter will produce beams with no tilt at the start of the link. (Obviously tilt could be introduced elsewhere in the link, but at least the integrated option would make it simple to ensure that the beams started straight). The net result is a clear loosening of four critical degrees of freedom, namely x,y,z and θ_{z}, and just a modest tightening in the remaining two degrees. This conclusion has been known for some time and has served to justify research into integrated lenslet/device packaging[72,73].

Clearly, this will only make economic sense if the lenslets are cheap and can be thrown away with the old chip and if the lenslet/device prealignment can be performed cheaply in a controlled environment. These are legitimate assumptions since lenslets can be made cheap and breaking down a problem into small-sized challenges is proper engineering practice anyway. Moreover, if rapid or even field replaceability is an issue, then the reinsertion of the integrated module will take less time, costing much less in the field and exposing the system to less dust and fewer other hazards outlined above. For this technique to be optimal, however, non-intrusive alignment diagnostics will still be necessary since these will obviate the need to open up even more of the system to mount an imaging/diagnostic system and will further reduce replacement time. This example thus gives the rationale for chapters 4,5, and 6 in this thesis: the development of non-intrusive *in-situ* diagnostic techniques to save time and money during assembly and repair, and the development of techniques simplifying the fabrication of integrated lenslet/device packages to further save time and money.

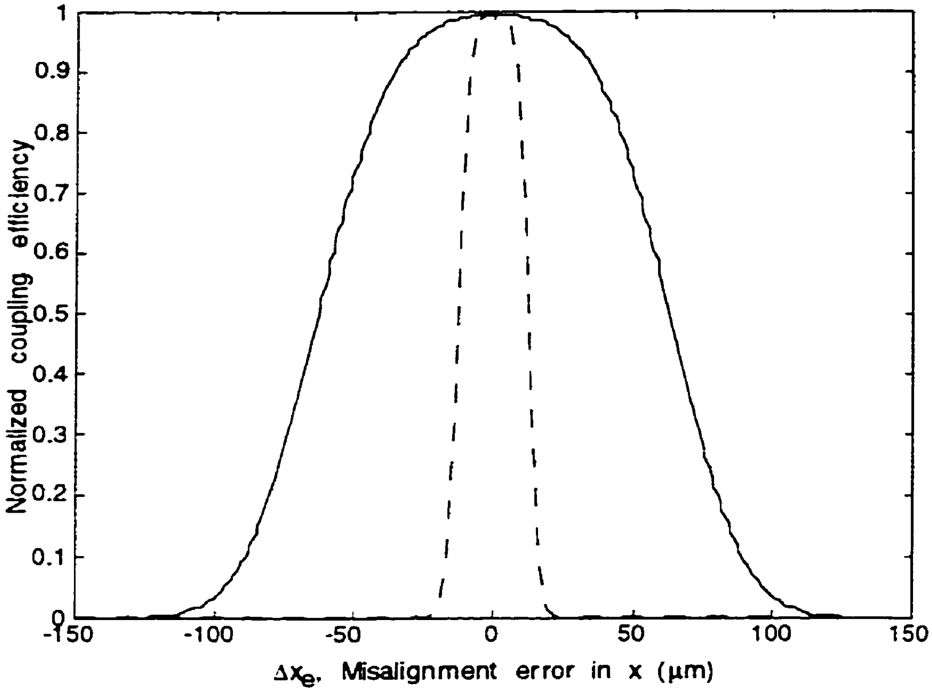

(a)

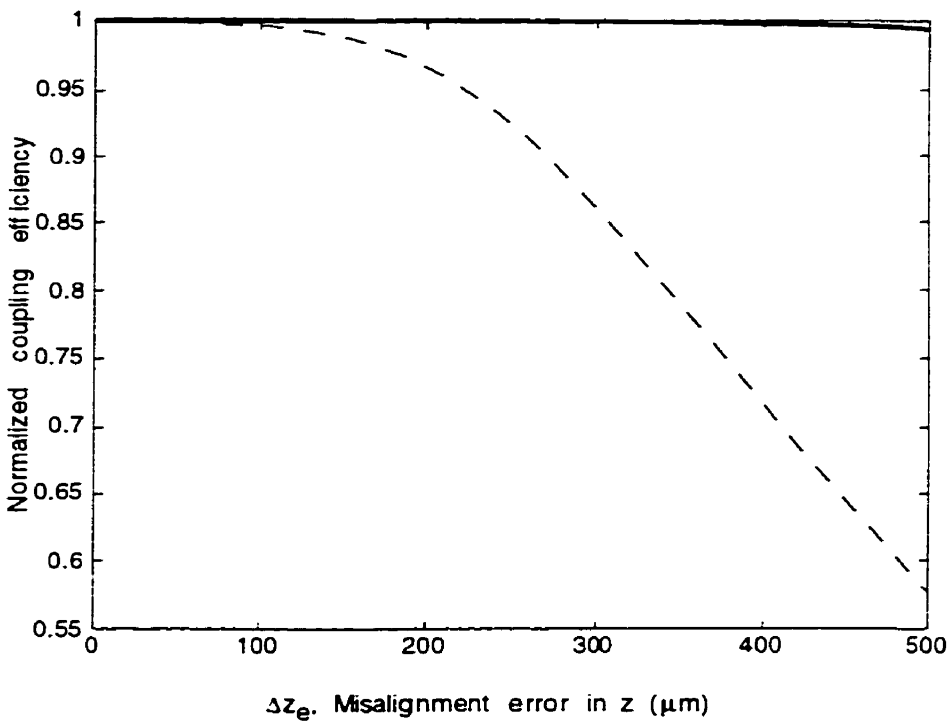

(b)

Figure 2.13: Comparison of alignment tolerance for 1st level packagingwith microoptics integrated into optoelectronic device packaging (solid) and decoupled (dashed) a) lateral tolerance b) defocus tolerance

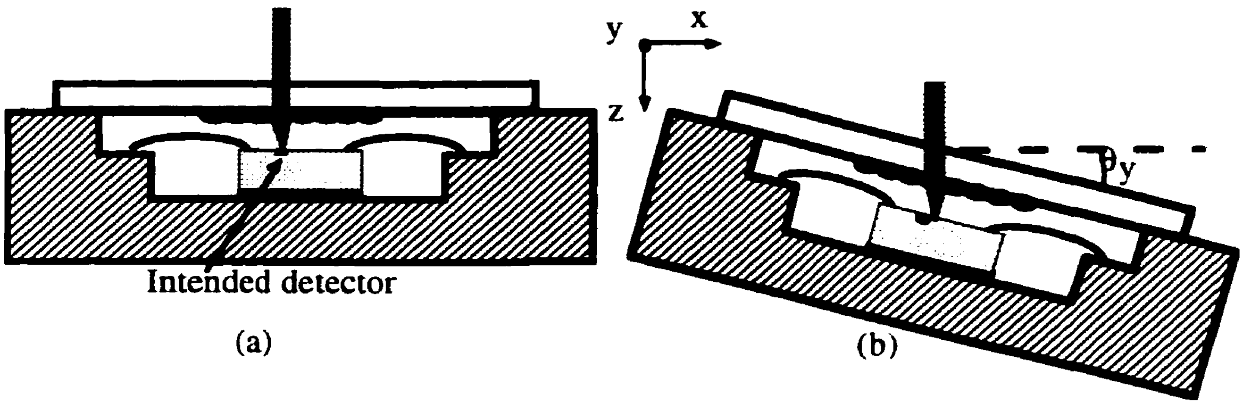

Figure 2.14: Effect of tilt of integrated package on alignment tolerance a) ideal b) tilt creates a lateral alignment error at the detector

A final comment on optical packaging concerns active alignment. Systems featuring active alignment, which involves a closed-loop feedback mechanism to monitor an alignment error and move components to correct the error, have been demonstrated before [74,75]. Unfortunately, these involve moving mechanical parts and it is hard to imagine that customers will accept the implications on system reliability of having dozens of moving parts to keep a real system functional. As such, active alignment, while interesting to study, does not yet seem to be a viable solution for FSOIs in computing systems unless practical, non-mechanical means such as piezoelectric actuators, which use crystal relaxation as a moving mechanism, are further developed on a large scale. Piezos, while successfully used in big adaptive telescopes, unfortunately offer very little travel per unit length of piezo– 0.1% is a typical strain[76] (i.e. 1μm movement per 1 mm thickness of crystal). This makes for very large piezo stacks for even modest alignment corrections. The best way to increase their travel is to use mechanical leverage, which once again brings up the question of mechanical reliability. Moreover, an important obstacle is the large voltage required to run them: very often the heavy-duty electrical connector designed to handle the ~100 Volts (admittedly at a very low current) fed to the crystal is actually bigger than the already big piezo stack structure itself. Techniques with non-moving parts using electrically-controlled refractive index materials look promising but they are expensive and still need development [77].

2.8 Conclusion

This review brought up many issues that must be considered by optical packaging engineers: optical design, device technology, environmental factors, and fabrication concerns. These issues have led optical packaging engineers to adopt a packaging hierarchy to simplify design and fabrication. Moreover, the review indicated that much work remains to be accomplished in the fields of optical packaging diagnostics and further component integration, which are the basic thrusts of this thesis.

2.9 References

1 G. Galilei, Il saggiatore. Milano. Feltrinelli, 1656.

2 P. R. Yoder. Optomechanical Systems Design. Marcel Dekker Inc., New York. 1993.

3 W. J. Smith. Modern optical engineering : the design of optical systems. 2nd ed.. New York: McGraw Hill. 1990.

4 D. Vukobratovich. "Advances in optomechanics," SPIE vol. 1396. pp. 436-446 (1990).

5 D. O'Shea. "Annotated bibliography of optomechanical design," *Optical Engineering*. 25. pp. 1160-1170 (1986).

6 P. R. Yoder. Ed.. "Optomechanical design." SPIE Vol. CR43. 1992.

7 F. B McCormick. F. A. P. Tooley. J. L. Brubaker. J. M. Sasian. T. J. Cloonan. A. L. Lentine. R. L. Morrison. R. J. Crisci. S. L. Walker. S. J. Hinterlong. M. J. Herron. "Optomechanics of a free-space photonic switching fabric: the system," SPIE Vol. 1533 (1991), pp. 97-114.

8 A. K. Agarwal and L. D. Hutcheson, "Performance and reliability of optical fiber connectors in the outside plant environment," *IEEE Transactions on Components, Packaging, and Manufacturing Technology– Part B*, 18, pp. 221-226 (1995).

9 See for example Bellcore document, GR-63-CORE, Network Equipment-Building System (NEBS) Requirements: Physical Protection.

10 See for example MIL STD 810 C, D, E.

11 R. Boudreau, "Packaging for optoelectronic interconnections,"*Journal of Metals*, 46, pp. 41-45 (1994).

12 S. D. Robinson, M. S. Acarlar, Y. C. Chen, L. T. Manzione, G. J. Shevchuk, and D. Stefanik, "Low-cost molded packaging for optical data links," *IEEE Transactions on components, packaging, and manufacturing technology-part B*, 18, pp. 235-240 (1995).

13 P. Thompson, "Chip-scale packaging," *IEEE Spectrum*, 34, no. 8, pp. 36-43 (1997).

14 See for example IEC Standard 917:1988, "Modular order for the development of mechanical structures for electronic equipment practices," (1988).

15 F. A. P. Tooley, "Challenges in optically interconnecting electronics," *IEEE Journal of Selected Topics in Quantum Electronics*, 2, pp. 3-13 (1996).

16 J. M. Sasian, F. B. McCormick, R. Webb, R. J. Crisci, K. O. Mersereau, R. P. Stawicki," Design, assembly, and testing of an objective lens for a free-space photonic switching system," *Optical Engineering*, 32, pp. 1871-1878 (1993).

17 D. V. Plant, B. Robertson, H. S. Hinton, W. M. Robertson, G. C. Boisset, N. H. Kim, Y. S. Liu, M. R. Otazo, D. R. Rolston, and A. Z. Shang, "An optical backplane demonstrator system based on FET-SEED Smart pixel arrays and diffractive lenslet arrays," *IEEE Photonics Technology Letters*, 7, pp. 1057-1059 (1995).

18 F. B. McCormick, Ph.D. Thesis, "Optical and mechanical design issues in free-space optical interconnection and processing," Heriot Watt University (1993).

19 F. B. McCormick. F. A. P. Tooley. T. J. Cloonan, J. M. Sasian. H. S. Hinton. K. O Mersereau, and A. Y. Feldblum, "Optical interconnections using microlens arrays." *Optical and Quantum Electronics*. 24, pp. 465-477 (1992).

20 F. A. P. Tooley. S. M. Prince. M. R. Taghizadeh. F. B. McCormick. M. W. Derstine. and S. Wakelin, "Implementation of a hybrid lens," *Applied Optics*. 34, pp. 6471-6480. (1995).

21 B. Robertson, "Design of a compact alignment tolerant optical interconnect for photonic backplane applications." *Proceedings of the fourth International Conference on Massively Parallel Processing Using Optical Interconnections*. IEEE Computer Society PR07974. pp. 68-77 (1995).

22 A. L. Lentine. D. J. Reiley. R. A. Novotny, R. L. Morrison. J. M. Sasian. M. G. Beckman. D. B. Buchholz. S. J. Hinterlong. T. J. Cloonan. G. W. Richards. and F. B. McCormick. "Asynchronous transfer mode distribution network by use of an optoelectronic VLSI switching chip." *Applied Optics*, 36. pp. 1804-1814 (1997).

23 C. P. Barrett. P. Blair. G. S. Buller. D. T. Neilson. B. Robertson. E. C. Smith. M. R. Taghizadeh. and A. C. Walker. "Components for the implementation of free-space optical crossbars." *Applied Optics*. 35. pp. 6934-6944 (1996).

24 S. Araki. M. Kajita. K. Kubota. K. Kurihara. I. Redmond. E. Schenfeld, and T. Suzaki. "Experimental free-space optical network for massively parallel computers." *Applied Optics*. 35. pp. 1269-1281 (1996).

25 Yao Li. Ting Wang. and Linke. R.A.. "A beam-steering opto-electronic cross-bar interconnect using VCSEL arrays." 1996 International Topical Meeting on Optical Computing. Technical Digest. OC 96. vol. 1 pp. 22-23.

26 Jang-Hun Yeh: Kostuk. R.K.: Kun-Yii Tu. "Hybrid free-space optical bus system for board-to-board interconnections." *Applied Optics*, 35. pp. 6354-6364 (1996).

27 D. V. Plant, B. Robertson, H. S. Hinton, M. H. Ayliffe, G. C. Boisset, W. Hsiao, D. Kabal, N. H. Kim, Y. S. Liu, M. R. Otazo, D. Pavlasek, A. Z. Shang, J. Simmons, K. Song, D. A. Thompson, and W. M. Robertson," A 4x4 VCSEL/MSM optical backplane demonstrator system," *Applied Optics*, 35, pp. 6365-6368 (1996).

28 Tsang, D.Z.; Goblick, T.J., "Free-space optical interconnection technology in parallel processing systems," *Optical Engineering*, 33, 1524-1531(1994).

29 J. H. Yeh, R. K. Kostuk, and K. Y. Tu, "Hybrid free-space optical bus system for board-to-board interconnections," *Applied Optics*, 35, pp. 6354-6364 (1996).

30 F. B. McCormick, F. A. P. Tooley, T. J. Cloonan, J. L. Brubaker, A. L. Lentine, R. L. Morrison, S. J. Hinterlong, M. J. Herron, S. L. Walker, and J. M. Sasian, "Experimental investigation of a free-space optical switching network by using symmetric self-electro-optic-effect devices," *Applied Optics*, 31, No. 26, pp. 5431-5446 (1992).

31 F. B. McCormick, T. J. Cloonan, A. L. Lentine, J. M. Sasian, R. L. Morrison, M. G. Beckman, S. L. Walker, M. J. Wojcik, S. J. Hinterlong, R. J. Crisci, R. A. Novotny, and H. S. Hinton, "Five-stage free-space optical switching network with field-effect transistor self-electro-optic-effect-device smart-pixel arrays," *Applied Optics*, 33, pp. 1601-1618 (1994).

32 F. B. McCormick, T. J. Cloonan, F. A. P. Tooley, A. L. Lentine, J. M. Sasian, J. L. Brubaker, R. L. Morrison, S. L. Walker, R. J. Crisci, R. A. Novotny, S. J. Hinterlong, H. S. Hinton, and E. Kerbis, "Six stage digital free-space optical switching network using symmetric self-electro-optic-effect devices," *Applied Optics*, 32, pp. 5153-5171 (1993).

33 A. C. Walker, D. T. Neilson, M. P. Y. Desmulliez, F. A. P. Tooley, "An optoelectronic bitonic sorter using CMOS/InGaAs smart pixel technology," 1996

International Topical Meeting on Optical Computing. Technical Digest. Japan Soc. Appl. Phys, 1996. vol.1, pp. 90-91.

34 M. Yamaguchi. T. Yamamato. K. Hirayabashi. S. Matsuo. and K. Koyabu. "High-density free-space photonic-switching fabrics using exciton absorption reflection switch (EARS) arrays and microbeam optical interconnections." *IEEE Journal of Selected Topics in Quantum Electronics*. 2. pp. 47-54 (1996).

35 R. A. Nordin. F.J. Levi. R.N. Nottenburg. J. O'Gorman. T. Tanbun-Ek. and R. A. Logan. "A systems perspective on digital interconnections technology." *Journal of Lightwave Technology*. 10. pp. 811-827 (1992).

36 H. F. Hofmann and O. Hess. "Quantum noise and polarization fluctuations in vertical-cavity surface-emitting lasers." *Physical Review A* .56, pp. 868-876. (1997).

37 D. L. Mathine. R. Droopad and G. N. Maracas. "A vertical-cavity surface-emitting laser appliquéd to a 0.8- mu m NMOS driver." *IEEE Photonics Technology Letters*. 9. pp. 869-871 (1997).

38 T. Egawa. Y. Murata. T. Jimbo. and M. Umeno. "Low-temperature continuous wave operation of AlGaAs-GaAs vertical cavity surface emitting lasers on Si substrates." *IEEE Photonics Technology Letters*. 9. pp. 872-874. (1997).

39 K. W. Goosen. J. A. Walker. L. A. D'Asaro. S. P. Hui. B. Tseng. R. Leibenguth. D. Kossives. D. D. Bacon. D. Dahringer. L. M. F. Chirovsky. A. L. Lentine. and D. A. B. Miller. "GaAs MQW modulators integrated with silicon CMOS." *IEEE Photonics Technology Letters*. 7. pp. 360-362 (1995).

40 R. J. Mears. W. A. Crossland. M. P. Dames. J. R. Collington. M. C. Parker. S. T. Warr. T. D. Wilkinson. and A. B. Davey. "Telecommunications applications of ferroelectric liquid-crystal smart pixels." *IEEE Journal of Selected Topics in Quantum Electronics*. 2. pp. 35-46 (1996).

41 H. S. Hinton. "Progress in the smart pixel technologies." *IEEE Journal of Selected Topics in Quantum Electronics*. 2, pp. 14-23(1996).

42 H. Kogelnik and T. Li. "Laser beams and resonators." *Applied Optics*. 5. pp. 1550-1567 (1966).

43 M. R. Taghizadeh and J. Turunen. "Synthetic diffractive elements for optical interconnection." *Optical Computing and Processing*, 2. pp. 221-242. (1992).

44 R. F. Carson. P. K. Seigal. D. C. Craft. and M. L. Lovejoy. "Future Manufacturing Techniques for Stacked MCM Interconnections." *Journal of Metals*. 46. pp. 51-55 (1994).

45 D. R. Rolston. B. Robertson. H. S. Hinton. and D. V. Plant. "Analysis of a microchannel interconnect based on the clustering of smart-pixel-device windows." *Applied Optics*. 35. pp. 1220-1233 (1996).

46 A. Kirk. A. Goulet. H. Thienpont. N. McArdle, K.-H. Brenner. M. Kujik. P. Heremans. and I. Veretennicoff. "Compact optical imaging system for arrays of optical thyristors." *Applied Optics*. 36. pp. 3070-3078 (1997).

47 S. M. Prince. Ph.D. Thesis. Heriot Watt University, 1996.

48 S. M. Prince. F. A. P. Tooley. S. Wakelin. and M. R. Taghizadeh. "Implementation of optical perfect-shuffle module." Applied Optics. 34, pp. 1775-11782 (1995).

49 M. Mizukami. K. Koyabu. M. Fukui. and K. Kitayama. "Free-space optical module configuration using a guide-frame assembly method." *Applied Optics*. 34. pp. 1783-1787 (1995).

50 Y. S. Liu. B. Robertson. D. V. Plant. H. S. Hinton. and W. M. Robertson. "Design and characterization of a microchannel optical interconnect for optical backplanes." *Applied Optics*. 36. pp. 3127-3141 (1997).

51 A. L. Lentine and D. A. Miller. "Evolution of the SEED technology: bistable logic gates to optoelectronic smart pixels," *IEEE Journal of Quantum Electromnics*. 29. pp. 655-668 (1993).

52 A. Abramovici, W. Althouse. J. Camp, D. Durance. J. A. Giaime. A. Gillespie. S. Kawamura, A. Kuhnert. T. Lyons, F. J. Raab. R. L. Savage. D. Shoemaker. L. Sievers. R. Spero. R. Vogt. R. Weiss. S. Whitcomb. and. M. Zucker. "Improved sensitivity in a gravitational wave interferometer and implications for LIGO." *Physics Letters A*. 218. pp. 157-163 (1996).

53 K. Tsubono. A. Araya. K. Kawabe. S. Moriwaki. and N. Mio. "Triple-pendulum vibration isolation system for a laser interferometer." *Review of Scientific Instruments*. 64. pp. 2237-2240 (1993).

54 P. J. Veitch. J. Hough. E. Morrison. and D. I. Robertson. "Can piezoelectric accelerometers be used to actively damp the mechanical suspensions in laser interferometric gravitational wave detectors." *Review of Scientific Instruments*. 67. pp. 633-640 (1996).

55 N. Hubin and L. Noethe. "Active optics. adaptive optics. and laser guide stars." *Science*. 262. pp. 1390-1394 (1993).

56 L. Ramos-Izquierdo. J. L. Bufton. and P. Hayes. "Optical system design and integration of the Mars observer laser altimeter." *Applied Optics*. 33. pp. 307-322 (1994).

57 T. Sakano. T. Matsumoto. and K. Noguchi. "Three-dimensional board-to-board free-space optical interconnects and their application to the prototype multiprocessor system: COSINE III." *Applied Optics*. 34. pp. 1815-1822 (1995).

58 G. Legg. "Small. rugged disk drives take (fairly) hard knocks." *EDN*.38. pp. 41-46. November 11. (1993).

59 Heat Sink # 341324B. from Aavid Inc.

60 T. H. Jamieson. "Thermal effects in optical systems," *Optical Engineering*. 20. pp. 156-160 (1981).

61 Y. Tamagawa. S. Wakabayashi. T. Tajime, and T. Hashimoto. "Athermalization of a single-component lens with diffractive optics," *Applied Optics*. 32. pp. 2295-2302 (1993).

62 Y. Tamagawa. S. Wakabayashi. T. Tajime, and T. Hashimoto. "Multilens system design with an athermal chart." *Applied Optics*. 33. pp. 8009-8013 (1993).

63 D. G. DeNure and E. S. Sproles Jr., "Dust test results on multicontact . circuit board connectors ." *Proceedings of the 41st Electronic Components and Technology Conference*. (IEEE) Atlanta. GA. pp. 249-255 (1991).

64 L. Smart and J. DePriest. "SIMM socket features tin-to-tin contact system." *InterConnection Technology*. pp. 16-19. December 1993.

65 Y. Belopolsky. "Interaction of multichip module substrates with high-density connectors ." *IEEE Micro*. 13. pp. 36-43. April 1993.

66 R. P. Hughes and D. Marx. Nortel Inc., personal communication.

67 R. C. Juvinall. Fundamentals of Machine Component Design, John Wiley & Sons. Inc. New York, 1983.

68 Shigley and Mischke. Mechanical Engineering Design. 5th Ed., McGraw Hill. N. Y., 1989.

69 G. Nakagawa. K. Miura. K. Tanaka. and M. Yano, "Multichannel fiber ferrule for a stable laser-diode array module." *IEEE Photonics Technology Letters*. Vol. 7. pp. 409-411 (1995).

70 Y. Arai. H. Takahara. K. Koyabu. S. Fujita. Y. Akahori. and J. Nishikido. "Multigigabit multichannel optical interconnection modules for asynchronous transfer mode switching systems." *IEEE Transactions on components. packaging. and manufacturing technology-part B*. 18. pp. 558-564 (1995).

71 D. B. Schwartz, C. K. Y. Chun, B. M. Foley, D. H. Hartman, M. Lebby, H. C. Lee, C. L. Shieh, S. M. Kuo, S. G. Shook, and B. Webb, "A low-cost high-performance optical interconnect.," *IEEE Transactions on components, packaging, and manufacturing technology-Part B*, 19, pp. 532-538 (1996).

72 S. K. Patra, J. Ma, V. H. Ozguz, and S. H. Lee, "Alignment issues in packaging for free-space optical interconnects," *Optical Engineering*, 33, pp. 1561-1570 (1994).

73 W. R. Imler, K. D. Scholz, M. Cobarruviaz, V. K. Nagesh, C. C. Chao, and R. Haitz, "Precision flip-chip solder bump interconnects for optical packaging," *IEEE Transactions on Components, Hybrids, and Manufacturing Technology*, 15, pp. 977-982 (1992).

74 K. Hirabayashi, T. Yamamoto, S. Hino, Y. Kohama, and K. Tateno, "Optical beam direction compensating system for board-to-board free-space optical interconnection in high-capacity ATM switch ," *Journal of Lightwave Technology*, 15, pp. 874-882 (1997).

75 G. C. Boisset, B. Robertson, and H. S. Hinton, "Design and Construction of an Active Alignment Demonstrator for a Free-Space Optical Interconnect," *IEEE Photonics Technology Letters*, 7, pp. 676-678 (1995).

76 C. G. O'Neill and C. H. O'Neill, "Ferroelectric actuators in the electromechanical interface," *Optical Engineering*, 29, pp. 1383-1388(1990).

77 K. Hirabayashi, T. Yamamoto, and M. Yamaguchi, "Free-space optical interconnections with liquid-crystal microprism arrays," *Applied Optics*, 34, pp. 2571-80 (1995).

Chapter 3: Optical packaging for a four-stage backplane

3.1 Introduction

The previous chapter indicated that past FSOI demonstration systems have already implemented sophisticated optical packaging techniques. However. it was also shown that several challenges in optical packaging still must be overcome in order for FSOIs to gain widespread acceptance in industry. Key among those challenges are a better understanding of fabrication issues and the development of better diagnostics tools to measure the effect of environmental disturbances such as vibrations. Moreover. it was shown that a thorough understanding of problems brought about by phenomena such as thermal cycling could lead to elegant designs. reducing overall engineering complexity. The insight gained from the literature search and the work described in chapter 2 was used in the design of a very aggressive optical packaging scheme for a free-space optical backplane demonstrator.

This chapter analyzes the design. fabrication and characterization of the optical packaging of a four-stage hybrid bulk-lenslet free-space optical backplane demonstrator system. The system implemented. in a unidirectional ring, the optical interconnection of four hybrid-SEED smart pixel arrays. A hybrid combination of microchannel relays and conventional (bulk) relay lenses were used to interconnect the smart pixel arrays. This system built on experience acquired in previous demonstrator systems and introduces several novel features such as vertical mounting of the baseplate and installation of the system in a standard backplane chassis. Moreover. this chapter will also describe the design and implementation of a diagnostic system for evaluating the effect of vibrations on optical packaging performance as well as a novel lens-mounting technique which uses radial thermal-loading to secure a lens in place.

This chapter is structured as follows. Section 3.2 overviews key system aspects. Section 3.3 examines the bulk relay and the baseplate, followed by other modules in section 3.4. Section 3.5 explores the key issue of interfacing optoelectronics to optomechanics by the use of a daughterboard. Section 3.6 describes a setup used to measure the performance of the daughterboard mounting technique. Section 3.7 gives experimental results and a conclusion follows.

3.2 System Overview

The optical backplane was designed to implement a ring optical interconnection of four optoelectronic chips[1,2], with each chip having 16 channels modulated at a maximum rate of 50 MHz. As a result, the peak theoretical bi-section bandwidth of this demonstrator system was about 1.6 Gbit/sec– comparable to middle-of-the-line backplanes available today[3], although the optical system is scalable to much higher values.

The principal optical packaging and optomechanical objective was to interconnect optically four printed circuit boards within a standard 482.6 mm (19") 6U VME [3] commercial backplane chassis. Fitting the system into the 6U chassis was a self-imposed design guideline to make the system mechanically compatible with many systems found in the field today. The objective was also to separate the optics from the electronics so that, eventually, a user inserting a 6U circuit board into the backplane would see a conventional VME backplane environment – from a mechanical and electrical DC power perspective – while accessing the tremendous bandwidth offered by the free-space optical interconnect. In this system, this was accomplished by using daughterboards and motherboards. The Hybrid-SEED optoelectronic chips[2] were glued and wirebonded to the daughterboards residing in the optical layer; the daughterboards were then linked to the motherboards via a short, impedance-matched high speed ribbon cable. As demonstrated previously [4], this technique for injecting electrical data from the motherboard into the optical backplane allowed for mechanical decoupling between daughterboard and motherboard while maintaining full electrical integrity between the two, provided the cable was short enough: an 8 cm length (~3") was sufficient for the expected 50 MHz maximum clock speed, according to commonly used criteria for transmission line integrity[5]. This example demonstrates a typical trade-off between electrical and optical packaging constraints: a slightly longer cable simplifies optical packaging, but a slightly shorter one increases electrical throughput.

System scalability was also a key goal. The demonstrated system occupied approximately the top half of the 6U chassis (which could therefore allow an identical system to occupy the bottom half) and featured expansion slots for interconnection of more boards if so desired.

A simplified assembly drawing of the system is shown in Figure 3.1. The system optical packaging had to accomplish the following tasks: 1) mechanically support the optics while respecting all tolerances demanded by the optical design 2) support the packaged optoelectronics and interface them to the rest of the interconnect, 3) act as an interface between a commercially available electronic chassis and the rest of the system, and 4) integrate diagnostic optics and electronics for alignment and system characterization. The system as a whole had to be rugged, scaleable and easily assembled. The optomechanics were modularized as much as possible in order to facilitate assembly and alignment.

A key feature of this system was its three-dimensional nature: in order to facilitate the discussions in this chapter, it is necessary to define a frame of reference, which is shown at the bottom of Figure 3.1. As can be seen, in this system the main relays based on bulk (conventional) optics implementing the optical ring were in an xy plane. However, the Optical Power Supplies (OPSs), which illuminate the modulator chips with an array of continuous wave (CW) power beams, as well as other relays such as the microchannels, were parallel to the z axis. Rotational directions are also defined. For example, θ_y is the angle of rotation about the y axis. Figure 3.2 shows a photo of the system.

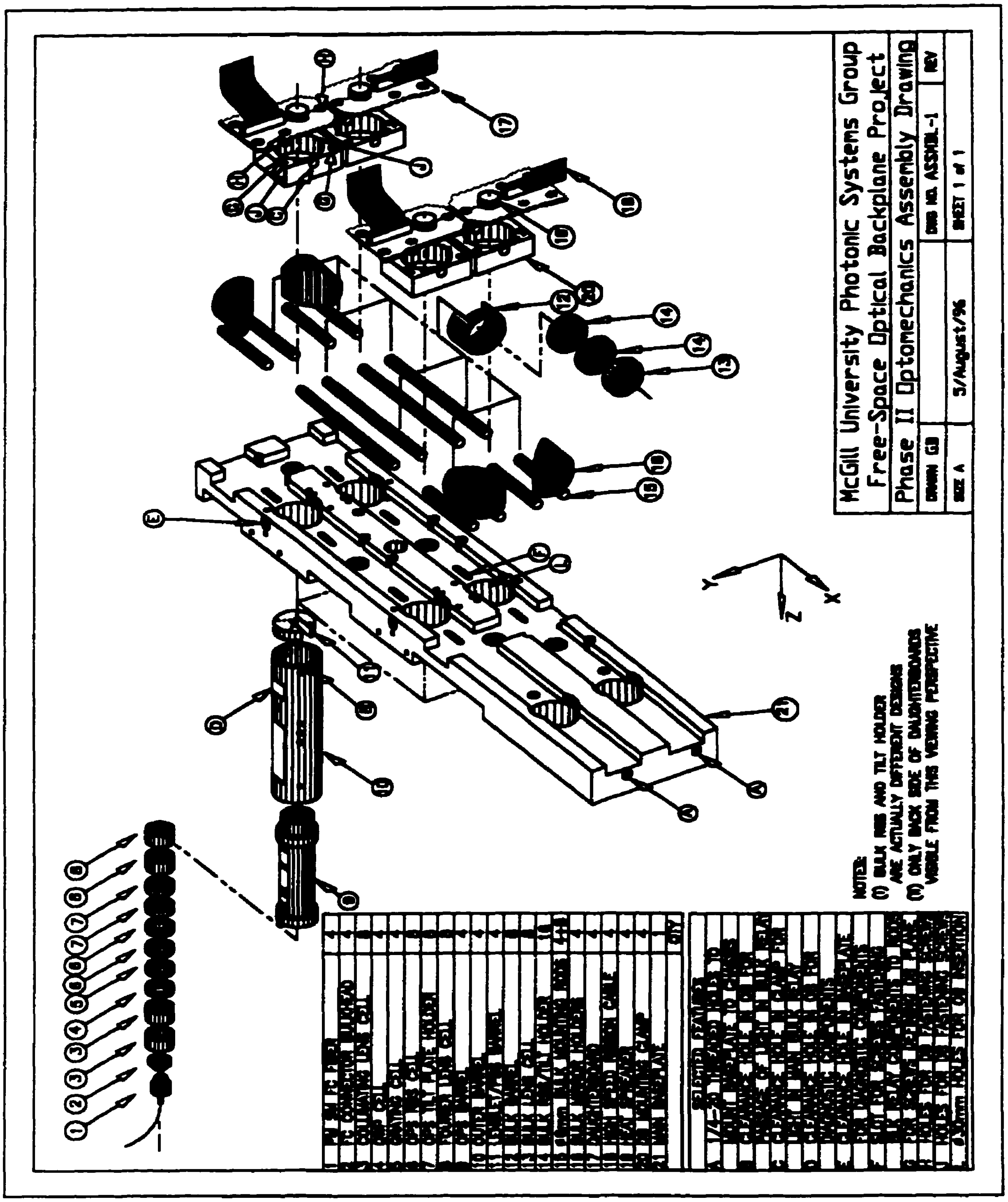

Figure 3.1: Simplified system assembly drawing

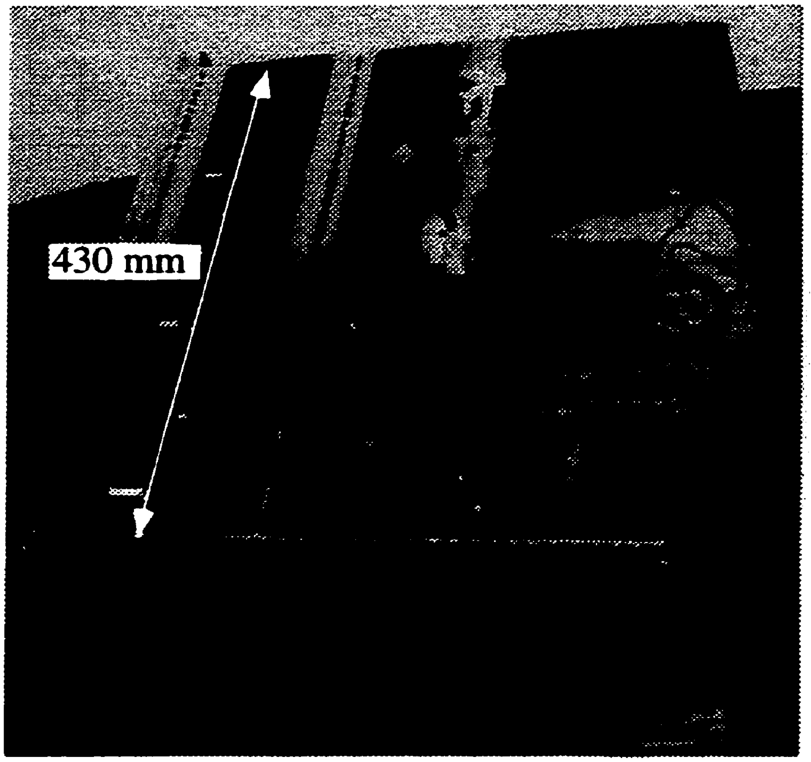

Figure 3.2: Picture of the system mounted in a standard 431 mm (17") wide 6U VME chassis

3.2.1 Overview of the Optical System

A brief overview of the optical layout is now presented. Figure 3.3 shows an unfolded view of the overall four-stage system. with one of the four (OPS) modules explicitly drawn. This unfolded view of the 3D system is slightly misleading since the OPSs actually should be coming into the plane of the paper and the daughterboards should be parallel to the plane of the paper. not perpendicular as is implied in the unfolded view.

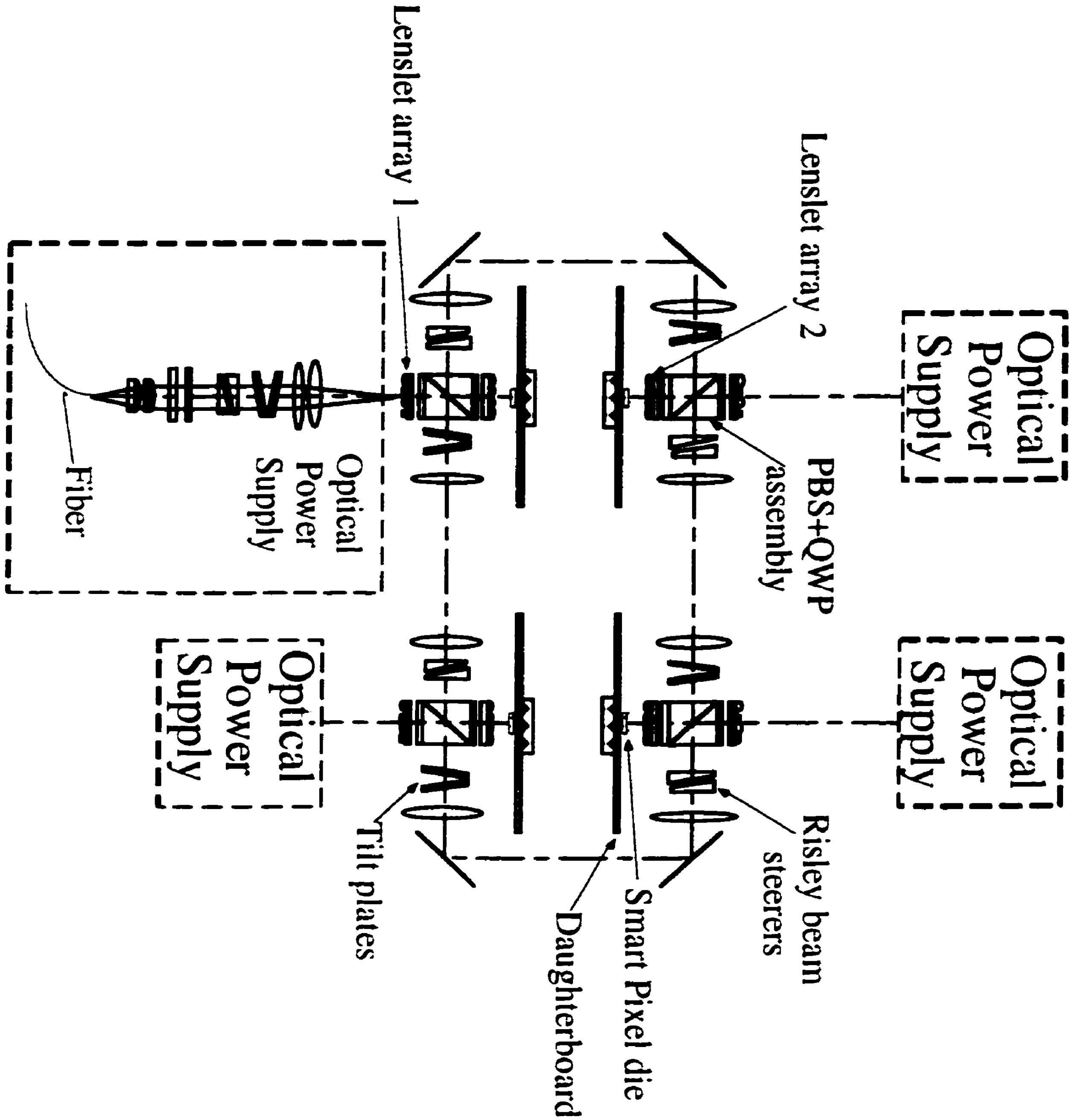

Figure 3.3: Unfolded system optical layout

A close-up of a hybrid stage-to-stage relay is shown in Figure 3.4. Gaussian beam propagation models were used in the design of the system. At each stage, lenslets were close to the smart pixel devices in order to collect the beams and reduce their numerical aperture, and bulk (conventional) lenses [6] relayed the beamlets from one stage to another.

The lenslets reduced the numerical aperture of the beams relayed by the bulk lenses to below 0.025. All lenslets were 125x125 μm 8-level diffractive structures with a focal length of $f\mu$=768 μm at λ=850 nm. Lenslet Array 1 (LA_1) consisted of alternating 1x8 lenslet strips and pixellated mirror strips 123 μm wide x 1 mm high. LA_2 consisted of an 8x8 array of lenslets. These are shown in Figure 3.5. Additional features for alignment diagnostic were placed around the periphery of the arrays: these will be described in the next chapter.

The fibre-connected OPS generated a 4x8 array of right-handed circularly polarized CW beamlets at the power array plane which was relayed by LA_1 and LA_2 to the smart pixel. The beamlets were then modulated by the chip, relayed through LA_2 and imaged by the bulk relay to stage 2. At stage 2, the beamlets were reflected by the Polarizing Beam Splitter, then reflected off the pixellated mirror on LA_1, and finally were imaged onto the receiver on board 2 via LA_2. The polarization components, namely the Quarter Wave Plates (QWP) and the Polarization Beam Splitter were used for beam combinations as discussed in ref [7]. The optical microlens relay was designed to relay the beams using the maximum lens-to-waist configuration [8]. Tilt plates and Risley Beam Steerers (RBSs) were included for alignment purposes. The dimension of the array of beamlets was nominally 1.2mm x 1.2mm.

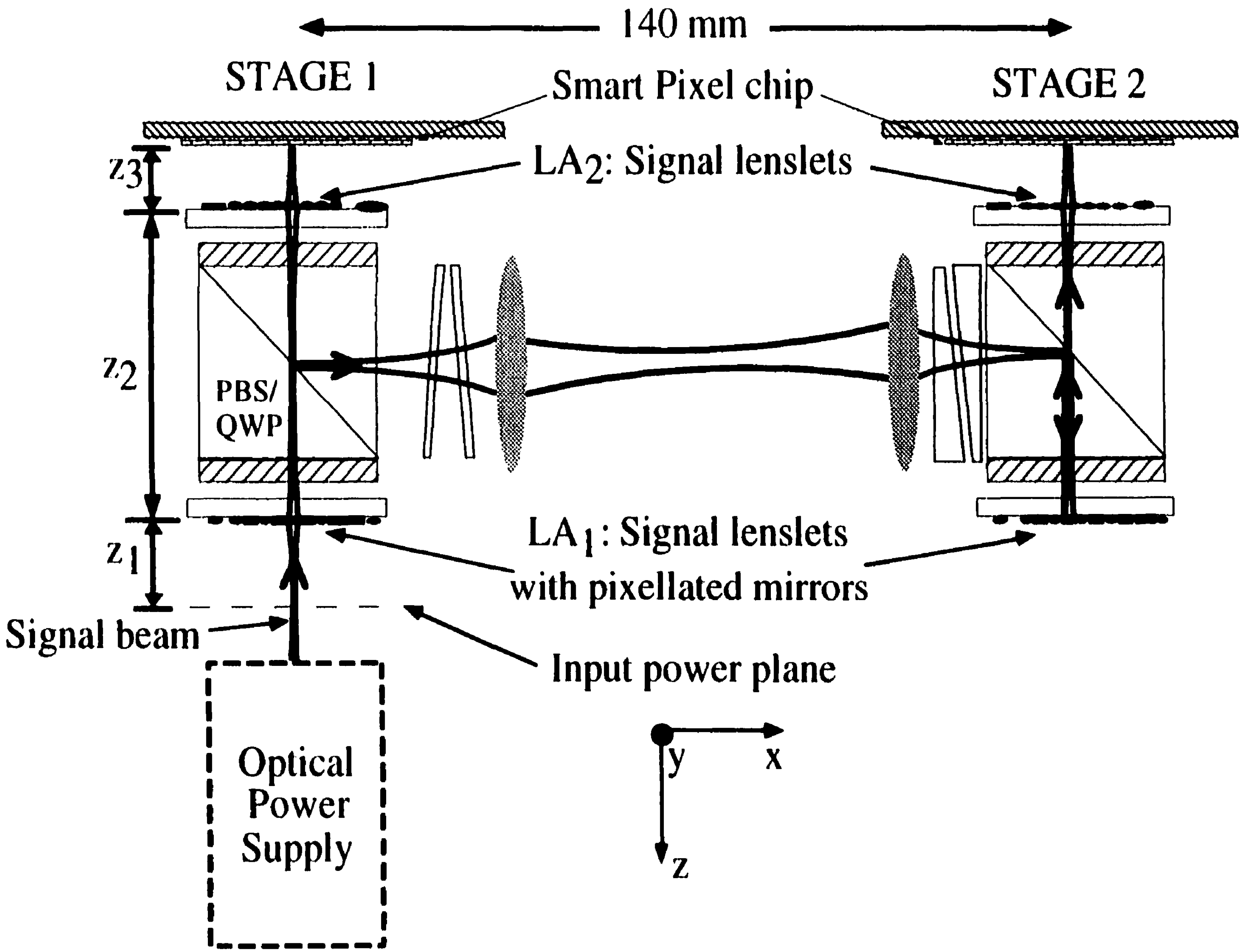

Figure 3.4: Close-up of one board-to-board relay showing the path taken by one signal beam

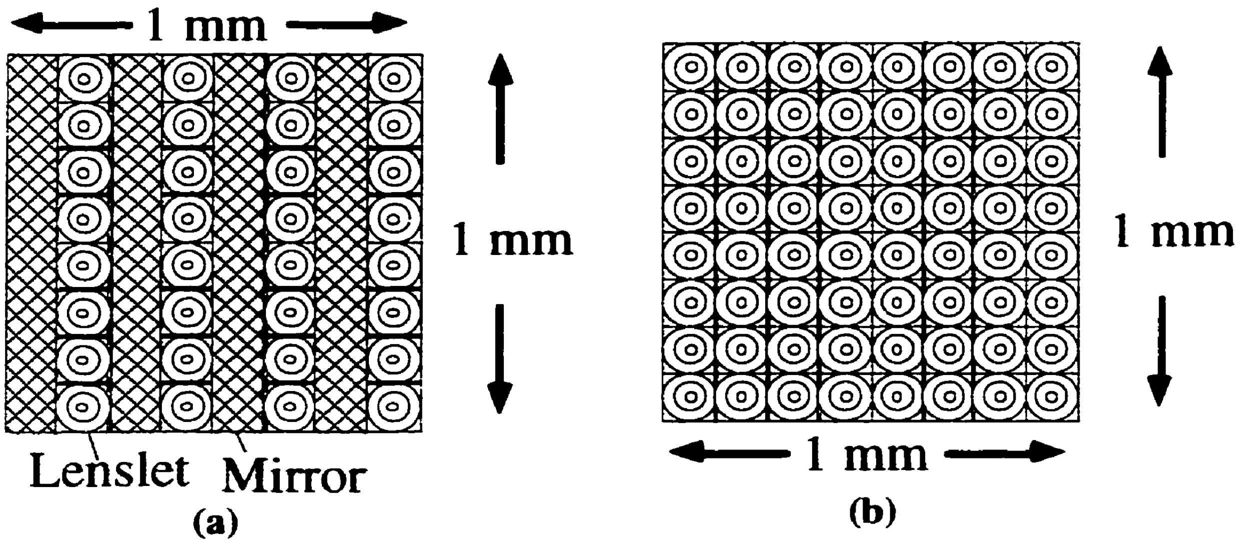

Figure 3.5: Lenslet array schematic a) Lenslet array # 1 b) Lenslet array # 2

Space constraints were such that the aperture stop for the bulk interconnect lay between the PBS/QWP assembly and the Risley Beam Steerers (RBSs), at the entrance to the lenslet barrel (described below). This stop was 4.10 mm in diameter. To a first order, this left a ~500μm clearance between the edge of the outermost beamlet and the stop. As a result, any offset greater than 500μm on the bulk interconnect would lead to considerable clipping of the outermost beamlet. However, as will be shown later, the alignment budget allowed only a smaller misalignment of 220 μm at the pixellated mirrors, since this was the maximum travel of the tilt plates.

This chapter will not present a detailed analysis of the optical system. However, there were several critical and extremely tight optomechanical alignment tolerances which influenced much of the design and which must be given here. These tight tolerances were driven by the extremely small size of the multiple quantum well (MQW) windows which all beams had to hit. The MQW windows were 20μm x 20μm [2] and the beams incident upon them had a nominal diameter (99% encircled power) of 19.5 μm. This imposed extremely tight tolerances which are given in Table I. Among other tolerances given, Table I indicates that the lateral (x-y) alignment error between the microlens array and the smart pixel device array had to be < 1μm in order to lose less than 1% optical power due to misalignment. Other demanding tolerances were the lenslet-to-lenslet alignment tolerances . key values of which are given in Table II.

As can be seen. the bulk interconnect tolerances (~220μm) were much looser than the lenslet-device tolerances (~ 1μm) or the lenslet-to-lenslet tolerances (~5μm).

Degree of freedom	Board position and tolerance to be met	Board position before gluing	Board position after gluing
Δx(μm)	0±1	0±2	3.2±3
Δy(μm)	0±1	0±2	-2±3
z_3(μm)	886±15	887±15	875±15
tilt θ_x(deg.)	0±0.5	0.06±0.1	0.55±0.27
tilt θ_y(deg.)	0±0.5	0.04±0.1	0.18±0.14

Table I: Positioning tolerances of die on daughterboard relative to optics. Columns respectively indicate a) target value b) measurement immediately before gluing, c) the final position after gluing to optomechanics and stage removal; Δx and Δy were measured 9 weeks after gluing; other values were measured 4 days after.

Degree of Freedom	Position and tolerance to be met
Lenslet array # 1 to # 2 (x.y)	0±5μm
z_1	922 ± 15 μm
z_2	6.98 ± 0.15 mm

Table II: Tolerances for lenslet-to-lenslet alignment as imposed by the optical design; z_1 and z_2 are as defined in Figure 3.4.

3.3 Baseplate and Bulk Relay

3.3.1 Baseplate Description

The baseplate was the central piece of the optomechanics and acted as the support structure for the entire optical/optomechanical layer. All other optical and optical packaging components were either attached to the baseplate or locked into barrels attached to the baseplate.

The baseplate, a simplified schematic of which is shown in Figure 3.6, was 431.8 mm (17") long (the inside of the standard VME rack is 50.8 mm shorter than the outside because of mounting flanges), was mounted vertically into the chassis, and was bolted to the side panels of the chassis.

Previous free-space optical switching demonstrator systems used aluminum or steel for baseplates, but it was determined that neither of these materials was suitable for production [9]. The baseplate for this system was made of Magnesium AZ31B: the main reason for choosing this metal was its ease of machinability, its lightness, and its low residual stress which minimizes the need for stress relief when compared to other metals [10]. This type of metal has already been used in applications such as lens mounting[11]. It is interesting to note that Mg is softer than other frequently used materials: the Brinell Hardness Number (BHN) of Mg is 82 compared to 95 for Al 6061-T6 or ~200 for 1080 steel (depending on drawing and other processes). This softness makes Mg easier to machine but more easily dented[12, 13], which prompted the use of rods for mounting bulk optics (described below).

The main outer barrels, each one containing an OPS and a microlens relay, fit into the holes labeled 'L', which were 30 mm in diameter. Of these six holes, four were used in the actual system (the ones at x=75 and x=215mm); two others (at x=355 mm) were kept for future system expansion.

Many holes and slots were included for diagnostic, assembly, and alignment purposes. Additionally, magnets were glued into holes machined at the back of the baseplate, serving to keep the bulk mounting rods (described below) in place on the vertical baseplate during assembly until bulk components were bolted onto the rods.

3.3.2 Baseplate Machining and Characterization

The machining of the baseplate was performed as follows. The magnesium plate from which the baseplate was machined was clamped to the apron of a Bridgeport DRC 600 milling machine and the three 9 mm deep main cuts in the y direction were made: these are the cuts which most affect the baseplate bow in θ_y. Most of the smaller clearance slots for the bulk barrel screws were also machined at this time. A fly cutter finish (cutter turning at 1200 RPM, feed rate 152 mm /minute, cut depth 125 μm) ensured a smooth surface for subsequent flatness measurements.

The flatness of the baseplate was measured in the main slots (along the x direction) along the 2 lines AA' and CC' as shown in Figure 3.6. To perform these measurements, the baseplate was rested on a granite measuring slab and a level indicator was passed along the bottom of the slots approximately at the place where the rods holding the bulk barrels made contact with the bottom of the slot. The maximum deviation was ~125 μm from one end of the baseplate to the other, and was considerably less (35μm) over the stretch (approx. $50<x<275$ mm) where the bulk relay actually resided. The use of rods (described below) for bulk mounting further helped reduce the effect of baseplate irregularities on the optical axis by averaging out surface irregularities. The repeatability of the flatness measurements was better than 10 μm. These flatness values were well within the overall bulk interconnect alignment tolerance budget. Improving the flatness in the future could be accomplished either by annealing or, even better, by reducing the number of big holes and slots in the baseplate since machining additional features usually releases stress, causing still more bow.

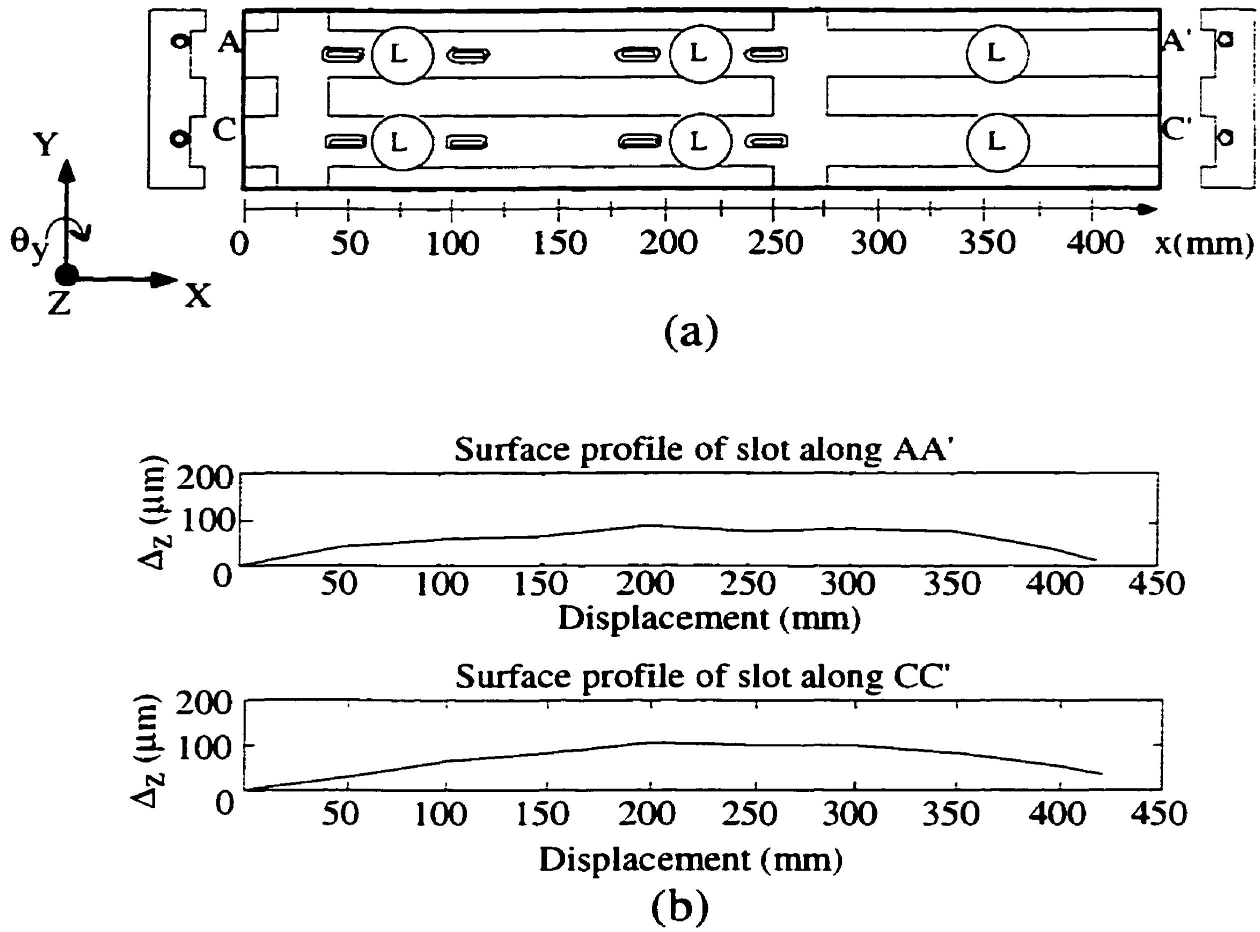

Figure 3.6: a) sketch of the baseplate b) Surface profile of baseplate along slots

3.3 Bulk Barrel Assembly

The bulk lenses. Risley Beam Steerers (RBSs) and tilt plates were mounted into their respective holders. Afterwards. as can be seen from the assembly drawing (Figure 3.1). the mounted bulk lens and a pair of mounted steering elements (either a pair of Risley Beam Steerers or a pair of tilt plates). respectively labeled components 13 and 14 in Figure 3.1. were inserted into a modular bulk barrel (component 12). This bulk barrel was then bolted to the baseplate. No deformation of the barrel was observed.

3.3.1 Thermal Effects in Bulk Relay Lens Inner Mounting

Although many techniques exist for mounting lenses into cells [14], none of these techniques left enough room to fit the bulk lenses and the steering elements (either Risley Beam Steerers or tilt plates) between the bulk turning mirror and the daughterboard. It was thus decided to forego any retaining ring and instead hold the lenses in their cells using the force of an interference fit between the outer diameter of the lenses, OD_{LENS} , and the inner diameter of the cells, ID_{CELL}, as shown in Figure 3.7. In other words, $OD_{LENS} - ID_{CELL} = I$, where I is a positive number called the interference. Interference fits are frequently used in industry to maintain a constant bore pressure in hole/shaft assemblies: in these fits, the difference between minimum and maximum values in the machining tolerances is kept small [12].

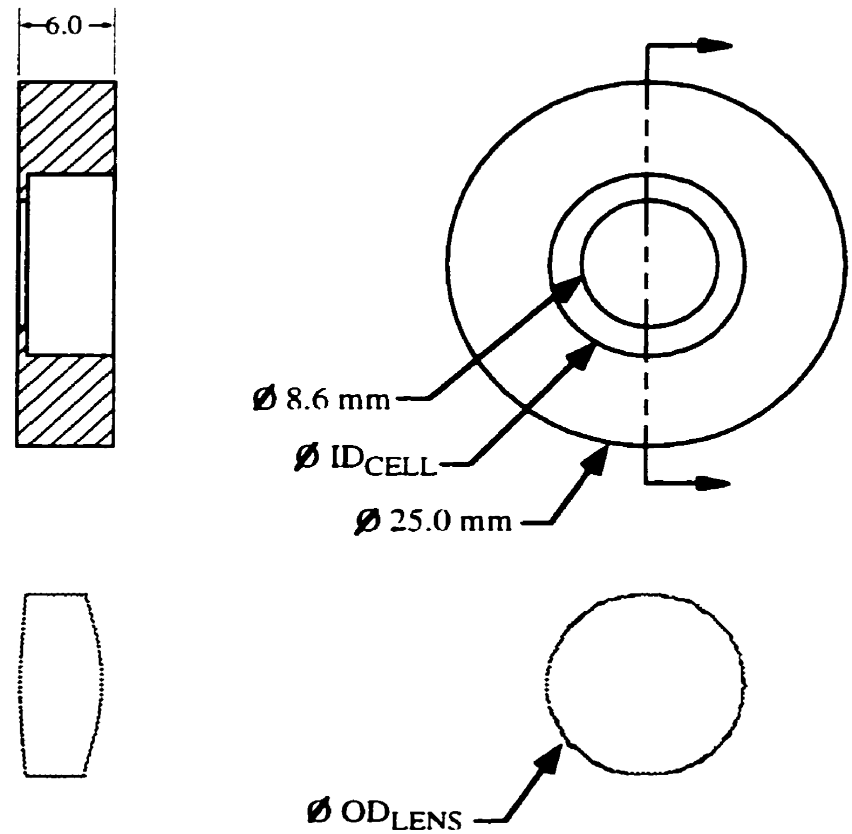

Figure 3.7: Bulk lens and holder used for the FN1 interference-fit lens holder. For an interference fit, $OD_{LENS} > ID_{CELL}$.

The OD_{LENS} of the eight bulk relay lenses in the system were measured to be between 12.468 and 12.479 mm (±2.5 μm).

The use of interference fits posed several design challenges, mostly related to thermal issues. The first challenge was assembly. In order to first put the lens into the cell, the easiest way was to heat the cell (but not the lens) to make it expand, then insert the lens. As the cell cooled and shrank, the lens was held snugly.

Another challenge was choice of material. The material chosen for the cell ended up being Delrin [15, 16]. Its main drawback, namely a high Coefficient of Thermal Expansion CTE_{DEL}=97 ppm/°C was compensated by its low cost, immediate availability, ease of machining, and low Young's Modulus (in both compression and tension) of E_{DEL}=2.76 GPa which reduced the stress due to thermal mismatch. In comparison, the numbers for the glass of the lens were similar to those of BK7: CTE_{LENS}=7.1 ppm/°C and E_{LENS} = 81 GPa. Using an interference fit with two such thermally mismatched materials can cause two main problems: 1) as the temperature, T, increases, the interference, I, decreases. Eventually, at T_{fall}, the lens can simply fall out. 2) as T decreases, I increases, causing severe radial stress. This can lead to birefringence and possibly damage the cell or lens or both.

Machining one different cell for each lens would have been prohibitively expensive, so one value of ID_{CELL} at 20°C, ID_{CELL20}, was chosen for all cells. The basic criterion for computing the nominal value of ID_{CELL20} was that at a maximum operating temperature, T_{max}, the interference should still lead to an FN1 interference fit (2.54 μm < I < 20.3 μm) for all lenses. This fit, described as a "light drive fit" is used for permanent assemblies and produces a light assembly pressure[12]. T_{max} was chosen to be 85°C, since this is the maximum allowable case temperature for a commercial-grade Pentium Pro [17]. The relationships for calculating the radial stress in the lens, S_{RLENS}, and in the cell wall, S_{RCELL}, are respectively[14]:

$$S_{RLENS} = \frac{(CTE_{DEL} - CTE_{LENS})\Delta T}{1/E_{LENS} + OD_{LENS}/(2E_{DEL}t_c)} \quad [1]$$

$$S_{RCELL} = \frac{OD_{LENS} \times S_{RLENS}}{t_c} \quad [2]$$

where the cell wall thickness t_c is nominally 6.3 mm.

Given the above, ID_{CELL20} was calculated to be 12.397 mm and Figure 3.8 plots (a) the stresses on the cell and lens and (b) T_{fall} as a function of OD_{LENS}. The bands above and below each solid line represent the effect of a machining error of ±12.7 μm on the value of ID_{CELL20}. It can be seen that a smaller cell inner diameter leads to a greater stress and to a greater T_{fall}. As a result, in the worst case combination of lens tolerances and cell inner diameter tolerances, the interference can fall to zero and the lens can fall out of the holder at 72°C. At the other extreme worst case, the radial stress in the cell can reach 38 kPa, which is slightly over half the 68 kPa nominal tensile strength of Delrin [15]. In all cases, calculations [14] revealed that the stress-induced birefringence was negligible. Birefringence, had it been present, would have affected the polarization of the transmitted beams and increased polarization losses at the next polarizing beamsplitter.

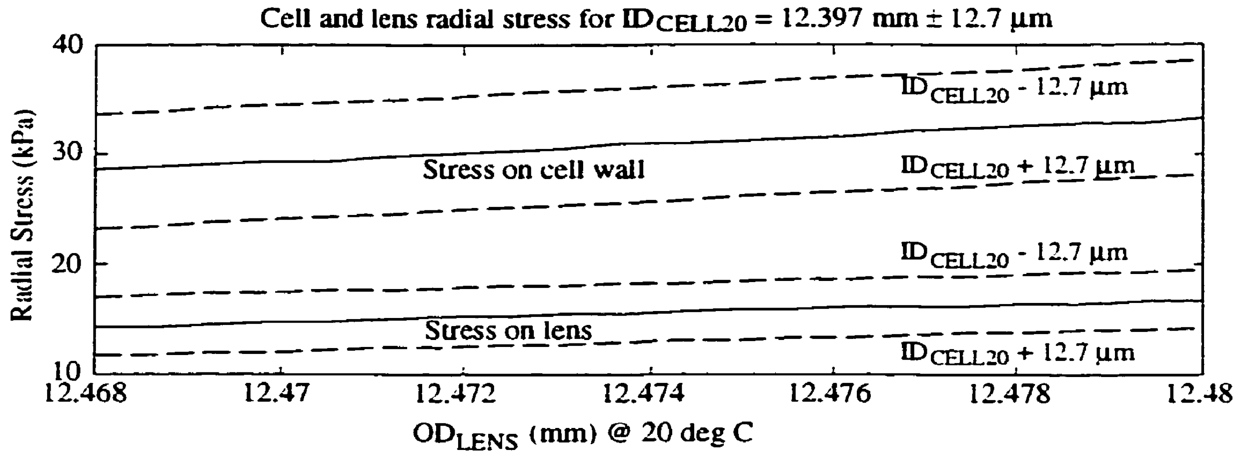

(a)

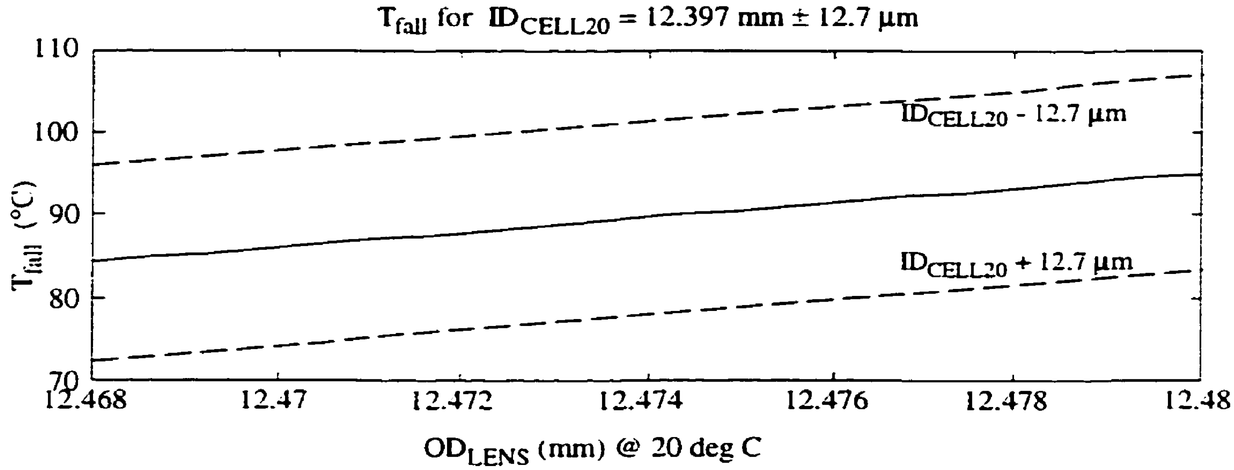

(b)

Figure 3.8: a) Curve relating radial stress on components to lens outer diameter b) Curve relating temperature at which lens falls out to lens outer diameter

Experimental validation was conducted on this technique. In the first experiment, the lens was mounted using the technique described above. A beam was then passed through the lens, the cell with the lens in it was rotated, and the movement of the spot caused by the focused beam was observed in the focal plane. The spot traced out a circle with a radius of 3.5 µm (±1µm). Since this passive mounting technique cannot correct for defects within the lens such as intrinsic wedge angle or centering of the lens optical axis with respect to its mechanical axis, these have to be added to obtain a true picture of the centering accuracy. For the current lens, this could have added up to 10 μm to the radius of the circle traced out by the spot [6]. Consequently, this is a cheap and rapid technique only for good quality, well-centered lenses: as a result, this technique demonstrates that the cost of lens mounting can be pushed back from the optomechanical assembler to the lens and cell fabricators. In another experiment, a mounted lens with outer diameter OD_{LENS}=12.469 mm at 20°C was heated until the lens fell out. The lens did indeed fall out at T_{fall} = 100 ±10 °C, showing the technique worked as expected.

This mounting technique illustrates the compromises between ease of assembly, operating temperature, material selection, and tolerances that must be considered when designing and building optomechanical components.

3.3.2 Bulk Barrel Mounting

Once the bulk barrels were assembled, they had to be mounted onto the baseplate at their proper position. As in other similar systems [18], slots were cut into the baseplate and the bulk barrels rested in these slots. However, given the vertical mounting and the rough handling the system was expected to receive in the chassis, the standard magnetic retaining techniques used in many other digital free-space optical interconnect demonstrations [18] were rejected; instead, all bulk relay components (bulk barrels and mirrors) were bolted into the baseplate. Furthermore, the barrels were not in direct contact with the edges of the slots. Instead, hard, precision-ground stainless steel rods of 6 mm in diameter were inserted into the slots and the components rested on the rods, as shown in Figure 3.9. Such rods are cheap and readily available [19]. The outer diameter tolerance of the above rods was = +0/-10μm and the outer diameters of the machined outer barrel components were measured to have a deviation of ± 10 μm from their nominal 30 mm.

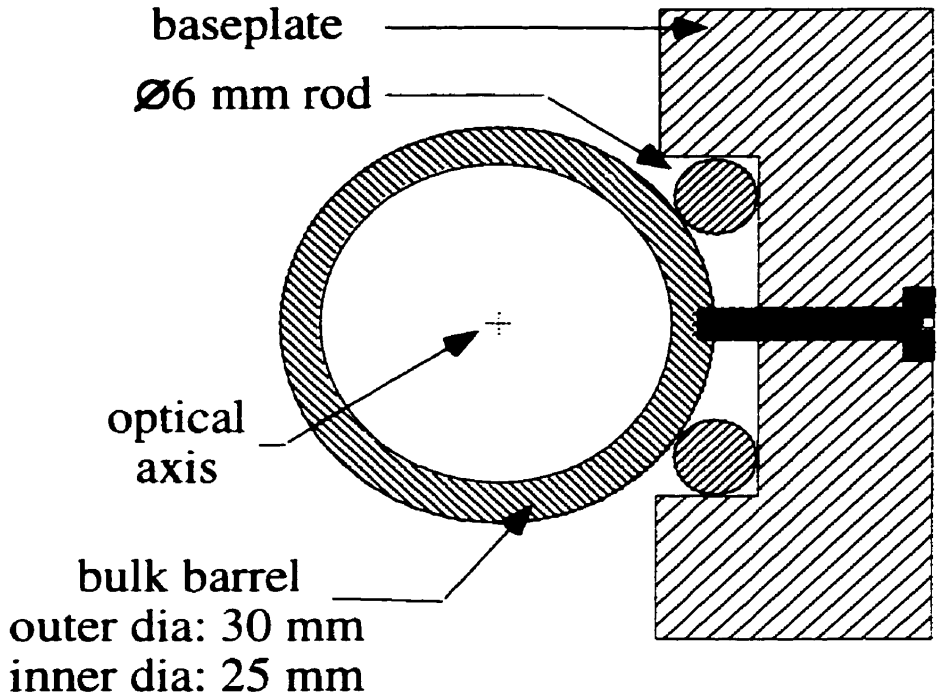

Figure 3.9: Technique for mounting bulk interconnect components onto vertical baseplate

Machining tolerances were the most important factor affecting the height of the optical axis. Other physical parameters were nonetheless studied as they gave insight into the design. One of these parameters was the deformation of the barrels due to the holding force exerted by the screws. Assuming the screw into the threaded hole in the barrel can be modeled by a nut-bolt fastening, the holding force, P, exerted by the screw can be estimated to be [20]

$$P=T/(KD) \qquad [3]$$

For the 4-40 screw used, T is the installation torque (nominally 0.6 N•m for a 18-8 steel 4-40 screw), K is the torque coefficient (~0.15 for plated finish fasteners), and D is the nominal screw diameter (2.79 mm for a 4-40 screw) [20]. This yields P=1434 N (M=1434N/9.8=146.3 kg).

This exerted force can damage the barrels, the rods, the baseplate, or any combination of these three by causing indentations in the material. The most critical interface is between the barrel and the rods and the damage to this interface can be estimated as follows. By using Brinell Hardness Numbers (BHN), the surface area, A, of the indentation into the barrel caused by the hard steel rods biting into the barrel can be approximated as [21]

$$A = 0.5 \times M/BHN \qquad [4]$$

where the 0.5 factor is due to the fact that each rod only exerts half of the force onto the barrel.

Using BHN=95 [12] for the 6061-T6 aluminum used in the barrels, A should be $0.5*146.3/95=0.77\ mm^2$. Further geometrical analysis indicates that for a line contact of 13 mm (the length of the barrel), and a rod diameter of 6 mm, the drop in the height of the optical axis due to the indentations is of the order of one micron, which is less than the machining error. This was further reduced by anodizing the barrels: the anodization increased the hardness of the barrels, thus reducing the indentation in the barrel to negligible levels.

To summarize, the considerable forces involved in bolting down the bulk barrels onto the baseplate caused no significant damage to any component. It will be seen below, however, that the force involved in bolting a daughterboard to optomechanics caused significant problems. Other forces, such as the force exerted between the baseplate and the rods were spread over the length of the rods and as such could be neglected.

3.3.4 Bulk Turning Mirror Alignment

The optical system was a closed-loop ring system. As such, turning mirrors had to be installed at the four corners of the optical system in order to close this loop. Since errors in the mirror alignment could only be corrected by the bulk RBSs and tilt plates which had respectively a wedge angle of 1° and a tilt angle of 10°, it was imperative that the mirrors be aligned as carefully as possible in order to reduce the travel requirements of the steering optics. Additionally, the mirrors had to be arranged so as to eliminate rotation of the 2D array of beams[22].

In the overall system assembly sequence, one of the first steps was the mounting of the bulk turning mirrors onto the baseplate, as outlined in Figure 3.10. This section describes the process.

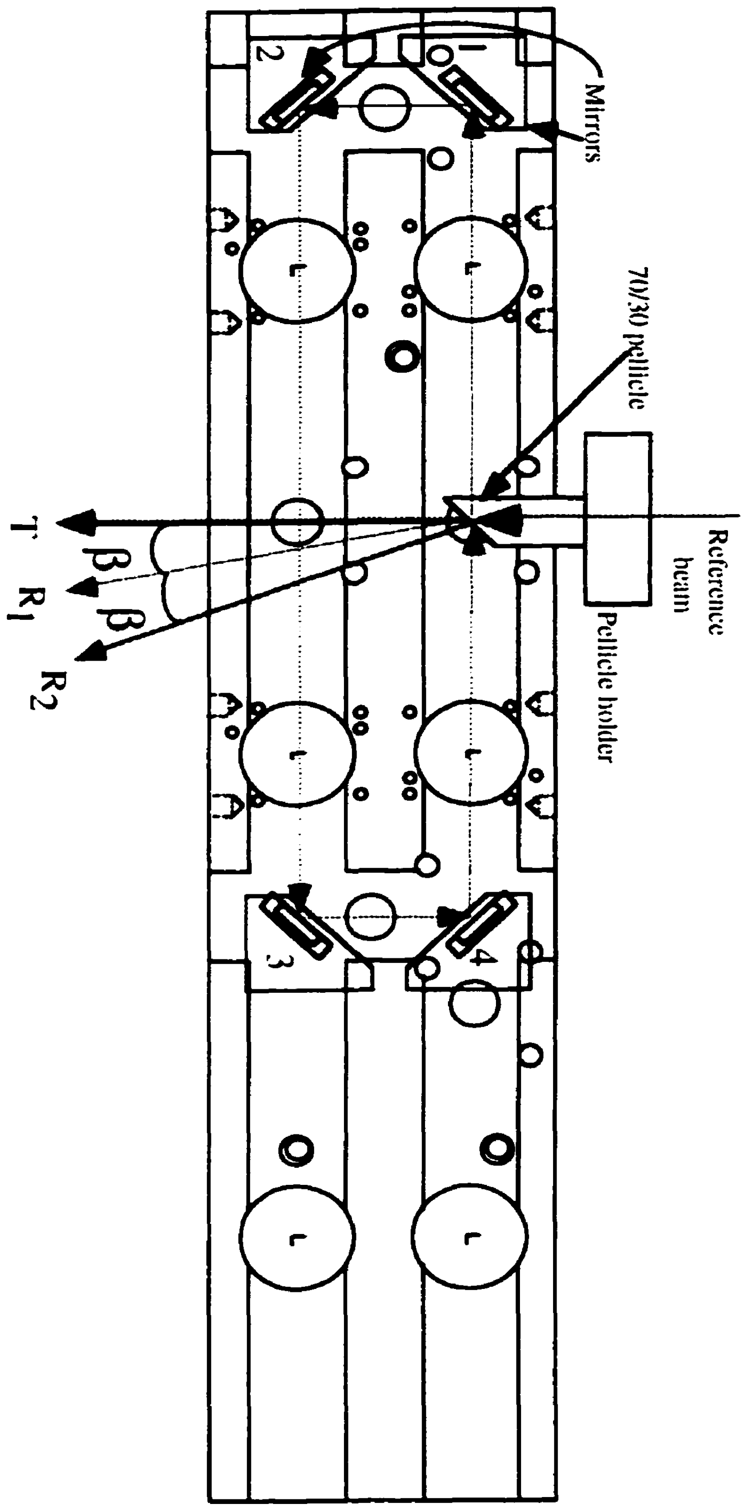

Figure 3.10: Setup for mounting and aligning bulk turning mirrors on baseplate

The alignment of the 4 mirrors into a loop presented a certain problem. In a system such as this one, the slots in the baseplate can be used to locate the optical axis as it goes through four 90° turns in the loop. Apertures placed along the slots or along mechanical extensions of the slots can be used to define the optical axis; the farther the apertures are from each other (i.e. the greater the lever arm) the better the optical axis can be defined. Before starting, all the mirrors were glued to their holders which allowed for two degrees of freedom in tilt and rotation.

It is therefore possible to align mirrors by launching a reference beam known to be on axis and monitoring the reflected beam on an aperture far from the baseplate. However, this only works for the first three mirrors; placing the fourth mirror will close the loop and no lever arm longer than the baseplate can be used. In order to avoid this problem, a technique involving a pellicle was used.

With no mirrors on the baseplate, a reference beam was launched down the barrel of the pellicle holder at the end of which was fixed a 70/30 (transmissive/reflective) pellicle, as shown in Figure 3.10. 70% of the beam went through (beam T) and 30 % was reflected toward position 1. Using custom alignment apertures on the baseplate and along the optical bench, the pellicle holder and incoming beam were adjusted until they delivered a beam that was coaxial with the optical axis on the baseplate. The beam was parallel to the ideal bulk optical axis to within a few minutes and was less than 50 μm off the axis. Afterwards, bulk turning mirror 1 in its holder was installed. After adjusting it so that the reflected optical beam going toward position 2 was again parallel to and on the axis, mirror holder 1 was bolted. This procedure was repeated for mirrors 2 and 3. For the final mirror holder (#4), the reflected beam R_1 was observed and the mirror holder was adjusted so as to minimize angle β; mirror holder 4 was then bolted. The pellicle thus brought the reference beam off the baseplate and allowed for a lever arm to improve the accuracy of the alignment.

In Figure 3.11a, spots resulting from beams T, R_1, R_2, R_3 ... being projected onto a screen 3 metres from the baseplate can be seen. This large (3m) distance allows for a lever effect to magnify the error in β. To obtain this picture, mirror 4 was deliberately misaligned: the actual alignment, which was much tighter (β<0.05°), was similar to that shown in Figure 3.11b. This misalignment was sufficiently small for eventual correction by the bulk Risley Beam Steerers and tilt plates.

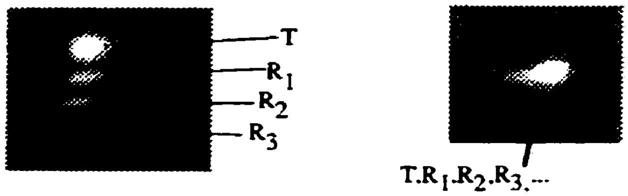

Figure 3.11: Results of bulk turning mirror alignment a) Mirror 4 greatly misaligned b) Mirror 4 at optimum alignment

3.4 Other Modules

This section covers the optomechanics associated with other key modules and concludes with a first order alignment tolerancing analysis.

3.4.1 Lenslet/beamsplitter Barrel

A simplified drawing of the Lenslet/beamsplitter barrel is shown in Figure 3.12a. To assemble the unit, first the Polarizing Beam Splitter with the Quarter Wave Plates mounted onto it (PBS/QWP) was aligned and glued inside the slot as shown in Figure 3.12b. With a custom setup, the PBS was glued such that its front face was normal to the incident optical axis to within θ_y<0.05°. The lenslets were then glued to the faces of the barrel, as shown in Figure 3.12c. The demanding lenslet-to-lenslet alignment tolerances in x,y of Table II were met by building a separate prealignment and imaging rig. The tolerances in the spacing (z_2=6.98 mm in Figure 3.4) between the lenslet arrays as well as the relative tilt (θ_x and θ_y) between the lenslet arrays were dictated by the machining tolerances, which were ±10 μm, in this case. These tolerances were well within those demanded by the optical design. When the Lenslet/beamsplitter barrel assembly was complete it was inserted into the outer barrel: these two components are respectively pieces 11 and 10 in Figure 3.1.

The optical microlens relay, which was designed to relay the beams using the maximum lens-to-waist configuration [8], also exhibited another interesting characteristic: letting z_2' (= 5.41 mm) be the optical distance between the actual lenslet arrays #1 and #2 and z_3 (=886 μm) be the optical distance from lenslet array # 2 to the device plane, then $1/z_2'+1/z_3 \approx 1/f_\mu$. As a result, each lenslet on lenslet array # 2 imaged a part of the #1 substrate and relayed it to the device plane. These relayed images, shown in Figure 3.13 with back illumination, clearly indicate the strips of pixellated mirrors and lenslets on lenslet array #1. In addition, the beamlets from the power array plane clearly appear as bright spots coming from the lenslets. This qualitatively demonstrated that the lenslets were properly aligned and was of great help during system alignment.

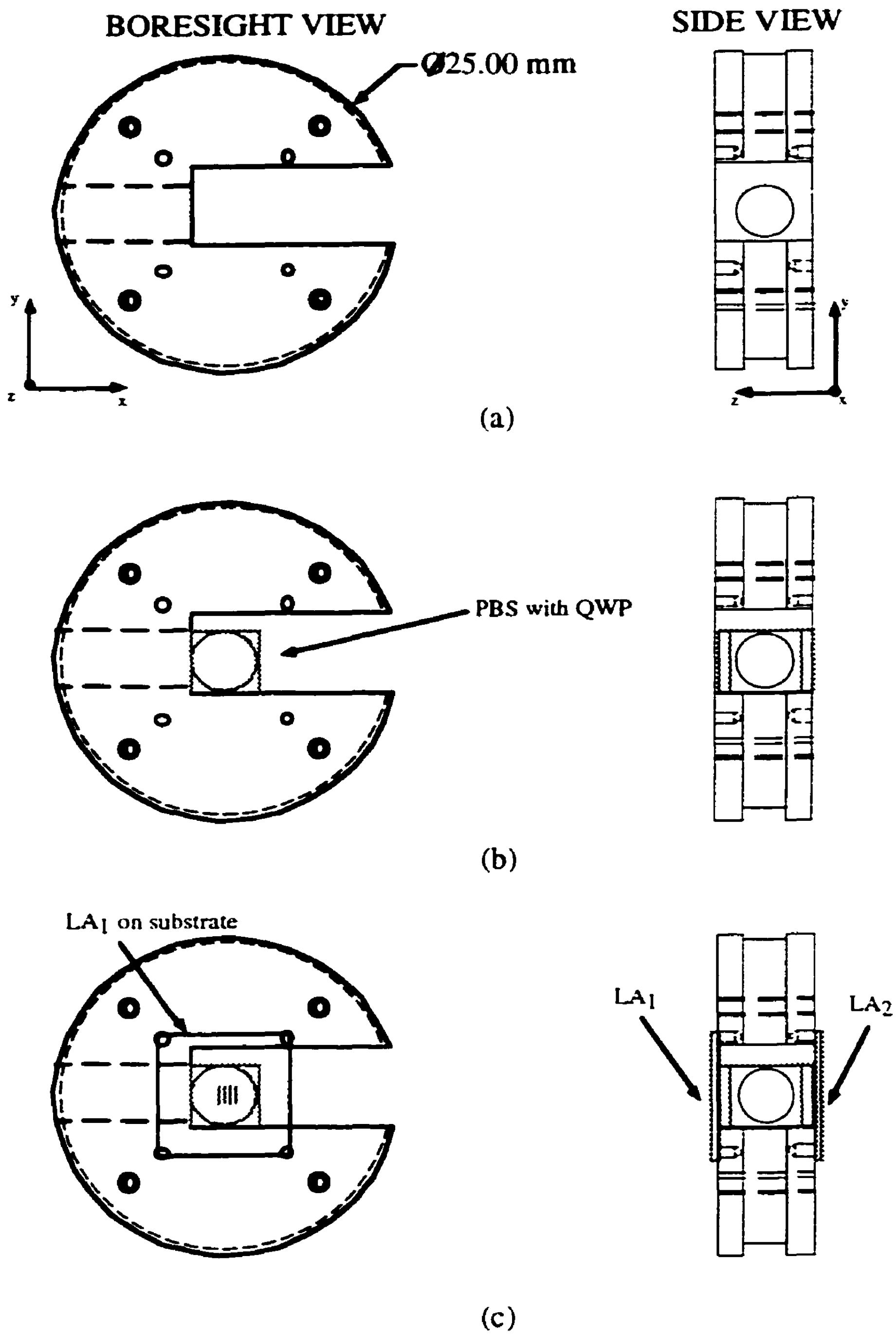

Figure 3.12: a) Lenslet/PBS barrel b) With mounted PBS c) With mounted lenslets

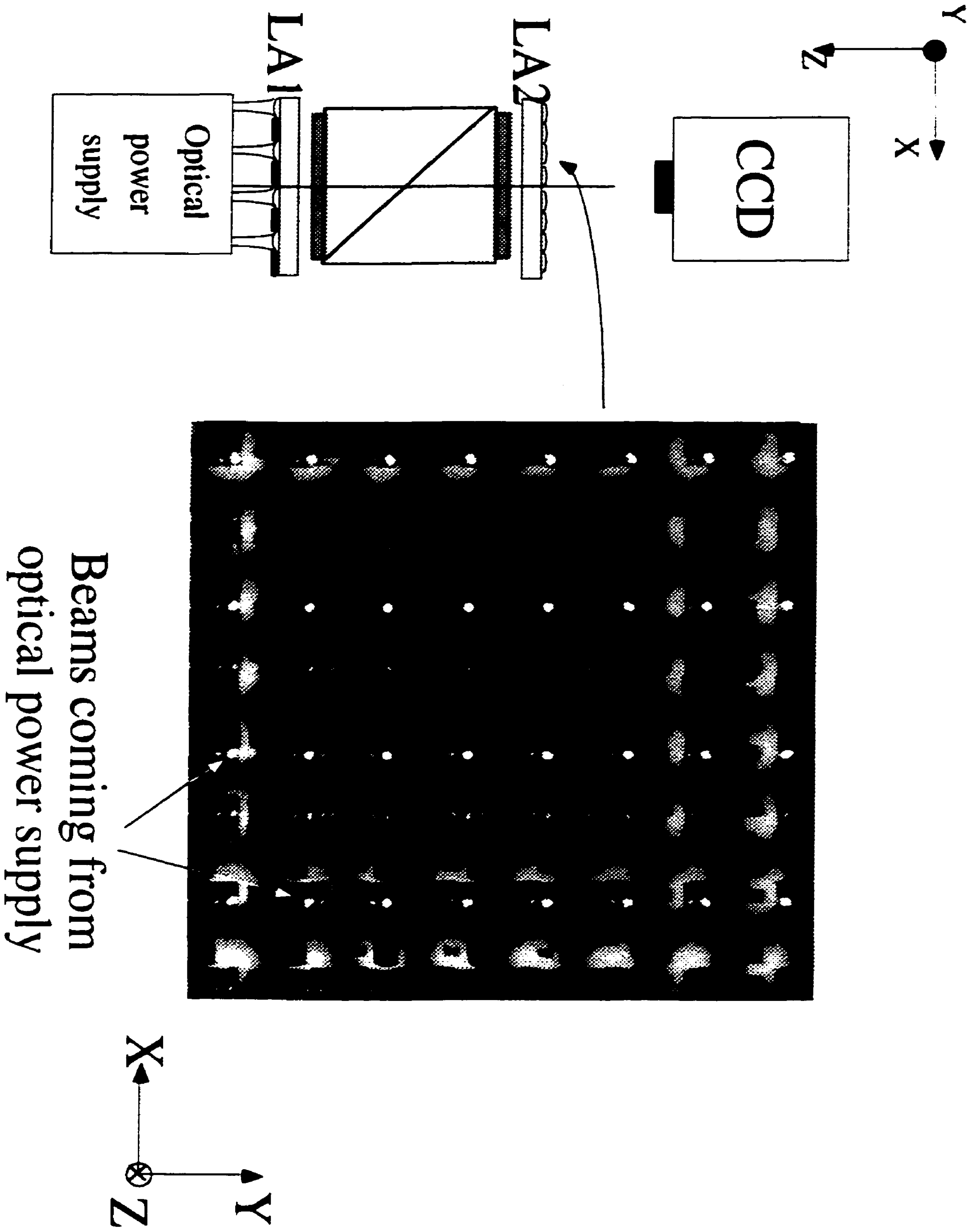

Figure 3.13: Imaging of Lenslet array #1 by Lenslet array # 2

3.4.2 Optical Power Supply (OPS)

The optical power supply (OPS) contained lenses to collimate the output from the fibre (one fibre per OPS), a multiple phase grating (MPG) as fan-out element (to produce a 4x8 array of spots and 8 additional alignment spots), a Fourier transform lens pair and additional components for beam steering and polarization control. Each OPS barrel was 80 mm long. Each fully assembled OPS was prealigned separately and inserted into an outer barrel assembly (respectively components 8 and 10 in Figure 3.1). At the end of this assembly sequence, therefore, each outer barrel assembly contained a Lenslet/beamsplitter barrel and an OPS. The outer barrels were then inserted into the baseplate. A full analysis of the OPS performance is given elsewhere [23].

3.4.3 Bulk Interconnect Tolerancing

As shown in Figure 3.4. the bulk interconnect had to relay the beams emerging from stage 1 onto the pixellated mirror of stage 2. The two bulk tilt plates, each 1.5 mm thick SF10 (n=1.71) at 10° tilt, could each move the beam array by approximately 110 μm at the pixellated mirror. By rotating the tilt plates such that their individual contributions canceled, it was possible to move the imaged beam array by 0 μm at the mirror plane: conversely, they could also be oriented such that they gave a total displacement of 220 μm at the pixellated mirror.

An ideal system would require no correction due to misalignment. In this non-ideal case, the following factors mentioned in the sections above contributed to misalignment which had to be corrected by the tilt plates: machining errors affecting the outer diameter of bulk barrels and depth and width of the baseplate slots (~25 μm): lens centering error (~10μm): rod deformation (~10μm): baseplate bow (~50μm) errors in inserting the outer barrels with the beamsplitters (~50 μm total) and alignment errors in the bulk mirrors (~50 μm). To a first order approximation. this could have caused a total alignment error of 90 μm (in quadrature addition), in addition to aberrations. This alignment error could easily be corrected by the tilt plates.

3.5 Daughterboard Mounting Techniques

Mounting the daughterboards to the optomechanics was the most critical step since it involved interfacing the optoelectronics to the optomechanics. This section describes the various techniques implemented and the challenges which had to be overcome.

3.5.1 Procedure

This operation, to be performed four times, once for each daughterboard, was the most delicate of the entire assembly. The key components are outlined in Figure 3.14a and b in a rear view and side view respectively. In short, the daughterboard was attached to an interface piece called the daughterboard clamp which was bolted to the baseplate.

The optical design specified that the smart pixel device plane be z_3=886 ± 15 μm away from the microlens array and that the xy alignment error between lenslets and smart pixel device windows be on the order of one μm, as shown in Table I. These very tight alignment tolerances were required to reduce loss of optical throughput due to daughterboard misalignment to below 1%. Misalignments greater than those in Table I will cause a loss greater than 1%.

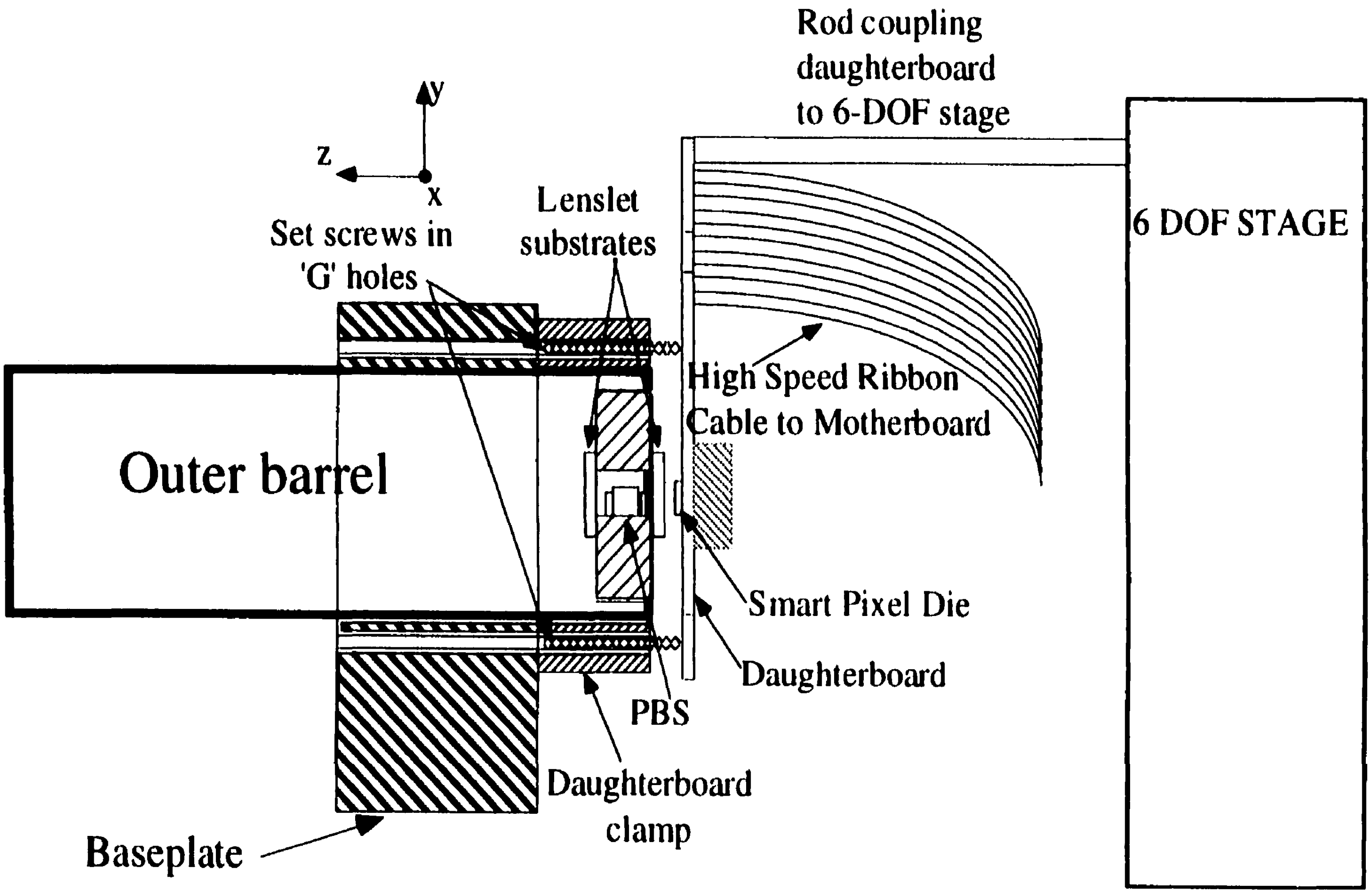

Figure 3.14a: Mounting of daughterboard to optomechanics: side view

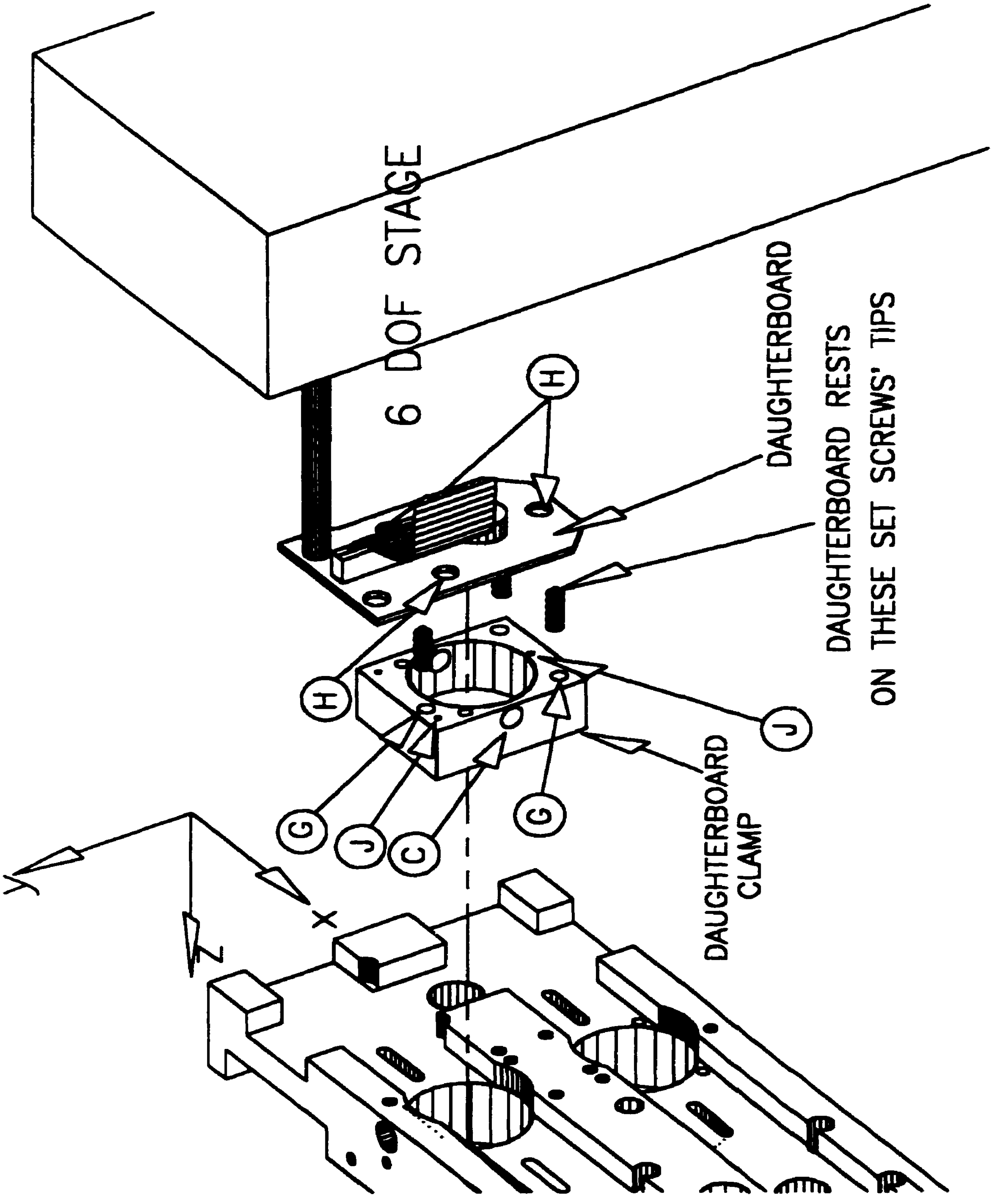

Figure 3.14b: Mounting daughterboard to optomechanics: rear view

Since there were very few optoelectronic chips or lenslets available, it was decided not to perform the step of gluing lenslet array #2 to the device packaging: rather, a four step assembly sequence was implemented. With the daughterboard mounting clamp already bolted to the baseplate, the objective was to align the daughterboard to the optomechanics and fasten it to the daughterboard clamp.

First, the device die was mechanically aligned, glued to the daughterboard to better than 150 μm of its nominal position [24], and wirebonded. In the second step, light was launched into the OPS. The OPS Risley Beam Steerers were aligned such that the beams went through the microchannel relay and onto the plane where the optoelectronic devices were to be located.

In the third step, the daughterboard was coupled to a six degree-of-freedom (6-DOF) precision positioning system and aligned to the optical beams as follows. The daughterboard was adjusted in Δz, θ_x, and θ_y until a traveling microscope setup indicated that these three DOFs were within the desired tolerance. When these three tolerances were achieved, three set screws emerging from holes in the daughterboard clamp (the holes are labeled 'G' in Figure 3.14) were adjusted such that the set screw tips just barely touched the front of the board. These three screw tips thus defined the proper plane of the daughterboard relative to the optomechanics. As a result, during the rest of this step the daughterboard never actually touched the clamp but rather rested and slid on three points about a millimetre in front of the clamp. The θ_z accuracy then was verified using the imaging system. Finally, the highest contrast ratio of the modulated beams could be used to indicate the optimal xy alignment of the beams to the device windows.

In the fourth step, after the tolerances in the six DOFs were met, the daughterboard, which was still coupled to the 6-DOF stage and just barely in contact with the three screw tips, was fastened: the 6-DOF stage was subsequently decoupled from the daughterboard.

This fourth step, namely fastening the aligned daughterboard to the optomechanics. was the most problematic of the entire system assembly sequence. Two techniques were tried to fasten the board properly: they are described below.

3.5.2 Daughterboard Fastening Techniques

3.5.2.1 First Daughterboard Fastening Technique: Bolting

In this technique. three additional screws were used. Fastening screws with large heads were inserted into the 'H' clearance holes of Figure 3.14 in the daughterboard and screwed into the 'J' holes in the clamp (the diameter of the fastening screw heads was greater than the 'H' holes' so that the fastening screw heads rested against the back side of the board). The fastening screws were then tightened so that the daughterboard did not simply rest on but rather was pressed very hard onto the set screw tips of step three above.

This technique proved to be very cumbersome and had fundamental problems. If the fastening screws were tightened too much. the daughterboard moved during the tightening, causing the board to be bolted into an improper position. If, on the other hand. the holding screws were not sufficiently tightened, the board drifted over time. The experimental results indicating the drift will be given below.

Compromising between the two extremes in tightening the screws led to an unsatisfactory compromise result in which the board slightly moved during tightening and slightly drifted afterwards. Consequently. the bolting technique was rejected.

3.5.2.2 Second Daughterboard Fastening Technique: Gluing

In this case. the board was glued to the set screw tips. After a careful analysis of viscosity, holding force. and ease of curing. a glue from Loctite (#403) was chosen. With a syringe, the glue was gently applied to the three set screw tips which were just barely touching the daughterboard. This yielded satisfactory results as the discussion below will show.

3.6 Mechanical Stability Experiments: Setup

This section describes the diagnostic setup used to measure the effect of mechanical vibrations and shock on the daughterboard x-y (lateral) alignment. Experimental results will follow the setup description.

The measurement setup was as follows.

In lieu of a smart pixel die, a quadrant detector (QD) from UDT Inc. [25], as shown in Figure 3.15, was glued and wirebonded to a daughterboard. Afterwards, one fiber-connected outer barrel/Lenslet/beamsplitter barrel/OPS assembly with all the components except the fan-out grating (held by piece # 5 in Figure 3.1) and the lenslets was inserted into the baseplate as per the assembly procedure. The daughterboard with the QD was then aligned and fastened to the optomechanics using one of the two techniques described above.

When light was launched into the OPS (with no fan-out grating), a single beam went through the OPS and impinged on the QD. At the QD, the beam had a nominal diameter of 3ω =1.02 mm (99% encircled energy).

The photocurrents generated by the four photodetectors, labeled 1,3,5, and 7 respectively, of the QD were fed via the high speed ribbon cable assembly to the dedicated alignment board. On the alignment board, each of the four signals was fed through a lowpass filter having cutoff frequency f_{3dB}= 402 Hz, buffered, then finally fed to a Lab-NB ™ A/D board from National Instruments which sampled each of the four voltages at 4096 samples/sec. The low-pass filter was necessary to eliminate aliasing, among other problems associated with frequency. The setup for generating alignment voltage V_1 is shown in Figure 3.16. The three other setups for generating V_3, V_5 and V_7 from the respective quadrants were analogous.

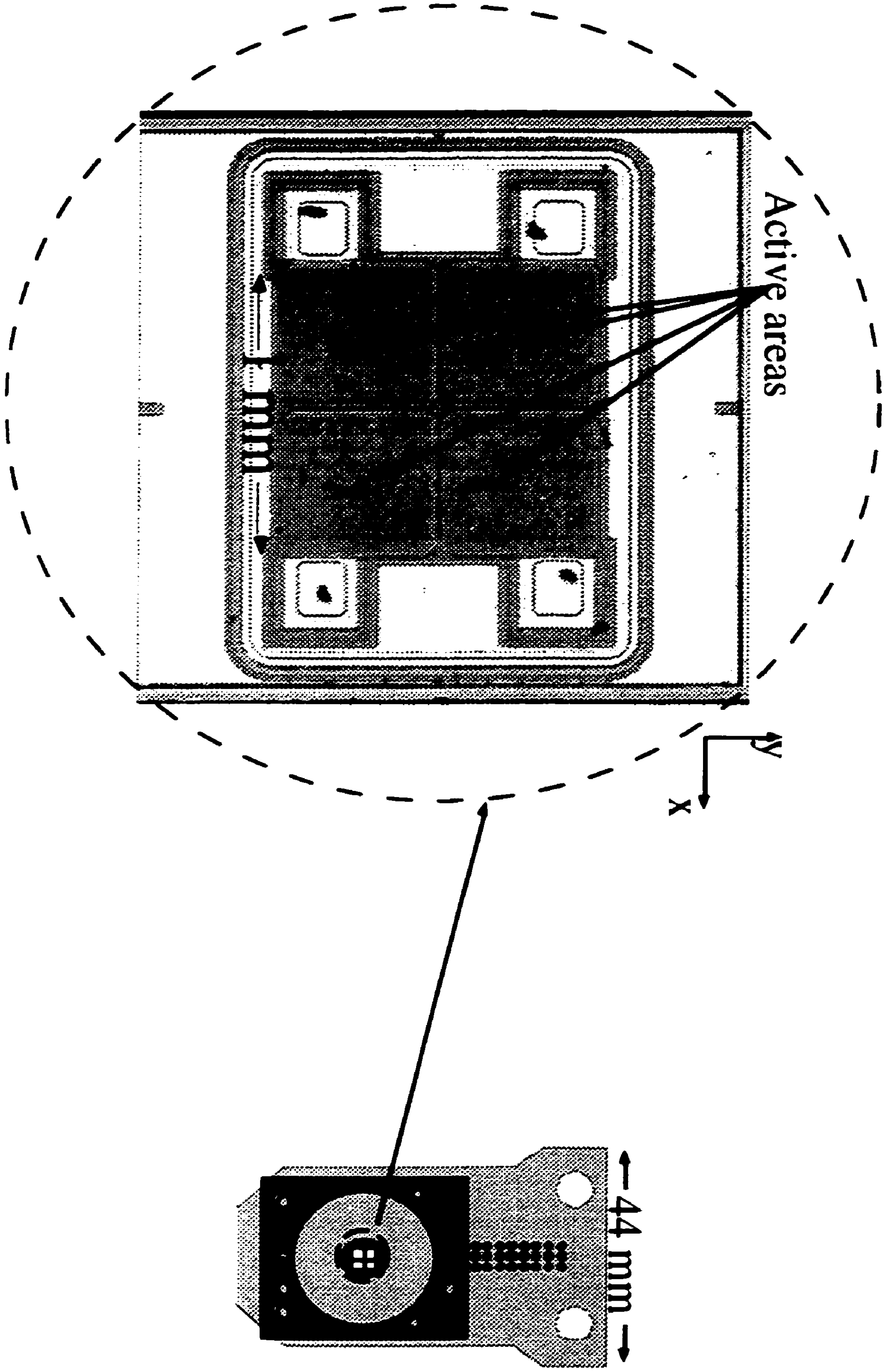

Figure 3.15: Quadrant detector mounted onto daughterboard for alignment diagnostic purposes

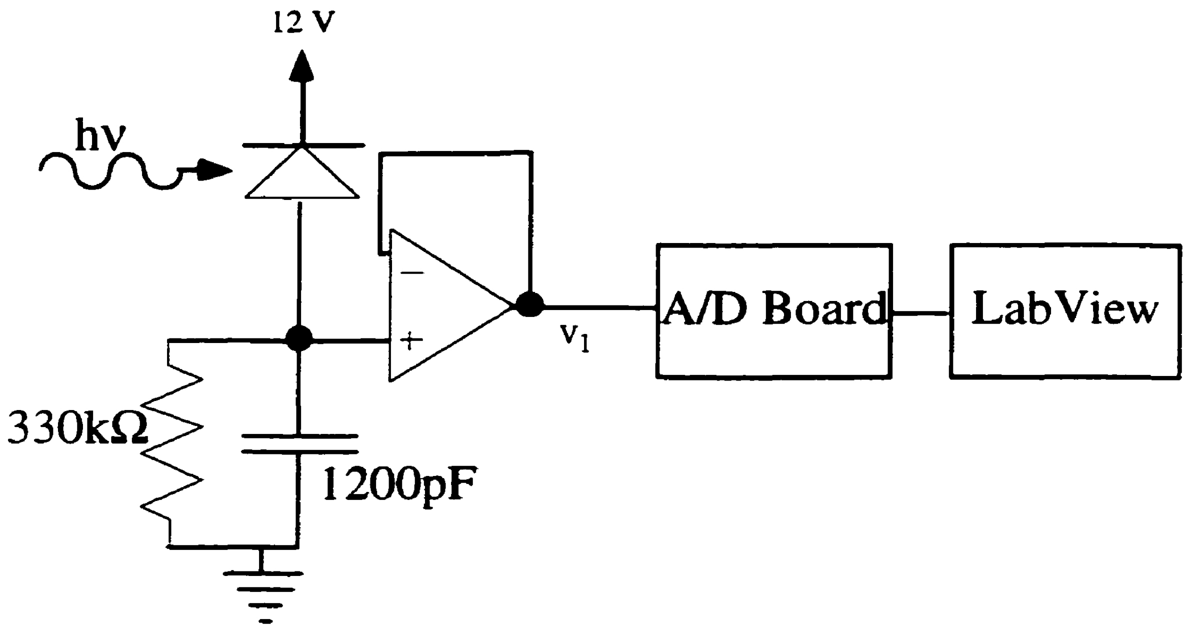

Figure 3.16: Electronic setup for generating, buffering, and processing one quadrant detector signal

Further processing, such as the calculations required to obtain the Δx and Δy signals from the four sampled voltages, was performed in LabView ™. To ensure repeatable results regardless of optical power fluctuations, all misalignment calculations were normalized to the total optical power hitting the detector. For example, from the QD picture in Figure 3.15, it can be seen that

$$\Delta x = k\frac{(V_1 + V_7) - (V_3 + V_5)}{V_1 + V_3 + V_5 + V_7} \qquad [5]$$

where k is a calibration constant which in this case was obtained experimentally. For this system, the calibration constant was such that the sensitivity was about 110 mV/μm for typical power levels. Figure 3.17 indicates that the system response was linear for Δx<80 μm.

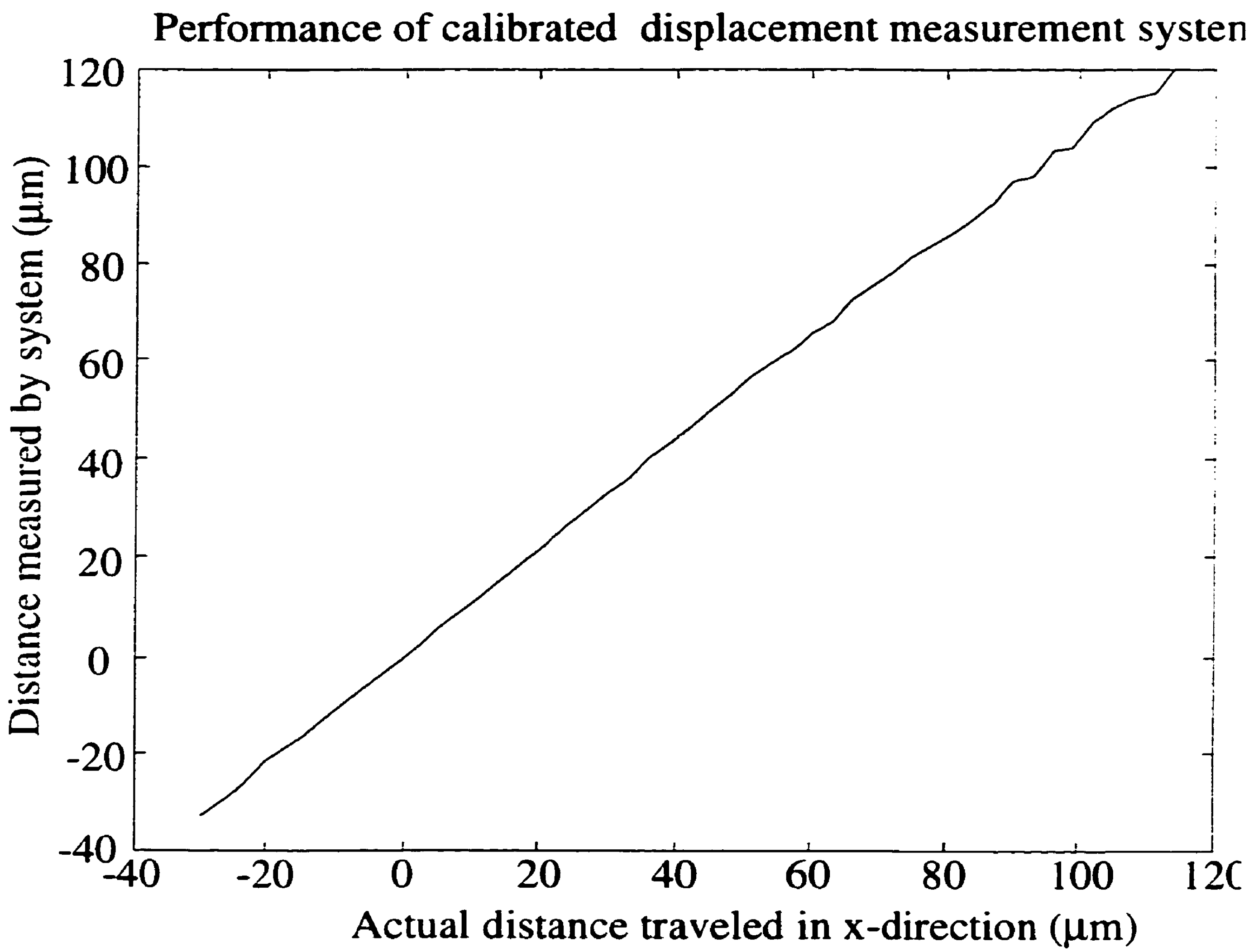

Figure 3.17: Calibration and performance of quadrant detector-based displacement

3.7 Mechanical Stability Experiments: Results

The measurement system described above was used to characterize many aspects of the optomechanics. This section gives experimental results obtained.

3.7.1 Impact on System Alignment of FC Connector Insertion/extraction

The field-serviceability of the FC-connected power supply was an advantage which this system offered. For this ease of connection to be of greatest use, however, it was imperative that the fiber be easily connected and disconnected without upsetting system alignment. The results of an experiment in which a new FC connection-effected fibre was connected to and disconnected from the receptacle on the FC connector bulkhead (part #2 in the assembly drawing, Figure 3.1) two dozen times within five minutes are shown in Figure 3.18. As can be seen, the spot never moved at all, to within the measurement uncertainty of ± 1 μm in this setup (Sub-micron measurements were not repeatable or constant over time using this setup). This result is more than a simple verification that a single mode fiber connector has excellent repeatability: this indicates that the system alignment was in no way affected either by the small shocks associated with the fiber insertion or by the torque imparted on the outer barrel as the connector was hand-tightened until the locking screw was snug. It should be noted, however, that if the connector was tightened extremely hard, the spot did move by about 2 or 3 microns. Similar results were obtained for both daughterboard mounting techniques (bolting or gluing).

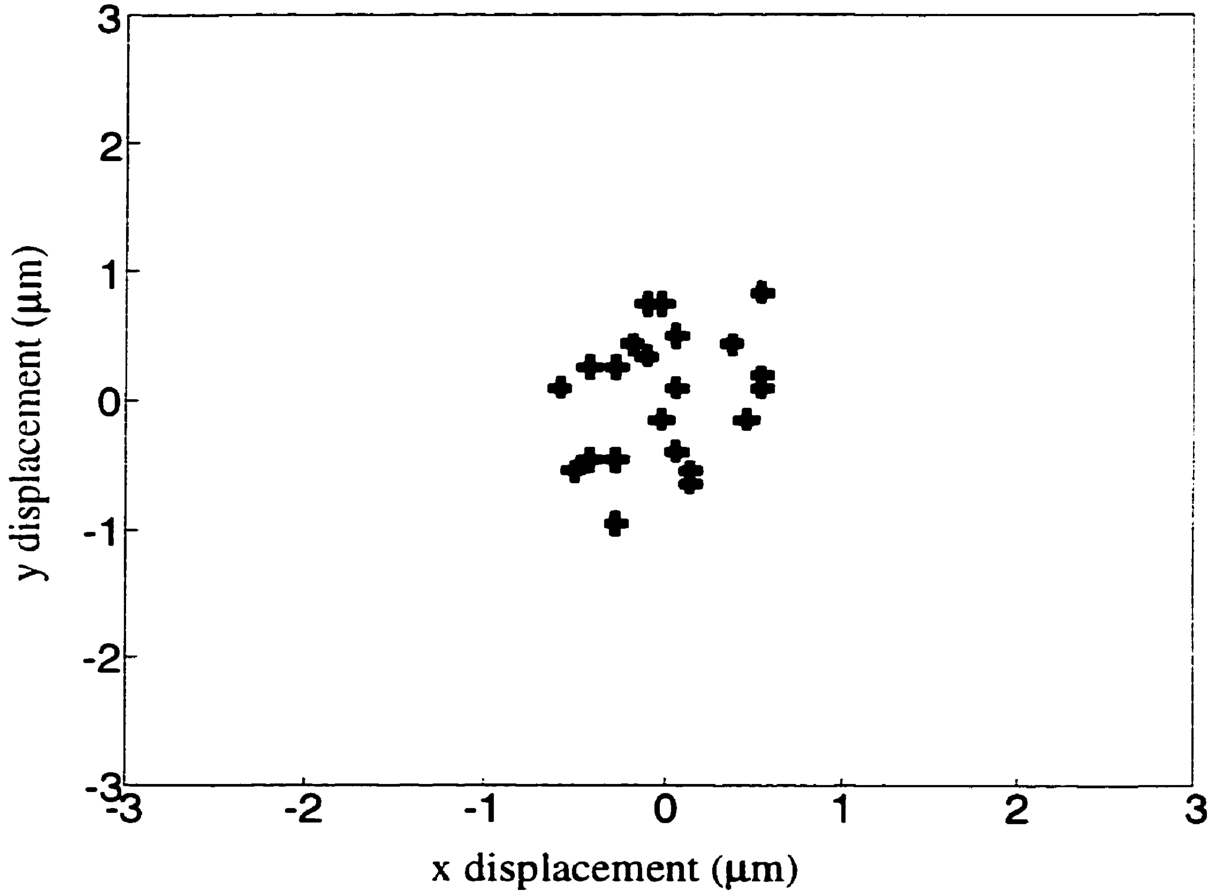

Figure 3.18: Effect of repeated insertion/extraction cycles of FC-connected fiber on system alignment. This indicates that inserting/ removing the fiber does not affect system alignment to within the ±1 μm measurement uncertainty.

3.7.2 Measurement of Long-Term Drift of Bolted Daughterboard

This experiment measured long term drift of the daughterboard after it was fastened using the bolting technique. The bolts were hand-tightened sufficiently to hold the board snugly to its mounting clamp on the optomechanics; further tightening of the bolts could have been possible, but repeated experiments indicated that excessive tightening caused the board to move from its aligned position during system assembly.

After the daughterboard was bolted, a large (120x120x38mm) industrial cooling fan typical of those mounted in conventional backplane chassis (model 125DH 1LP11000 from ETRI inc.) was bolted to the VME chassis and was located 50 mm away from the daughterboard: the fan was oriented such that it blew air directly onto the daughterboard. There was considerable clearance around the fan to allow for unimpeded air flow. The fan was fed 500 mA at 12 V_{DC} (as per specifications) which made it rotate at ~3000 RPM (50 Hz). At this frequency, if the flow is unimpeded, the fan is specified to blow 102 CFM (Cubic Feet/min). The chassis was simply resting on a table and was not clamped down in any manner.

Every day for almost two weeks, with the fan always on at full power, the position of the daughterboard was measured. As can be seen from the results, shown in Figure 3.19, the daughterboard "fell" in the y direction by about 1 micron per day then stabilized after a week. The repeatability of these measurements was ±1 μm. As stated above, the poor long-term stability of the daughterboard bolting technique led to its rejection for system assembly.

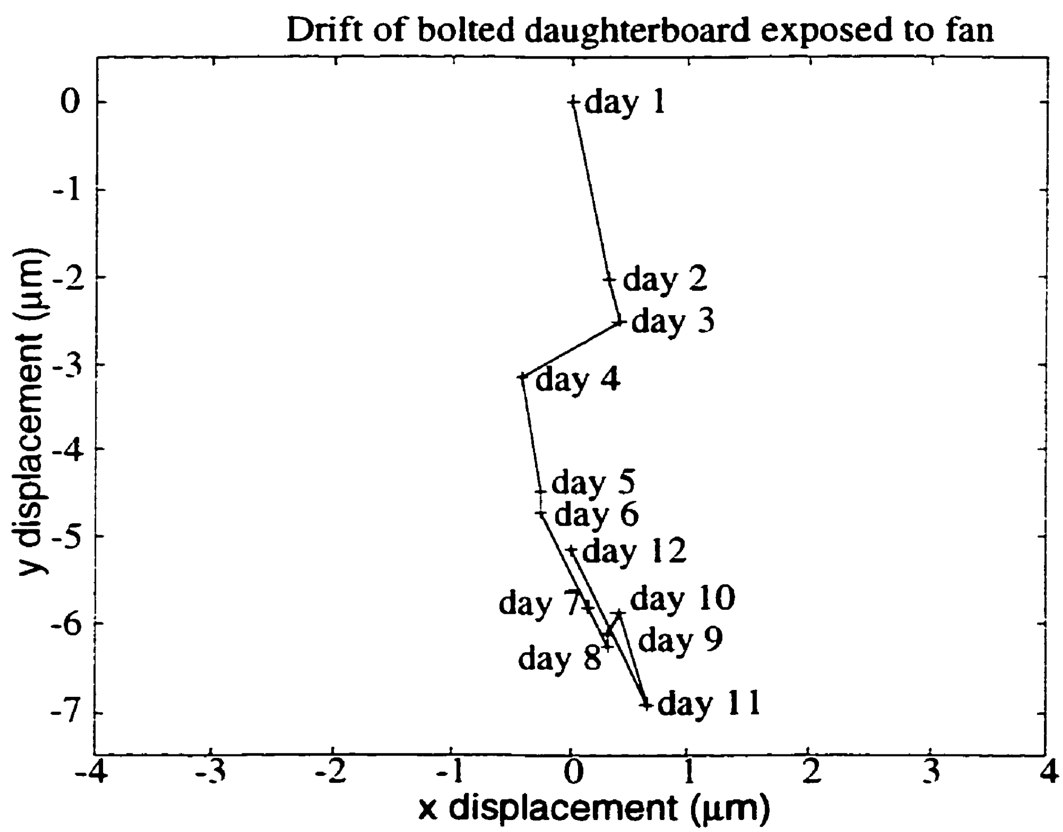

Figure 3.19: Drift of daughterboard fastened using first (bolting) technique

3.7.3 Measurement of Long-term Drift of Glued Daughterboard

This experiment measured long term drift of the daughterboard after it was fastened at (x,y)=(0,0) at day 1 using the gluing technique. Measurement results for x and y are shown in Figure 3.20.

The most logical interpretation of the long-term drift results in Figure 3.20 is as follows: the board was glued at (0,0) ±2 μm and moved about one micron during the curing. For over two months after the curing, the board never moved to within the measurement error regardless of whether or not the ETRI 125DH fan in the setup described above was blowing air onto the daughterboard. It should be noted that after the glue had cured, decoupling the daughterboard from the motorized xyz stage or extracting/inserting the high speed ribbon connector on the daughterboard produced no measurable misalignment. The final results are shown in Table I. It should also be noted that adjusting the RBSs in the OPS can compensate for small errors in xy. In the case of this long-term drift measurement experiment, the measurement repeatability was ±3 μm.

It should also be noted that after the glue had cured (which took a few minutes), the glue left a slight residue on some of the optics through which the broad alignment beam passed. However, this residue was subsequently measured to be extremely uniform over many millimetres: as a result, this residue only had the effect of attenuating by ~30% the light impinging on the quadrant detector. This attenuation did not affect the measured results since the calculations normalized all power received. A different glue with no outgassing ("blooming") during curing or a different setup would eliminate this problem. The glue used was black-toughened cyanocrylate known under the trade name Black Max™ from LocTite™.

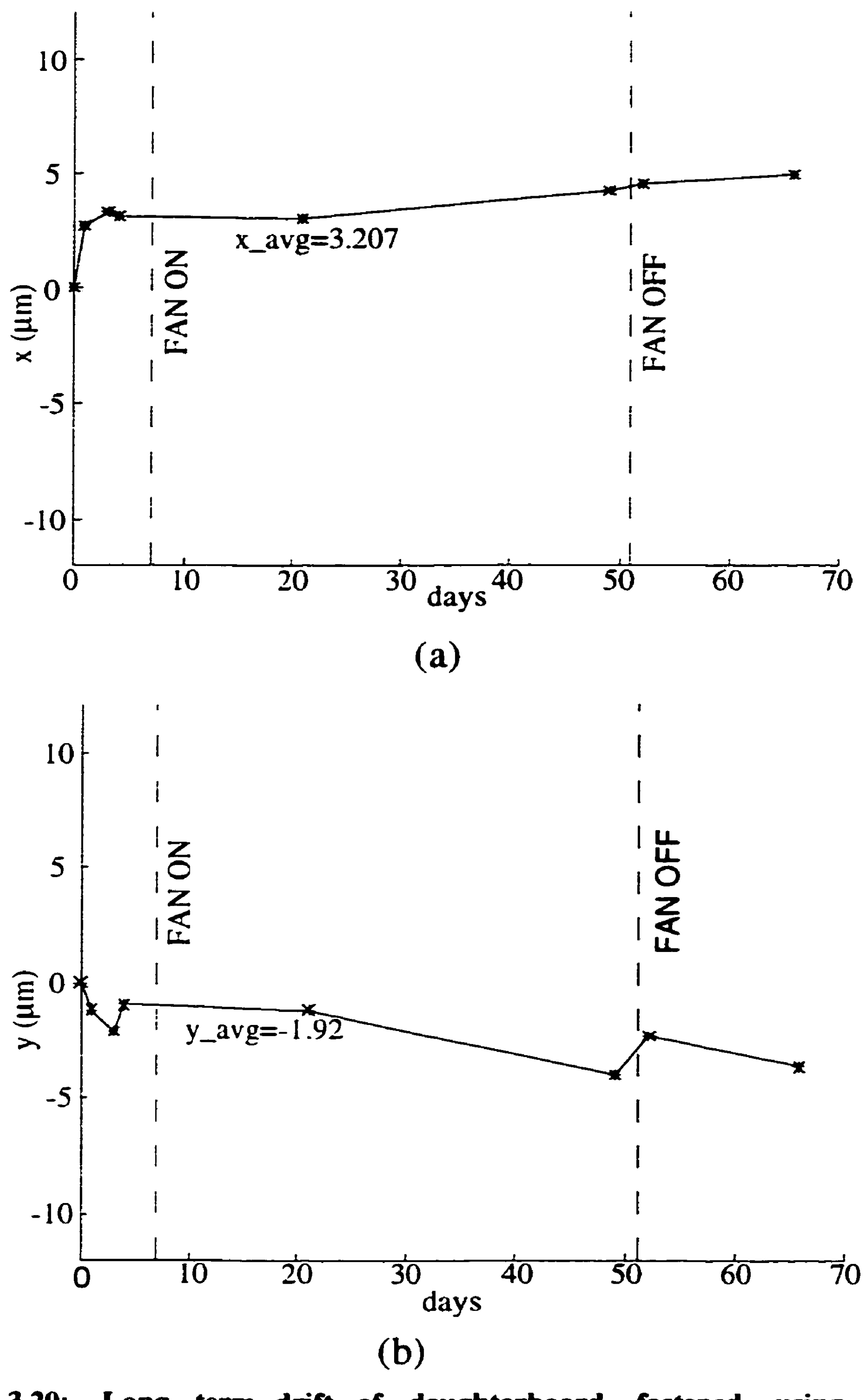

Figure 3.20: Long term drift of daughterboard fastened using second (gluing) technique

3.7.4 Real-time Measurements of Mechanical Vibrations of Glued Daughterboard

While the glued daughterboard exposed to the large air currents generated by the fan did not move to within measurement error over several months, it did exhibit a very interesting behaviour when its real-time displacements were analyzed in the spectral domain. In order to analyze the spectral behaviour of the board's misalignment, Fast Fourier Transforms (FFTs) of the board's misalignment were performed under LabView™.

Figure 3.21a shows the result of the control experiment in which the ETRI 125DH fan was turned off. Besides small spikes at low frequencies (<100 Hz), probably due to electrical interference, the spectrum was generally quiet.

For the measurements shown in Figure 3.21b, however, the fan was turned on to full power as in previous experiments. In this case, spikes at 410 Hz and at subsequent integer multiples of this fundamental frequency can be discerned for Δx and are readily visible for Δy. The conclusion to be drawn from these observations is that the daughterboard mounting system has a mechanical resonance frequency of 410 Hz. This is very encouraging since it is almost an order of magnitude away from most cooling fans' 3000 RPM (50 Hz) rotational frequency: as a result, cooling fans should not cause this system to become mechanically unstable. More sophisticated modeling and measurement techniques obviously would yield more insight: this is a promising route for further research.

Even though the low-pass filter at the input signal source had a half power cutoff frequency of 402 Hz, the very slow (1st order) roll-off allowed signals in the 800 Hz range to be picked up, albeit with an attenuation of over 50%.

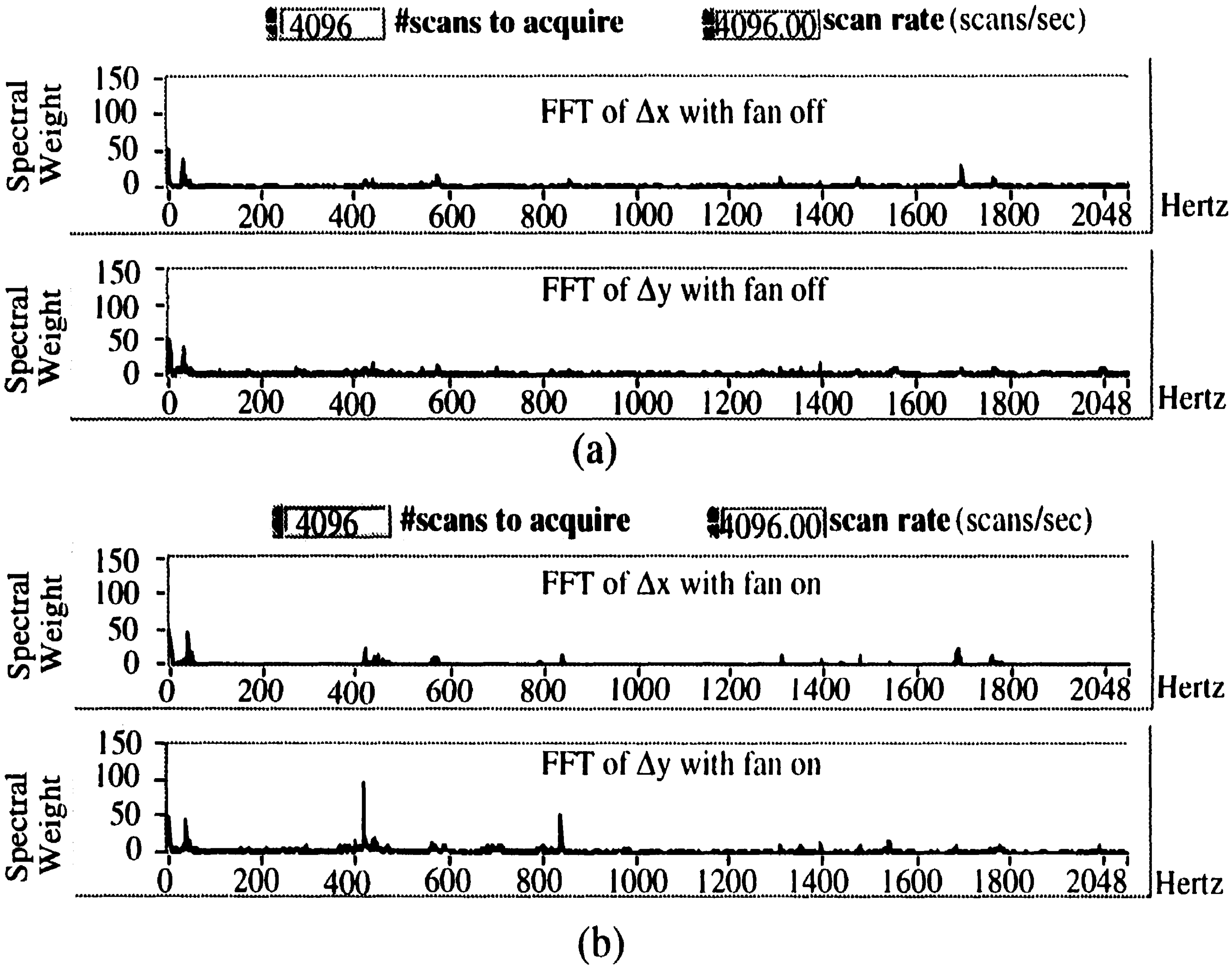

Figure 3.21: Spectral behaviour of optomechanical misalignment a) with fan off b) with fan on

The vibrations from the fan could have been coupled to the daughterboard in at least two main ways: 1) since the fan was bolted to the chassis and since the daughterboard was glued to optomechanics which were also ultimately bolted to the chassis, the fan's mechanical vibrations could have been coupled mechanically from the fan to the daughterboard via the chassis and optomechanics, or 2) since the powerful air flow was blowing straight onto the daughterboard and the electrical connector, the air flow itself could have caused the board to vibrate.

Experiments were conducted to determine which of these two factors was most responsible for the daughterboard vibration. In one experiment, the fan was placed in the same position and orientation as before, but was attached to the table instead of to the chassis. As a result, the same airflow passed over the board but there was no direct mechanical coupling. In the other experiment, the fan was bolted to the chassis as before, but the airflow to the daughterboard was blocked by a stiff piece of cardboard.

Results were inconclusive: both experiments yielded a spectrum similar to the one in Figure 3.21b. More research must be performed in this area and sources such as building vibrations and so on must be considered.

3.7.5 Daughterboard Positioning in Other Degrees of Freedom

The above measurements on daughterboard positioning only address two degrees of freedom: x and y. Of the 4 remaining degrees of freedom, 3 were considered critical: the error in the two tilts (θ_x and θ_y) and the error in z_3 (defined in Figure 3.4). Given the small size of the array (8x4), a quick visual check before gluing was sufficient to ensure that daughterboard rotation (θ_z) was satisfactory.

With a traveling microscope arrangement, measuring z_3 was accomplished by measuring the distance from the edge of the daughterboard to the optomechanics and then subtracting the known thickness of the die and its glue. Measuring the tilt was accomplished by measuring z_3 at several positions along the daughterboard edge and using simple geometrical relationships to subtract from these readings a known tilt of the die with respect to the daughterboard. The results are summarized in Table I (p. 60).

3.7.6 Discussion of Results

The daughterboard mounting technique was labour intensive and, from Table I, it can be seen that most objectives were probably not met. This is partly due to the extremely tight constraints that were imposed (the target values are for 1% loss) and partly due to the novelty of the mounting technique which is quite different from traditional slug-based techniques, given the system constraints. While the system can still function with the results obtained, a certain number of conclusions can nonetheless be drawn from this work. 1) the interface between optoelectronics and optics is by far the most critical in any system of this nature, 2) a better way of aligning lenslet array #2 to the optoelectronics, either by using mechanical means or by prealigning these components to each other before insertion, is necessary , and 3) once assembled, a system like this one is very stable.

3.8 Conclusion

This chapter presented the first truly 3D, vertically-oriented, rack-mounted, multi-stage optomechanical system implementing a free-space optical interconnect. Additionally, the approach chosen can scale to much larger systems.

This chapter outlined some of the design tradeoffs and issues to be faced when designing optomechanics for a free-space digital computing system. It was shown that optical constraints, machining tolerances, optoelectronic technology, electronic packaging, material parameters, thermal effects, and component availability all have a major impact on the optomechanics. Moreover, diagnostic techniques were developed and shown to yield considerable information on the status of the optomechanics. Finally, further avenues of research, such as a better understanding of vibration mechanisms, were proposed.

3.9 References

1 T. H. Szymanski and H. S. Hinton, "Reconfigurable intelligent optical backplane for parallel computing and communications," Applied Optics, 36, pp. 1253-1268 (1996).

2 D. R. Rolston, D. V. Plant, T. H. Szymanski, H. S. Hinton, W. S. Hsiao, M. H. Ayliffe, D. kabal, M. B. Venditti, P. Desai, A. V. Krishnamoorthy, K. W. Goosen, J. A. Walker, B. Tseng, S. P. Hui, J. E. Cunningham, and W. Y. Jan, "A Hybrid-SEED smart pixel array for a four-stage intelligent optical backplane demonstrator," *IEEE Journal of Selected Topics in Quantum Electronics*, 2, pp. 97-105 (1996).

3 IEEE Standard 1014-1987 for a Versatile Backplane Bus: VMEbus. IEEE Ref # [1-55937-674-0] [SH11544-NYF] (1987).

4 D. V. Plant, B. Robertson, H. S. Hinton, M. H. Ayliffe, G. C. Boisset, W. Hsiao, D. Kabal, N. H. Kim, Y. S. Liu, M. R. Otazo, D. Pavlasek, A. Z. Shang, J. Simmons, K. Song, D. A. Thompson, and W. M. Robertson, "A 4x4 VCSEL/MSM optical backplane demonstrator system," *Applied Optics*, 35, pp. 6365-6368 (1996).

5 S. Nimmagadda, J. Dillon, and A. Moncayo," A 533 Mbits/sec/wire modular bus with single or double parallel termination," 1996 Electronic Components and Technology Conference, pp. 974-983, IEEE ref # 0-7803-3286-5/96.

6 Lens 322286 from the catalog of Spindler & Hoyer Corp., Göttingen, Germany.

7 H.S. Hinton, "An Introduction to Photonic Switching Fabrics," Plenum Press, New York, 1993.

8 F. B. McCormick, F. A. P. Tooley, T. J. Cloonan, J. M. Sasian, H. S. Hinton, K. O Mersereau, and A. Y. Feldblum, "Optical interconnections using microlens arrays," *Optical and Quantum Electronics*, vol. 24, pp. 465-477 (1992).

9 J. L. Brubaker, F. B. McCormick, F. A. P. Tooley, J. M. Sasian, T. J. Cloonan, A. L. Lentine, S. J. Hinterlong, M. J. Herron, "Optomechanics of a free-space switch: the components," SPIE Volume 1553 (1991), pp. 88-96.

10 Metals handbook, 1948 Edition, American Society for Metals, Materials Park, Ohio, pp. 237-243.

11 P. R. Yoder, "Parametric investigation of mounting-induced axial contact stresses in individual lens elements," Spie Vol. 1998, Optomechanical Design, pp. 8-19, (1993).

12 R. E. Green, C. J. McCauley, E. Oberg, F. D. Jones, H. L. Horton, and H. H. Ryffel. Machinery's Handbook, Industrial press, Inc., New York, 25th Ed. 1996.

13 R. A. Flinn and P. K. Trojan, Engineering materials and their Applications, Houghton Mifflin Company, Boston, 1981.

14 P. R. Yoder, Optomechanical Systems Design, Marcel Dekker Inc., New York, 1993.

15 Properties of Polymer's Engineering Thermoplastics, Polymer Corp. Reading, PA., Publication BR/5000-1 5/94.

16 C. P. MacDermott, Selecting Thermoplastics for Engineering Applications, Marcel Dekker, Inc., New York, 1984.

17 Data sheet 242769-001, Intel corp., Santa Clara, Calif., 1995.

18 F. B. McCormick, T. J. Cloonan, A. L. lentine, J. M. Sasian, R. L. Morrison, M. G. Beckman, S. L. Walker, M. J. Wojcik, S. J. Hinterlong, R. J. Crisci, R. A. Novotny, and H. S. Hinton, "Five-stage free-space optical switching network with field-effect transistor self-electro-optic-effect-device smart-pixel arrays," *Applied Optics*, 33, pp. 1601-1618 (1994).

19 See for example Nordex Inc., Danbury, Connecticut., Design Guide 101 Catalog, p. 15A, 1991.

20 Parmley, Robert. O. Standard Handbook of Fastening and Joining, McGraw-Hill, p. 1-24, 1989.

21 Hugh O'Neill, Hardness measurement of metals and alloys, Chapman & Hall, 1967, ch. 2.

22 S. Wakelin, "Design and construction of a free-space digital optical information processor," Ph.D. Dissertation, Heriot-Watt University, 1991.

23 R. Iyer, Y. S. Liu, G. C. Boisset, D. J. Goodwill, M. H. Ayliffe, B. Robertson, W. M. Robertson, D. Kabal, F. Lacroix, and D. V. Plant, "Design, Implementation and Characterization of an Optical Power Supply Spot Array Generator for a Four Stage Free-Space Optical Backplane," *Applied Optics*,36, pp. 9230-9242.

24 D. N. Kabal, G. Boisset, D. R. Rolston, and D. V. Plant, "Packaging of two-dimensional smart pixel arrays," IEEE/LEOS Summer Topical Meeting on Smart Pixels, paper ThA5, August 1996.

25 Quadrant Detector: Spot 4D M1 from UDT Sensors inc. (formerly United Detector Technologies), Hawthorne, Calif.

Chapter 4: *In-situ* Alignment Diagnostics

4.1 Introduction

The assembly of the optical backplane demonstrator brought up many problems associated with the assembly of and alignment diagnostic systems for FSOIs. A key problem with most current diagnostic systems, such as the vibration monitoring described in the previous chapter, is their intrusive nature. For example, the backplane could not function normally with the vibration diagnostic system in place since the daughterboard with the smart pixel had to be taken out and a daughterboard with a quadrant detector had to be mounted in its stead; additionally, some microoptic components had to be removed to simplify measurement, further perturbing the system. Another intrusive alignment diagnostic system used in the backplane consisted of an imaging system with a camera and pellicle attached which was used to observe the system at various planes of interest: this affected power throughput. Moreover, intrusive imaging systems such as this one and others of a similar nature [1,2] are often bulky and the alignment information produced must be interpreted by an experienced observer to be of use. As well, viewports must be included for them, often increasing system size. In short, current techniques for alignment diagnostic are intrusive, labour-intensive, and very expensive for large-scale fabrication of multi-stage interconnect systems. The problem is greatest in modulator-based systems which have the added requirement of aligning an array of optical power supply (OPS) beams, as shown in Figure 4.1a.

Future diagnostic techniques will have to eliminate imaging systems and human intervention as much as possible, and the most elegant way to do so is to produce electrical diagnostic signals that can be interpreted by automated test equipment. One can envision an eventual photonic extension to boundary scan standards such as IEEE 1149 [3] in which dedicated alignment circuitry would respond to test vectors by communicating the extent of system misalignment. This information would be used to answer either basic questions – such as whether or not the system works – or more quantitative questions – such as whether or not the misalignment is small enough to be corrected, or what is the maximum clock rate the system can run at (which is a function of the misalignment, among many other factors).

The key therefore is to generate – in a non-intrusive manner – analog electrical signals proportional to misalignment. In this chapter, a novel concept of *in-situ* lateral (xy) alignment diagnostic is proposed and then demonstrated in an optical backplane interconnect. The concept can be summarized as follows [4]. As seen in Figure 4.1b, the OPS generated additional higher order beams, called alignment beams, which ran parallel to the main signal beams. The alignment beams were used to monitor the alignment status of the system at various planes in the system. More specifically, at each stage of the system, the OPS [5] generated a pattern of beams which included a 4x8 array of signal beams and four alignment beams, as shown in Figure 4.2. Two of these alignment beams, named 1x and 1y, were used to monitor the lateral alignment of the beam array onto the modulators of stage #1; the other two alignment beams, named 2x and 2y, were used to monitor the alignment of the modulated beams onto the receivers at stage # 2. The alignment beams were relayed using dedicated microoptics and impinged on silicon alignment detectors located on the periphery of the smart pixel chips at each stage.

No previous free-space optical interconnect has made use of deliberately generated higher order beams and associated optics for alignment diagnostic purposes, although analogous techniques have been used in other contexts such as in particle accelerators [6]. Some VCSEL-based systems have successfully used discrete alignment beams in feedback systems[7]. Other techniques for determining alignment error in free-space optical systems involve deducing the alignment status by using several staggered detectors per channel and custom circuitry [8]. Innovative ways of using stroboscopic illumination to gather information about pulse shapes even at high modulation rates have been presented and are very promising, but they still rely on intrusive techniques and as such disturb the system being measured[9].

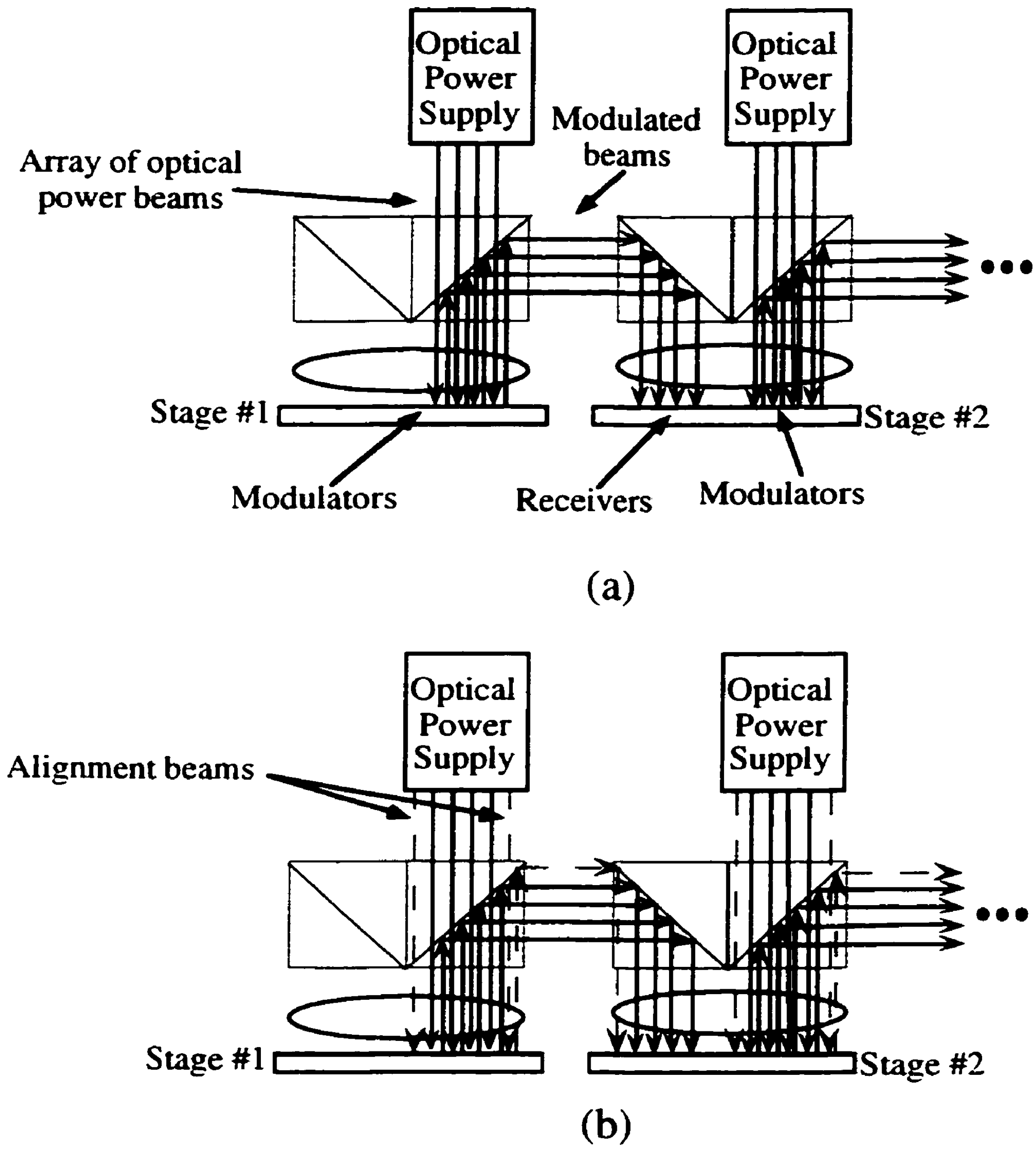

Figure 4.1: a) Typical modulator-based interconnect in which an array of optical power beams is modulated by stage #1 and imaged over to stage #2 b) Alignment monitoring beams generated by Optical Power Supply run parallel to signal beams

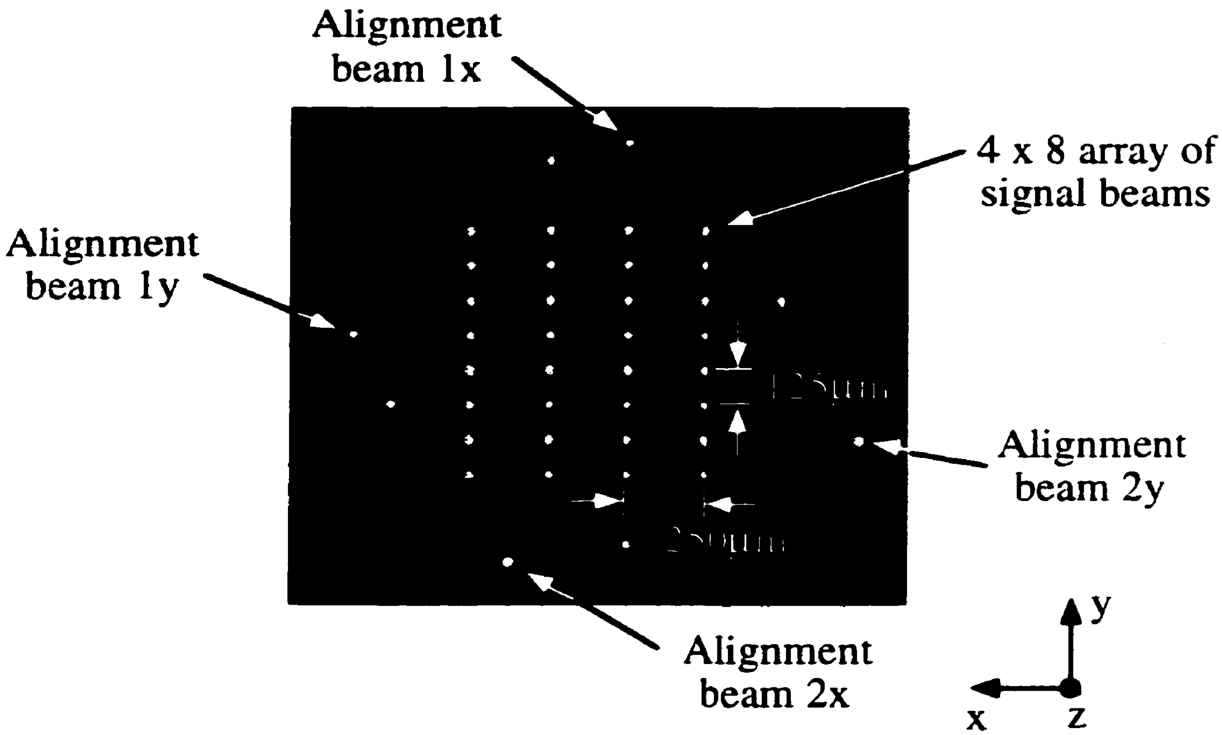

Figure 4.2: Beam pattern generated at the output of the Optical Power Supply, which is at the input power plane of each stage

The organization of this chapter is as follows. Section 4.2 describes how beam width and detector layout are factors which affect measurement range: the desired range is chosen and these parameters are then chosen as a function of the measurement range required for system assembly. Section 4.3 presents the design of the alignment diagnostic system which meets the measurement requirements. Section 4.4 outlines physical characteristics of key components, such as the chip and the microoptics. Section 4.5 gives system characterization and experimental results, and section 4.6 provides a discussion of the results, section 4.7 overviews the costs associated with the diagnostic system and a conclusion follows.

4.2 Alignment detectors and measurement range

Measurement range is an important attribute of a diagnostic system. This section starts by demonstrating that the type and geometry of the alignment detector, along with the profile of the alignment beam, are important design parameters which determine the range and accuracy of a measurement system. The desired measurement range for system assembly is chosen and beam widths appropriate for this desired measurement range are obtained.

4.2.1 Choice of Alignment Detectors

One way to measure the alignment of an incoming array of beams is to have one or many of the alignment beams impinge on alignment detectors. Several techniques for measuring the position of an incoming beam have been demonstrated previously. These include MOS Position Sensing Detectors [10] and quadrant detectors, which are generally four independent photodiodes arranged in a square or diamond and which are used to measure the lateral (x and y) alignment error of an incident beam in many applications such as compact disk players and active alignment demonstrations[11, 12]. With additional optics and processing, a quadrant detector can measure defocus (Δz error) as well [12].

If several alignment beams are available and if they cannot be misaligned independently of each other, then another technique for measuring the position of an incoming array in x and y is to use bi-cell detectors (BCDs). A bi-cell detector, which consists of two detectors beside each other, as shown in Figure 4.3, can be used to measure beam position in one direction only (x or y). As shown in Figure 4.3, two sets of BCDs can be used to measure the xy misalignment of an incoming array of beams: one BCD with an alignment beam to measure misalignment in the x direction, and another BCD with another alignment beam to measure y.

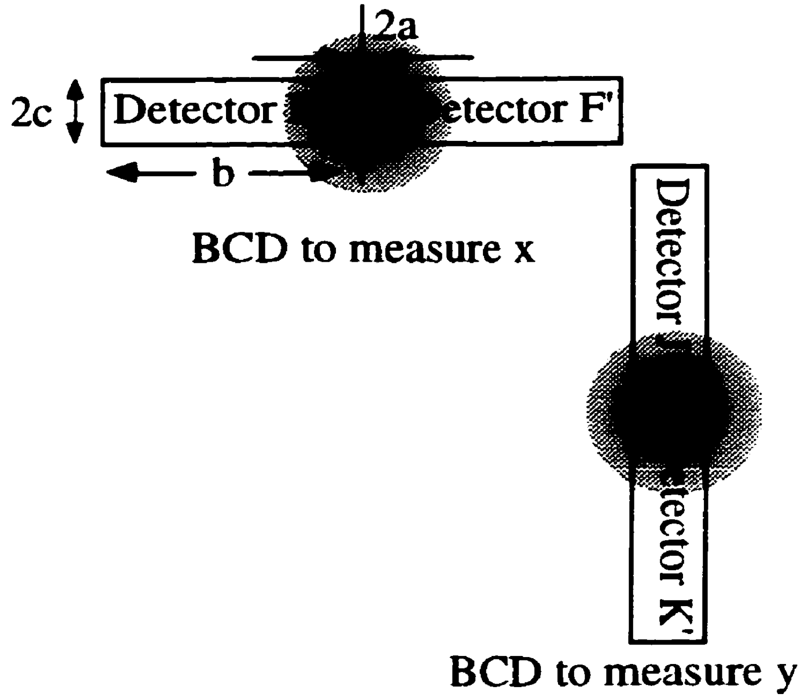

Figure 4.3: Bi-cell detectors (BCDs) with two incident beams for lateral (x-y)alignment measurement

4.2.2 Desired Measurement Range

An important conclusion drawn from the work of system assembly was that the x-y alignment of the daughterboard with respect to the last lenslet array (LA_2) was the most critical step. The system still could receive and transmit if the xy misalignment was of the order of a few (<5) μm, but beyond 5 μm of misalignment, little data could be modulated or received. As a result of this situation, there was no way of knowing the extent of misalignment beyond 5 μm without resorting to a difficult imaging system to look through the microoptics onto the device windows. Obviously if the misalignment was very large, then a coarse imaging system could help with coarse alignment. For the current system, a coarse imaging system could yield visual alignment information to within ~25 μm at best. Therefore, the *in-situ* measurement system could be useful if it could help to bridge the gap between 'coarse' alignment and the last few microns. This gap had to be the minimum measurement range of the alignment diagnostic system.

4.2.3 Effect of beam width on measurement range

Optical interconnects will not work if misalignment between smart pixel devices and microoptics exceeds a certain value. For the current backplane, as stated above, the system could not work if the misalignment exceeded 5μm. Moreover, without a sophisticated imaging system for peering through lenslets, the magnitude of the misalignment could not be determined once this value was exceeded since the system could not work whether the misalignment was 5 μm or (say) 15 μm. (Obviously if the misalignment was very large, then a coarse imaging system could help with coarse alignment). Therefore, a measurement system is useful if it can help to bridge the gap between 'coarse' alignment and the last few microns. This gap should be the nominal measurement range of the alignment diagnostic system.As this section shows, the useful measurement range is a function of the width of the spot created by the incident beam.

A few definitions are necessary for this discussion: if an alignment beam with Gaussian irradiance profile is incident on a bi-cell detector composed of detectors E' and F', then P_E and P_F are defined to be the total power incident on detectors E' and F' respectively. If the beam is off-centre (i.e. misaligned) relative to the bi-cell detector, then one detector will have more power incident than the other one. The error signal, Δx_e, is then:

$$\Delta x_e = k \frac{P_F - P_E}{P_F + P_E} \tag{1}$$

where k is a scaling constant with units in μm. The error signal is thus k times the normalized differential power. The normalization, namely dividing by the total power hitting the alignment detectors, is performed in order to minimize the effect of fluctuations in the laser power on the measured values.

For a given wavelength and detector, the width of the spot on the bi-cell determines the measurement resolution and range. If a beam with a Gaussian irradiance pattern

$$I = I_o \exp\left(-2\frac{r^2}{w^2}\right) \tag{2}$$

where I_o is the peak irradiance, $r^2 = x^2 + y^2$ and w is the $1/e^2$ (86.5% encircled power) radius, is incident on the bi-cell detector composed of E' and F', then P_F can be calculated as follows for a given actual misalignment Δx:

$$P_E = I_o \frac{\pi}{4} w^2 \left\{ \operatorname{erf}\left[(b-\Delta x)\frac{\sqrt{2}}{w}\right] - \operatorname{erf}\left[(a-\Delta x)\frac{\sqrt{2}}{w}\right]\right\}\left\{\operatorname{erf}\left[(c-\Delta x)\frac{\sqrt{2}}{w}\right]\right\} \tag{3}$$

A similar expression can be derived for P_F.

The plot of normalized differential power $(P_F-P_E)/(P_F+P_E)$ vs the actual misalignment, Δx, is as shown in Figure 4.4 for w =1μm, a=0.1 μm, b=20 μm, c=10μm. The plot indicates that when Δx >1.5 μm, $(P_F-P_E)/(P_F+P_E) \approx 1$. Conversely, when Δx<1.5 μm, $(P_F-P_E)/(P_F+P_E) \approx -1$.

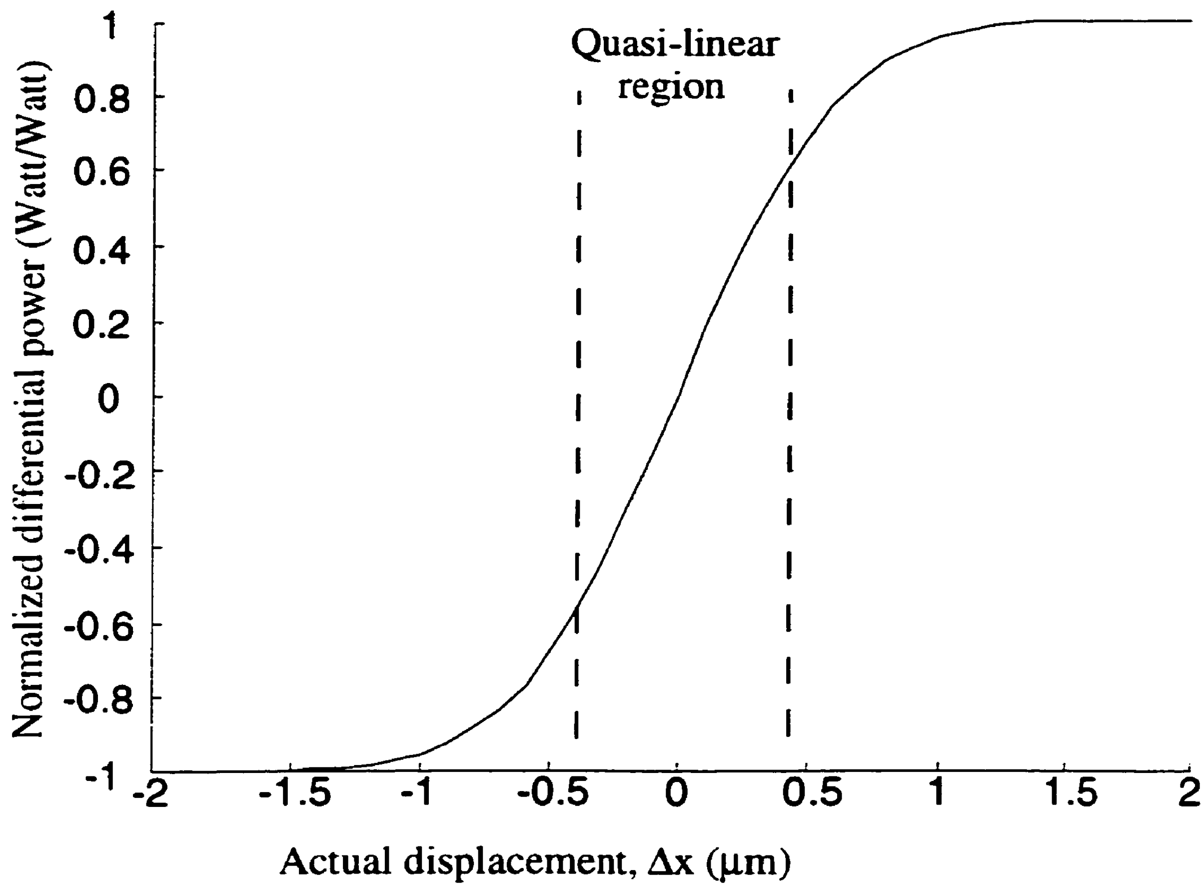

Figure 4.4: Theoretical plot of normalized error signal vs actual displacement for a beam with a 1μm radius (86.5% encircled power) incident on a bi-cell detector. In the quasi-linear region, the curve is linear to within 10%.

As can be seen from the plot, there is a quasi-linear relationship between the normalized differential power and the actual misalignment over the region $-0.4w<\Delta x<0.4w$; in this region, the curve is never more than 10% off the value of the best linear fit. This relationship, which indicates that the maximum linear range of the measurement system is $\pm$ $0.4w$ and which holds for most detector dimensions of interest, is exploited in the optical and electronic design of the alignment detection systems described in this chapter.

Furthermore, the value of k in Equation (1) can be chosen to yield a one-to-one relationship between the error signal Δx_e and the actual displacement, Δx, over the linear range. For example, in the situation plotted in Figure 4.4, $(P_F-P_E)/(P_F+P_E) = 0.4$ when $\Delta x = 0.6\mu m$. Therefore, choosing a value of k=1.5 μm would yield the desired one-to-one relationship between Δx_e and Δx.. Additionally, as can be seen from the plot, a misalignment of up to ~0.8w will still yield an appreciable error signal which increases monotonically with misalignment, although the error signal will not be linearly related to the actual misalignment beyond 0.4w.

Given the ~25 μm range of a coarse imaging system, the width of the beams 1x and 1y incident on their respective BCDs on the stage # 1 die was chosen to be $w_{1x}=w_{1y}=30$ μm. As calculated above, this allowed for a linear measurement range of ±12 μm and a non-linear measurement range of approximately ±25 μm.

The same reasoning also applied to the 2x and 2y beams. However, in order to verify the concept of linearity over a different measurement range, it was decided to increase the measurement range provided by 2x and 2y. This also allowed for an even simpler imaging system for the alignment of that stage. As a result, the width of the beams 2x and 2y incident on their respective BCDs on the stage # 2 die was chosen to be $w_{2x}=w_{2y}=50$ μm.

4.3 Optical and Detector Design

The main constraints in the design of the alignment beam system were: 1) the beams impinging on the alignment detectors on the CMOS die had to be wide enough to yield useful alignment information; 2) the path of the alignment beams had to be as close as possible to that of the signal beams[7]; 3) the additional components for the alignment beams were not to hinder the proper operation of the main signal beam relays; and 4) all space constraints imposed by the CMOS die area as well as existing optomechanics and optics had to be respected. BCDs were chosen for alignment measurement. As a result, the stage #1 OPS had to generate four alignment beams: 1x, 1y, 2x, and 2y.

4.3.1 Overview of alignment beam optical relay

The optical path followed by beams 1x and 1y was as shown in Figure 4.5. As with all beams emerging from the OPS, beam 1x was generated at the input power plane a distance z_1 in front of LA_1, as shown in Figure 4.5. Beam 1x was then relayed by lenslets L_{1ax} and L_{1bx} onto its alignment detector on the Hybrid-SEED chip. Similarly, beam 1y was relayed by lenslets L_{1ay} and L_{1by} onto its alignment detector on the Hybrid-SEED chip (not shown in Figure 4.5).

The optical path followed by beams 2x and 2y was as follows. As shown in Figure 4.5, beam 2x was relayed by L_{2ax} onto mirror M_{2ax} and, after reflection and polarization change, was imaged by the bulk lenses onto mirror M_{2bx} in the next stage. After reflection off M_{2bx} and another polarization change, beam 2x was imaged by L_{2bx} onto the smart pixel die. A similar path using L_{2ay}, M_{2ay}, M_{2by} and L_{2by} was followed by the second alignment beam 2y (not shown in Figure 4.5).

4.3.2 Optical Relay for Alignment Beams 1x and 1y

This section and the next describe the design of the optical relays which generated the alignment beams of appropriate width (determined above) at the appropriate alignment detectors. Key parameters of the design for the signal beam relay were summarized in the previous chapter. The optical design for the alignment beams had to respect all spacing and optomechanical constraints imposed by the signal beam relay optical design.

For the 1x and 1y beams, it was necessary to design an optical relay which would image the alignment beams from the input power plane onto their respective alignment detectors on the die. Furthermore, since the OPS generated all beams with a $1/e^2$ radius of w_p=6.47 μm at the power array plane, the relay had to have a magnification of

w_{1x}/w_p=30/6.47 = 4.64. This section will describe the design of the relay for the 1x beam: the 1y beam relay is analogous to the 1x relay.

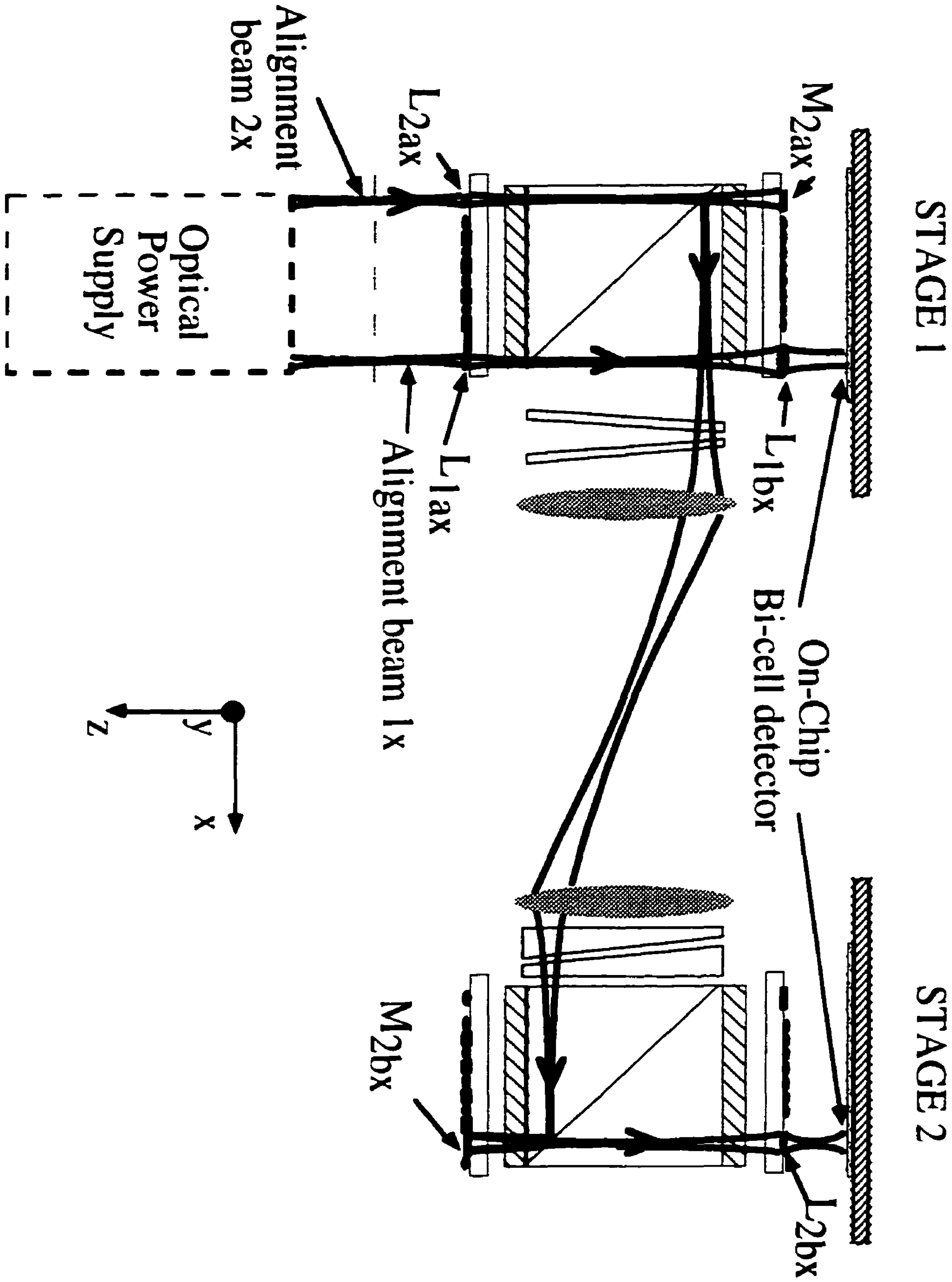

Figure 4.5: Path taken by alignment beams 1x and 2x.

Referring to Figure 4.5. the relay for the 1x beam consisted of two lenses which had focal lengths of L_{1ax} and L_{1bx} respectively. Standard Gaussian beam propagation models were used in the analysis [13].

Because of the design constraints, the 1x alignment beam had a waist at the input power plane located at a distance z_1=922 μm in front of the L_{1ax} lens. To simplify calculations, the focal length of L_{1ax} was chosen to be 768 μm since this was also the focal length for all signal lenslets. This yielded z_1=768+z_R, which is the criterion for the maximum lens-to-waist distance: another waist was located halfway between L_{1ax} and L_{1bx}, at a distance $z_2/2$ =2.7 mm behind L_{1ax}. At this halfway point, the beam radius can be calculated to be w_t=22.8 μm. Similar calculations indicated that the focal length of L_{1bx} had to be 1.87 mm in order to generate w_{1x}= 30μm. The nominal specifications of all components for the transmission of the 1x and 1y beams are given in Table 1 and Table 2 respectively.

lens	focal length (μm)@ λ=850 nm	position of center (μm)	size (μm)	f/#
L_{1ax}	768	(-62.5,750)	∅123	6.24
L_{1bx}	1870	(-62.5,750)	∅123	15.2

Table 1: components for transmission of alignment beam 1x. Note: ∅ stands for diameter

lens	focal length (μm)@ λ=850 nm	position of center (μm)	size (μm)	f/#
L_{1ay}	768	(812.5,62.5)	∅123	6.24
L_{1by}	1870	(812.5,62.5)	∅123	15.2

Table 2: components for transmission of alignment beam 1y

4.3.3 Optical Relay for Alignment Beams 2x and 2y

This section will describe the optical relay for the 2x and 2y alignment beams. As in the previous section, only the design of the relay for the 2x beam will be described: the 2y beam relay is analogous to the 2x relay.

4.3.3.1 Effect of on-die space constraints on optical relay

As stated above, the 2x beam had to follow as closely as possible the path of the signal beams which left the OPS, were reflected by the modulating mirror/quantum well stacks of the first stage chip, and were then relayed to the second stage chip.

In order to closely follow the path of the signal beams, therefore, the 2x alignment beam should ideally impinge on a mirror beside – and at the same height as – the modulators on the first stage chip. This would cause any tilt or misalignment of this chip to equally affect the propagation of the signal and alignment beams.

Unfortunately, on-die space and grid constraints similar to the ones dictating the location of the bi-cell detectors were present in this case, leaving no room for simple mirrors for the 2x beam on the first stage chip. As a result of these space constraints, the mirror for the 2x beam was put on the LA_2 substrate, which is as close to the first stage chip as possible. This mirror is labeled M_{2ax} in Figure 4.5.

While this arrangement is not optimal since it does not measure the effect of any daughterboard misalignment in the overall alignment measurement, it still yields valuable information on the alignment status of all other components in the optical relay such as the PBS, the alignment prisms, and other lenses.

4.3.3.2 Design of optical relay

The optical path length for alignment beam 2x from lens L_{2ax} to lens L_{2bx} was 140 mm + $3z_2$, where the 140 mm component was the optical length of the conventional lens relay and the $3z_2$ component was due to the microchannel relay.

Using Gaussian beam propagation equations, an optimization was performed with the objective of minimizing the beam width at mirror M_{2bx} and lens L_{2bx}, where there was the least space available. This led to a beam radius (86.5 % encircled power) of 75 μm at M_{2bx}. To allow for any misalignment error, the mirror size for M_{2bx} was chosen to be at least 300μm x 300 μm. Furthermore, the beam had a radius of 116 μm at L_{2bx}. Given the calculations outlined above, the nominal specifications of all components for the transmission of the 2x and 2y beams are given in Table 3 and Table 4.

lens or mirror	focal length (μm)@ λ=850 nm	position of center (μm)	size (μm)	f/#
L_{2ax}	872	(312.5,-750)	Ø123	7.08
M_{2ax}	-	(312.5,-750)	150 x 150	-
M_{2bx}	-	(-312.5,750)	300 x 300	-
L_{2bx}	1405	(-312.5,750)	Ø354	3.98

Table 3: components for transmission of alignment beam 2x

lens or mirror	focal length (μm)@ λ=850 nm	position of center (μm)	size (μm)	f/#
L_{2ay}	872	(-812.5,-312.5)	Ø123	7.08
M_{2ay}	-	(-812.5,-312.5)	150x150	-
M_{2by}	-	(812.5,312.5)	300 x 300	-
L_{2by}	1405	(812.5,312.5)	Ø354	3.98

Table 4: components for transmission of alignment beam 2y

4.3.4 Alignment Detector Configuration

Bond-pads are necessary to get electrical signals off the chip. Since there were to be four BCDs per chip – one for each of beams 1x, 1y, 2x and 2y – and since each BCD needed two lines (one for each detector of the BCD), the ideal number of bond-pads per chip for the alignment photocurrents would have been eight (plus an optional ground), as shown in Figure 4.6a.

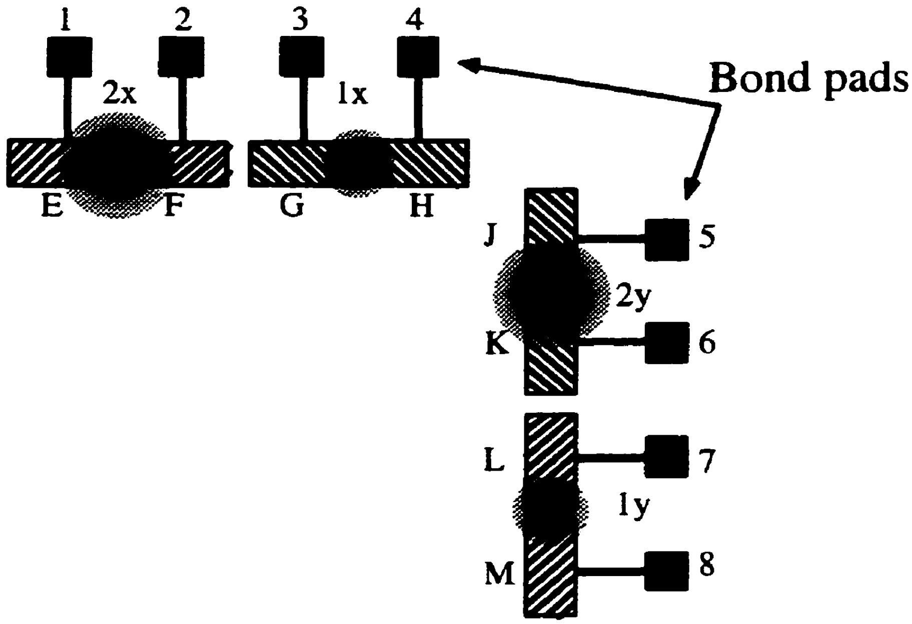

(a)

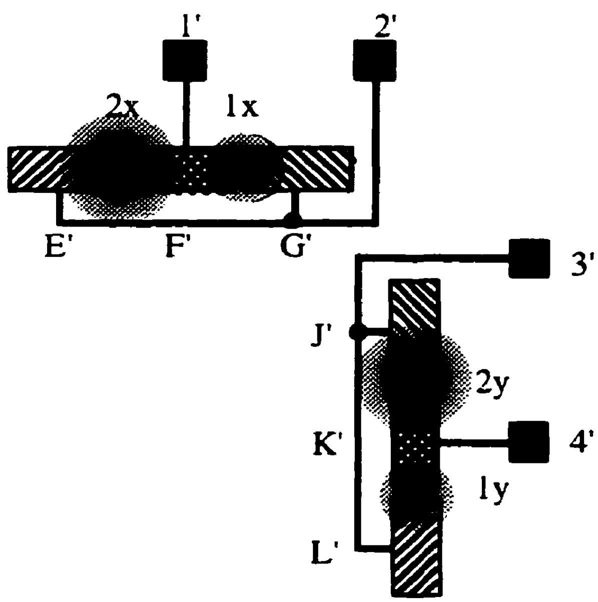

(b)

Figure 4.6 a) Ideal bi-cell detector layout if no electrical pin-out limitations exist b) Sharing of alignment detectors imposed by pin-out limitations. In this case, only (1x and 1y) or (2x and 2y) can be on at the same time or an incorrect reading will be taken.

However, in order to save on pin-outs, BCDs can be combined by overlapping a detector common to both of them. As can be seen from Figure 4.6b, two BCDs can be built using just three detectors provided only one BCD is used at a time. This can be described as follows.

In the straightforward case of non-overlapping BCDs, the situation is as shown in Figure 4.6a. If the chip in Figure 4.6a is at stage # 1, then beam 1x is incident on detectors E and F which combine to give information on misalignment in the x direction. Similarly, if the chip in Figure 4.6a is at stage #2, then beam 2x (from the previous stage) is incident on G and H.

On the other hand if the BCDs are overlapped to produce a common detector, then the situation is as shown in Figure 4.6b: beam 1x is incident on detectors E' and F' whereas beam 2x (from a previous stage) is incident on detectors F' and G'. For this to work, only one OPS at a time can be on when alignment measurements are being performed: if not, beams 1x and 2x both impinge on F', leading to a false measurement. This leads to an additional saving in pin-outs: since only one of 1x or 2x is incident at any given time when alignment measurements are performed, detectors E' and G' can be tied together, leading to further savings in pin-outs.

A similar reasoning applies to the detectors for the 1y and 2y beams and associated detectors.

4.3.5 Off-chip processing of alignment detector signals

Each of the four alignment detector lines, namely 1',2',3',and 4', as well a common line 5' (not shown), were tied to a 1MΩ resistor which converted the photocurrent into a voltage. Each voltage was then buffered and fed via an A/D board into a computer for processing and display. The net result of all these operations was that a voltage signal proportional to the power incident on each alignment detector was generated and read by a computer which performed all necessary calculations. The noise across the resistor was measured to be less than 0.3% of the maximum voltage swing.

4.4 Components

4.4.1 Microoptics

The lenslet arrays are shown in Figure 4.7. All diffractive optical components were designed for an operating wavelength of λ=850 nm. All diffractive components had eight phase levels if the component had an f/# >6; for those components with f/# < 6, the component had eight phase levels up to the fabrication limit, and then 4 levels beyond. For example, lens L_{2bx} in Table 3 was composed of eight phase levels up to a diameter of 234 µm and then had only four phase levels up to the diameter of 354 µm. All signal lenslets on LA_1 and LA_2 had a focal length of f_μ=768 µm.

On LA_1, the signal lenslets were 123 µm x 125 µm, and they were laid out in 1 x 8 strips that were 123µm wide x 1 mm high. Mirror strips 123µm wide x 1 mm were alternated with the lenslet strips. On LA_2, the signal lenslets were 125µm x 125 µm and were laid out in a 8x8 square.

All mirrors were made of gold deposited on silver on the substrate. The substrates were made of fused silica 500µm thick and were anti-reflection coated for 850 nm light on the side with no diffractive components.

The fan-out element within the Optical Power Supply was an 8-level non-separable Multiple Phase Grating.

4.4.2 Optoelectronics and packaging

The silicon chip was a 0.8µm, three-metal layer, n-well CMOS chip. The chip was post-processed by Lucent Bell Labs with an array of multiple quantum well (MQW) modulators and photodetectors using solder-bump bond technology [14]. The chip is shown in Figure 4.8 with the alignment detectors highlighted.

The silicon alignment detectors were p/n+ diodes on a p substrate where p contacts were made with a p diffusion layer in a ring as shown in Figure 4.9 to isolate the three different diodes. Three separate n+ diffusions were used. During operation, the alignment detectors were reverse-biased to 5V.

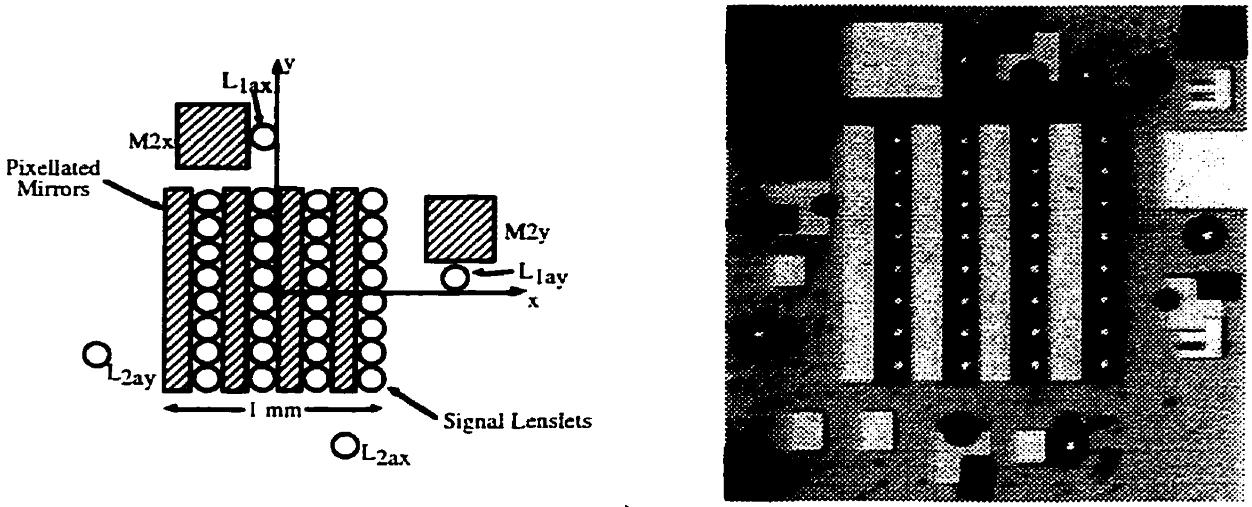

a)

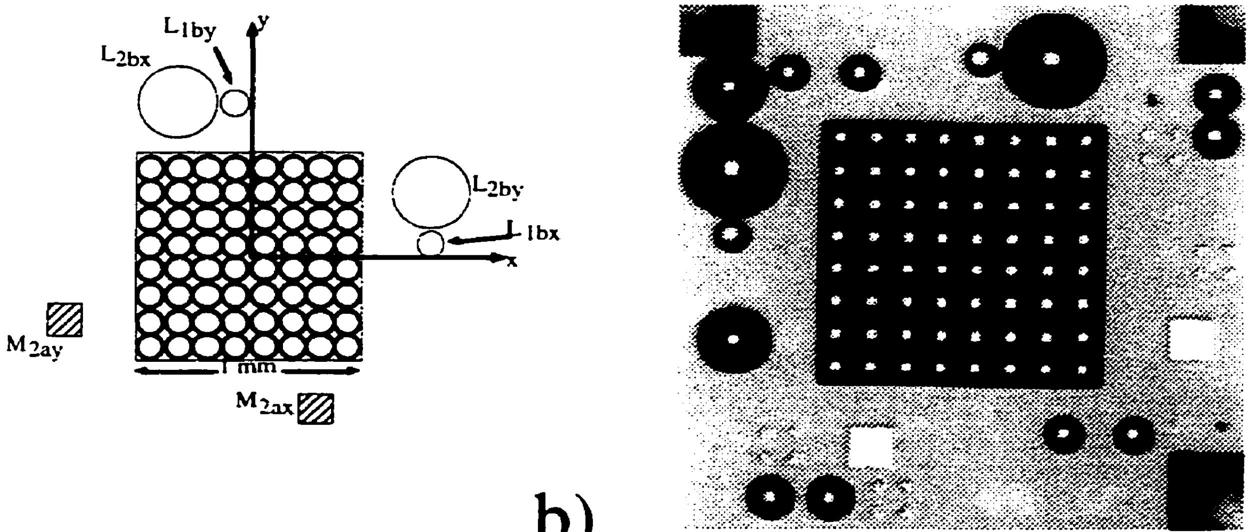

b)

Figure 4.7: Lenslet arrays a) LA_1: drawing and picture b) LA_2: drawing and picture (mirror image)

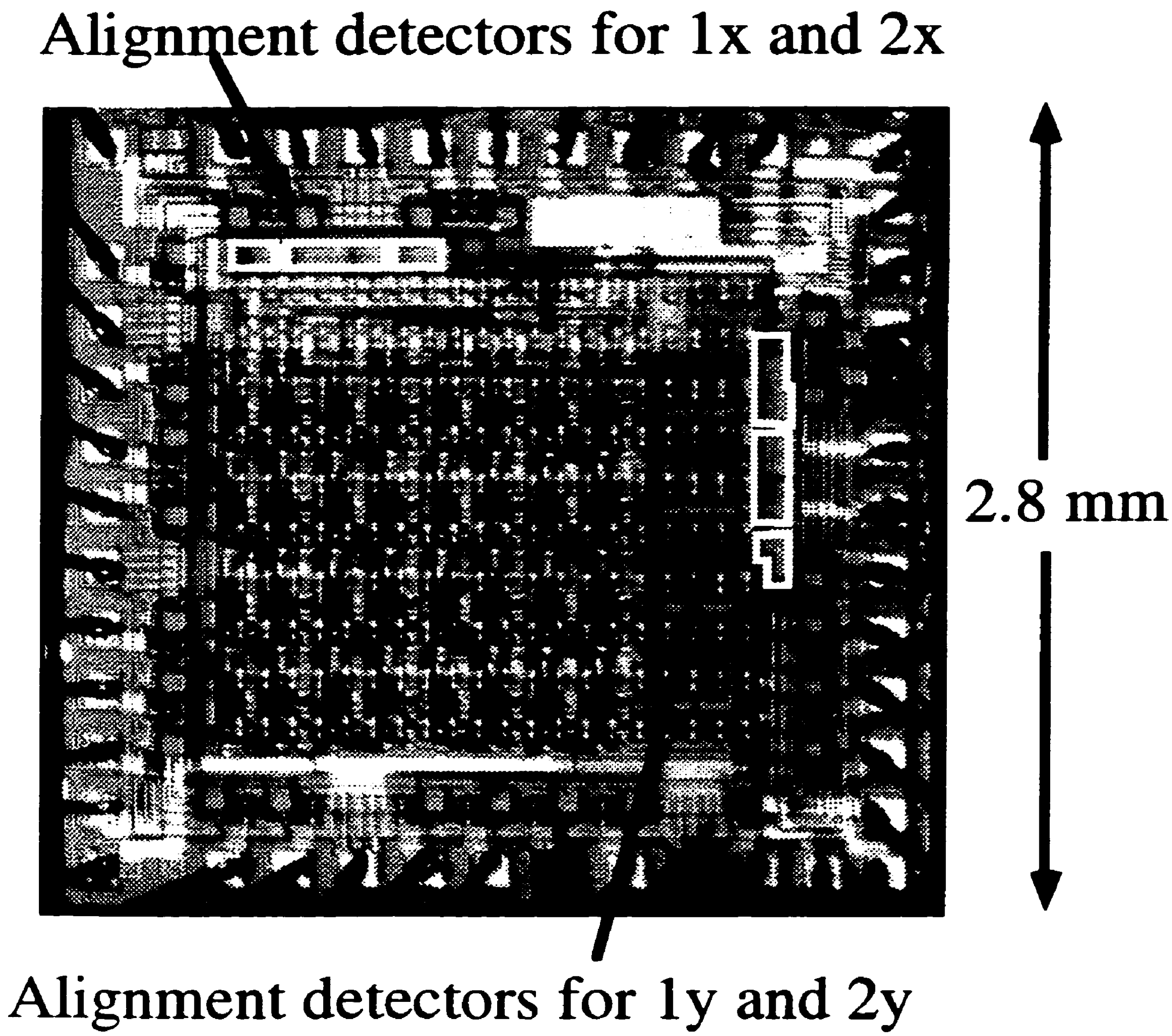

Figure 4.8: Smart Pixel Chip with (highlighted) alignment detectors on the side.

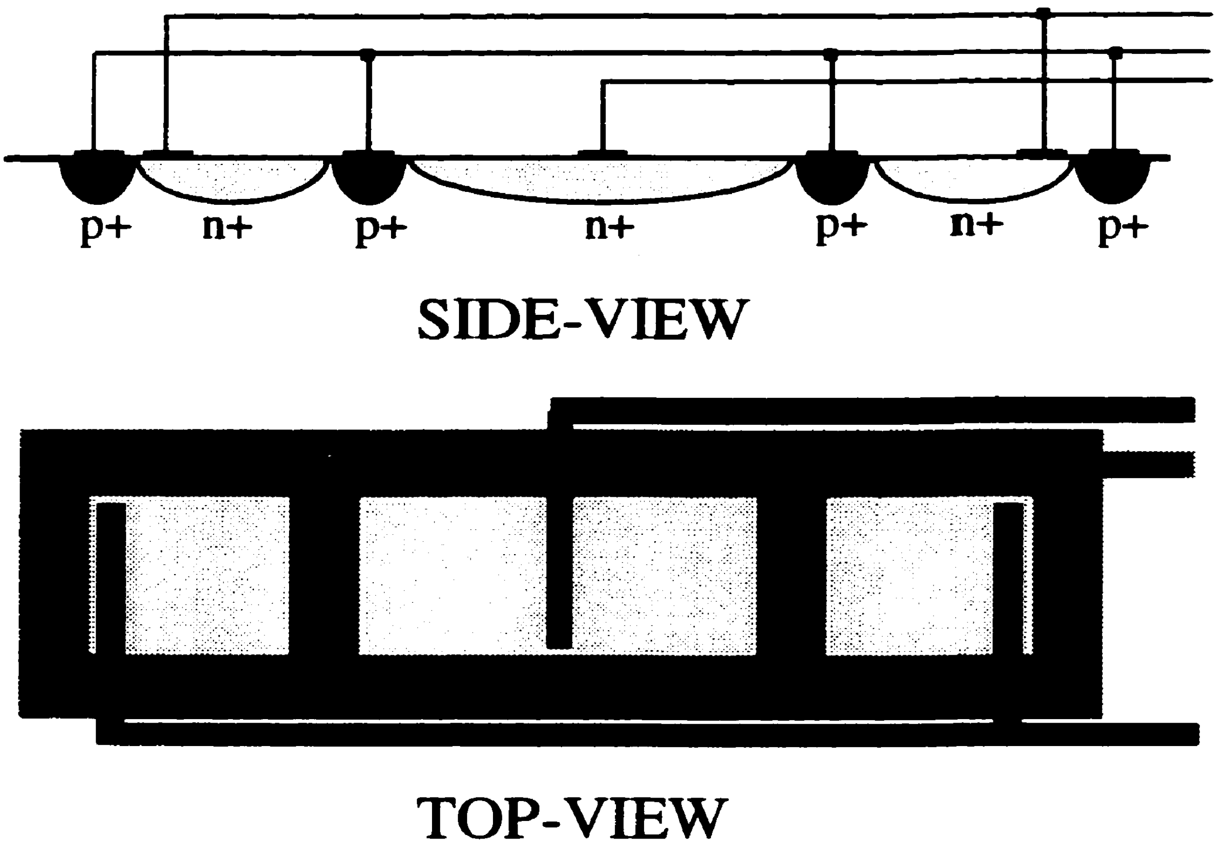

Figure 4.9: Layout of silicon alignment detectors

Referring to Figure 4.3b, the nominal dimensions for the alignment detectors were as follows: a=7.5 μm, c=70μm, and b varied from 100 to 200 μm, depending on the detector.

The measured responsivity of one of the actual chips used in the experiment was 0.08 A/W at λ=850 nm. A SiN layer which absorbed ~70% of the light was present on the detectors, contributing to the low sensitivity.

The chip was glued and wirebonded to the small, custom-designed, daughterboard [15], which offered mechanical support and an electrical connection to the rest of the test equipment.

4.5 Experimental Results

4.5.1 Images of Beam Array at Selected Planes

As a stage-to-stage link was being built up, images of the beam array at various planes in the system were taken via a CCD camera/frame grabber setup.

Figure 4.2 shows the beam array at the input power plane with the 32 signal beams and the alignment beams.

Figure 4.10 shows the beam array at a distance z3 beyond LA_I of stage #1 at the plane where the stage #1 chip would be located. At this plane, only 34 beams are visible, namely the 1x and 1y alignment beams as well as the 32 signal beams. The 2x and 2y beams are not visible in Figure 4.10 since they impinged on the M_{2ax} and M_{2ay} mirrors respectively and were sent to stage #2.

Finally, Figure 4.11 shows the beam array at a distance z3 beyond LA_I of stage #2, at the plane where the stage #2 chip would be located. At this plane, only 34 beams are visible, namely the 2x and 2y alignment beams as well as the 32 signal beams reflected from stage #1.

4.5.1.1 Systematic error due to beam profile

All calculations for the propagation of the alignment beams assumed an ideal Gaussian irradiance profile. In a real system, a perfect Gaussian profile is not achievable due to component non-idealities. These imperfections had at least two consequences of interest to the measurement system described here.

The first consequence was the impact on measurement linearity. The assumption of linearity to within 10% used above may not be valid if the beam is not Gaussian. In fact, as is shown below, there were occasional kinks in the measurement curve which can be attributed to non-ideal Gaussian beams

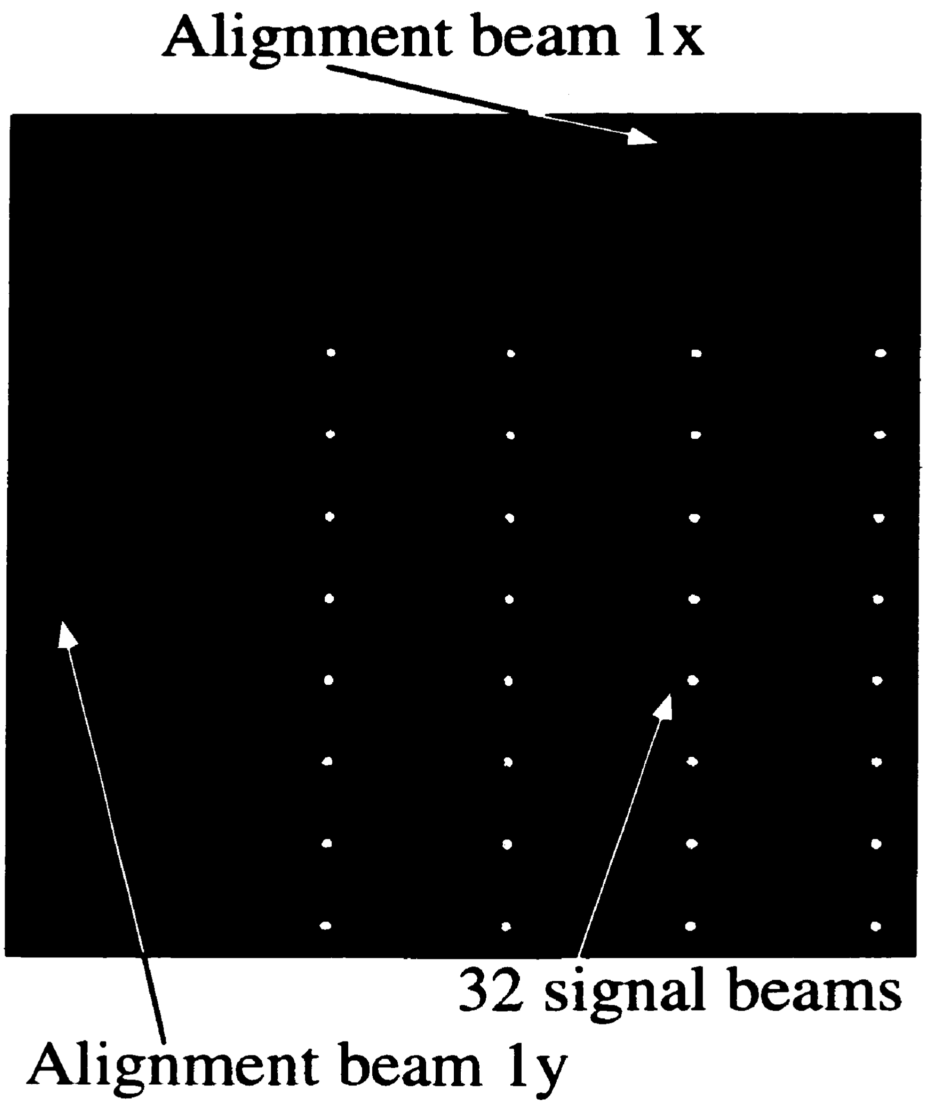

Figure 4.10: Beam pattern at the plane of the stage #1 chip.

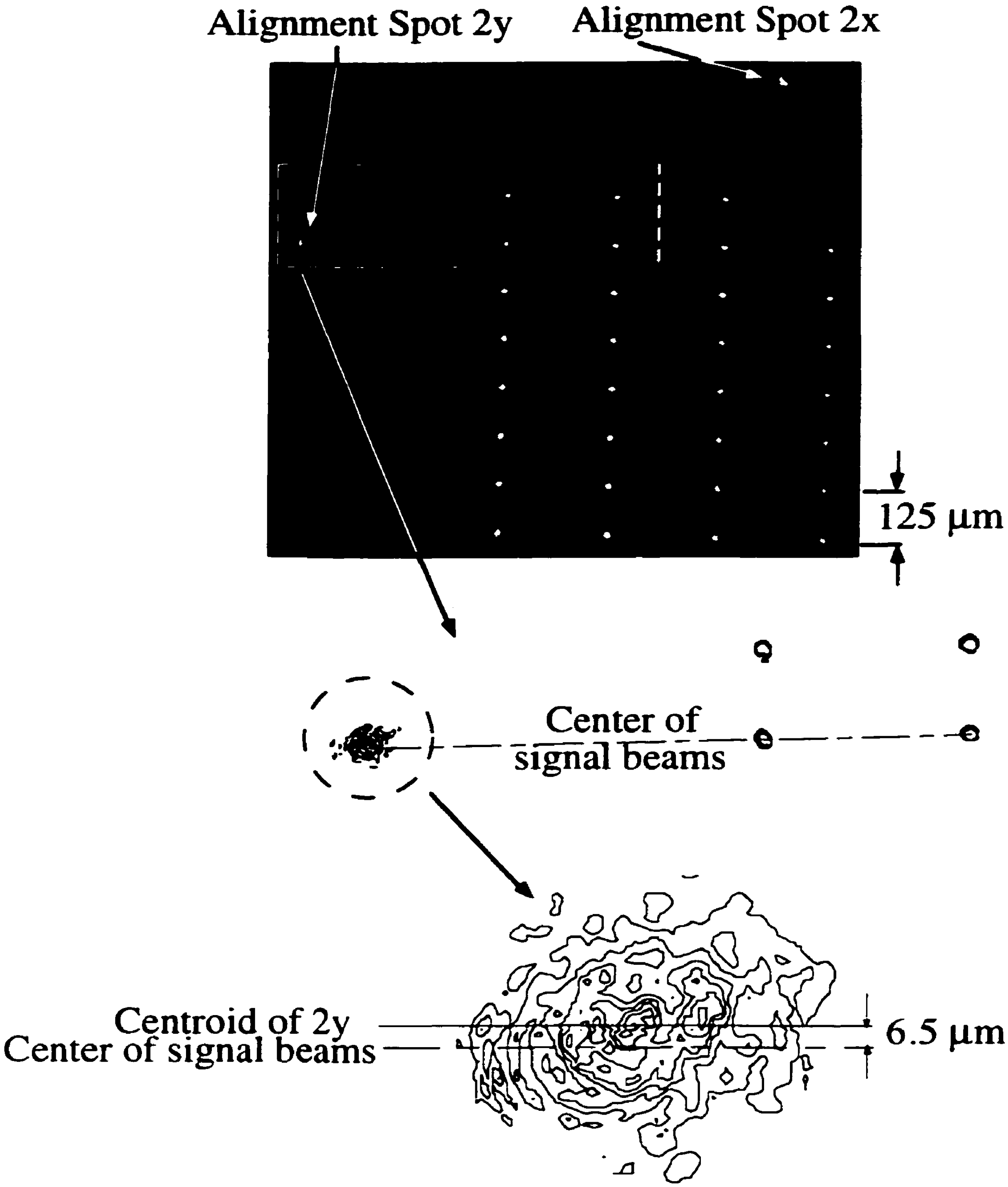

Figure 4.11: Beam array at the plane of the stage #2 chip. Increasing magnifications show systematic error brought about by difference between centroid of alignment beam and centre line of signal beams.

The second consequence was one of systematic error. As stated above, the system was designed such that the centroid of each alignment beam was located on the 125 μm grid on which all signal beams were located. For example, in Figure 4.11, the centroid of alignment spot 2y should have been on the line labeled 'center of signal beams'. However, calculations on the measured data indicate that the centroid was actually 6.5 μm above this line. As a result, there was introduced a systematic error of 6.5μm on all measurements using the 2y alignment beam.

This error can be attributed to many factors such as dust or fabrication errors on the large lenslets and mirrors, as well as to the path of the alignment beam which is approximately 500μm farther from the optical axis than the signal beam farthest from the optical axis. The ragged profile of the 2y alignment beam can be attributed to the fact that the 2y alignment beam, like the signal beams it ran parallel to, had gone through well over 30 optical surfaces – ranging from lenses to prisms to polarization components – after its generation by the OPS. It should also be noted that the optical relay inherently magnified all imperfections in the beam by a considerable amount in order to generate the wide beam (~100 μm, 86.5% encircled power) at the alignment detector. These factors can also explain the slight lack of radial symmetry of the alignment beam at the detector.

Similar observations and calculations indicated that the offset error of the 2x beam was 11 μm.

Offset errors of this magnitude clearly indicate that this alignment system was not accurate unless proper calibration was performed beforehand, possibly at the expense of overall measurement range. However, as shown below, this system was precise and maintained a linear response over a large measurement range.

4.5.2 Alignment Measurement

After the calibration steps described above were conducted, the performance of the system was measured in the optical backplane demonstrator system. The experimental setup was as shown in Figure 4.5, namely the chip on the daughterboard of stage #1 communicated to the chip on the daughterboard of stage # 2 chip via the optical interconnect. Both chips were identical and were as shown in Figure 4.8.

The power incident on the alignment detectors was adjusted such that the photocurrents generated 5V across the 1MΩ resistors at full misalignment (i.e. when all the power contained in the alignment beam was entirely on one detector).

The measurement results are given below.

4.5.2.1 Performance of 1x and 1y measurement

The 1x and 1y beams measured the lateral alignment of the beam array from the Optical Power Supply (OPS) onto the modulators of stage #1. The setup to measure the performance of the alignment measurement system was as follows.

The daughterboard (with the chip glued and wirebonded onto it) was mounted on a 6 degree-of-freedom precision stage. The modulators were then set to modulate at 1 Hz and light was fed into the OPS. Without using the alignment beams and detectors for alignment information, the daughterboard was moved until the chip was properly aligned. This could be accomplished by moving the daughterboard and monitoring the contrast ratio of the modulated signal beams transmitted to stage #2. When the contrast ratio of the signal beams was maximized at stage #2, board #1 could be judged to be optimally aligned at the true zero since the incoming power supply beams were then properly aligned onto the modulators.

At this point, the performance of the alignment detectors was measured. The daughterboard was moved by known increments in the x and y directions and the differential voltage was measured and displayed.

A plot of the normalized differential power vs Δy is shown in Figure 4.12. The solid line is the measured data, the dashed line is the theoretical value. The constant offset value due to background noise (obtained for each alignment detector by measuring the photocurrent when the alignment beam was not incident on the detector) was subtracted for all data points.

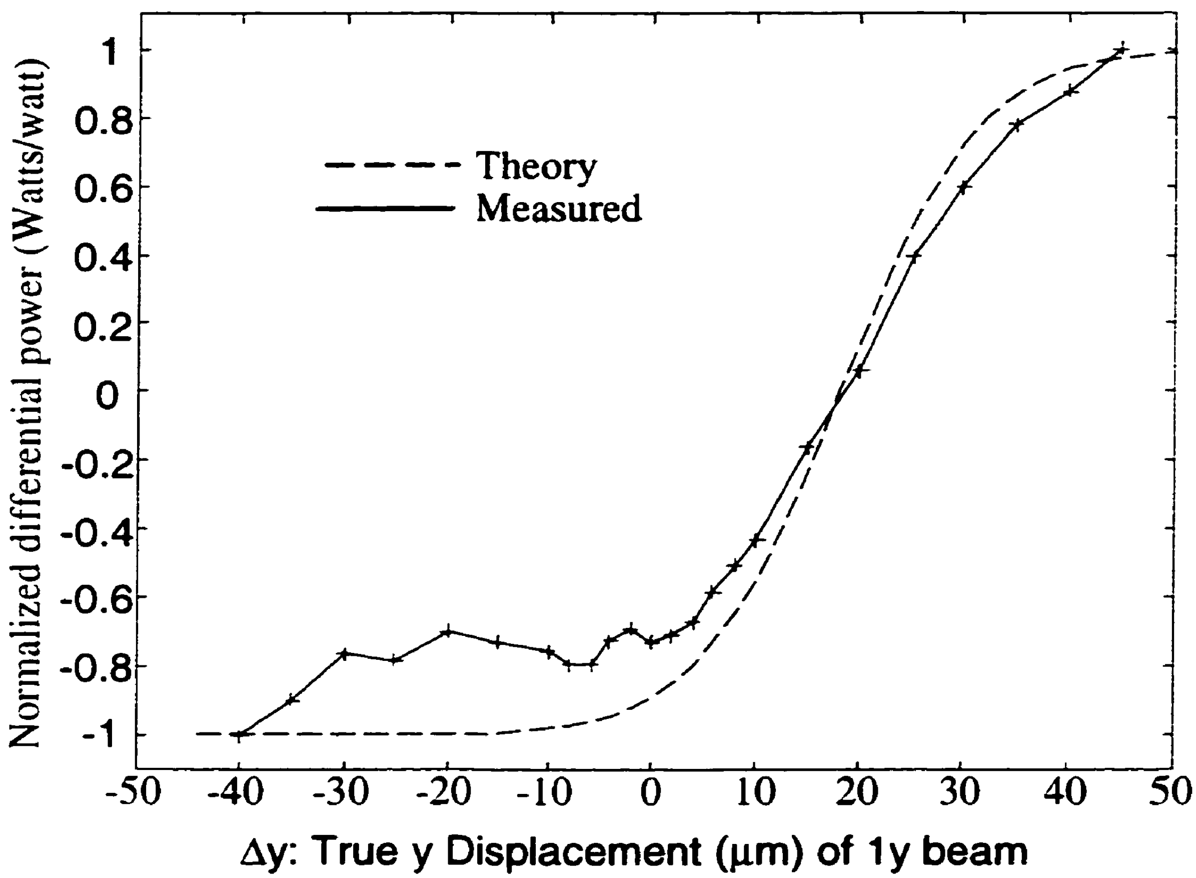

Figure 4.12: Theoretical and measured normalized differential power vs displacement of 1y alignment beam.

The major problem revealed by the plot is the systematic error: there is an 18 μm difference between the zero crossover of Δy and that of the normalized differential power. This error was not caused by any differences between the centroid of the 1x and 1y beams and the centre of the signal beams, since these differences were insignificant. The main cause of the systematic error in this case turned out to be the scattered light impinging on the alignment detectors: the very large alignment detectors could easily integrate all the scattered light arising from all the higher orders of the diffractive components in the system before the alignment detectors (i.e. the fan-out grating and all the lenslets in the vicinity of the detectors) as well all the other components in the system. Since the alignment detectors were of different size, the big alignment detector captured more light than the other, leading to the error. As a result, the theoretical value on the plot is actually shifted by 18μm.

Once the systematic error is taken into account, however, the measured value tracks the theoretical value quite closely, with the measured value rising slightly slower than the theoretical value. This discrepancy can be attributed to the actual width of the beam, which was measured to be approximately w_{1y} = 32μm±5 μm (instead of the desired 30μm) as well as to the residue partly covering the silicon alignment detectors–a factor not taken into account in the original model. Other sources of error could be the occasional copper trace line running over a detector and the varying shape of the detectors, as well as the scattered light pointed out above and noise across the large 1MΩ resistors.

From the measurements and theory, the scaling constant, k, of Equation (1) was determined to be k=15μm.

A plot of the normalized differential power vs x displacement is given in Figure 4.13. It should be noted that in this case there was a problem with receiver F': it was stuck at 0 and as such it was impossible to obtain a differential error signal which was the result of a subtraction of two photocurrents. As a result, the plot in Figure 4.13 was obtained by assuming that the power gained by receiver F' was equal to the power lost by receiver E'. Therefore, the line labeled 'measured data' is actually a combination of measured data and reconstructed data. This partial reconstruction therefore adds an additional error to all the sources of error pointed out above.

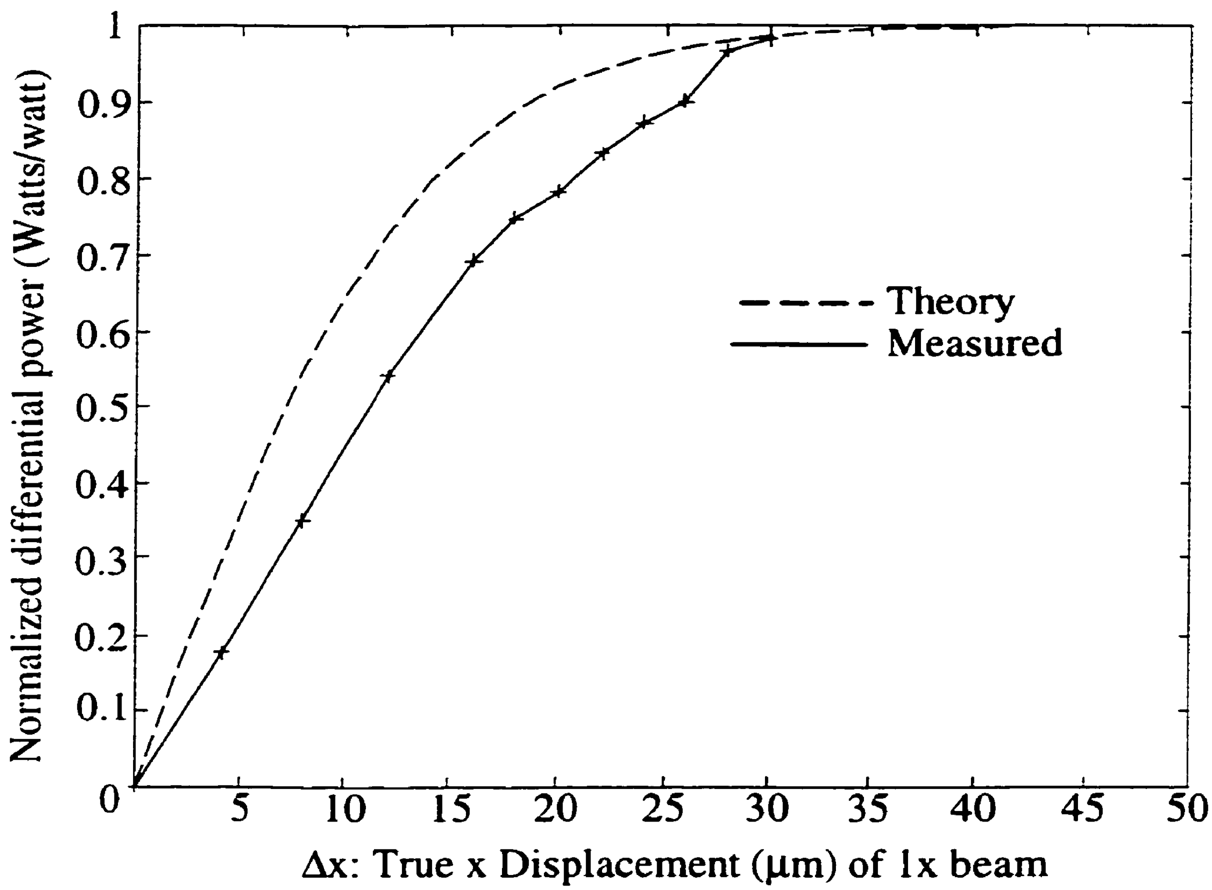

Figure 4.13: Theoretical and measured normalized differential power vs displacement of 1x alignment beam. Only one alignment detector was used for this run.

4.5.2.2 Performance of 2y measurement

A setup analogous to the one for measuring the 1x and 1y beams was again performed, this time with another chip identical to the first one.

The first problem encountered in this measurement was finding the true zero, as had been done on the first chip by observing the contrast ratio of the signal beams. In this case, the intent was to find the true zero by monitoring the operation of the receivers: the highest operating speed of the receivers would mean that the incoming beams were best centered on the quantum well windows. Unfortunately, the amount of power reaching the signal detectors was not sufficient for even low speed operation. Since, it was impossible to fully determine the accuracy of the 2x and 2y beam system, it was assumed that the only systematic errors affecting the accuracy were the 6.5μm and 11μm errors determined above for the 2y and 2x beams respectively.

This being determined, the alignment system performance was measured.

Since, again, a 'stuck at 0' fault was found on this second chip for one of the detectors needed for the 2x measurement, only the 2y measurement was performed, which is shown in Figure 4.14. Again, the background noise was subtracted for all points.

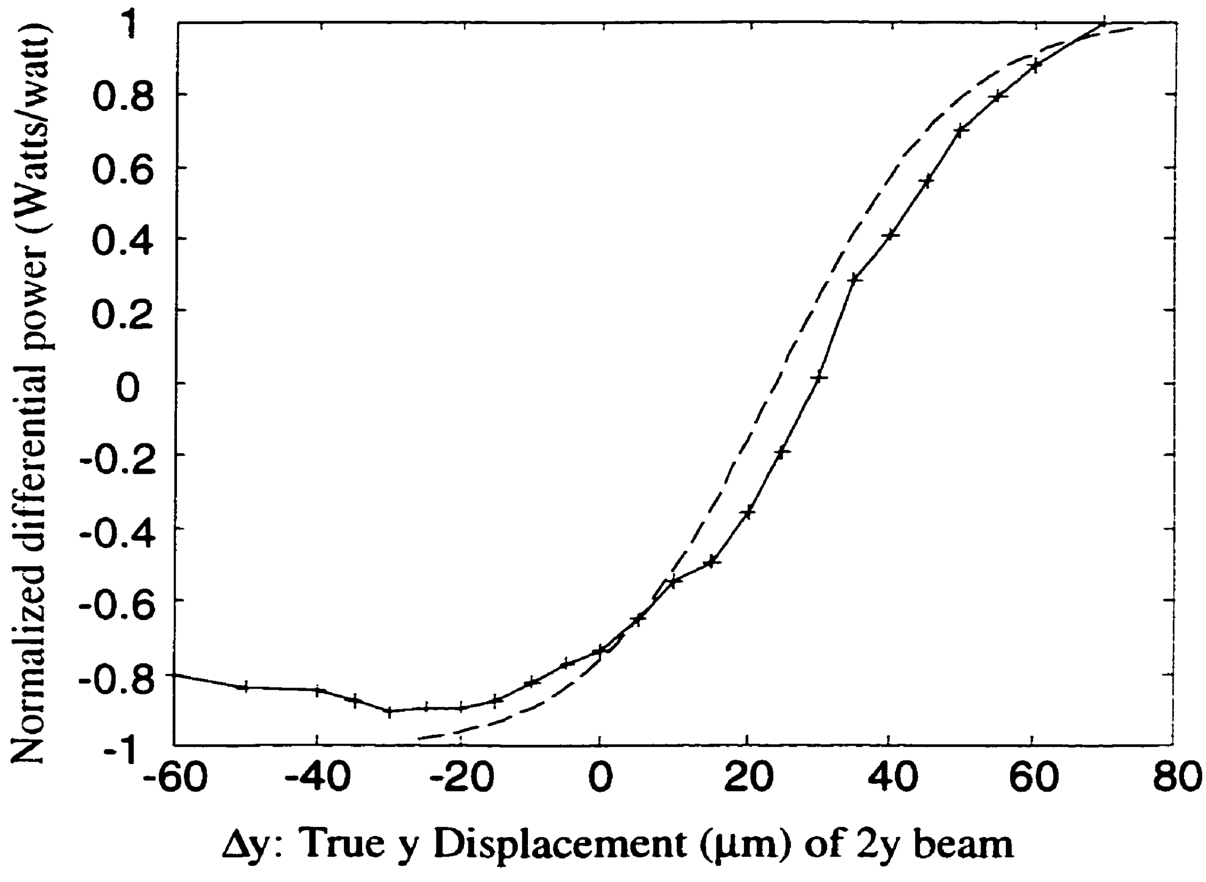

Figure 4.14: Theoretical and measured normalized differential power vs displacement of 2y alignment beam.

The Figure 4.14 plot shows a good fit between theory and measured, except for a systematic error of 24 μm. This systematic error is considerably greater than the 6.5 μm calculated above. The additional error can be explained by the same reasons given for the 1x and 1y beams, namely the scattered light, the imperfections on the alignment detectors and noise across the resistors.

In this setup, the scaling constant for the 2x and 2y beams is k= 25μm.

4.5.2.3 Differential voltage swing

All the measured displacements so far have been given in terms of normalized differential power. However, the results could also have been given in terms of differential voltage per micrometer. In this setup, the 1x and 1y beams could generate a differential voltage swing of 330 mV per micrometer of misalignment and the 2x and 2y beams generated a differential voltage swing 200mV/μm.

4.6 Discussion of Results

A novel technique for *in-situ* monitoring of lateral alignment in free-space optical systems was proposed and then implemented in an free-space optical backplane demonstrator system.

Several conclusions can be drawn from the experimental demonstration. The principal conclusion is that the system can be used as it was intended to: positional measurements from the alignment detectors can be obtained and used to adjust the system when misaligned during system assembly. However, the system was quite cumbersome for many reasons. First, the systematic errors were troublesome and imposed complicated calibration steps. Second, the constraints on pin-outs and especially chip real estate, combined with the need to keep the alignment spots on a 125μm grid, led to non-optimal configurations. Third, fabrication imperfections ranging from the scattering off lenslets and other components to the residue left on the chips affected system performance and considerably reduced the measurement accuracy. Fourth, the alignment detectors were made too large and as such captured too much stray light. The system would have been better with thinner detectors. Nonetheless, all these practical problems can be eliminated in future implementations of this concept.

4.7 Cost of Diagnostic System

This chapter has indicated the benefits brought about by *in-situ* diagnostics and testing. However, diagnostics and testing of systems always add cost. In certain chips, for examples, external testing can represent up to 40% of the final chip cost[16]. The cost is a function of the desired coverage, the use of external vs built-in testing, and so on. Cost is a vital factor in all test schemes, and so costing the diagnostic system described in this chapter is an important exercise.

The costs considered are the following: on-die chip area, bond pads, additional microoptic components, power loss due to fan out and additional components. The costs will be expressed as a percentage of system functionality.

There were six alignment detectors and associated traces occupying a total of approximately 63 000 μm^2 on the die: this represented ~1% of the total 2.8 mm x 2.8 mm chip area. The five bond pads for the alignment signals represented ~10 % of the total bond pads on the periphery of the chip (multiplexing could have allowed trade-offs between pin-outs and area). The four alignment beams had as much power as the signal beams; as a result, they reduced the power available to the signal beams by 4/(4 x 8) = 12.5%. The additional lenses and mirrors represented about 15% of the total area on the occupied glass substrate. Additional components and lines on the ribbon cable and PCBs added about 5% in cost to the design. Finally, the amount of engineering time to design and build the in-situ system relative to the total amount of time spent on the total project was about 15%. Assuming that all the above factors have equal weight, it can be seen that the alignment diagnostic system added ~12% to total system cost.

This value must be compared to what the cost would be to build the system without the alignment diagnostic system. Since no time sheets were kept during system assembly, this is obviously an estimate with a high value of uncertainty. Nonetheless, given the months spent in the lab by all the group members to align the system and the costs of using an external alignment system with cameras and bulky optics, it can be said that a 12% increase in cost is well worth the time saved. Moreover, the ability to monitor the FSOI in real-time without perturbing it in any way is incalculable. Finally, this cost is relatively fixed and should decrease relative to total cost as systems increase in size. For example, the total power lost to alignment beams will decrease in relation to total optical power as the number of signal beams increases.

This section indicates that the cost of using built-in, or in-situ, diagnostics is small. In any case, the electronics industry has already accepted the merits of such testing and photonics must do so as well. The key is to reduce the cost.

4.8 Conclusion

The key point put forward in this chapter is that diagnostic systems in future free-space optical systems will have to be built-in during the system design phase and will have to generate electronic signals compatible with existing industrial test standards. Parallel alignment beams as presented in this chapter are an elegant way of achieving this goal. However, more accurate cost-benefit studies will have to be performed in the future to determine the desirable balance between built-in and external testing – just like the electronics industry does[16].

4.8 References

1 A. L. Lentine, D. J. Reiley, R. A. Novotny, R. L. Morrison, J. M. Sasian, M. G. Beckman, D. B. Buchholz, S. J. Hinterlong, T. J. Cloonan, G. W. Richards, and F.

B. McCormick, "Asynchronous transfer mode distribution network by use of an optoelectronic VLSI switching chip," *Applied Optics*, 36, pp. 1804-1814 (1997).

2 D. V. Plant, B. Robertson, H. S. Hinton, W. M. Robertson, G. C. Boisset, N. H. Kim, Y. S. Liu, M. R. Otazo, D. R. Rolston, and A. Z. Shang, "An optical backplane demonstrator system based on FET-SEED Smart pixel arrays and diffractive lenslet arrays," *IEEE Photonics Technology Letters*, 7, pp. 1057-1059 (1995).

3 IEEE Standards Office, "1149.1-1990, The Test Access Port and Boundary-Scan Architecture," 1990.

4 G. C. Boisset, D. R. Rolston, R. Iyer, Y. S. Liu, B. Robertson, D. Kabal, and D. V. Plant, "In-situ measurements of misalignment errors in free-space optical interconnects," submitted to *IEEE Journal of Lightwave Technology*, May, 1997, accepted Jan. 1998.

5 R. Iyer, Y.S. Liu, G.C. Boisset, D.J. Goodwill, W.M. Robertson, B. Robertson, M.H. Ayliffe, D. Kabal, F. Lacroix, and D.V. Plant, "Design, implementation, and characterization of an optical power supply spot array generator for a four stage free-space optical backplane", *Applied Optics*, in press.

6 M. D. Roper, P. A. Buksh, I. W. Kirkman, G. van der Laan, H. A. Padmore, and A. D. Smith, "Performance of the Daresbury synchrotron radiation source soft x-ray double-crystal monochromator," *Review of Scientific. Instruments*., 63 pp. 1322-1325(1992).

7 K. Hirabayashi, T. Yamamoto, S. Hino, Y. Kohama, and K. Tateno, "Optical beam direction compensating system for board-to-board free-space optical interconnection in high-capacity ATM switch," *Journal of Lightwave Technology*, 15, pp. 874-882 (1997).

8 F. A. P. Tooley, "Challenges in optically interconnecting electronics," *IEEE Journal of Selected Areas in Quantum Electronics* , 2, pp. 3-13 (1996).

9 R. L. Morrison, Steven G. Johnson, A. L. Lentine, and W. H. Knox. "Design and demonstration of a high-speed, multichannel, optical sampling oscilloscope." *Applied Optics*, 35, pp. 1187-1194 (1996).

10 R. M. Turner and K. M. Johnson, "CMOS photodetectors for correlation peak location," *IEEE Photonics Technology Letters* , 6, pp. 552-554 (1994).

11 G. C. Boisset, B. Robertson, and H. S. Hinton, "Design and construction of an active alignment demonstrator for a free-space optical interconnect," *IEEE Photonics Technology Letters*, 7, pp. 676-678 (1995).

12 W. H. Lee, "Holographic optical head for compact disk applications." *Optical Engineering*, 28, pp. 650-653 (1989).

13 H. Kogelnik, and T. Li, "Laser beams and resonators," *Applied Optics*, 5, pp. 1550-1567 (1966).

14 D. R. Rolston, D. V. Plant, T. H. Szymanski, H. S. Hinton, W. S. Hsiao, M. H. Ayliffe, D. Kabal, M. B. Venditti, P. Desai, A. V. Krishnamoorthy, K. W. Goosen, J. A. Walker, B. Tseng, S. P. Hui, J. E. Cunningham, and W. Y. Jan,"A hybrid-SEED smart pixel array for a four-stage intelligent optical backplane demonstrator," *IEEE Journal of Selected Topics in Quantum Electronics*, 2, pp. 97-105 (1996).

15 D. N. Kabal, G. Boisset, D. R. Rolston, and D. V. Plant, "Packaging of two-dimensional smart pixel arrays." IEEE/LEOS Summer Topical Meeting on Smart Pixels, paper ThA5, August 1996.

16 R. Chandramouli and S. Pateras, "Testing systems on a chip," *IEEE Spectrum*, 33, pp. 42-47 (1996).

Chapter 5: Optical Crosstalk as an Alignment Diagnostic Tool

5.1 Introduction

Chapters 2 and 3 presented the optomechanics and optical packaging of demonstrator systems which were built over several years. A key conclusion from this work was that alignment diagnostic systems for optical packaging had to be further developed since they were critical for simplifying system assembly and analyzing the performance of completed systems. Moreover, these diagnostic systems had to be as non-intrusive as possible in order to minimize any perturbation of the system. Chapter 4 presented a novel *in-situ* diagnostic system which worked well and which served to introduce the idea of non-obtrusive diagnostic . However, the diagnostic system did have a cost in terms of additional components and especially design complexity. A diagnostic system which is even less costly would be very beneficial for free-space optical interconnects. With this in mind, this chapter presents a simpler and cheaper idea for generating diagnostic information on system alignment. In this technique, the crosstalk generated by misaligned optical beams incident on lenslets is measured and used to deduce the alignment status of a system.

The concept is described in Figure 5.1. If an array of incident beams is misaligned with respect to its intended lenslets, there will be optical crosstalk. This chapter proposes the concept of capturing some of the crosstalk power with dedicated alignment lenslets and detectors in order to deduce the alignment status of the system.

As shown in Figure 5.2, eight dedicated alignment lenslets and associated detectors can be used to determine all possible misalignments. An ideal situation is shown in Figure 5.2a in which all alignment detectors receive an equal and minimal amount of power. If there is a lateral misalignment, for example in the positive x direction, then detectors associated with lenslets D and E will receive more light and A and H will receive less light, as seen in Figure 5.2b. For a defocus, all detectors will receive more light, as seen in Figure 5.2c. Tilt and rotation can be interpreted as combinations of the above. This chapter will present the theory, design, and fabrication for a diagnostic system optimized to measure lateral (x-y) misalignment errors in a lenslet-based interconnect.

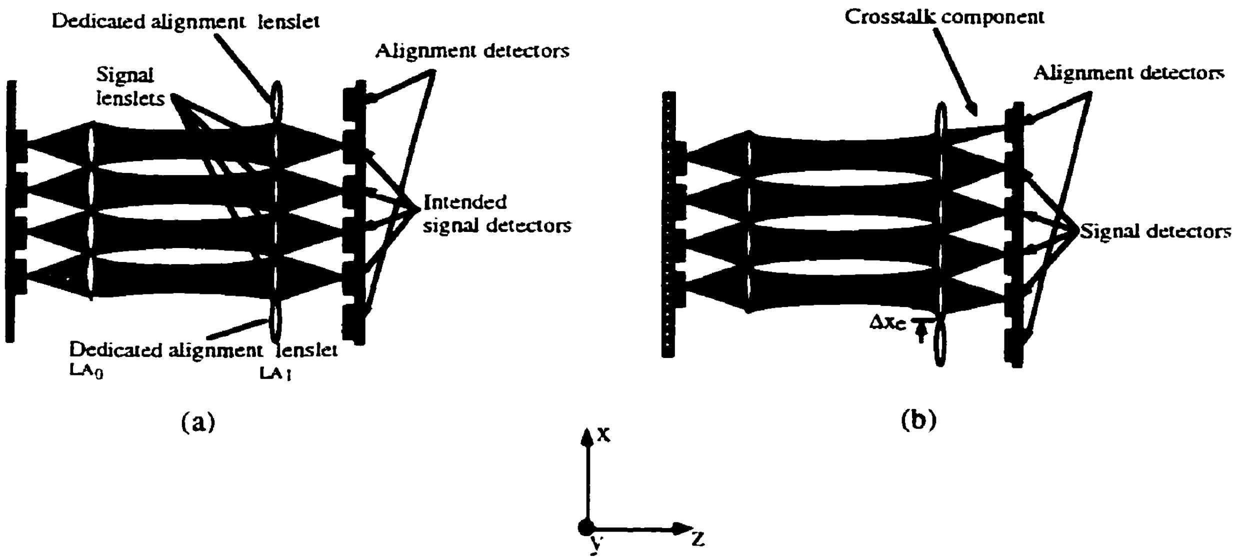

Figure 5.1 a) Perfect alignment of incoming beam onto lenslet array b) Misalignment leads to optical crosstalk component captured by dedicated alignment lenslet and associated alignment detector

The effect of crosstalk and associated diffractive spreading in optical links has been studied in many different contexts before. Analyses and experiments using ideal round lenslets have been performed to determine a design space which would maintain a signal-to-crosstalk ratio SXR of over 12 dB for dense (3460 channels/cm^2) interconnects[1]. System demonstrators, especially those using lenslets in their systems, generally also consider crosstalk [2,3,4], although designers for systems with just bulk macrolenses have also studied the issue and determined that crosstalk from Airy function sidelobes can be reduced by appropriate apodizing at the spatial light modulators [5]. Moreover, the clipping at aperture edges of free-space demultiplexers for WDM systems has also led to analysis of optical crosstalk [6]. The conclusion drawn from these and other works is that crosstalk has always been seen as strictly an undesirable effect to be minimized. While crosstalk certainly lowers system performance, crosstalk can also be used to generate useful information.

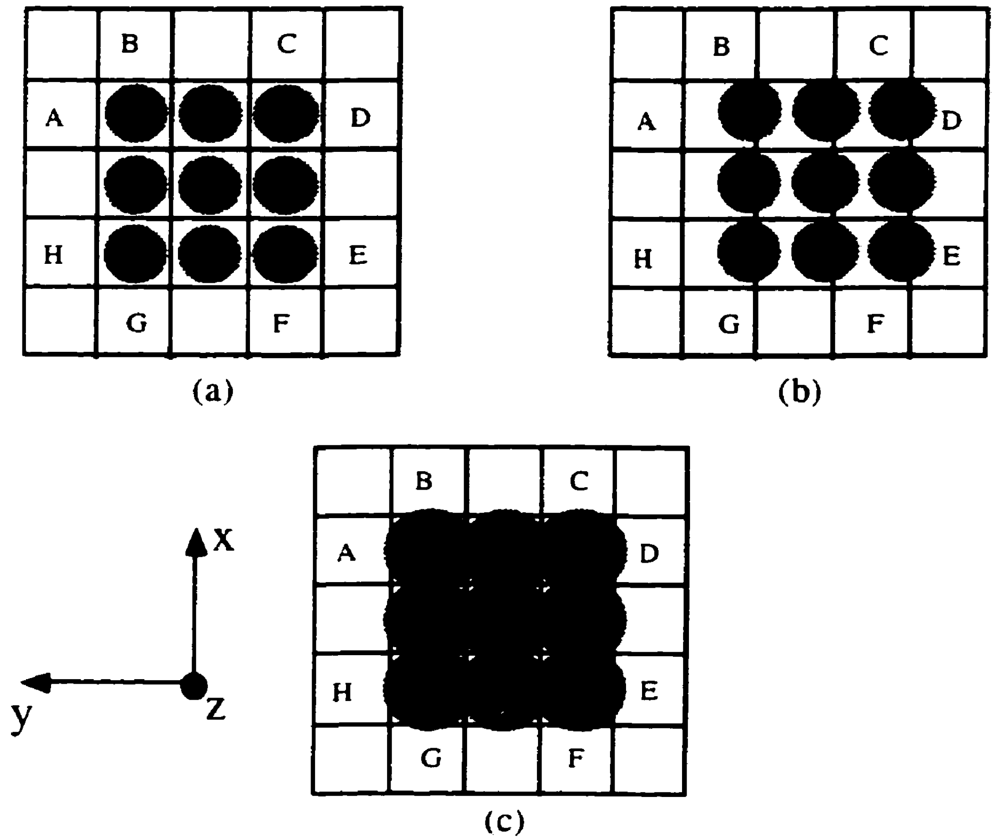

Figure 5.2a) Ideal alignment b) lateral misalignment c) defocus

This chapter is organized as follows. Section 5.2 presents definitions and the geometrical setup necessary for a proper understanding of the technique. Section 5.3 presents the mathematical foundation for the analysis of crosstalk and associated diffractive effects. It is shown that for small misalignments the diffracted crosstalk power is spread out over a great area; as a result, the signal-to-crosstalk ratio (SXR) at the detector plane is higher than that at the lenslets, which is a beneficial effect. In section 5.4 the alignment detectors for capturing the crosstalk power are designed and the diffractive spreading effect is used to optimize their efficiency. In section 5.5 experimental observations are conducted to validate the model and in section 5.6 experimental results with a custom made detector array including dedicated and optimized alignment detectors are presented. Section 5.7 concludes by explaining the significance and implications of this technique, as well as of other similar diagnostic techniques.

The work in this chapter is described in part in Reference [7].

5.2 Definitions and Geometrical setup

Since this chapter deals with optical crosstalk caused by the misalignment of arrays of signal beams incident on arrays of lenslets, it is imperative to define key terms.

Signal beams are beams which contain data: as far as this work is concerned, they could originate either from modulators or from emitters such as vertical cavity surface emitting lasers (VCSELs).

The term 'intended target' of a signal beam is the lenslet or detector which the beam would impinge upon if the system were perfectly aligned. The term 'victim' is used to describe the lenslet or detector for signal beams which receives crosstalk power from an adjacent misaligned beam. The term 'victim' is commonly used in electrical engineering to describe lines or connectors affected by Ldi/dt electrical crosstalk interference caused by fast-changing currents in adjacent conductors, especially in backplanes and their connectors[8].

In this chapter, unless otherwise specified, the term 'crosstalk' will mean optical crosstalk due to physical misalignment of beams relative to their target. Other types of optical crosstalk, such as wavelength-based crostalk in WDM systems[9], for example, or polarization crosstalk will not be covered.

As will be explained, this chapter proposes an evolution of the concept – introduced in the previous chapter – of having two different types of lenslets: signal lenslets and dedicated alignment lenslets. These are shown in Figure 5.1. As before, signal lenslets are used to relay signal beams: each signal lenslet is always an intended target and serves to relay optical beams to conventional signal detectors. However, there is a difference for the alignment lenses: a dedicated alignment lenslet is never an intended target. Its only function is to couple optical crosstalk power into a dedicated crosstalk detector in case of misalignment. There are no dedicated alignment beams.

It is also important to define the geometry of the problem. The interconnect between the two lenslet arrays could be either telecentric, minimum waist or any hybrid lenslet/macrolens combination. For the current discussion, the system is a telecentric 4f relay with lenslets having a focal length of f_μ=1 mm, although this discussion could apply to many other configurations and to different scaling. As a result, the optical path distance between the lenslets is $2f_\mu$ and the optical distance between detectors and lenslets is f_μ.

The following defines the coordinate axes and frames of reference to which all subsequent calculations will refer. As shown in Figure 5.1, the lenslet arrays (LAs) and the detector array reside on (x,y) planes. LA_0 is located on plane (x_0,y_0), LA_1 is located on plane (x_1,y_1) and the detector array is on plane (x_f,y_f). LA_0 contains just signal lenslets whereas LA_1 contains signal lenslets along with dedicated alignment lenslets at the periphery of the array. To preserve generality, no assumption will be made of the source of the beams: they could come either from emitters or modulators.

5.3 Calculations of Theoretical Crosstalk Diffraction Pattern

This section serves to give a theoretical foundation for the discussions in the rest of this chapter.

5.3.1 Derivation of the Diffractive Lens Model

The lenslets used in all experiments in this thesis were diffractive and as such their characteristics must be studied. An ideal diffractive lens will have many focal lengths due to the many diffractive orders present. If the first order (N=-1) focal length is f_μ, then other focal lengths corresponding to converging wavefronts will be [10]:

$$f_{\mu N} = \frac{f_\mu}{|N|} \tag{1}$$

where N < 0 and |N+1| is an integer multiple of the number of phase levels used to define the diffractive lens.

For example, an ideal 4 level diffractive lens will have focal lengths of f_μ, $f_\mu/5$, $f_\mu/9$ for the first (N=-1), fifth (N=-5), and ninth (N=-9) orders respectively; an 8 level lens will have focal lengths at f_μ, $f_\mu/9$ for the first and ninth order respectively. The power diffracted by each of these higher order focal lengths decreases geometrically with increasing order[10].

The diffractive lenses in the experiments had eight phase levels in the middle and four at the periphery, due to fabrication constraints. For the purpose of this analysis, the model chosen to describe the diffractive lenses in these experiments includes zeroth, first and estimated fifth order effects. Based on the results obtained in the appendix, it is assumed that for a unit irradiance, I_o, incident on a microlens, $0.79I_o$ is diffracted into the first order, and $0.07I_o$ goes into the zeroth order. It is further assumed that approximately one third the remaining power, $0.05I_o$ goes into the fifth order, with the remaining 9% scattering into other orders and elsewhere.

A final operation must be performed on the model. The measured values above correspond to power whereas diffraction calculations below compute field strength which is proportional to the square root of the power. As a result, the calculations below use the field diffraction coefficients $C_1 = \sqrt{0.79} = 0.89$, $C_0 = \sqrt{0.07} = 0.26$, and $C_5 = \sqrt{0.05} = 0.22$ for the first, zeroth, and fifth orders respectively. While this model obviously simplifies a complex situation by lumping some of the power unacccounted for into the fifth order and neglecting the remaining power into other converging and diverging orders, it nonetheless yields considerably more insight than the simple ideal lens case, and in fact predicts results comparable to the experimental results obtained below.

5.3.2 Setup of the Diffraction Integral

This section sets up the diffraction integral which gives a mathematical representation of the physical situation depicted in Figure 5.1. When evaluated, this integral gives the amount of power coupled into the crosstalk component defined above for various values of lateral misalignment, Δx_e, of the incoming beam relative to the intended lenslet.

The geometry of the problem is given in Figure 5.3, with Figure 5.4 further giving boundary conditions and approximate irradiance profiles at the Fourier plane. Given an optical setup in which Gaussian beams are relayed by a telecentric lenslet-based 4f system from transmitter to receiver, the field incident on LA_1 is[11]:

$$G(x_1, y_1) = \exp\left\{-j(kz_w - \Phi) - \left[(x_1 - x_g)^2 + (y_1 - y_g)^2\right]\left(\frac{1}{w^2} + \frac{jk}{2R}\right)\right\} \tag{2}$$

where $\Phi = \arctan(\lambda z_w / \pi w_o^2)$, R is the radius of curvature also defined in [11], w is the $1/e^2$ encircled irradiance radius, and $z_w = f_\mu$, the distance from the beam waist between the two lenslets to LA_1 in this telecentric system. In effect, equation (2) states that the beam incident at the microlens has a Gaussian field profile with a curved phase front and has a peak value at (x_g,y_g).

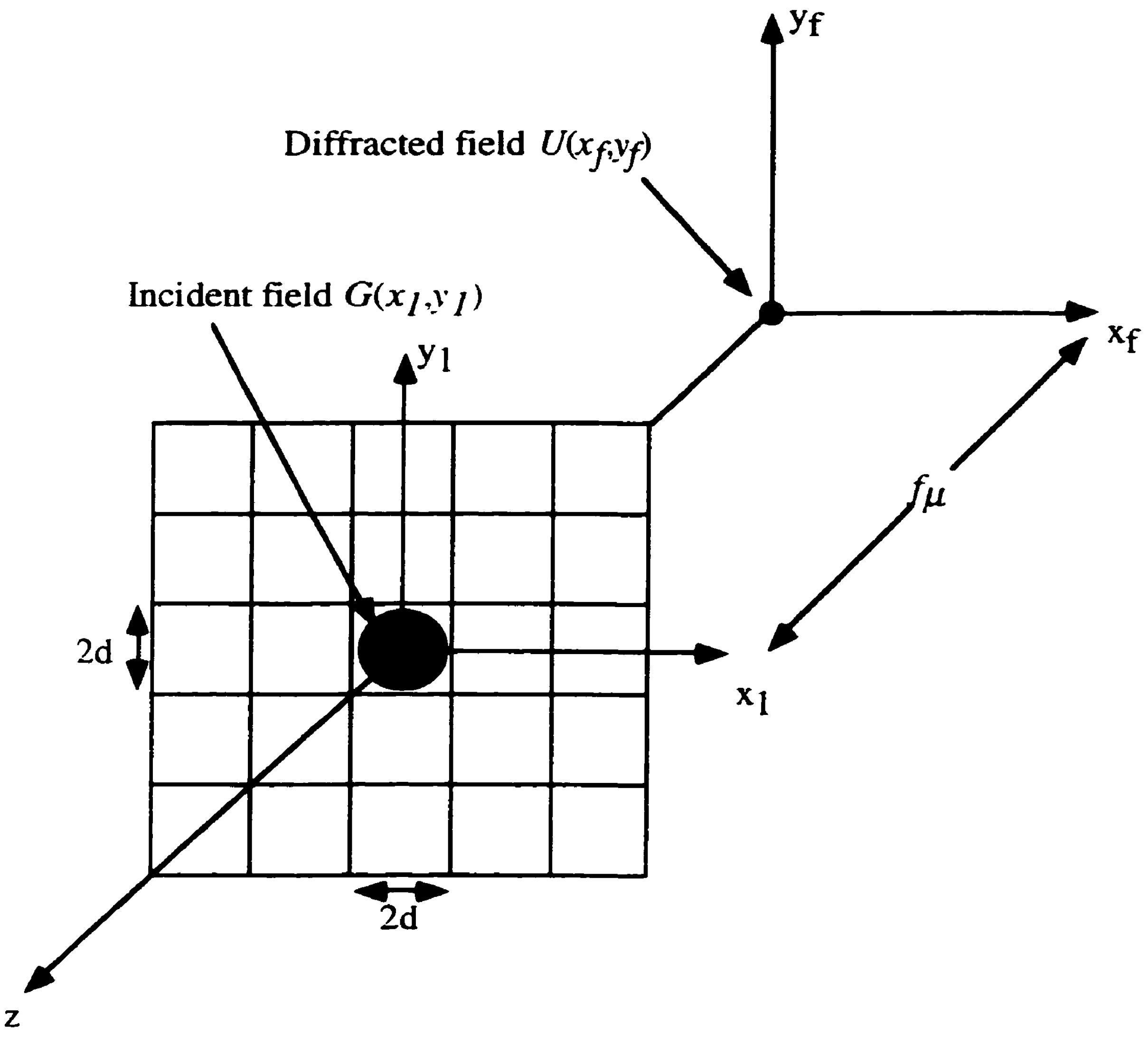

Figure 5.3: Geometry of the diffraction problem

If the illumination field defined by $G(x_l,y_l)$ were incident on an ideal square lens of focal length f_μ, of dimensions $2d \times 2d$, and centered at $(x_l,y_l)=(0,0)$ as shown in Figure

5.4. then the diffracted field distribution $U'(x_f,y_f)$ at a distance f_μ behind the lens (for $-d<x_f<d$ and $-d<y_f<d$) would be[12]:

$$U'(x_f,y_f)=\frac{P(x_f,y_f)}{j\lambda f_\mu}\int_{-d}^{d}\int_{-d}^{d}\{G(x_1,y_1)\}\times\left\{\exp\left(-j\frac{2\pi}{\lambda f_\mu}\left(x_f x_1+y_f y_1\right)\right)\right\}dx_1 dy_1 \quad (3)$$

where $P(x_f,y_f)$ is a unity-amplitude complex phase term. The irradiance would be the square of the absolute value of the above expression.

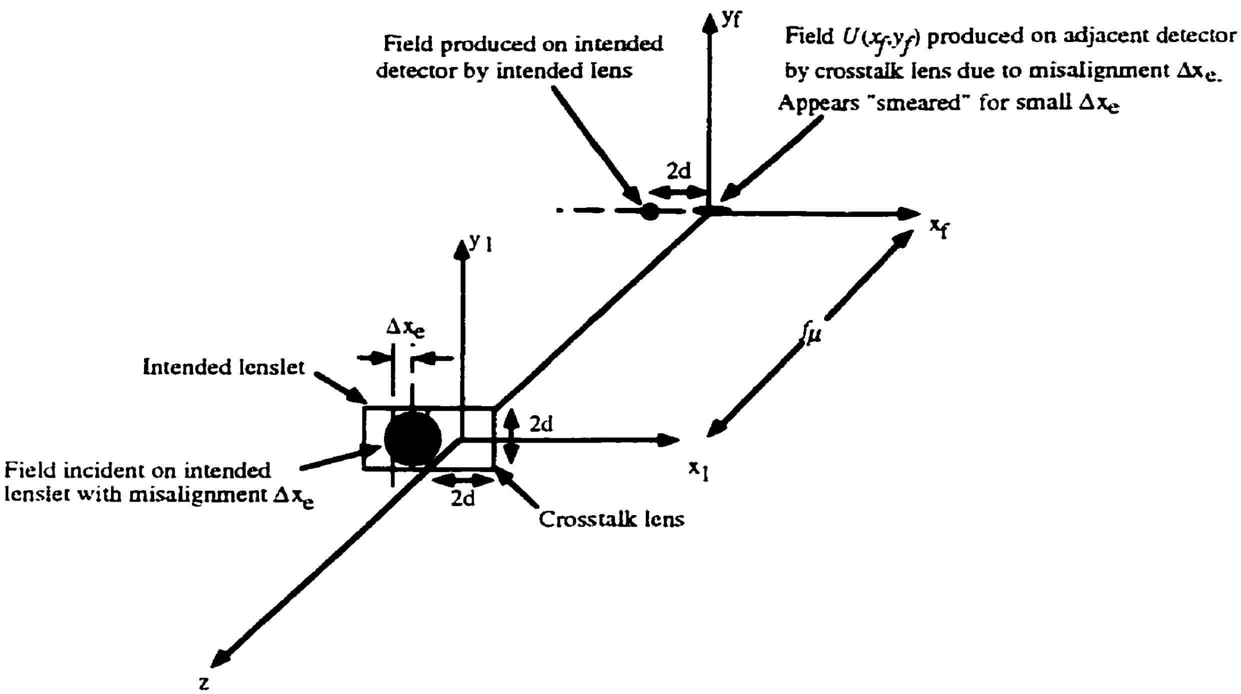

Figure 5.4: Boundary conditions for calculations and approximate irradiance profiles at Fourier plane

However, the actual diffractive lens is quite different from the ideal lens. As a result of the model obtained above and in the appendix, the diffracted field at the focal plane is more accurately represented by $U(x_f,y_f)$ as follows:

$$U(x_f,y_f)=\frac{P}{j\lambda f_\mu}\int_{-d}^{d}\int_{-d}^{d}\left\{\begin{array}{l} G(x_1,y_1)\times\exp\left(-j\frac{2\pi}{\lambda f_\mu}(x_f x_1+y_f y_1)\right)\times \\ \left[\left[C_o\exp\left(j\frac{k}{2f_\mu}(x_1^2+y_1^2)\right)+C_1+C_5\exp\left(j\frac{k}{2}(x_1^2+y_1^2)\left(\frac{1}{f_\mu}-\frac{1}{f_\mu/5}\right)\right)\right]\right]\end{array}\right\}dx_1dy_1 \quad (4)$$

In equation (4), diffraction due to a lens of focal length f_μ is given weight C_1, diffraction due to a lens of focal length $f_\mu/5$ is given weight C_5, and a beam freely propagating in free space is given weight C_o, as per the model. Thus, the term with coefficient C_5 indicates a lens of focal length $f_\mu/5$ observed at a distance f_μ away from the lens.

Finally, in order to calculate the crosstalk due to optical misalignment, the boundaries for equation (4) are as shown in Figure 5.4 and mathematically described as follows. The intended lens is centered about $(x_1,y_1)=(-2d,0)$ and the dedicated crosstalk lenslet is centered about $(x_1,y_1)=(0,0)$. The Gaussian beam, described by $G(x_1,y_1)$, is nominally incident on the intended lens: a misalignment Δx_e brings the beam closer to the crosstalk lens, which means that $G(x_1,y_1)$ defined in equation (2) has the following values: $x_g=2d-\Delta x_e$ and $y_g=0$.

5.3.3 Calculation Results

Equation (4) for various values of misalignment error Δx_e was numerically evaluated using Matlab™ running on a Pentium processor. The incident beam had a diameter of $3w=3\text{x}38.8=116\mu\text{m}$ (99% encircled power) and the lens had side dimension $2d=125$ µm. These values were chosen because they were similar to those used in the systems described in the previous chapters: about 5µm of misalignment were permitted before close to 1% of the power was lost to clipping and crosstalk. Other values were λ=850 nm, f_μ=1mm.

Normalized contour plots of the crosstalk irradiance $I(x_f,y_f)$, where $I(x_f,y_f)=|U(x_f,y_f)|^2$ are given in Figure 5.5 for the region centered about $(x_f,y_f)=(0,0)$. Figure 5.5a-k show the contour plot of the normalized crosstalk irradiance as Δx_e is swept from 15μm to 115 μm in 10 μm increments.

For small values of the misalignment Δx_e, the diffractive effect at the discontinuity between the two microlenses is considerable and has the effect of smearing the crosstalk component incident about $(x_f,y_f)=(0,0)$ into a thin and narrow streak. As Δx_e increases, the diffraction at the discontinuity has a relatively smaller impact and the crosstalk irradiance is closer to being circularly symmetric. When Δx_e is approximately 125 μm, the beam is completely misaligned: the beam is incident on and centered on the crosstalk lenslet and the intended lenslet receives practically nothing.

It is interesting to note that the crosstalk irradiance patterns in Figure 5.5 are skewed toward the negative x direction, or toward the intended detector. This is due to the various diffraction orders of the diffractive lenslet. Simulations carried out for an ideal lens, namely a lens with coefficient C_l set to one and all other coefficients set to zero, reveal a crosstalk irradiance pattern which has symmetry in both x_f and y_f. This interesting aspect eventually could be exploited to develop a technique for testing the quality of diffractive microlenses.

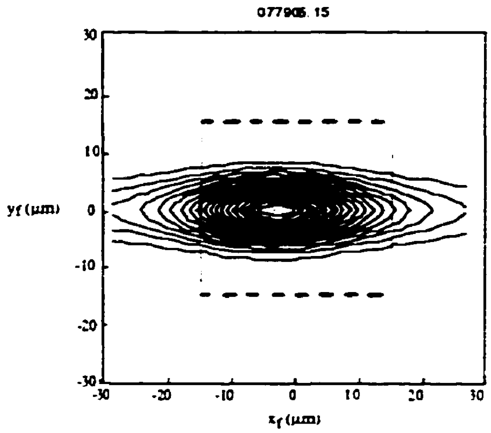
077905.15
y_f (μm)
x_f (μm)

(a)

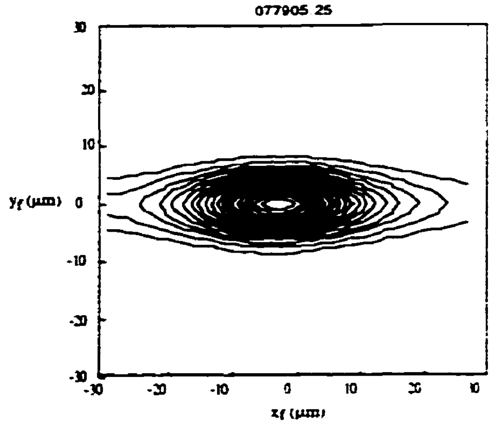
077905 25
y_f (μm)
x_f (μm)

(b)

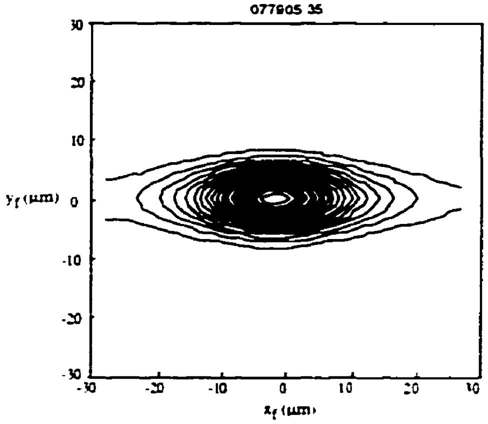
077905 35
y_f (μm)
x_f (μm)

(c)

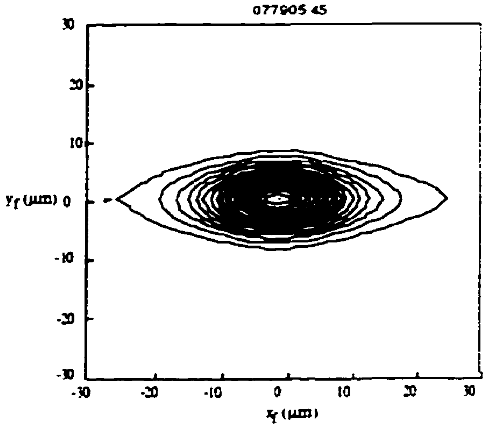
077905 45
y_f (μm)
x_f (μm)

(d)

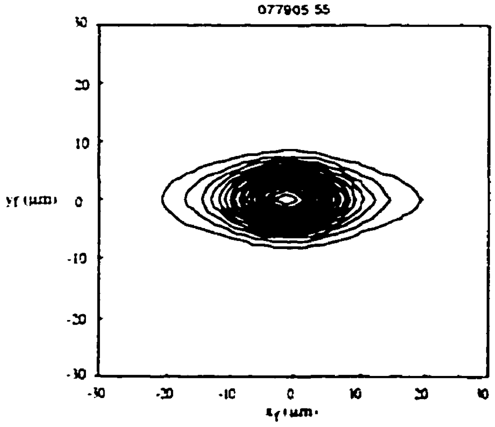
077905 55
y_f (μm)
x_f (μm)

(e)

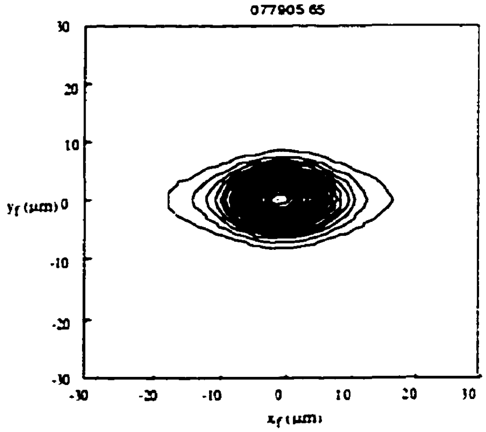
077905 65
y_f (μm)
x_f (μm)

(f)

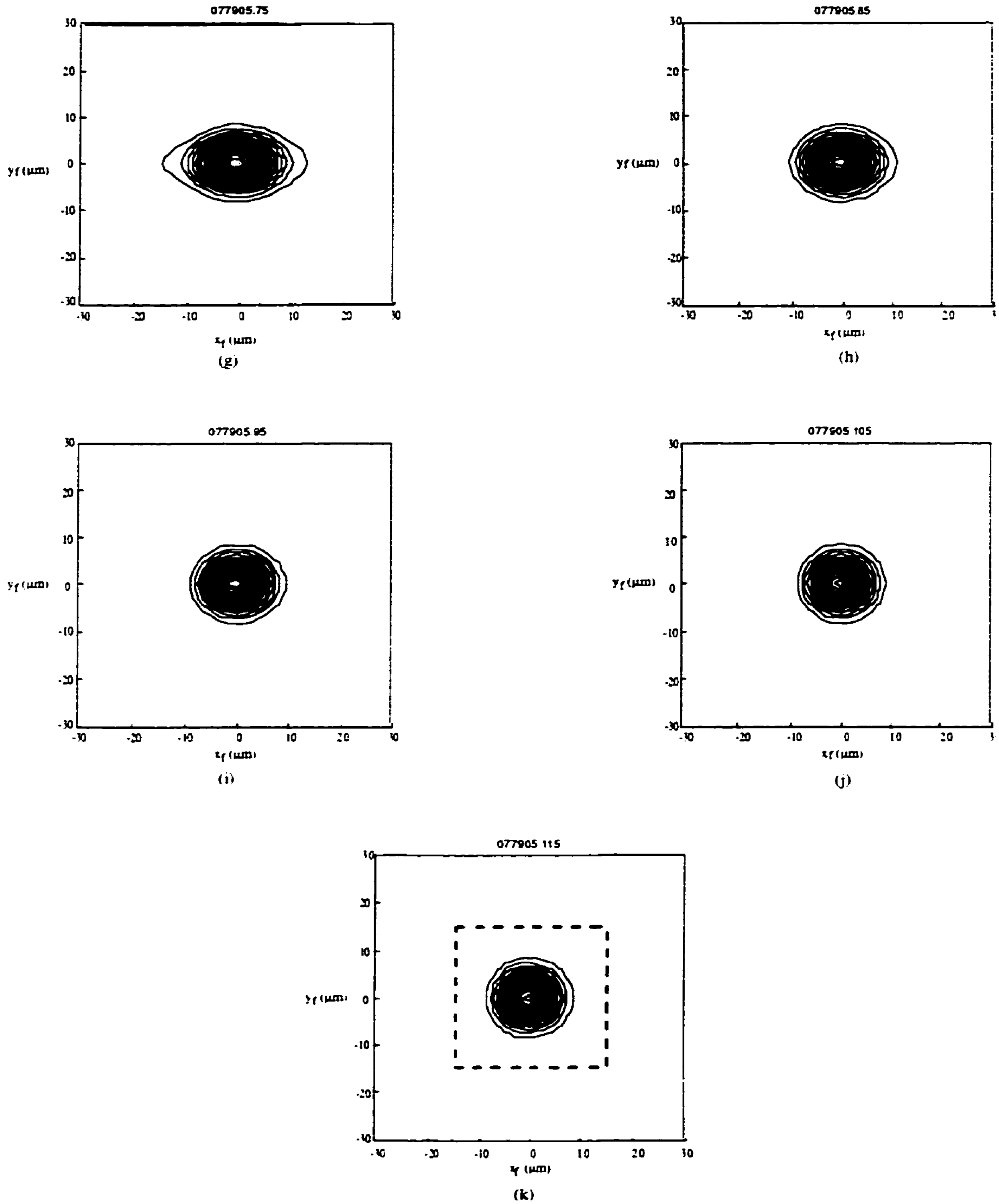

Figure 5.5a)-k): Irradiance pattern in the fourier field of the alignment lenslet as misalignment Δx_e is swept from 15μm to 115μm

5.3.4 Significance of the Calculation Results

The results above show that in situations of optical misalignment in a microlens-based relay, not all the optical crosstalk power will be coupled into a victim detector adjacent to the intended detector: because of the spreading effect shown in Figure 5.5, the victim detector will receive only a fraction of the power incident on the crosstalk lens, the rest being smeared out beside the victim detector. This can be seen in Figure 5.5a, where the dashed box shows the outline of a hypothetical 30μm x30 μm detector.

Another interesting observation can be made from Figure 5.5. Figure 5.5k, which represents the irradiance pattern produced by the crosstalk lens for a 115μm misalignment, can also be interpreted as being the irradiance pattern generated by the intended lens for a (125-115)=10 μm misalignment. This irradiance pattern is quite circular and close to the optimal perfect alignment case. The same can also be said for Figure 5.5i which can represent a misalignment of (125-95)=30 μm. This indicates that even for considerable misalignments (e.g. 30 μm for the case of this 125 μm lens), the intended detector will still see a reasonably compact, uniform and circularly symmetric irradiance pattern, and all the power incident on the intended lens will land on the intended detector. This can be seen in Figure 5.5k where the dashed box again represents a 30 μm x 30 μm detector.

In other words, for a situation of misalignment as shown in Figure 5.3, the signal-to-crosstalk ratio (SXR) at the detectors will be higher than the SXR at the lenslets for all reasonable values of misalignment ($\Delta x_r < d$).. This interesting phenomenon is a benefit of the diffractive spreading effect. To further illustrate this point, Figure 5.6 shows a plot of SXR (power) vs misalignment for the situation calculated above (w=38.8 μm, f_μ=1 mm, d=62.5μm). The solid lines indicate the SXR at the detector for $0 < \Delta x_r < 62$ μm with detector sizes ranging from 6 to 30 μm on a side. The dashed line represents the SXR at the lenslet. As can be seen, for a considerable range of misalignment the SXR at the detector is always at least 2.5 dB or more higher than the SXR at the lenslet, with smaller detectors having a higher SXR. Obviously, smaller detectors will couple less absolute power. as Figure 5.7 shows. The optimal detector dimension will depend on receiver characteristics. Therefore, in a major system design exercise where optoelectronic. optomechanic. optical and packaging designers collaborate, the plots in Figure 5.6 and Figure 5.7 could form part of a design space for and influence receiver design. For example, a smaller detector could have a lower bit error rate since the SXR would be lower but would receive less power and thus run slower than a large detector, assuming the receiver design is of the sense-amplifier type which is relatively unaffected by detector size and its associated capacitance [13]. The diffractive analysis presented in this section thus could be used as an input parameter for a receiver design optimization.

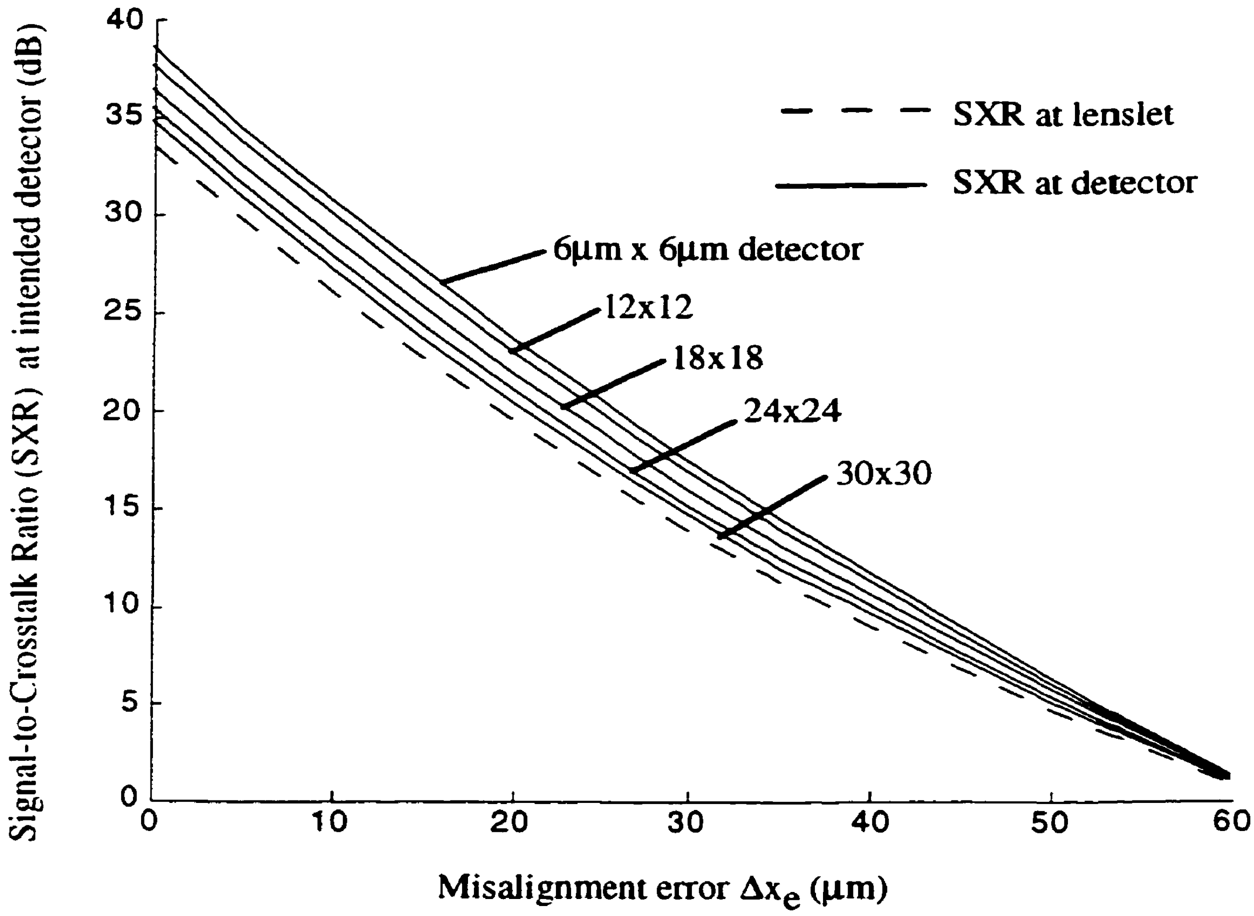

Figure 5.6: SXR at lenslets and SXR vs misalignment Δx_e for various detector sizes

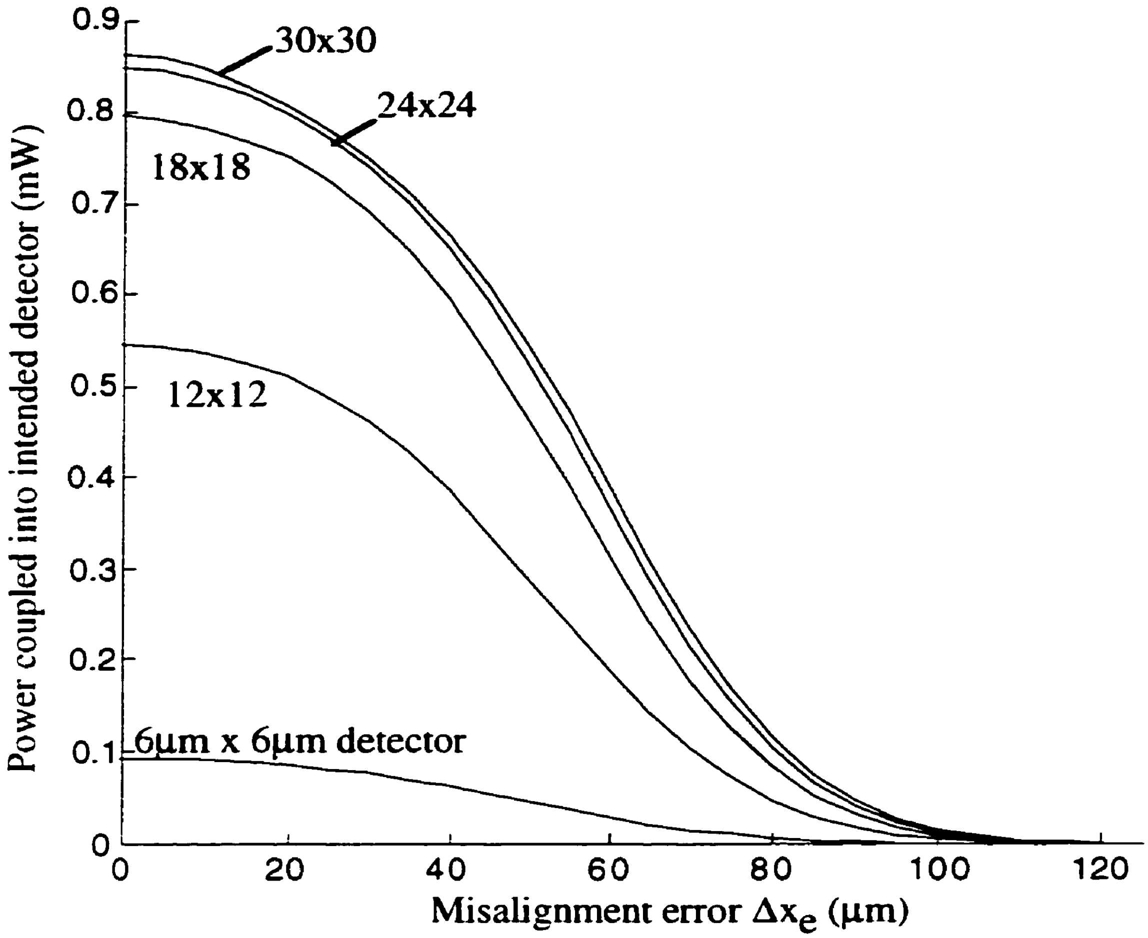

Figure 5.7: Total power coupled vs misalignment error

5.4 Dedicated Alignment Detectors

The crosstalk effect which was analyzed in the preceding section can be exploited to yield practical results. This section presents a novel concept which consists of inserting additional lenslets with corresponding dedicated alignment detectors at the focal plane in order to collect the crosstalk light from a misaligned signal beam, as shown in Figure 5.1; appropriate processing can then be performed to determine the extent of the misalignment. (Additionally, if detectors on either side of the array record an increase in crosstalk power, then defocus, as opposedto lateral misalignment, is most likely the problem.)

For the work presented here, a 6x6 array of signal detectors with eight dedicated alignment detectors at the periphery was fabricated. The upper right 3x2 subarray of detectors along with alignment detectors is shown in Figure 5.8. The chip will be further discussed in the next chapter.

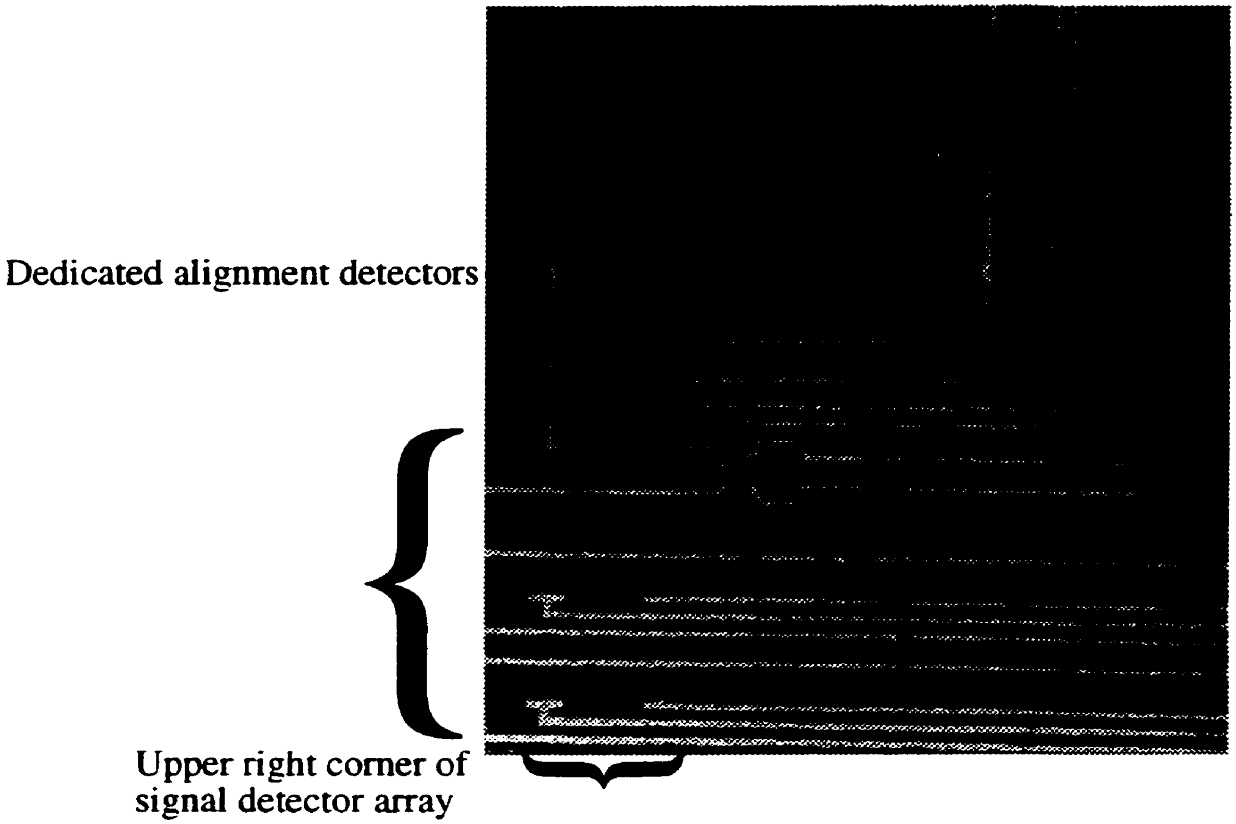

Figure 5.8: Portion of 6x6 signal detector array along with dedicated alignment detectors at the corners

5.4.1 Optimization of Alignment Detectors

Given a dedicated alignment lenslet sending crosstalk power into a dedicated alignment detector, it is desirable to have the alignment detector collect as much crosstalk power as possible. An optimal choice would be to have the dedicated alignment detectors laid out in the approximate shape of the crosstalk 'smear' shown in Figure 5.5a,b,c and as such collect more crosstalk power than any signal detector with a conventional rectangular or circular shape having the same total area. As a result, the full extent of the misalignment can be measured and ultimately be corrected or at the very least flagged before the crosstalk has a significant adverse effect on overall system performance.

Ideally, the alignment detector would have infinite area since the crosstalk power is theoretically spread out over an infinite area. A more practical consideration limiting alignment detector area is the dark current of the receiver: if the alignment detector is too big, the photocurrent produced by the optical crosstalk incident on the alignment detector could be drowned out by the dark current of the alignment detector itself. An optimization is thus required for best performance.

(An aside about dark current considerations is now in order. Admittedly, the dark current is DC whereas the crosstalk photocurrent would come from a modulated signal beam: as a result, the crosstalk power would also be modulated and the modulated crosstalk photocurrent could then be separated from the dark current. However, this could require sophisticated processing, especially if the data stream has such a high bit rate that the alignment receiver can only detect the envelope of the modulated crosstalk power: this sophisticated processing goes against the grain of this concept which is to simplify alignment error detection. This is especially true since the alignment detector is much greater than the signal detector and therefore has a greater capacitance, reducing the rise time. Much of the research directed toward receiver design [14] could be used in this context, although receiver design is beyond the scope of this work).

The practical reality, therefore, is that dark current will limit the size of the detector. To optimize and design the alignment detector for the demonstration below a three step optimization process was performed. This process took into account the (claimed) dark current and other performance characteristics of the particular device technology used for the array in Figure 5.8. The MSMs used were to have a dark current, i_d, on the order of 700pA/μm^2 along with a responsivity of S=0.4A/W[15] at typical operating conditions and bias voltages (~3V) and at wavelengths close to 850nm.

In the first step, the MSM electrical characteristics were used in a custom Matlab™ program which defined the alignment detector one square micron at at time. Effectively, the program performed thresholding at every square micron and the detector was defined such that at every square micron of the detector, the dark current was less than the expected photocurrent due to crosstalk irradiance, $I(x_f,y_f)$, originating from a λ=850 nm, w=38.8μm, 1mW beam with a misalignment of Δx_e=10 μm with respect to an intended lenslet adjacent to the crosstalk lenslet. Mathematically, the optimization could be expressed as the boolean expression:

$$D(x_f,y_f) \quad = \quad [S \times I(x_f,y_f) > i_d] \tag{5}$$

where $D(x_f,y_f)$ is the boolean array defining the detector, and all other terms are as defined above.

This yes/no thresholding generated a boolean array which resembled the diffraction pattern at the given 10μm misalignment, as shown in Figure 5.9. In this case, however, the optimization was performed for the (symmetric) diffraction pattern of an ideal lens (i.e. with no higher or zero orders), making it more general, although the optimization process is identical for any diffraction pattern. Moreover, space constraints dictated that the maximum length be set to 125 μm even though the optimization algorithm could have made the detector longer. In step 2, for ease of fabrication, only the envelope of the pattern was retained to avoid leaving gaping holes in the detector, as shown in Figure 5.9. This was acceptable since these holes shifted considerably whereas the overall envelope shifted less as Δx_e changed. In step 3, a further program was written which generated a .CIF file corresponding to the finger layout of the MSM implementing the alignment detector based on the envelope of the thresholded array. The net result was an optimized alignment detector as shown in Figure 5.8. It should be noted that the alignment detector geometry was further modified by stretching it 4 μm in both the x and y directions in order to take into account possible misalignment between the device array and the microlens array. This had the effect of giving the alignment detector a slightly rounder shape and as such gave, in theory, a slightly less efficient detector compared to the optimal design. This was a cost associatedwith difficulties in device-to-lenslet alignment. For fabrication purposes, the ideal shape had to be further truncated, although the diffraction outline is still quite visible.

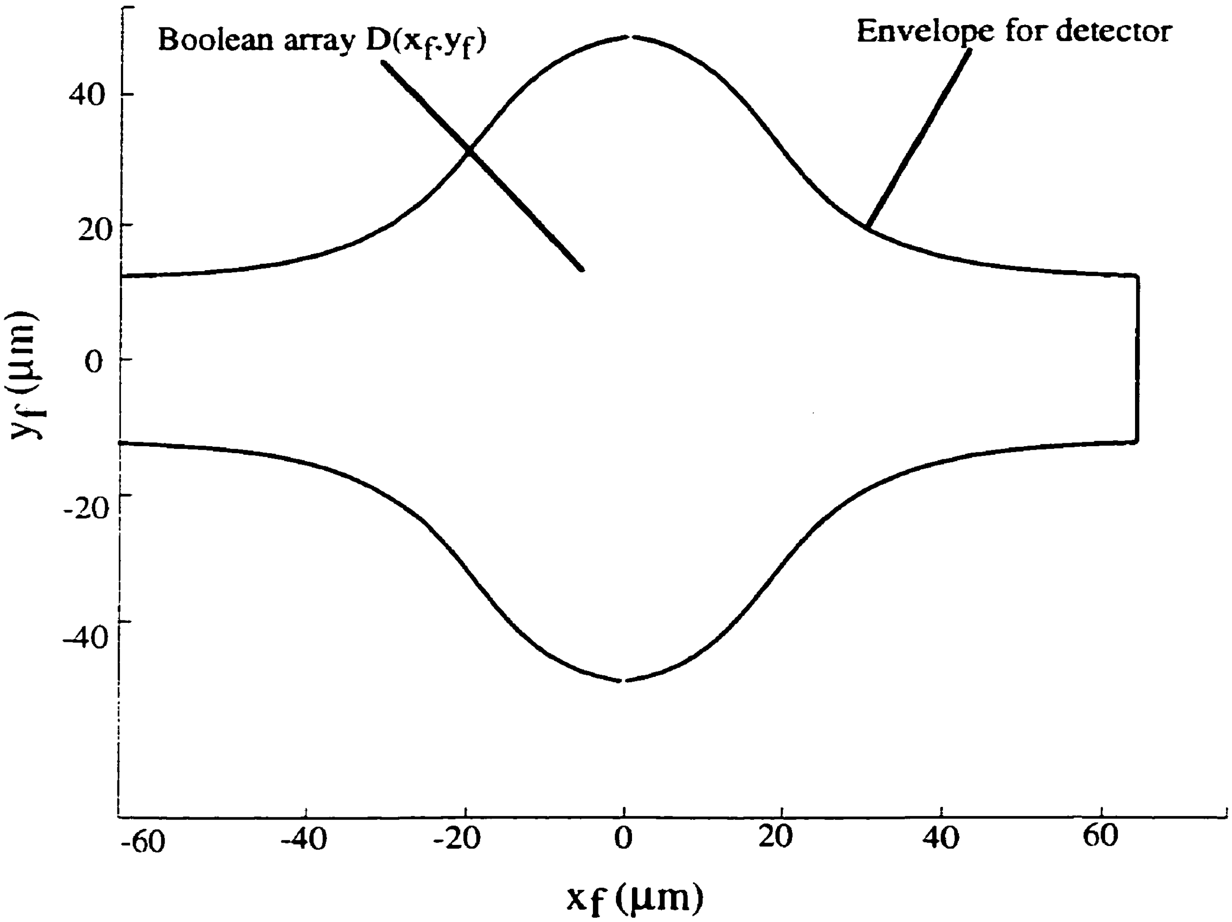

Figure 5.9: Optimum alignment detector shape. Each black dot marks a position (x_f, y_f) for which $D(x_f, y_f)$=TRUE

The 10 μm criterion used for the definition of the detector was justified as follows: experimental work in previous chapters indicated that components often move by ~5 μm when components are tightened or glued. Moreover, a 5μm drift thereafter can be expected as was shown in plots of long term drift of previous chapters. Therefore, optimizing a system to detect best a 10μm misalignment is reasonable. However, for any value close to Δx_r = 10 μm, the theoretical performance will only be slightly sub-optimal, and will degrade quite slowly with increasing misalignment. It should be noted that this configuration is optimal for misalignments in either x or y, although small combined displacements will still yield a good performance. For large combined x-y displacements, a detector optimized with different parameters should be designed.

Looking closely at the alignment detectors in Figure 5.8, it can be seen that they have different shapes based on their orientations: the alignment detectors along the x-direction have a shape very similar to that of the ideal optimized detector of Figure 5.9. However, the ones along the y-direction are starkly different and effectively look like big squares. The device growers later explained that fabrication difficulties encountered in the epitaxial lift-off process were such that it was feasible to have fine features in only one of either the x or y directions. As a result, some experiments below were only performed for the Δx_r case, although it is safe to assume that Δy_r would have behaved similarly if different technology had been used.

5.5 Measured Diffraction Patterns from Crosstalk Lens

Experiments were conducted to validate the above models and calculations. The first experiment, described in this section, consisted of observing the irradiance pattern at the focal plane of a crosstalk microlens as the misalignment Δx_r was increased. In this setup, the misalignment Δx_r was swept from 0 to 125 μm and the irradiance pattern at the focal plane of the crosstalk lens was observed.

5.5.1 Observation Setup and Calibration

The observation setup consisted of a x40 objective which imaged the crosstalk irradiance pattern into a linear CCD camera, as shown in Figure 5.10. The CCD output was then sent to a frame-grabber which digitized the image and converted it to a 640x480 image matrix with an 8 bit depth (256 grey levels).

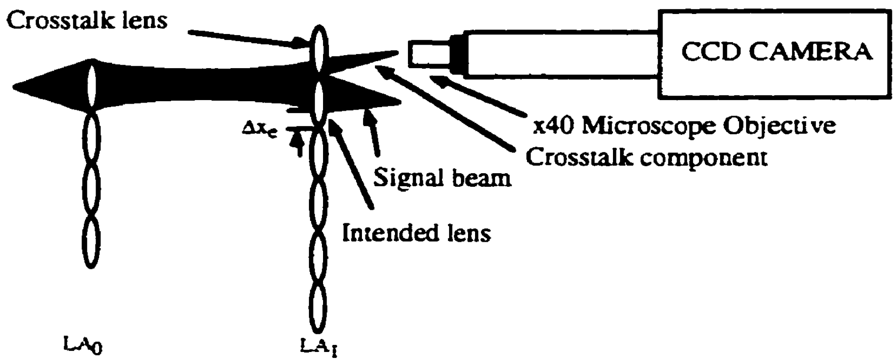

Figure 5.10: Setup for observing crosstalk at focal plane

All practical observation setups, including this one, have a non-ideal impulse response and effective transfer function (ETF). If $I(x_f,y_f)$ is the actual irradiance distribution under observation and $S(x,y)$ is the combined ETF of the frame grabber, camera, and microscope objective, then the measurement result $M(x,y)$ can be expressed as:

$$M(x,y)=I(x_f,y_f)*S(x,y) \tag{6}$$

where * is the convolution operator.

In order to correct this situation, a four part process must be employed. The first part consists of observing a known irradiance step function. The second part consists of deducing the mathematical step response based on the observation of the known step function. In the third part, the combined ETF $S(x,y)$ is calculated from the step response measured in part 2. Finally, in the fourth part, the measured result $M(x,y)$ is deconvolved with $S(x,y)$ to obtain $I(x_f,y_f)$. In this case, a photomask with sharp edge was imaged to obtain the step response. From there the ETF was obtained and used to deconvolve measured images. An excellent explanation of this process can be found in ref [16]. It should be noted that the objective and camera were of good quality and as such deconvolution had little impact on the observed results. The image was then smoothed by averaging each pixel with the value of its eight adjacent neighbours and all background noise was subtratced. Each pixel corresponded to 0.39 μm.

The incident beam on the LA_1 lenslets had a width w measured at 39μm ± 2μm. calculated using digitizing and a Gaussian curve fitting algorithm: its profile is shown in Figure 5.11a and the beam incident on LA_1 is shown in Figure 5.11b. Note that Figure 5.11 is taken with the objective observing the actual LA_1 (x_l, y_l) plane (in Figure 5.11a the lenslets were moved out of the way to show just the beam through the substrate) whereas the data presented below are of course of the back focal plane (x_f, y_f) of the lens where the detector would normally reside.

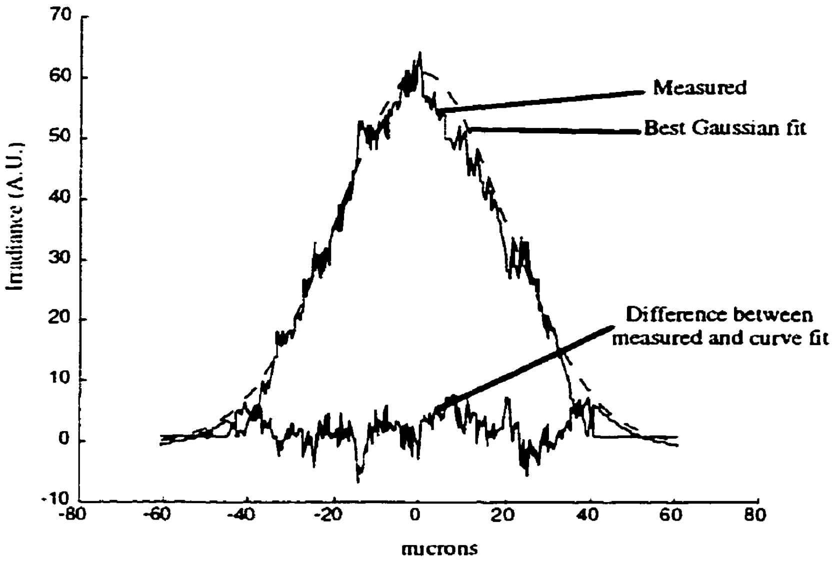

(a)

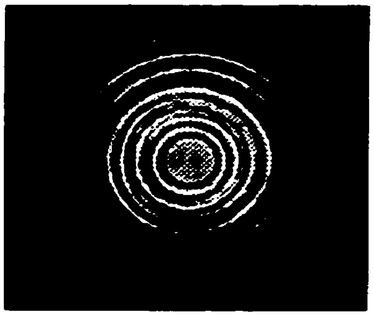

(b)

Figure 5.11: a) Profile of beam incident on LA_1 b) beam incident on LA_1

5.5.2 Qualitative Analysis

An image of the irradiance profile on the (x_f, y_f) plane of the signal beam with a misalignment of Δx_e = 15 μm along with the associated crosstalk component is shown in Figure 5.12a. For this misalignment value, the power in the crosstalk component was very small compared to the power in the signal beam; therefore, in order to see the crosstalk component, the incident power had to be greatly increased such that the signal beam saturated the camera. (This very low crosstalk power relative to the large amount of power into the system increased the measurement error for the 15 μm plot given below). A section cut of the two spots can be seen in Figure 5.12b. The smearing effect can be seen in the crosstalk component.

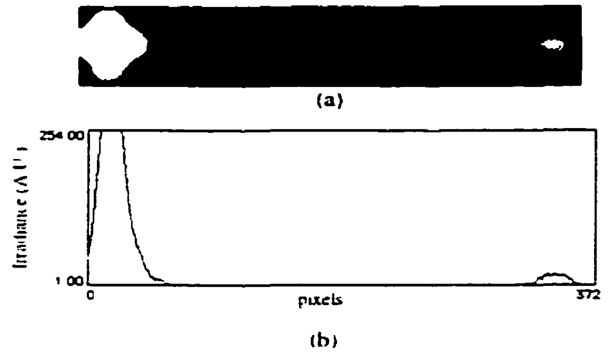

Figure 5.12: Signal spot and crosstalk spot a) picture b) profile

The deconvolved normalized contour plots of the crosstalk components are given in Figure 5.13for Δx_e.varying from 15 to 115 μm in increments of 10 μm. In general, the shapes of the measured contour plots are similar to the theoretical ones: as Δx_e increases, the shape of the crosstalk component changes from an elongated smear to one more closely approximating a circularly symmetric pattern.

Also, for small values of Δx_e, the centroid of the irradiance is distinctly shifted toward the -x direction, toward the intended target, as predicted by the calculations.

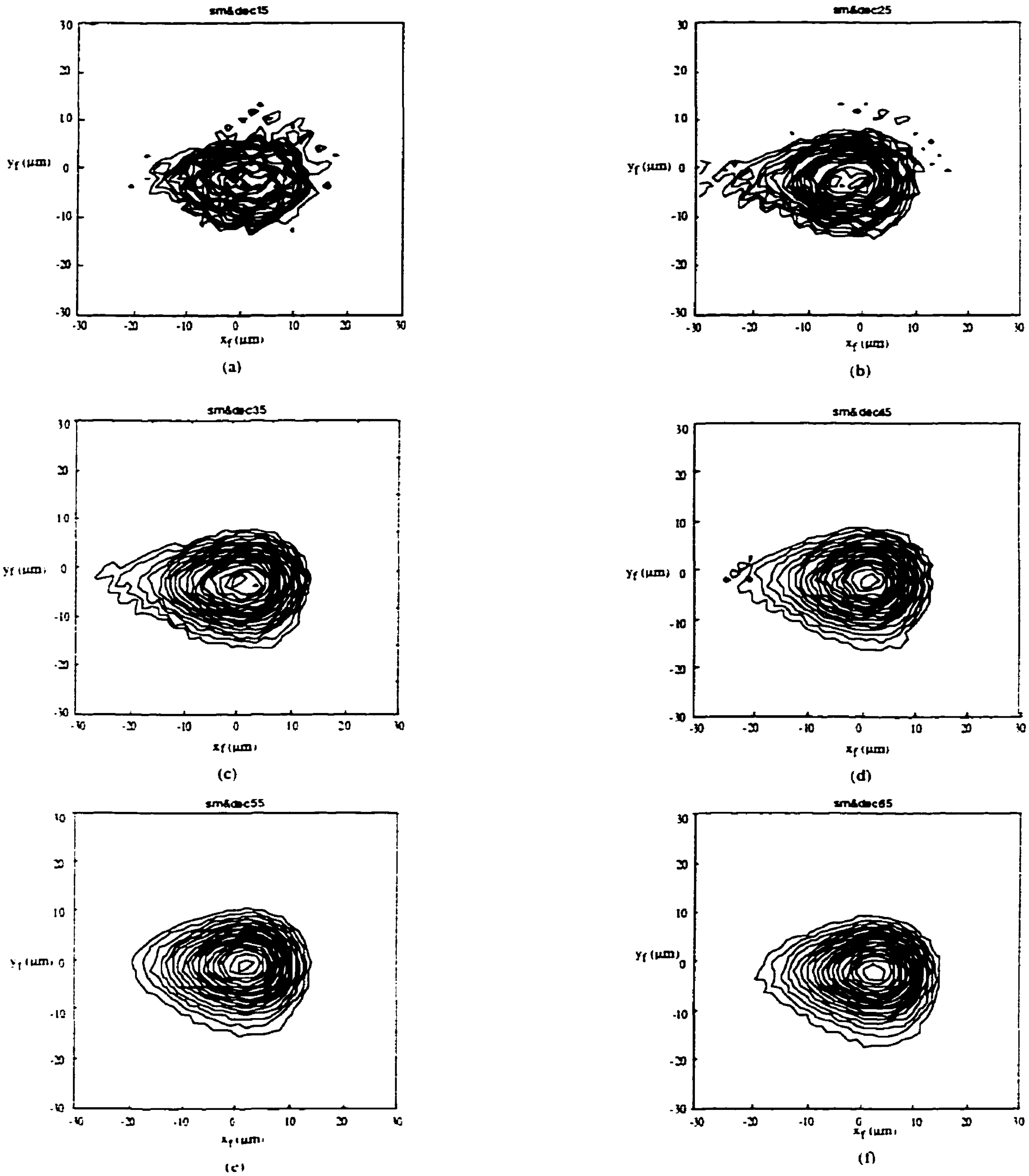
sm&dec15
sm&dec25
sm&dec35
sm&dec45
sm&dec55
sm&dec65
y_f (µm)
x_f (µm)
(a)
(b)
(c)
(d)
(f)

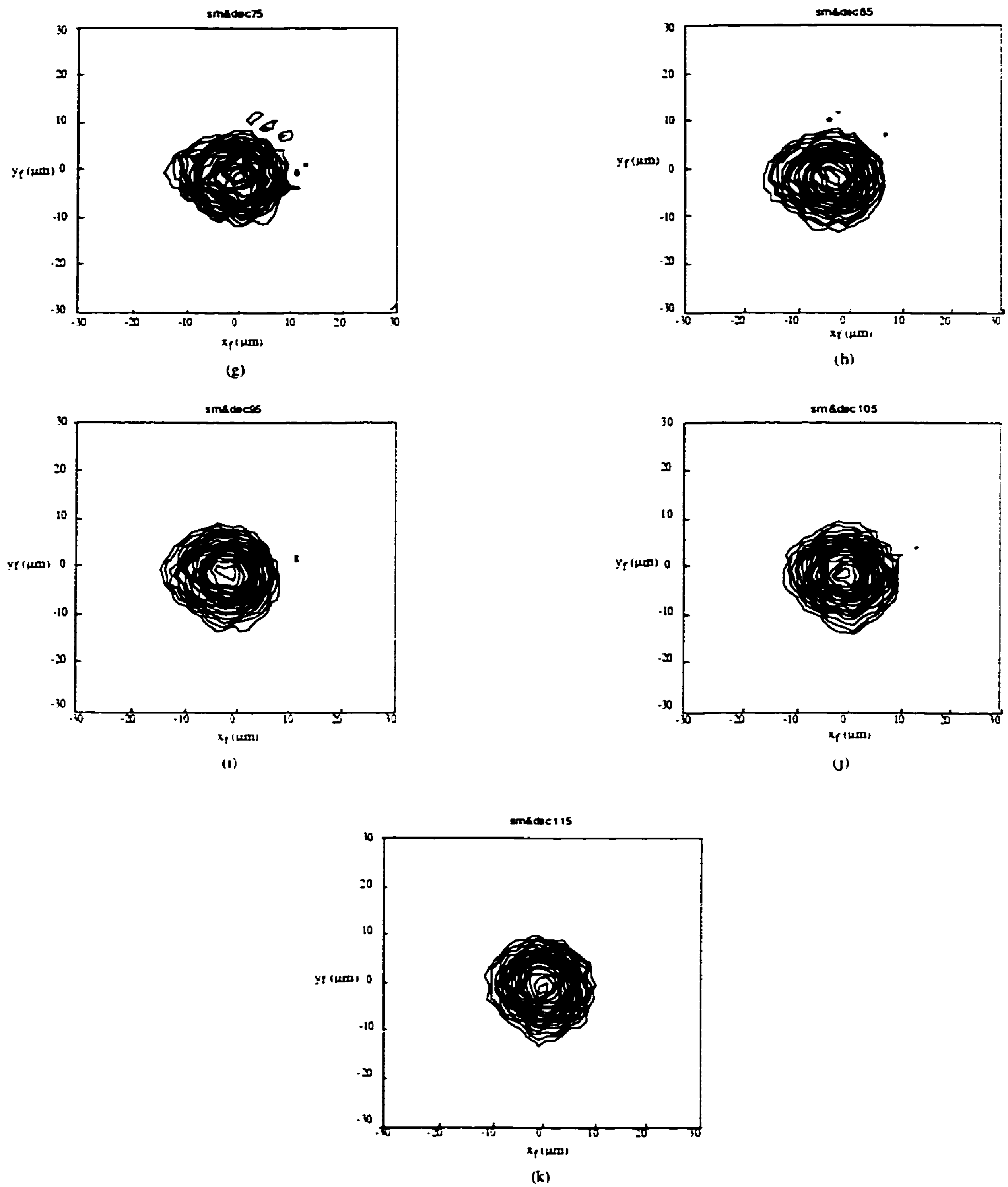

Figure 5.13: a)-k) Profile of measured irradiance crosstalk power as misalignment error swept from Δx_e=15 to Δx_e=115 μm

5.5.3 Quantitative Analysis

There appears to be a difference between the measured and theoretical plots in that the measured plots seem to be considerably more skewed toward the -x direction than the theoretical plots. To quantify this discrepancy, section cuts along the y_f=0 line were taken for all theoretical and measured plots and plotted on common axes. These are shown in Figure 5.14. The measured and theoretical section cuts are given. For each point along the section, the theoretical and measured value were compared. Table 5.1 lists the average error and standard deviation between measured and theoretical. As can be seen, the average error is generally under 10%. Since large positive and negative errors can cancel out in the averaging process, the standard deviation is also an interesting metric. The standard deviation is also in the 10% range.

Δx_e (μm)	% error between measured and theoretical along section	standard deviation of error along section (%)
15	-16	10
25	-7	9
35	2	9
45	1	9
55	5	9
65	9	10
75	2	8
85	4	10
95	8	10
105	9	10
115	8	11

Table 5.1: Comparison of measured and theoretical normalized irradiance profiles.

It should be pointed out that each line on the contour profiles represents a 5% increment in power, so differences in the lower contour profiles look impressive but actually represent very little power.

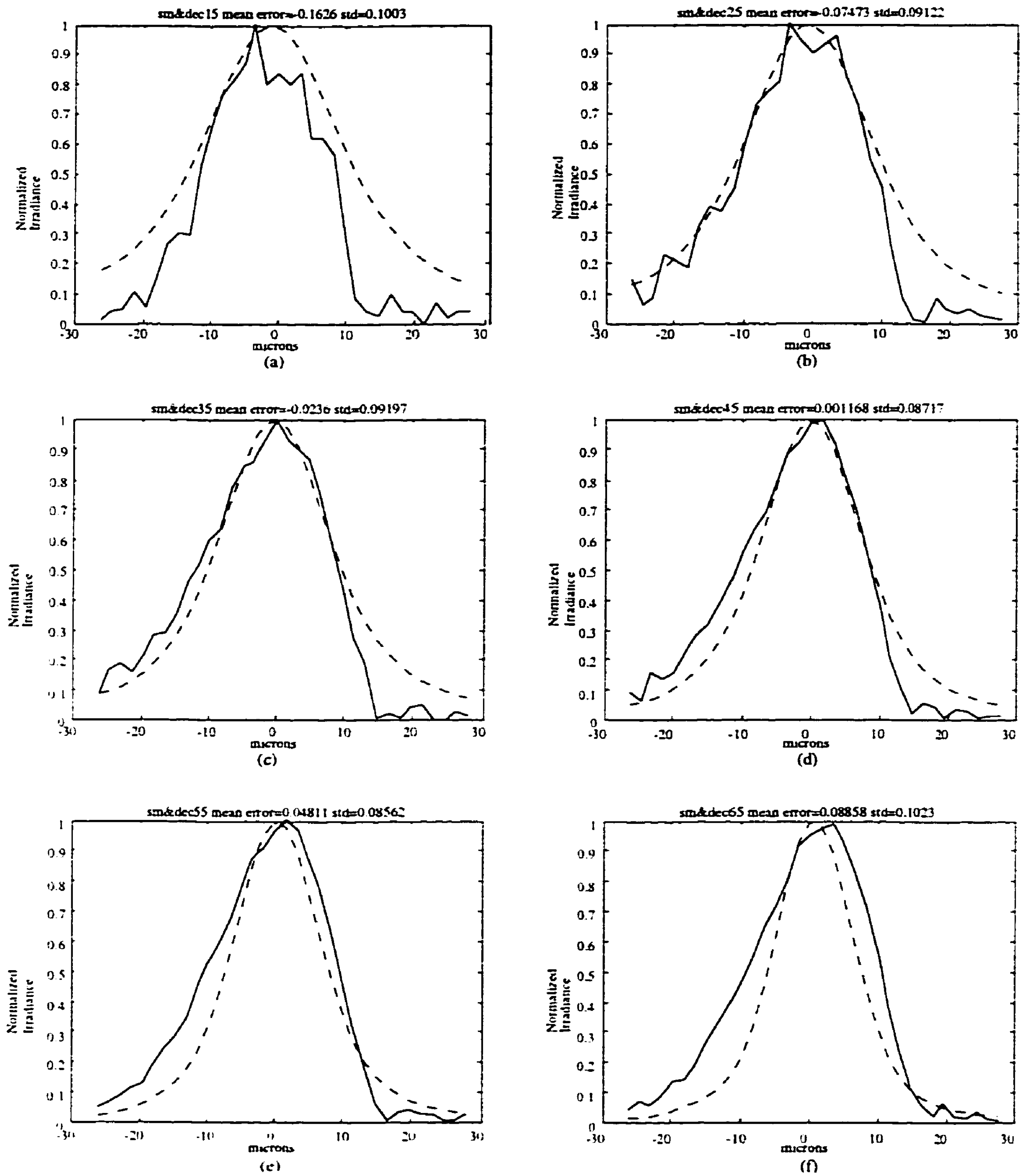

sm&dec15 mean error=-0.1626 std=0.1003
Normalized Irradiance
microns
(a)
sm&dec25 mean error=-0.07473 std=0.09122
Normalized Irradiance
microns
(b)
sm&dec35 mean error=-0.0236 std=0.09197
Normalized Irradiance
microns
(c)
sm&dec45 mean error=0.001168 std=0.08717
Normalized Irradiance
microns
(d)
sm&dec55 mean error=0.04811 std=0.08562
Normalized Irradiance
microns
(e)
sm&dec65 mean error=0.08858 std=0.1023
Normalized Irradiance
microns
(f)

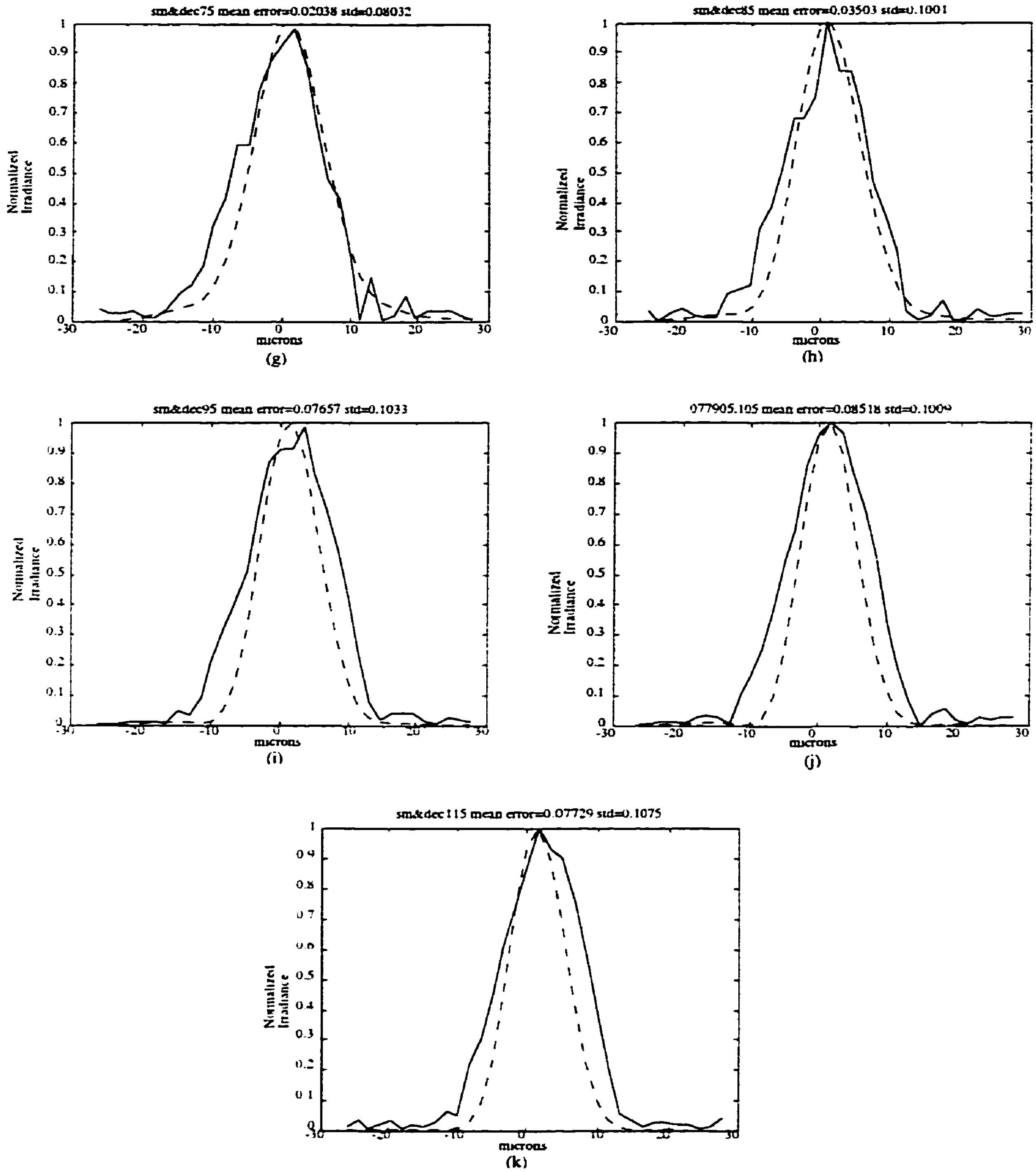

Figure 5.14a)-k) Section cuts comparing predicted with measured crosstalk irradiance

5.5.4 Discussion of the Results

The principal cause for this discrepancy is the model itself. As was pointed out above and in the appendix, the diffractive lens actually has 8 diffractive levels in the middle and 4 at the periphery whereas the model assumed the lens was uniform with "average" field diffraction coefficients C_0, C_1, and C_5. Therefore, as the incoming signal beam was swept across the lens, different parts of the beam effectively encountered different diffraction efficiencies. Other sources of error include non-idealities in the original beam as well as error in obtaining and measuring the original beam width. Additionally, the position of the microscope objective could have been such that it did not image exactly at the (x_f, y_f) plane but rather could have been up to 10μm off in the z direction, causing the images to be defocused. Finally, even though every effort was made to clean the lenses and keep them clean, there still could have been a small amount of dust which could have scattered light into the observed areas.

5.6 Performance of Alignment Detection System

The second experiment, described in this section, consisted of placing the detector array at the appropriate place behind the lenslets and quantifying the performance of this system for using crosstalk to measure misalignment. Proper alignment of the detector array behind the lenslet array was a difficult task in its own right: the following chapter indicates how this was accomplished.

Before starting, it was necessary to measure MSM performance. All voltage sweeps and current measurements below were conducted using a Hewlett Packard 4145B semiconductor parameter analyzer.

5.6.1 MSM Characterization

Responsitivity, measured in amps/watt of incident power, and dark current, measured in amps were measured for both signal and alignment detectors. A separate measurement rig was built for this purpose. The results are shown in Figure 5.15 and Figure 5.16 respectively. The first plot indicates that the responsitivity for 850nm light, at about 0.17 A/W was less than half the expected 0.4 A/W. The second plot indicates that the total dark current for the alignment detector was about 7 μA at the recommended 3V operating voltage. Dividing this value by the area of the alignment detector, approximately 5000μm^2, yielded a dark current value of 1.4nA/μm^2, or twice the 0.7nA/μm^2 design value. All detectors had similar values, although the signal detectors had a responsitivity about 10% lower than the alignment detectors'.

Since the alignment detector was optimized for an incident power of 1mW and a sensitivity of 0.4 A/W (among other parameters given above), it was necessary to double the incident power to compensate for the actual detector which had only half the sensitivity.

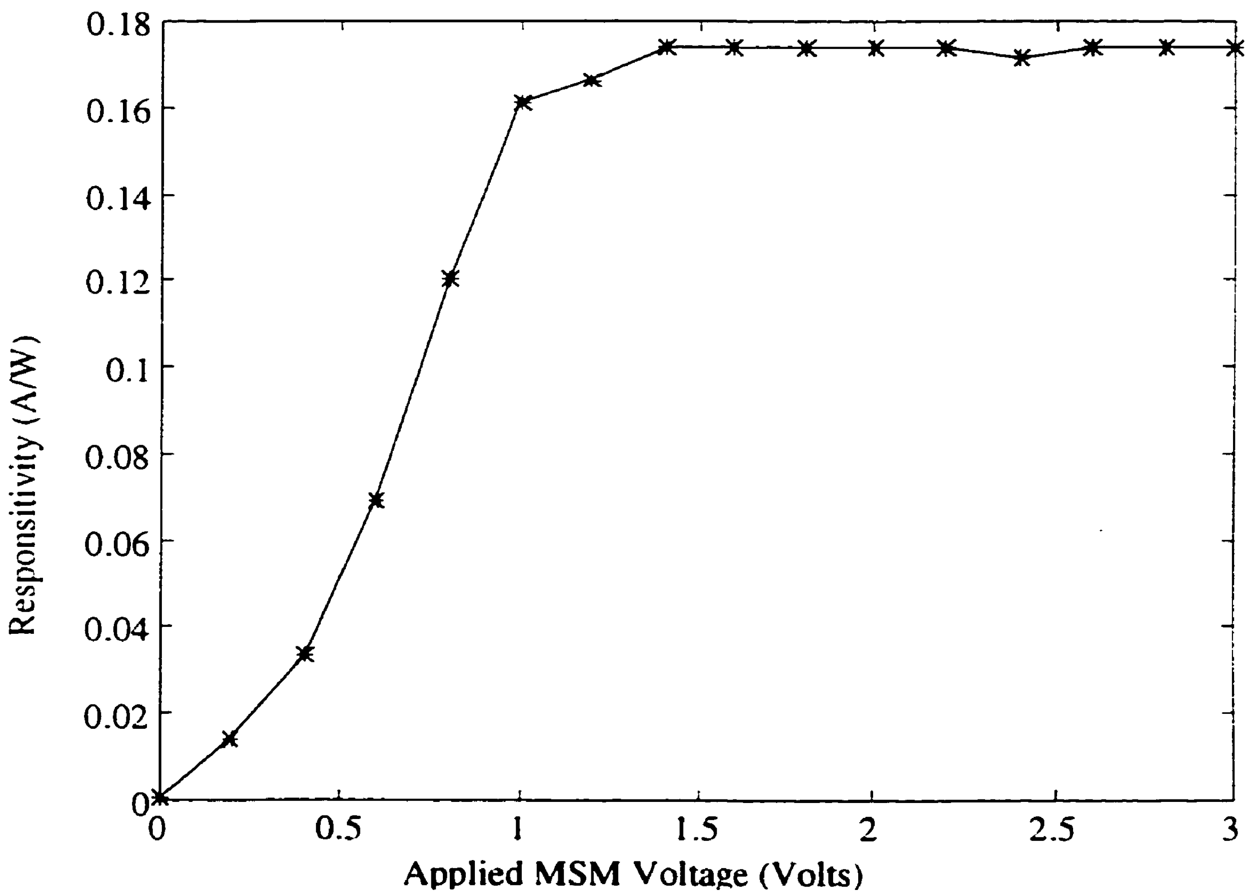

Figure 5.15: Responsivity of MSM alignment detector

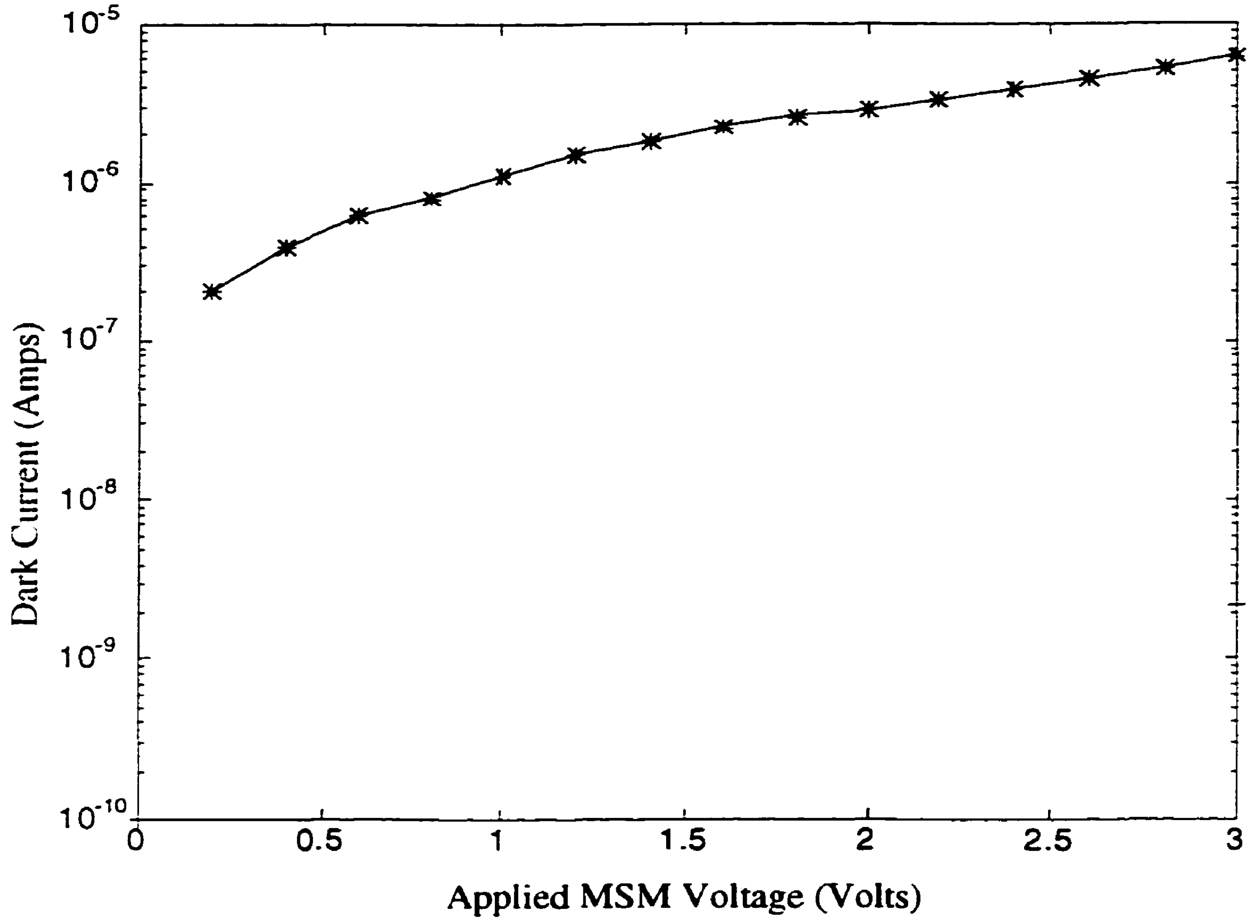

Figure 5.16: Dark current vs applied voltage for alignment detector

5.6.2 Results

The misalignment Δx_r of a beam incident on an intended lenslet was swept from 0 to 125 μm. Two photocurrents were monitored while this was carried out: 1) the photocurrent from the intended signal detector behind the intended signal lenslet and 2) the photocurrent from the optimized crosstalk alignment detector behind the alignment lenslet. The result is shown in Figure 5.17, along with theoretical curves.

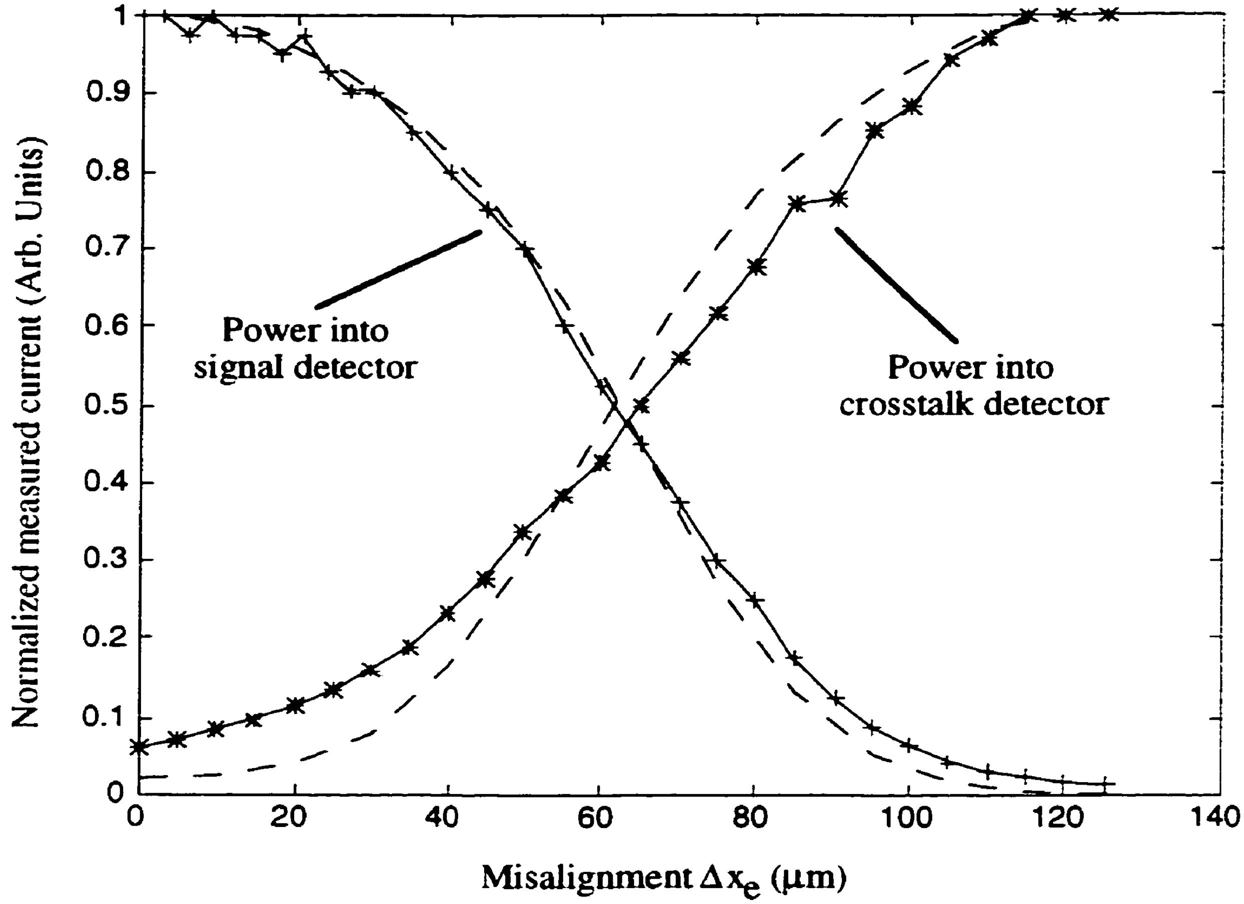

Figure 5.17: Power coupled into signal and alignment detector as misalignment swept from 0 to 125 μm. Solid: measured; dashed: theory

5.6.3 Discussion

Overall, the system worked as expected: information about misalignment was generated by measuring crosstalk in dedicated alignment detectors and the measured values were quite close to the theoretical ones. There are a few discrepancies. The photocurrent from the crosstalk detector can be seen to higher than expected, especially at the critical lower values. This is attributable to many factors, such as an incident beam slightly too large, a few microns of misalignment between the detector and lenslet array, and inaccuracies of the model which averaged the effect of a discontinuity in the lenslet. Moreover, the actual MSM specs were not quite what had been expected.

Finally, the lenslet fabrication technology is important and is worthy of mention. Today, designers can choose from two leading approaches, namely refractive and diffractive as well as from other approaches, such as holographic and graded index lenslets. Proponents of refractive components point to their higher efficiency due to the absence of higher orders, their ability to achieve higher numerical apertures and their approximate invariance of focal length for different wavelengths[17,18]. Diffractive optics, on the other hand, have the advantage of very controllable and repeatable characteristics as well as higher fill factors in arrays since they can be made in any shape[19]. Both technologies claim to be able to deliver inexpensive lenslets in industrial quantities. From the specific perspective of crosstalk performance, however, the calculations indicate that refractive lenslets (which could be approximated using C_l=1, in equation (4)) scatter crosstalk light into a smaller area: this could be interpreted as meaning that refractive lenslets have better crosstalk performance when compared to diffractive lenslets. This conclusion had already been arrived to in another context, namely one of space-variant interconnects[20]. However, if the technique presented in this chapter is used to generate diagnostic information, then diffractive components could be more desirable since an optimized alignment detector could capture more crosstalk power and ultimately serve to detect a state of misalignment before it started affecting overall system performance.

5.7 Implications

This chapter presented a novel concept of using optical crosstalk for diagnostic of misalignment in free-space optical interconnects and gave results of experiments conducted to verify the concept.

The significance of the work extends to beyond simple alignment diagnostics, however. It was shown that diffractive effects have an impact on SXR performance of the overall system: the SXR at the detector is generally several dB higher than that at the lenslets for moderate misalignments. But there may be other consequences of the spreading effect. For example, diffracted light spreading out across considerable regions of a smart pixel die could generate photocurrents in places not expected by the integrated circuit layout team: these currents could upset bias points of transistors and cause them not to work properly. Designers should be aware of these potential effects. Moreover, in several instances, such as in the case of the orientation of the alignment detectors and the varying device characteristics, closer collaboration would have improved optimization. All these effects further demonstrate the importance of proper collaboration between all design teams in multidisciplinary projects such as FSOIs. (In a real system demonstrator, for example, it is rarely possible simply to double incoming power at the touch of a dial, as was done for a stand-alone experiment described above). Finally, this chapter further confirmed previous observations that the device-to-lenslet alignment and packaging is of critical importance and deserves further study. This is covered in the following chapter.

5.8 References

1 S. Tang, R. T. Chen, L. Garrett, D. Gerold, and M. M. Li, "Design limitations of highly parallel free-space optical interconnects based on arrays of vertical cavity surface-emitting laser diodes, microlenses, and photodetectors," *Journal of Lightwave Technology*, 12, pp. 1971-1975 (1994).

2 H. J. Zhou, V. Morozov, and A. Fedor, "Analysis of a vertical-cavity surface-emitting laser-based bidirectional free-space optical interconnect," *Applied Optics*, 36, pp. 3835-3853 (1997).

3 T. Yamamoto, M. Yamaguchi, K. Hirabayashi, S. Matsuo, C. Amano, H. Iwamura, Y. Kohama, T. Kurokawa, and K. Koyabu, "High-density digital free-space photonic switches using micro-beam optical interconnections," *IEEE Photonics Technology Letters*, 8, pp. 358-360 (1996).

4 H. Yamazaki, T. Matsunaga, S. Fukushima, and T. Kurokawa, "4*1204 holographic switching with an optically addressed spatial light modulator," *Applied Optics*, 36, pp. 3063-3069(1997).

5 K. Raj and R. A. Athale, "Cross-talk analysis and reduction in fully parallel matrix-matrix multipliers," *Applied Optics*, 34, pp. 6752-6757 (1995).

6 E. G. Churin, P. Bayvel, J. E. Midwinter, and A. M. Hill, "The influence of aperture size and shape on crosstalk level in free-space grating demultiplexers for WDM networks," *IEEE Photonics Technology Letters*, 8, pp. 1337-1339 (1996).

7 G. C. Boisset, B. Robertson, W. Hsiao, H. S. Hinton, and D. V. Plant, "Detection of x-y misalignment error using optical crosstalk in a lenslet-array based free-space optical link in Optical Computing, Vol. 10, 1995 OSA Technical Digest Series (Optical Society of America, Washington DC, 1995), pp. 62-64.

8 A. Simpkins, "Measurement and performance of the modern backplane," *Electronic Engineering*, 67 (823), pp. 51-56 (1995).

9 G. H. Song, "Asymmetric dilation of multiwavelength cross-connect switches for low-crosstalk WDM optical networks," *Journal of Lightwave Technology*, 15, pp. 430-435 (1997).

10 J. Jahns and S. J. Walker, "Two-dimensional array of diffractive microlenses fabricated by thin film deposition," *Applied. Optics*, 28, pp. 931-936, (1990).

11 H. Kogelnik and T. Li, "Laser beams and resonators," *Applied Optics*, 5, pp. 1550-1567, (1966).

12 J. Goodman, "Introduction to Fourier Optics," Wiley and Sons, New York, (1985).

13 T. K. Woodward, A. V. Krishnamoorthy, K. W. Goosen, J. A. Walker, J. E. Cunningham, W. Y. Jan, L. M. F. Chirovsky, S. P. Hui, B. Tseng, D. Kossives, D. Dahringer, D. Bacon, amd R. E. Leibenguth, "Clocked-sense-amplifier-based smart pixel optical receivers," *IEEE Photonics Technology Letters*, 8, pp. 1067-1069 (1996).

14 A. Z. Shang, Ph.D Thesis, "Transceiver Arrays for Optically Interconnected Electronic Systems," McGill University, 1997.

15 M. A. Matin, K. C. Song, B. J. Robinson, J. G. Simmons, D. A. Thompson, and F. Gouin," Very low dark current InGaP/GaAs MSM-photodetector using semi-transparent and opaque contacts," *Electronics Letters*, 32, pp. 766-767 (1996).

16 G. L. Yip, P. C. Noutsios, and L. Chen, "Improved propagation-mode near-field method for refractive-index profiling of optical waveguides, *Applied Optics*, 35, pp. 2060-2068 (1996).

17 N. C. Craft and A. Y. Feldblum, "Optical interconnects based on arrays of surface-emitting lasers and lenslets," *Applied Optics*, 31, pp. 1735-1739 (1992).

18 C. van Berkel, B. P. McGarvey, and J. A. Clarke, "Microlens arrays for 2D large area image sensors," European Optical Society, Topical Meeting Digest Series: volume 2, Microlens arrays, pp. 81-85 (1993).

19 B. Dhoedt, P. De Dobbelaere, J. Blondelle, P. VanDaele, P. Demeester, and R. Baets, "Monolithic integration of diffractive lenses with LED-arrays for board-to-board free-space optical interconnect," *Journal of Lightwave Technlogy*, 13, pp.1065-1073(1995).

20 M. Hutley, "Case for refracting rather than diffracting optics in spatially variant interconnections," *Applied Optics*, 34, pp. 2448-2451 (1995).

Chapter 6: Integration of Optoelectronics and Microoptics

6.1 Introduction

As was indicated in previous chapters, a major problem encountered in the construction of optical interconnects is the alignment of optoelectronic device arrays to lenslets. This is a crucial step since accurate lenslet-optoelectronic alignment was shown to loosen considerably most alignment tolerances in the rest of the system. Moreover, integrated microoptic-optoelectronic packaging lets the components offer each other mutual protection. Consequently, developing techniques for producing these prealigned device/lenslet packages is an important part of optical packaging.

Current techniques addressing similar alignment problems in fibre and other optical interconnects include imaging fiducial alignment marks on the component substrate [1] – a technique widely used for alignment of different masks in VLSI circuit fabrication [2,3]. However, fiducial marks are of limited use for alignment during assembly of 3D optical interconnects since it is difficult to avoid lateral alignment errors incurred when imaging fiducial alignment marks on different xy planes.

A lenslet array on xy plane P_0 is to be aligned to an optoelectronic device array on another xy plane, P_B: the nominal z separation between the two planes is d and the lateral alignment error between the two, ε, must be kept below a given tolerance. The components with their marks are shown in Figure 6.1. By using traditional fiducial marks, alignment would consist of the following steps, 1) using a camera and microscope objective, image P_0 2) find fiducial marks F_{01} and F_{02} and register their position on a monitor screen 3) move camera and objective along the z direction a distance d and image P_B 4) find fiducial marks F_{B1} and F_{B2} and move the lenslet array in x-y until F_{B1} and F_{B2} coincide with their corresponding marks registered in the second step 5) glue the assembly with the appropriate spacers.

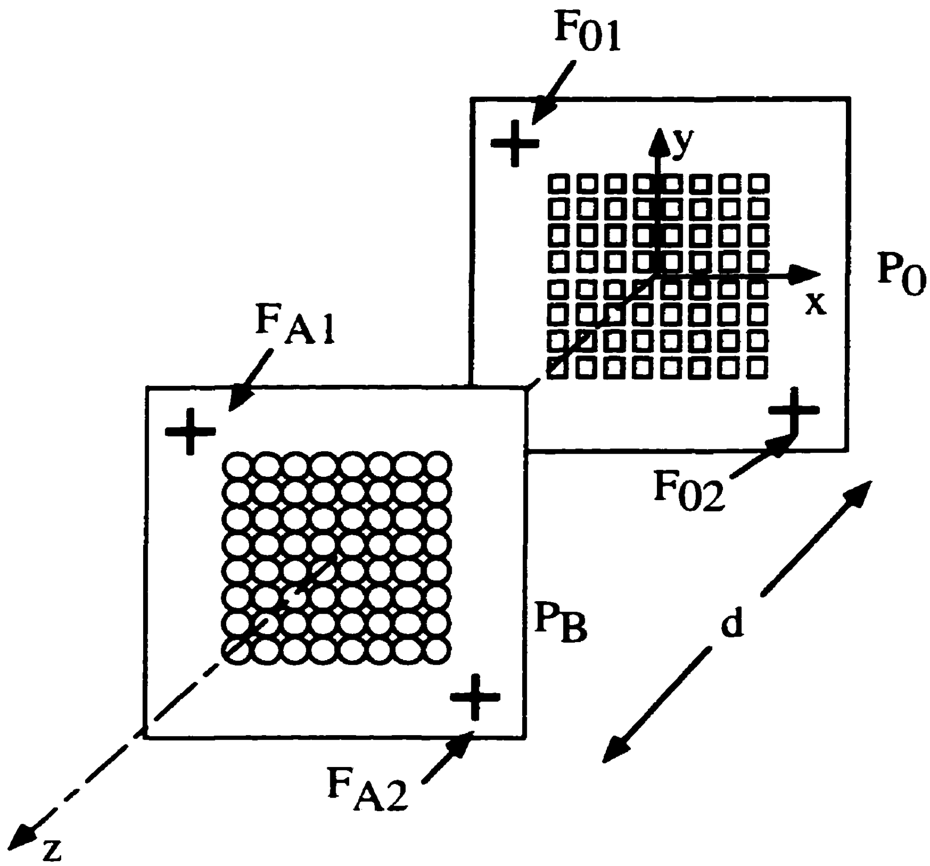

Figure 6.1: geometry of the lenslet-optoelectronic alignment problem.

The problem with this and similar techniques is that there are too many steps which can introduce errors, especially step 3. Accurately moving a camera and microscope objective back in z is time-consuming and inappropriate if more than prototype quantities are required. Moreover, movement in z also causes x-y movement, reducing the accuracy of the movement: the runout (deviation from intended axis of movement) of a typical laboratory-grade motorized stage has been noticed to increase rapidly from ~1 μm when new [4] to several microns after a few months of use. Modifying step 3 to move the components instead of the imaging system will not change the problem.

In order to avoid the third step, previous techniques have resorted to inserting additional components in the system, complicating assembly [5]. Other techniques in which lenslets are attached or defined during device fabrication also exist [6.7.8.9.10]. but these techniques, especially those involving solder-bump bonding, often have a maximum height of only several hundred microns, depending on geometry [6], which limits the range of values for d.

This chapter presents a new technique for aligning a lenslet array to an optoelectronic device array: reflective diffractive structures fabricated on the device die provide registration images during alignment. The advantages of this technique are that it requires very few steps during assembly and will work over a large range of values for d. The chapter is organized as follows. Section 6.2 gives a description of the proposed technique, along with packaging and fabrication considerations as well as a discussion of the results. Section 6.3 presents an improvement of the technique which consists of using actual electrical signal traces as the diffractive structure in order to save real estate on-die. Section 6.4 analyses the effect of perturbations on the diffractive structure in chips with several metal layers and suggests ways of minimizing this problem by appropriate choice of alignment wavelength. Section 6.5 concludes and gives a further discussion.

6.2 Description of technique

The objective of the technique is to align an array of lenslets of focal length f with respect to a packaged array of optoelectronic devices a distance d away from the lenslets, as Figure 6.2 shows. The technique can yield precise alignment in x, y and θ_z, and to some extent alignment in the other three degrees of freedom. There are three steps.

The first step consists of laying out reflective FZPs of focal length $f_{fzp} = d$ on the edge of the device array, and laying out alignment marks at corresponding positions on the edge of the lenslet array. For the experiment in this section, FZPs are defined beside an array of Metal Semiconductor-Metal (MSM) detectors, and corresponding marks ('donuts') are on the lenslet substrate as Figure 6.3 and Figure 6.4 respectively show.

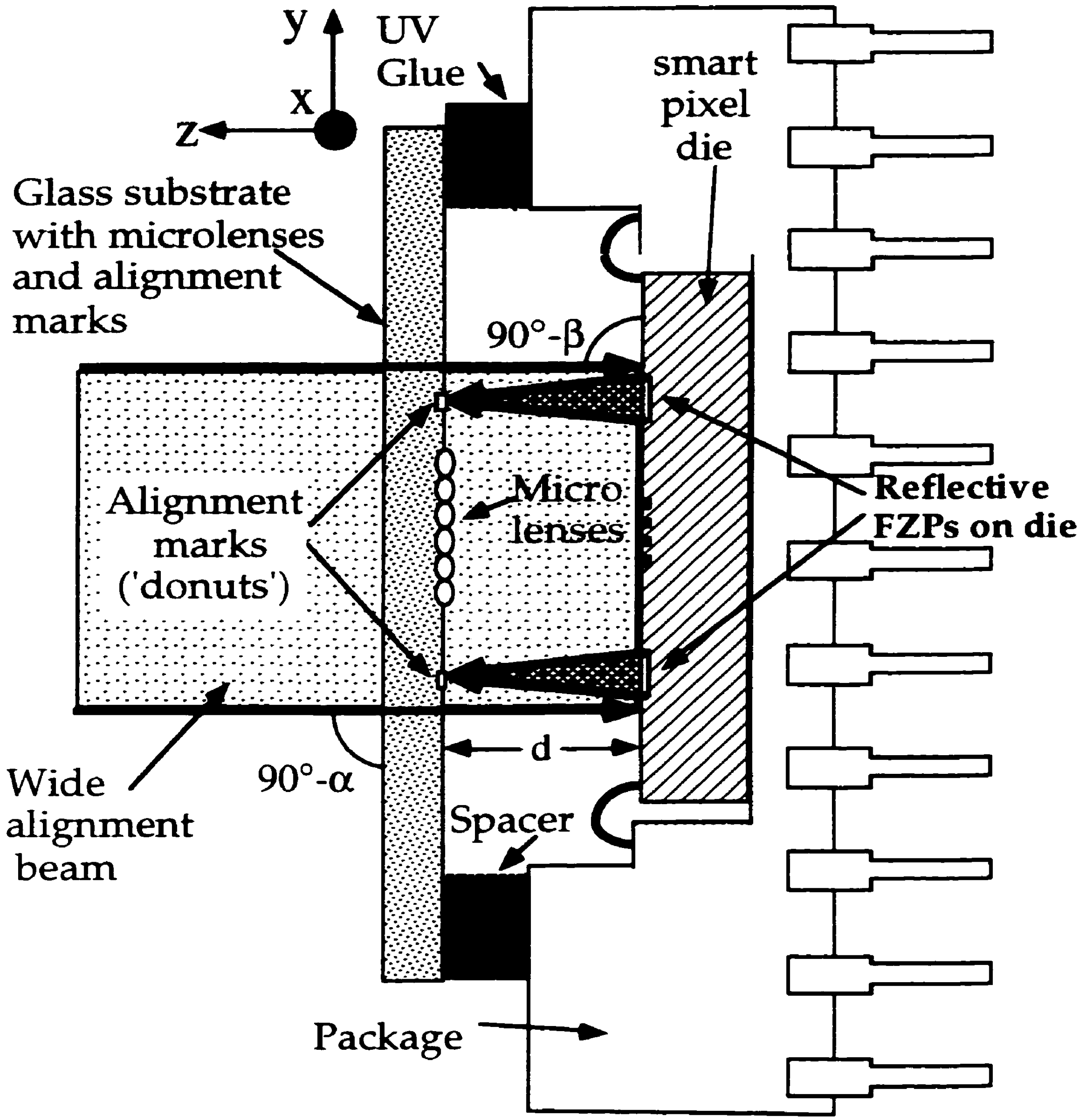

Figure 6.2: Schematic of technique: reflective diffractive structures on device die focus light back onto alignment marks

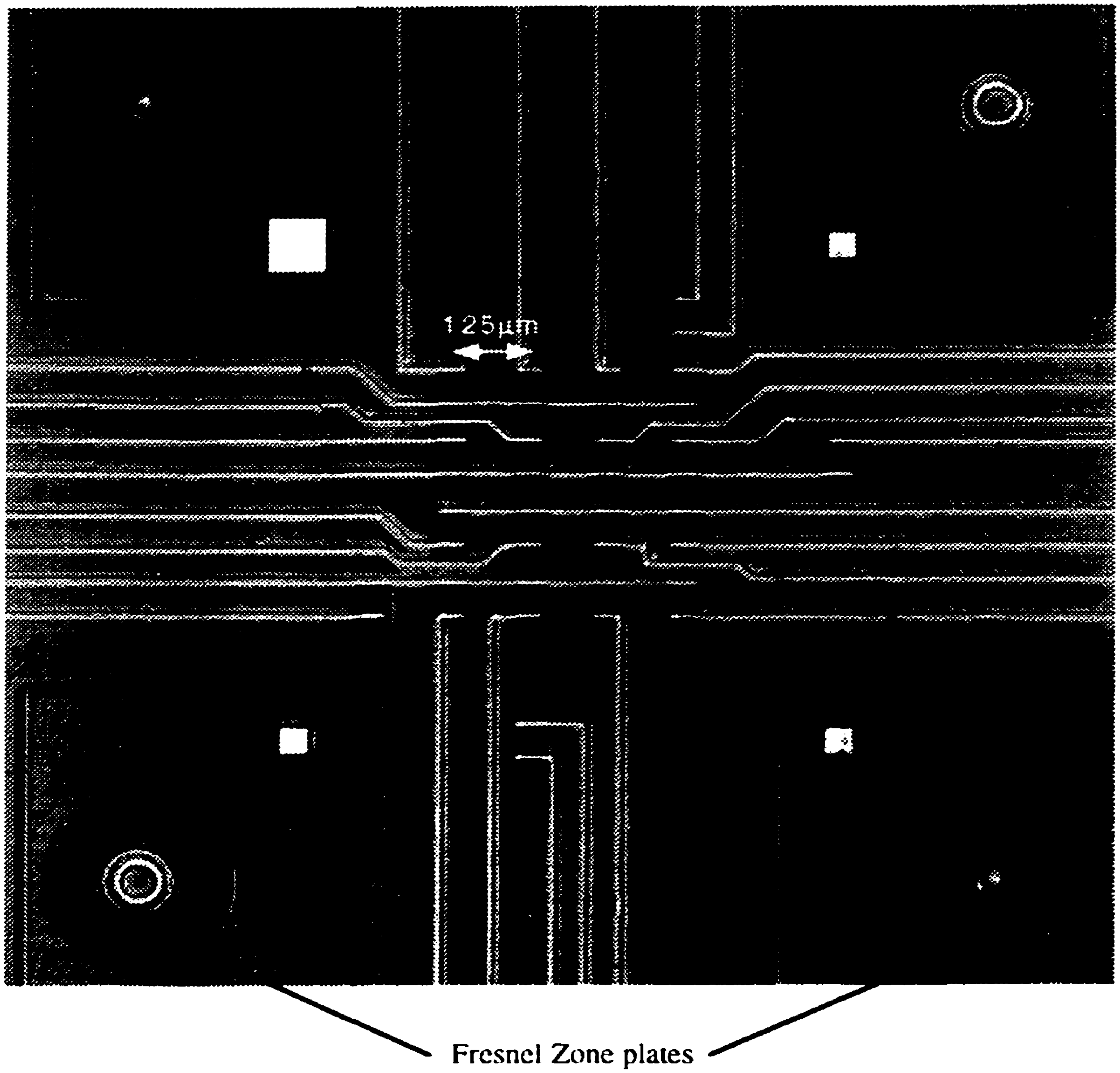

Figure 6.3: Fresnel Zone Plates for generating alignment spots defined beside an array of detectors

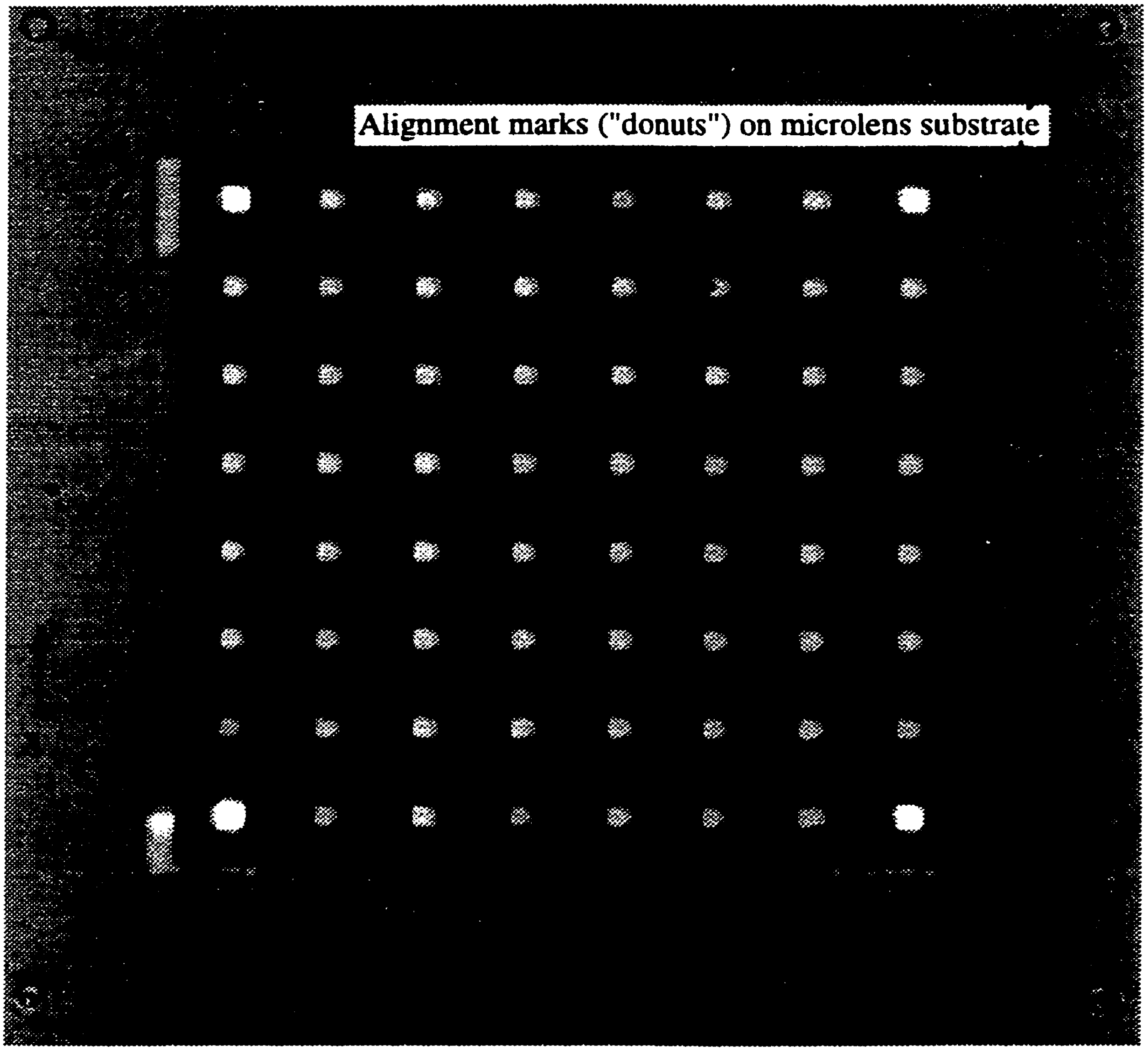

Figure 6.4: Lenslet array with alignment marks ('donuts') in which the alignment spots are to register

In the second step, a wide, planar alignment beam with uniform irradiance distribution is generated as shown in Figure 6.2 (the wide beam covers all FZPs). The lenslet substrate is brought into the beam path, with the substrate perpendicular to the beam, and secured in place.

In the third step, UV glue is deposited on top of the package and the package is placed directly behind and moved into contact with the substrate. The alignment beam is then reflected off the FZPs and forms spots a distance f_{fzp} in front of the die. The package is then moved until the reflected spots from the FZPs coincide with the alignment marks on the lenslet substrate, at which point the glue can be UV cured. A spacer may be required between the package and the substrate.

6.2.1 Alignment Accuracy

Four main sources of errors affect this technique's lateral (xy) alignment accuracy: misalignment of FZPs relative to the optoelectronic device array during fabrication. misalignment of the alignment marks to the lenslet arrays during fabrication, the effect of an angular tilt ($\alpha,\beta \neq 0$ in Figure 6.2) in the alignment beam on the position of the spots generated by the FZPs. and error in judging when the FZP spot is aligned to the alignment mark.

For operations in which the FZPs and the device array are defined in the same step, the error will be minimal and defined by the accuracy of the mask fabrication process. In most other processes, for example when devices are flip-chipped onto metal pads on a die. the error can also be under one micron [6]. During lenslet fabrication. the accuracy of the alignment mark position relative to the lenslet array is determined by the mask aligner: conventional mask aligners routinely align to within 0.5-1 μm [11].

In Figure 6.2. the angle between the die and the alignment beam is $90-\alpha$. Since the interference pattern between the part of the alignment beam reflected from the substrate and that reflected from the die is used to determine the perpendicularity of the alignment beam to the die, a deviation from the normal of β between the alignment beam and the die will cause the spot generated by the reflective FZPs to be misaligned with respect to the die by approximately Δ where

$$\Delta = f_{fzp} \tan\left(2(\alpha^2+\beta^2)^{0.5}\right). \tag{1}$$

For f_{FZP}=1 mm, $\Delta < 1\mu m$ if $2(\alpha^2+\beta^2)^{0.5} < 0.057°$. Thus, in principle, a lateral alignment error of $\varepsilon < 2$ μm is achievable.

Two FZPs can yield rotational (θ_z) alignment information. For FZPs on diagonally opposite corners and a distance $r/2$ away from the array centre, the θ_z error is under arctan (ε/r). If this technique is also used for z alignment, the error is determined mainly by the depth of focus of the FZPs.

Other minor diffractive effects have been neglected in this analysis: these had negligible impact on the results below.

6.2.2 Components

The central 4x4 array of an 8x8 diffractive lenslet array was aligned to a 4x4 MSM array using the above technique (MSMs were 50μm x 50μm with Ni/Pt/Au metallization on InP). The array pitch was 125 μm. The lenslet glass substrate had nominal dimensions of 15 x 15 x 1 mm. Two binary amplitude FZPs (D_{FZP}=295 μm) a distance r = 1909 μm apart on diagonally opposite corners of the MSM array were defined: alignment donuts with an inner diameter of 25 μm were fabricated at corresponding places on the lenslet substrate. Both the lenslets and the FZPs had a focal length of f_{FZP} = 1000 μm at λ=850 nm. The design of the FZP was done in the classical manner: the mth zone had a radius R_m where [12]

$$R_m = \sqrt{m\lambda f_{FZP}}\,. \tag{2}$$

Finally, the MSM die was glued and wire bonded into a side brazed 22 pin dual in-line package. A close-up of one of the on-die FZPs is shown in Figure 6.5.

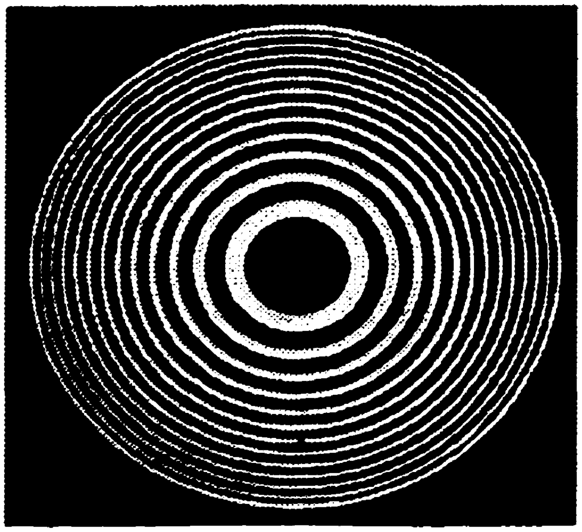

Figure 6.5: Close-up of one on-die FZP. Diameter=295 μm, focal length=1 mm (for λ=850nm)

An image of the reflected spot generated by the FZP when illuminated by a planar wavefront is shown in Figure 6.6a(to show the lower power Airy disk, the power was increased, causing the peak value to saturate locally the camera); with its profile in Figure 6.6b (lower power–no saturation). The spot was the smallest obtained and was located 1 mm in front of the die, as expected: this fact, combined with the figures, indicates that no error took place during either calculation or layout of the FZP.

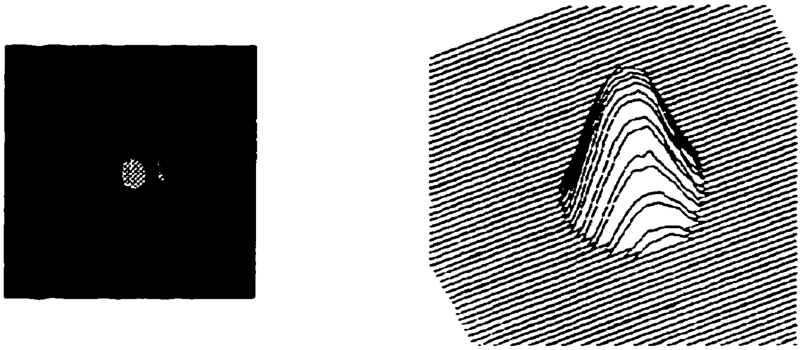

(a) (b)

Figure 6.6: Characterization of FZP at focal plane a) spot (saturated) b) profile (no saturation)

6.2.3 Effect of Glue on Chip Height and Tilt

Important parameters in optical packaging are the height and tilt of the chip relative to the chip carrier. The height is needed to calculate the thickness of the spacer and the tilt is required to determine if the lenslet or spacer should be tilted to compensate for the chip angle. It was thus necessary to measure these two values for a typical chip glued into a typical chip carrier.

The setup was a simple traveling microscope with a x10 microscope objective (NA=0.25). To measure the Δz distance between the plane defining the top of the die and plane defining the bottom of the package cavity, the objective was simply moved using an xyz stage with micrometers and successively focused on one plane then the other: the difference between the initial and final position on the micrometer gave the net displacement.

A total of 16 points was measured. The first 8 points were A, B, C, D, E, F, G, H to determine the distance from the bottom of the cavity to the top of the die. These points were the 4 corners and 4 middle points of the die periphery, as shown in Figure 6.7. The next 8 points were A', B', C', D', E', F', G', H', to determine the distance between the top of the package and the bottom of the cavity.

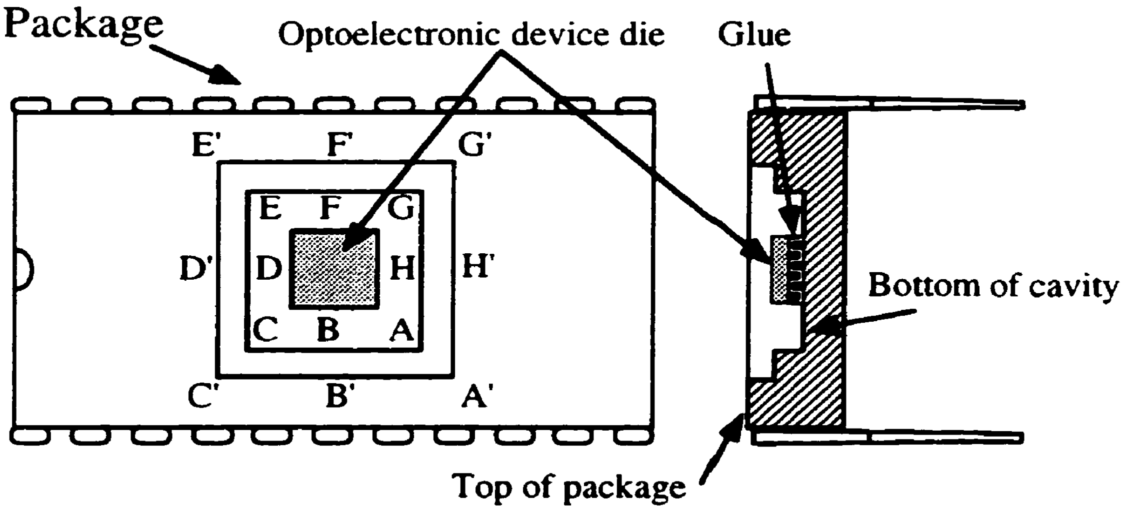

Figure 6.7: Device die in package

6.2.3.1 Sources of Error in Glue Measurement Setup

The first source of error was the depth of field of the objective. Rayleigh's quarter wave criterion for defocus states that the depth of field, δ, for an objective focusing an incoming planar wavefront is approximately [13]

$$\delta = \frac{n\lambda}{2(NA)^2} \tag{3}$$

Thus, assuming n=1 and 850 nm light, δ = 6.8 µm at best. Empirically, it was found to be closer to 10 µm. Other sources of error arose when a lateral (xy) movement was required in order to measure the Δz distance, as was the case in the A', B', C', D', E', F', G', H' measurements: the lateral travel could also introduce errors proportional to the displacement. Other sources of uncertainty included backlash on the micrometer stage, which added ~5µm uncertainty. The total uncertainty in z measurements was estimated at 15µm.

6.2.3.2 Glue Measurements and Discussion

Table 6.1 gives the traveling measurement results. The values for calculated distance from top of die to top of package take into account the tilt of the board relative to the traveling microscope.

The average distance from the top of the die to the top of the package was 0.451 mm with a standard deviation of 13 µm. As a result, the spacer was made 1-0.451 ≈ 0.55 mm thick. Moreover, these measurements indicate that the die and package top surfaces were parallel to within 0.1°, obviating the need to shave the spacer at an angle.

	Measured			Calculated	
Point	Bottom of Cavity	Top of Die	Top of Package	Distance from top of die to bottom of cavity	Distance from top of die to top of package
A	5.54	5.97	6.39	0.43	0.47
B	5.61	5.97	6.39	0.36	0.47
C	5.47	5.97	6.37	0.50	0.44
D	5.71	6.08	6.54	0.37	0.46
E	5.60	6.15	6.65	0.55	0.45
F	5.86	6.16	6.65	0.30	0.44
G	5.61	6.16	6.65	0.55	0.43
H	5.85	6.08	6.57	0.23	0.44

Table 6.1: Measurements and calculation results for glue thickness and distance from top of die to top of cavity. All dimensions in mm.

It is interesting to note that the distance from the top of the die to the bottom of the cavity varied considerably. The corner values (A,C,E,G) were systematically higher than the middle values (B,D,F,H). This is due to the fact that the glue did not quite reach the corners but did spread out beyond the die footprint in the middle points (B,D,F,H). As a result, the middle point measurements indicate the distance from the top of the glue to the top of the die, whereas only the corner spots indicate the true distance from the bottom of the cavity to the top of the die. Based on the measurements and the above interpretation, the thickness of the glue was 200 μm, and the thickness of the die was 300 μm.

6.2.4 Optical Setup

Figure 6.8 shows the optical train which generated the flat beam with uniform irradiance necessary for the alignment technique. Only the central 1% of the light emerging from the fibre was captured by the x40 microscope objective, ensuring a uniform irradiance distribution. A very flat beam was obtained by longitudinally moving the x40 microscope objective until the back focal plane of the x40 objective coincided with the front focal plane of the triplet. The beam flatness was measured with a shear plate interferometer and found to be better than $\lambda/10$ over the regions of the beam incident on the FZPs.

6.2.4.1 Beam Perpendicularity

For the experiment to succeed, it was critical to ensure the perpendicularity of the wide alignment beam to the lenslet substrate and MSM substrate. A three step approach was implemented. First, as shown in Figure 6.8a, the mirror on tilt stage was adjusted so that it was normal to the incident wide alignment beam. Second, as shown in Figure 6.8b, the lenslet substrate was brought into the beam and adjusted until the interference fringes between the beams reflected from the substrate and mirror indicated that the substrate was normal to the alignment beam. Third, the MSM substrate was brought and adjusted until it too was parallel to the substrate, as shown in Figure 6.8c. A more detailed description of each step is as follows

In the first step, the mirror on the tilt stage was adjusted until the beam was reflected back into the fibre. This was accomplished by imaging the chuck from which the fibre emerged.

In the second step, the lenslet substrate was brought into the alignment beam and moved until it was normal to the alignment beam. This was done by observing the interference pattern between the beam component reflected from the substrate and that reflected from the mirror. According to standard interference theory, the angle α between two interfering coherent wavefronts is [14]:

$$\alpha = \arcsin\frac{\lambda}{2t} \tag{4}$$

where t is the period of the fringe pattern.

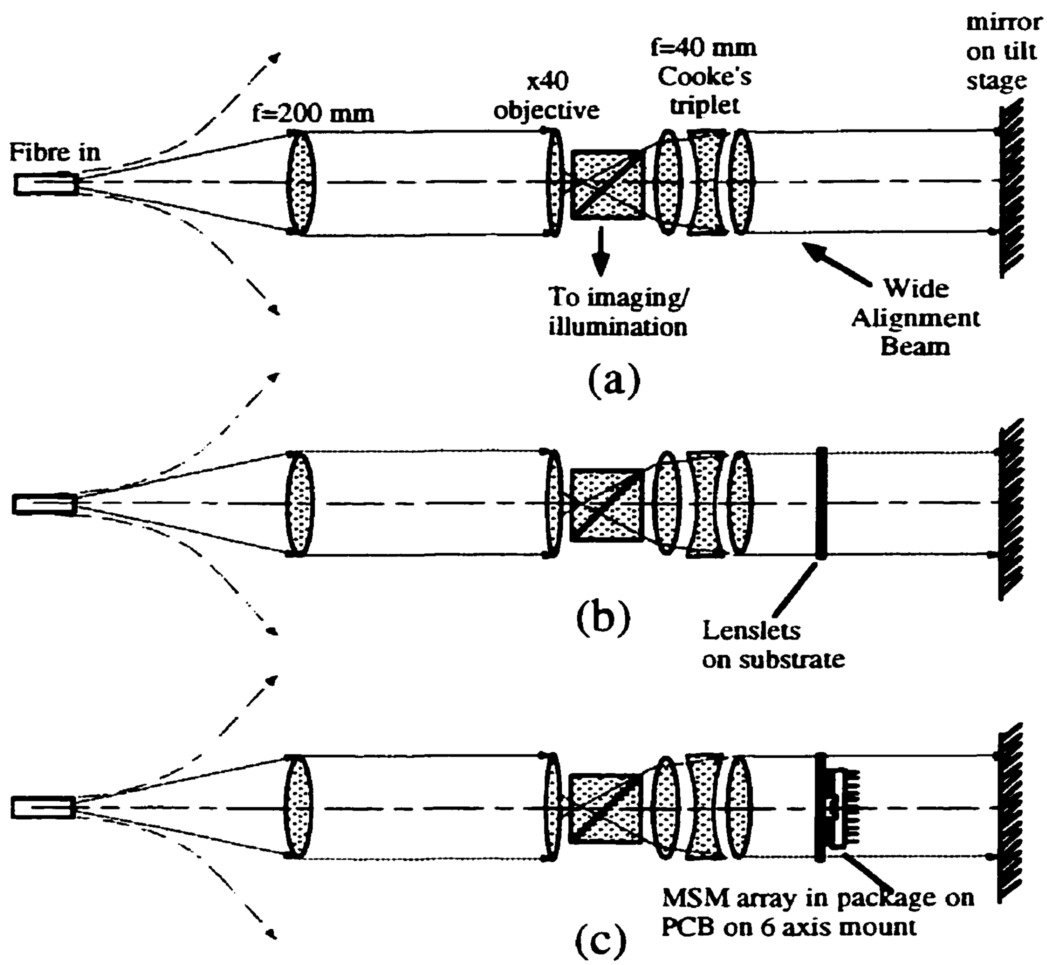

Figure 6.8: Optical setup to achieve a proper beam for lenslet packaging a) collimation of wide alignment beam b) insertion of lenslet substrate normal to beam c) insertion of MSM chip in package parallel to substrate

However, obtaining the interference pattern was a complex task which required some signal processing. Figure 6.9a shows the substrate seen from the imaging port of Figure 6.8. The only fringes clearly visible were those generated by beams reflecting from various other flat faces in the imaging system such as the beam splitters, the cover glass on the camera, and so on. These fringes were undesired and cluttered the image. To obtain the desired fringes, it was necessary to take two images, the first one being Figure 6.9a, and the second one being taken from exactly the same position, but with a sheet of paper between the mirror and substrate. The sheet served to block the desired fringes and left only the undesired fringes. Subtracting the two figures and enhancing yielded Figure 6.9b in which the desired fringes are clearly visible: the period t was measured to be 147 μm. Using equation (4), the deviation from perpendicularity between substrate and alignment beam was then calculated to be α =0.1°. The calculations assume the substrate faces to be parallel, with any deviation from perfect parallel adding to this value.

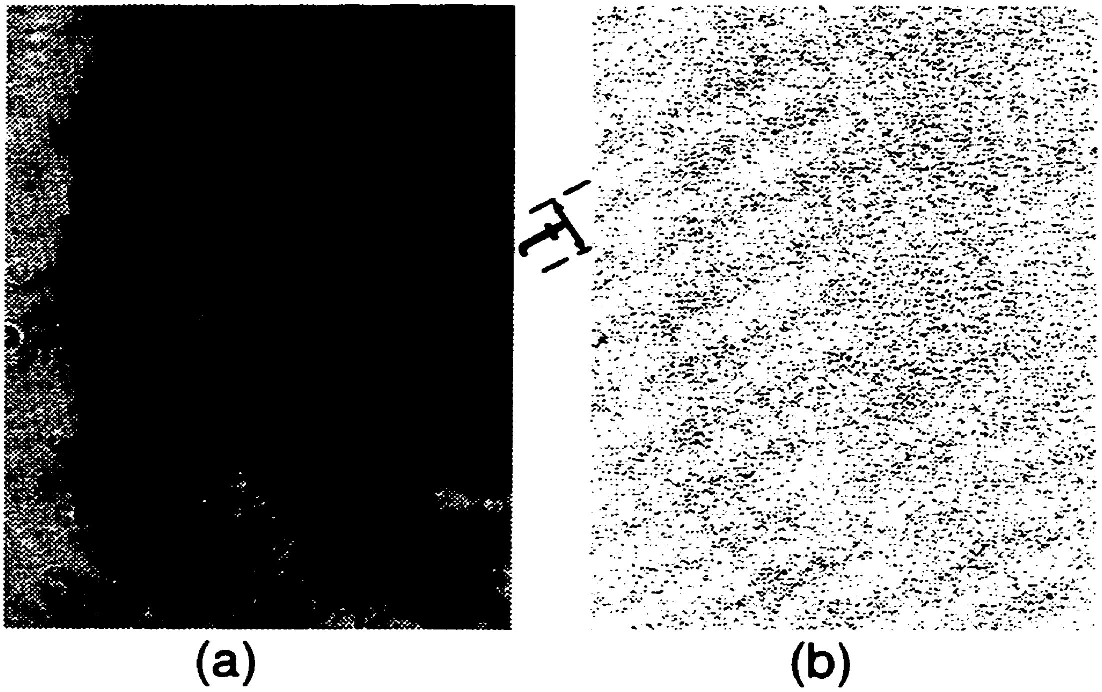

Figure 6.9: a) substrate before processing of image b) resultant picture after processing to reveal fringes

For the third step, a similar technique was then used to ensure that the MSM substrate was parallel to the lenslet substrate, although this time the interfering beams used were the one reflecting from the lenslet substrate and the one reflecting from the MSM substrate. The deviation from perpendicularity between the MSM substrate surface and the lenslet substrate was found to be β=0.09°.

6.2.5 Results

Figure 6.10 shows images of the FZP-generated spots and the donuts on the lenslet substrate. Figure 6.10a shows the spot in the donut on the upper right hand corner of the lenslet substrate: Figure 6.10b shows the lower left hand corner. Figure 6.10c shows the spot deliberately misaligned by ~40 μm and thus falling outside the donut. The large bright smear is due to the light from the illumination LED (λ=880 nm) which was also partly focused by the reflective FZP. The LED was misaligned in order not to have the bright smear drown out the donut and alignment spot.

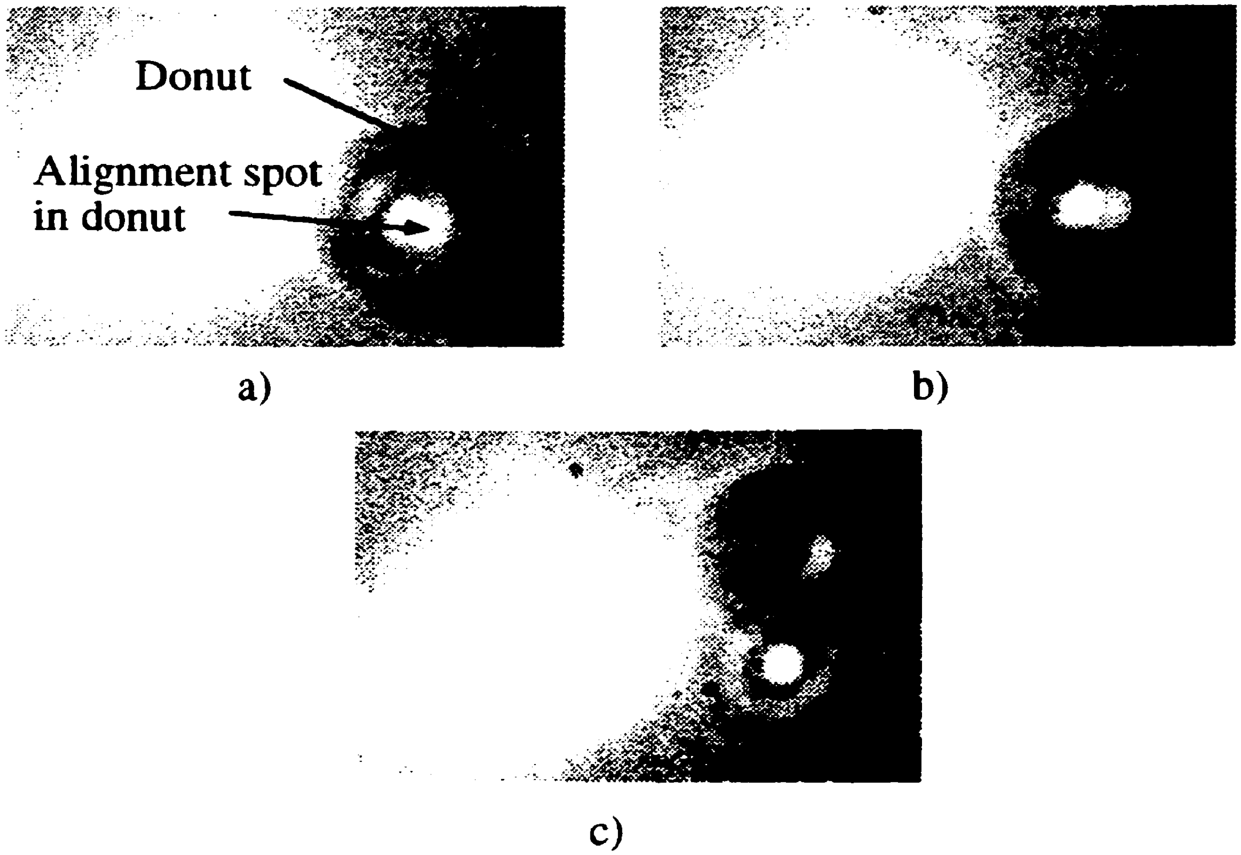

Figure 6.10: FZP-generated alignment spot a) in one alignment mark ('donut') on lenslet substrate b) in diagonally opposite alignment mark c) deliberately misaligned by ~ 40 μm to show spot beside donut

The measured diameter of the spot inside the donut was 12.5 μm (± 3μm) and the spot was measured to be ~4μm off centre (this 4 μm error was due to the low resolution of the manual xyz stage used). Given the angular misalignments α and β, a further error of Δ=4 μm could have been introduced. Assuming a total error of 1μm in mask alignment during various device fabrications, the total xy misalignment error was thus ~9 microns for this experiment. This was verified by imaging the spots on the MSMs through a hybrid lenslet-bulk lens relay. Additionally, first order calculations reveal that the 12.5 μm spot diameter corresponded to a 42 μm error in z alignment[13].

6.2.6 Discussion

The technique was thus shown to work as intended. An extension to this technique could involve the use of on-die astigmatic FZPs for precise information on z misalignment, as in CD players[15]. Several such FZPs could then be combined to give information on tilt as well, but this is probably overkill. Time and effort probably would be better spent ensuring that the die is glued flat in the first place rather than trying to compensate afterward.

The principal drawbacks to this technique, however, remain the large amount of space consumed on-die and the possibility that traces running beneath the FZPs could upset the phase profile of the difractive structure, possibly affecting image quality. The next sections address both these concerns.

6.3 Electrical Signal Traces as Diffractive Alignment Structures

Using on-die FZPs is expensive in terms of on-die real estate. For example, the FZPs above with focal length f_{FZP} = 1mm and diameter D_{FZP}=295μm consume nearly 70000 μm^2 each.

An improvement to the technique described above is one in which actual electrical signal traces are used as the diffractive structure wherever possible and relevant. Thus, as

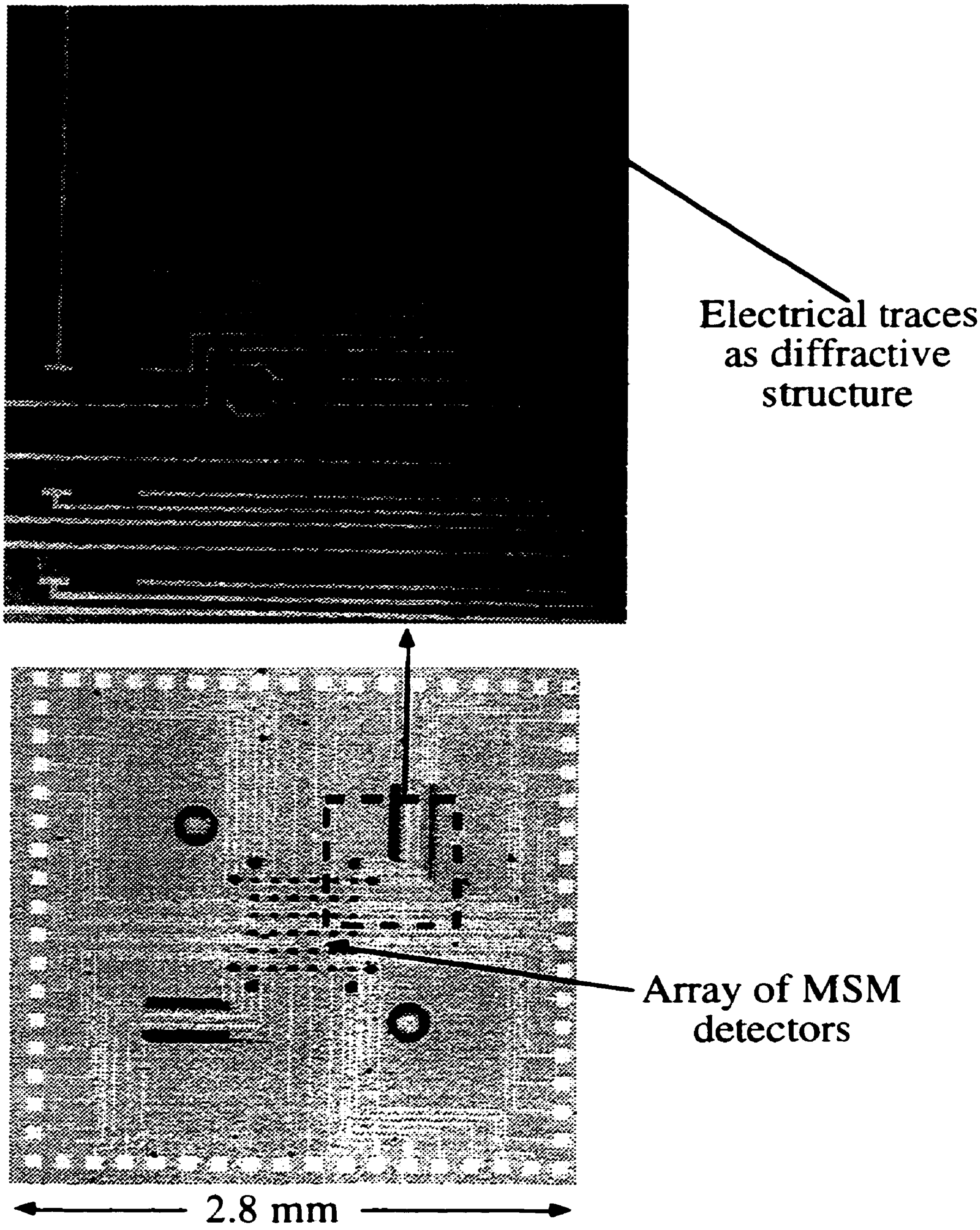

Figure 6.11: Picture of chip along with close-up showing electrical traces laid out as diffractive structures

shown in Figure 6.11, the traces are diffractive structures (anamorphic elements) whose feature width and spacing are determined using equation (2) above.

6.3.1 Description and theoretical performance

The basic operating principle when designing and using these structures is similar to the one described in section 6.2. The only difference is in the last step: the reflected diffracted light patterns which must be aligned to their corresponding lenslet substrate marks are now streaks of light, instead of points of light.

Certain particularities of the present technique must be pointed out. As the inset of Figure 6.11 shows, some signal lines fan out into two or more lines of the diffractive structure and then subsequently recombine beyond. This occurs wherever a trace width - imposed by diffractive calculations - is too small given the current carrying requirements of that line. Another particularity is that a dummy line is inserted between two different signal-carrying lines if the line spacing — again, imposed by diffractive calculations — is too small, which could lead to undesired crosstalk, especially if the traces run parallel over a considerable distance. While this is potentially wasteful of die area, it is a small waste compared to an entire FZP area.

6.3.2 Experimental Results and Discussion

The chip in Figure 6.11 was aligned to the lenslet array substrate of Figure 6.4. The top view shows the vertical light streak going through the alignment mark ('donut') on the lenslet substrate. The bright smear to the left is due to (white) illumination light, and is analogous to the smear beside the alignment spot created by the FZP and shown in Figure 6.10. The horizontal alignment streak was similar (bottom), although here the illumination light smear also went through the donut. For proper alignment, the streaks had to go through the centre of the donuts and be parallel to their respective edge of the lenslet array. The measured error in lateral alignment accuracy was < 5 μm in both x and y. The rotational accuracy was better than $\theta_z < 0.12°$, measured by comparing the parallelism of the edge of the lenslet aray and the streaks.

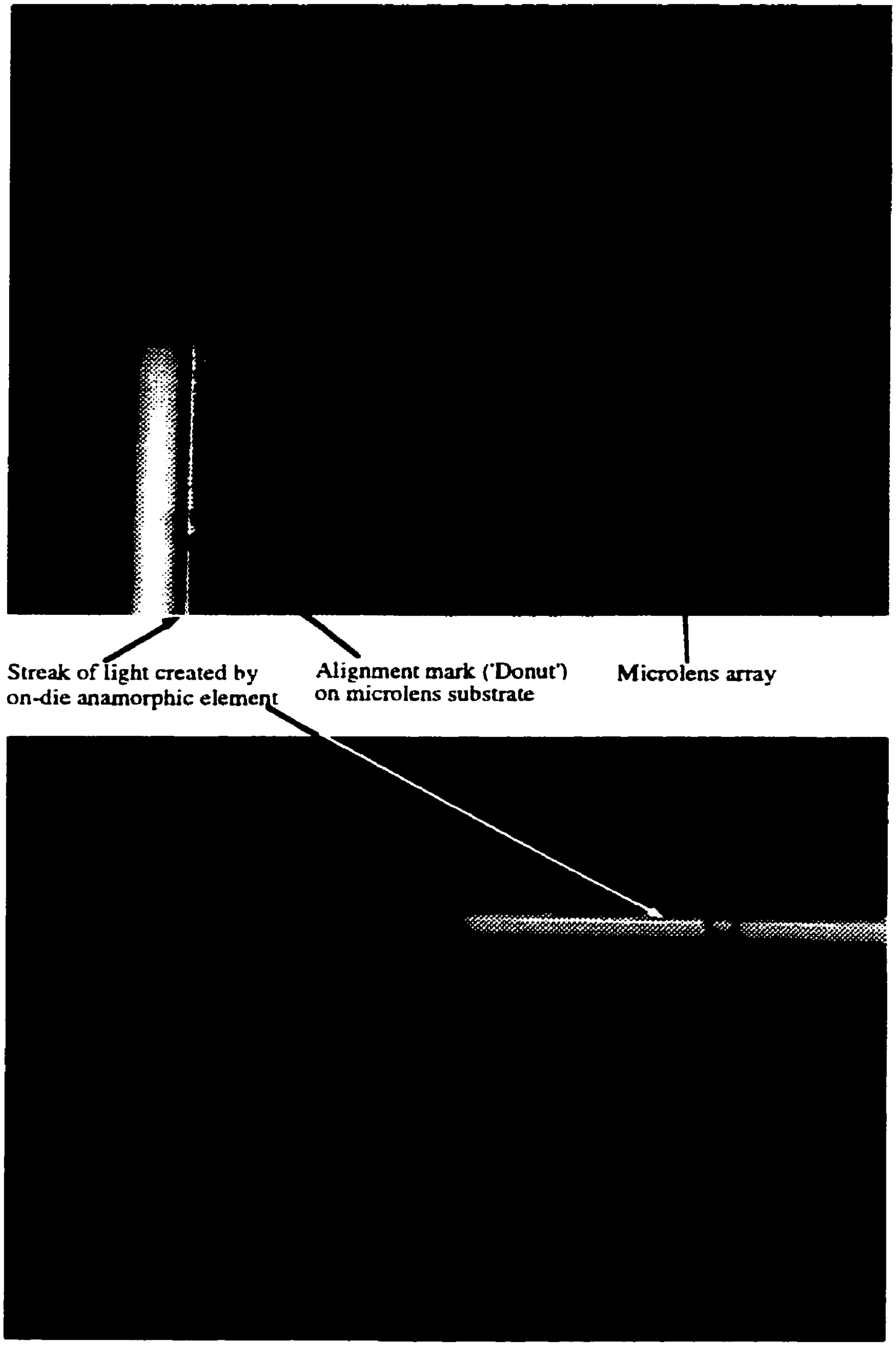

Figure 6.12: Alignment streaks going through their respective alignment marks on lenslet substrate

The dual use of electrical signal traces proposed by this technique addresses the high on-die space consumption inherent in the FZP approach. However, it was noted that the brightness of the streaks generated by the diffractive traces was considerably less than that of the spots generated by the FZPs. While this was to be expected since the same amount of light power is spread over a line instead of concentrated in a spot, it also made alignment more challenging since the streak was harder to distinguish from the background noise. Measurements in fact revealed that the spots were about 10 times brighter than the background whereas the streaks were only 2 to 3 times as bright.

6.4 Minimizing The Effect of Perturbations on Diffractive Patterns

A potential problem with either of the techniques given above is the effect of traces and other perturbations running beneath the diffractive structures. If there are many such disturbances beneath a diffractive structure, its phase profile could be considerably changed. This could happen, for example, if the diffractive structures were on the top layer, Metal layer 2, and traces ran beneath the structure on Metal 1. Simulations were performed to determine the effect on the generated diffractive light patterns of traces below the diffractive structures using the two metal-layer process described above. Using the Fresnel approximation from standard scalar diffraction theory[16], $I(x_o,y_o)$, the irradiance at a point (x_o,y_o), can be calculated to be:

$$I(x_o,y_o)=\left|\frac{1}{\lambda d}\int_{-\infty}^{\infty}\int_{-\infty}^{\infty}\left\{U(x_1,y_1)\exp\left[j\frac{k}{2d}\left(x_1^2+y_1^2\right)\right]\right\}\exp\left[-j\frac{2\pi}{\lambda d}\left(x_o x_1+y_o y_1\right)\right]dx_1 dy_1\right|^2 \qquad (5)$$

where $U(x_1,y_1)$ is the complex two-dimensional function representing the diffractive structure on Metal 2 and the phase delays associated with the traces on Metal 1.

The wavelength of the alignment illumination for all simulations was λ=850 nm. For this analysis, all metal traces on both Metal 1 and Metal 2 were assumed to have the same thickness t_{tr}, although this may not necessarily be true for all production processes. All traces were assumed to have sharp corners and a reflection coefficient of 1. The substrate was GaAs (n=3.35), which gave a field reflection coefficient of 0.54.

Figure 6.13 shows numerical simulations of the diffracted light pattern generated by a reflective on-die anamorphic element as would be seen at the focal plane by a CCD camera with linear response. In Figure 6.13a and Figure 6.13b, only the Metal 2 structures were present (i.e. no Metal 1 traces underneath), and $t_{tr}= \lambda/2$ (425 nm) and $\lambda/4$ (212 nm) respectively. In Figure 6.13c and (d), phase perturbations simulating the effect of traces running on Metal 1 beneath the diffractive structure were incorporated into the simulation. In Figure 6.13a and c the trace thickness is t_{tr} = 425 nm (which is equivalent to $\lambda/2$) whereas in Figure 6.13b and d t_{tr}=212 nm ($\lambda/4$). The pattern of traces running below the diffractive structure and creating the phase perturbations is shown in Figure 6.14. The spacing and width of the perturbing traces were respectively 3 μm and 2.5 μm with random variations to simulate an actual layout.

In Figure 6.13a and b the diffracted pattern is the horizontal streak with ripples, which is analogous to a typical Airy disk pattern. However, the light is more efficiently coupled into the main order with $t_{tr}=\lambda/4$ because the path difference between the zones is then $\lambda/2$ for the reflective diffractive structure. Now, with the addition of metal traces beneath the diffractive structure on Metal 1, the pattern changes. In Figure 6.13c ($t_{tr}=\lambda/2$), the diffracted pattern is greatly disturbed, whereas in Figure 6.13d ($t_{tr}=\lambda/4$) it is only slightly disturbed. The calculations thus reveal that the trace thickness, t_{tr}, relative to the wavelength of the alignment beam is critical and the best design uses diffractive structures with $t_{tr}=\lambda/4$. However, the trace thickness is often a function of fabrication parameters, and since changing t_{tr} would likely upset production processes, it is simpler to choose the alignment wavelength as a function of t_{tr} and design the diffraction structures and alignment rig accordingly. Note that the alignment wavelength need not be the same as the system operating wavelength.

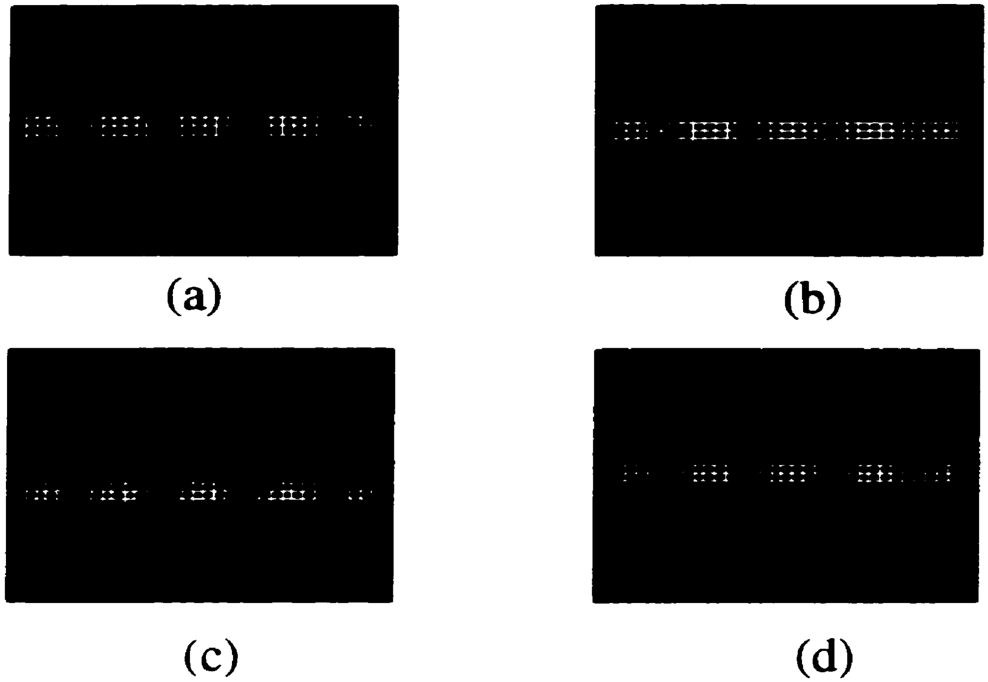

Figure 6.13: Effect of perturbations on diffracted pattern a) t_{tr}=λ/2 no perturbation b) t_{tr}=λ/4 no perturbation c) t_{tr}=λ/2 with perturbation d) t_{tr}=λ/4 with perturbation

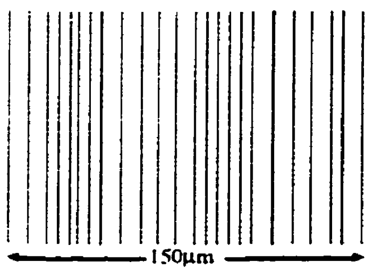

Figure 6.14: Perturbing Metal 1 traces beneath diffractive structure

The thickness of the isolation between metal layers as well as other factors such as different reflectivities at different layers were neglected in this analysis; taking these into account would lead to a similar result, which is that the alignment wavelength can be chosen independently of system operating wavelength to simplify fabrication.

6.5 Conclusion

A novel technique for using on-die reflective diffractive structures was proposed and demonstrated. The technique is robust and can be made efficient in terms of on-die area consumed. Moreover, it was shown that appropriate choice of the illuminating wavelength can reduce the effect of traces running beneath the diffractive structures.

However, beyond all these aspects, the key conclusion to be drawn from this chapter and the previous ones is that multi-disciplinary collaboration between design teams is essential to generate new and potentially beneficial ideas. For example, ASIC layout engineers must look beyond placing transistors, windows, and traces, and optical packaging designers must try to use all hardware to their advantage, and stop thinking of the optoelectronic chips simply as elusive targets to which beams must be aligned. Collaboration and imagination are required.

6.6 References

1 M. S. Cohen, M. J. DeFranza, F. J. Canora, M. F. Clina, R. A. Rand, and P. D. Hoh. "Improvements in index alignment method for laser-fiber array packaging," *IEEE Trans on comp. packaging. and manuf. tech-part B*, 17, pp. 402-411, 1994.

2 A. K. Kanjilal, R. Narain, R. Sharma, V. T. Chitnis, B. P. Singh, J. Liu, J. Yamada, and Y. Uchida, "Automatic mask alignment without a microscope," *IEEE Transactions on Instrumentation and Measurement*, 44, pp. 806-808 (1995).

3 X. Y. Cai, R. W. Blore, and F. Kvasnik, "Fiducial markers for increasing the versatility of optical correlation in the measurement of faults on integrated-circuit wafers," *Applied Optics*, 34, pp. 5140-5145 (1995).

4 Specifications for UTM class motorized stages, 1994 Catalog, Newport Inc., Irvine California.

5 J. M. Sasian and D. A. Baillie, "Simple technique for out-of-focus feature alignment." *Optical. Engineering*, 34, pp. 564-566, 1995.

6 Y. C. Lee and N. Basavanhally, "Solder engineering for optoelectronic packaging." *Journal of Metals*, 46, pp. 46-50 (1994).

7 K. Rastani, M. Orenstein, E. Kapon, and A.C. Von Lehmen, "Integration of planar microlenses with vertical-cavity surface emitting lasers," *Optics Letters*, 16, pp. 919-921 (1991).

8 S.S. Lee, L. Y. Lin, S. J. Pister, M. C. Wu, H. C. Lee, and P. Grodzinski, "Passively aligned hybrid integration of 8 x 1 micromachined micro-fresnel lens arrays and 8 x 1 vertical cavity surface emitting laser arrays for free-space optical interconnect." *IEEE Photonics Technology Letters*, 7, pp. 1031-1033 (1995).

9 S. K. Patra, J. Ma, V. H. Ozguz, and S. H. Lee, "Alignment issues in packaging for free-space optical interconnects," *Optical Engineering*, 33, pp. 1561-1570 (1994).

10 M. E. Motamedi, W. E. Tennant, H. O. Sankur, R. Melendes, N. S. Glick, S. Park, J. M. Arias, J. Bajaj, J. G. Pasko, W. V. McLevige, M. Zandian, R. L. Hall, and P. D. Richardson, "Micro-optic integration with focal plane arrays," *Optical Engineering*, 36, pp. 1374-1381 (1997).

11 J. M. Miller, M. R. Taghizadeh, J. Turunen, and N. Ross, "Multilevel-grating array generators: fabrication error analysis and experiments," *Applied Optics*, 32, pp. 2519-2525 (1993).

12 E. Hecht, Optics, (Addison Wesley, Reading, Mass., 1990).

13 W. J. Smith, Modern Optical Engineering, (McGraw-Hill, San Francisco, 1990).

14 R. J. Collier, C. B. Burckhardt, and L. H. Lin, Optical Holography, (Academic Press, New York, 1971), p. 10.

15 W. H. Lee, "Holographic optical head for compact disk applications," *Optical Engineering*, 28, pp. 650-653 (1989).

16 J. Goodman, Introduction to Fourier Optics (McGraw Hill, San Francisco. 1968). pp. 50-54.

Chapter 7: Conclusions and Future Directions

7.1 Conclusions

Free-Space Optical Interconnects (FSOIs) promise to eliminate interconnection bottlenecks that plague high-performance computing systems, especially at the very important backplane level. In order for FSOIs to deliver on their promise, however, optical packaging techniques must be improved. Key problems to overcome include the impact of environmental conditions, reducing cost in parts and labour, simplifying assembly, and reducing overall system size.

The thesis draws the following conclusions which are relevant for all designers of optical packaging:

- Design of diagnostic tools must be considered at the earliest phase of system design and must be not added-on as an afterthought.
- The requirement for bringing in optical power supply beams makes optical packaging for modulator-based systems more complicated and space-consuming than that for emitter-based systems. However, modulator-based systems offer more design flexibility because of characteristics such as generally lower divergence angles and reduced on-chip power consumption.
- Environmental effects such as changing temperatures can be exploited to simplify system assembly. A technique for lens mounting using thermal expansion and contraction was given as an example.
- Many environmental problems that affect FSOIs affect electronic interconnects as well: lessons learned by electronic packaging designers and standards applying to electronic packaging should be applied to FSOIs where possible and relevant.
- Adhesives are a very effective way of attaching critical components and are often better than screws and bolts to minimize drift and improve overall stability.

- Packaging which integrates microoptics and optoelectronics considerably loosens key alignment tolerances. Moreover, integrated packaging offers better mutual protection of components.
- Diffractive effects are such that the signal-to-crosstalk ratio at the detector plane is higher than that at the preceding lenslet plane for small misalignments in lenslet-based interconnects. Care should be taken during chip design and layout to ensure that the diffracted crosstalk power does not cause localized photocurrents which could have a negative on the chip electrical performance.
- Diffractive alignment components can be laid out on-chip to aid in alignment and fabrication of integrated packages.
- Multidisciplinary collaboration is essential to ensure optimal use of all resources available during system design and fabrication
- Diagnostic tools can be implemented in many different ways such as by measuring movement of higher order beams or by measuring crosstalk components of misaligned signal beams. Information generated by these tools can be used for both manual alignment and automated alignment.

7.2 Future Directions

The following are key issues that will have to be addressed in future research in optical packaging.

7.2.1 Choice of Materials

Extensive machining of metal precision parts is not a cost-effective solution. A much cheaper way of producing high-precision parts in large volumes is to use processes such as plastic injection molding (understandably, this has not been done yet since these processes are much more expensive when only a few piece are required, as has been the case for all FSOI demonstrator systems to date). The greatest apparent drawback to these processes may be that they limit the choice of materials to plastics and their derivatives and plastics usually have much higher rates of thermal expansion than any metal. However, this is not such a major problem since most future FSOI solutions will likely involve chips mounted on metal slugs (for heat sinking and possibly for very localized EMI shielding) which are fastened onto circuit boards; since board materials such as FR4 usually have properties similar to those of plastics, the consequences should be less severe. The key point is that precision-machined metal components should disappear from all FSOIs except in the immediate vicinity of the chips. Big (cheap, low-precision machining) metal enclosures may still be necessary for a computing system with high-clock-rate CPUs radiating considerable EMI, but the FSOIs themselves in the chassis should have as much plastic as possible in order to reduce costs.

7.2.2 Diagnostics

The generation of diagnostic information in the form of electronic signals will have to increase considerably, and imaging systems will have to disappear. The reason is that the engineers and technicians who will install and – especially – troubleshoot these systems are used to oscilloscopes, multimeters, and so on; FSOIs will have to adapt to their needs, not the other way around. However, at first, it is probable that "tweaking" in the field will be tolerated, just like certain high speed electronic systems today have many tiny adjustable resistors and capacitors for appropriate terminating. The key is to generate unambiguous information.

7.2.3 Safety

Another important aspect related to diagnostics is that of safety: *in-situ* systems eliminate the potentially dangerous act of opening up the system to insert partially reflective and imaging components into the beam path. To avoid litigation, it is very likely that lawyers for companies producing FSOIs will impose on engineers class I radiation constraints (the safest level in the 4-level eye-safe laser radiation hierarchy)[1] for all phases of system operation and maintenance; a typical example was Motorola bending over backwards to ensure that its Optobus fibre ribbon link met the class I specs at all times even when all ten fibres were uncovered and all lasers were on. This may have been done at the expense of system performance. Safety constraints will play a capital role as FSOIs leave the laboratory and will impose additional engineering hurdles not faced by experimentalists designing systems built and maintained by highly trained researchers.

7.2.4 Final Comments

By far the best way to improve optical packaging technology is to design. build and test systems and sub-systems. Simulations. calculations and CAD tools. while essential. are not sufficient since they give an overall view of the problem that is much too "clean" and rarely indicative of real problems encountered. For example, a very time-consuming practical problem encountered over the course of the work presented in this thesis was the gluing and fastening problem: for these problems. simulations and CAD-based predictions often ended up being marginally relevant at best, misleading at worst.

Designing, building and testing alone will not suffice, for what cannot be measured cannot be improved. Improving optical packaging will necessarily involve improving diagnostic techniques. Future diagnostic techniques could involve diffractive components measuring wavelength shifts. polarization instability and even dust contamination. It is important however to keep diagnostic costs low: some testing could be done outside the system. This is the case in integrated circuit (IC) fabrication today: some testing is done by on-chip circuitry. and some is done on specialized external IC testers. Just as in IC fabrication. cost-benefit analyses will dictate which testing takes place where and when.

Current FSOI systems are still too big and have too many components of all types. More components lead to more failures. Until component counts are reduced, designers of computing systems will be reluctant to adopt FSOIs. Aggressive and innovative ways to reduce size and component counts should be envisaged. The optical power supply (OPS) generating the continuous wave (CW) beams to run the modulators could be one subsystem to eliminate or considerably reduce in size[2]. One such way could be as follows. VCSEL arrays could be used as optical power supplies (OPS) to generate the continuous wave (CW) beams required to run modulators. This would have two advantages. 1) the dozens of pieces such as lenses, isolators, gratings, fibre distribution schemes, beam circularizers and so on making up the OPS would be eliminated, considerably reducing system size and component count 2) a form of athermalization could be obtained whereby the VCSEL emission wavelength could be made to change at the same rate as the peak absorption wavelength of the modulators, eliminating the need for sophisticated temperature monitoring and cooling techniques. There would of course be drawbacks, the first one being the replacement of a passive device, namely the OPS, with an array of active components. Also, VCSEL properties such as beam divergence angles or unreliable polarization could be problematic. Nonetheless, these problems can be addressed. Sacrificing modulation bandwidth, reliable VCSELs optimized for CW operation could perhaps be fabricated. Moreover, it should be noted that many problems with VCSEL performance and reliability today arise on VCSELs that have gone through hybrid attachment or growth onto silicon, which would not be the case here (the modulators would be the ones attached to silicon). In addition, optical interconnects not relying on polarization for beam combinations can be devised, albeit usually at the cost of power. Appropriate layout and clustering could help address the divergence angle problem. Finally, cost is always an issue: uneventful batch fabrication of VCSELs will eventually arrive and drive their costs down along the well known exponentially decaying semiconductor fabrication price/performance curves whereas mounting costs for lenses, prisms, gratings, and other optical components for optical subsystems like an OPS have, in comparison, barely budged in decades (if not centuries!). The point is that many aggressive and novel solutions must be considered and old established doctrines must be challenged and forced to justify themselves. System design must start on a fresh sheet of paper.

7.3 References

1 American National Standard for Safe Use of Lasers, ANSI Z136.1-1993.

2 D. G. Goodwill and H. S. Hinton, "Compact and extensible optical interconnect module for a free-space optical backplane," SPIE Proc. Vol. 2692, "Optical Interconnects in Broadband Switching Architectures," T. Cloonan ed. January 1996.

Appendix I: Diffractive Lenslet Efficiency

AI.1 Introduction

As shown in Figure A1, the lenslets used in the diffractive crosstalk experiments were diffractive lenses with 8 phase levels in the centre and 4 phase levels at the periphery, for fabrication reasons. The minimum feature size, x_{min}, required for a multi-level diffractive lens is:

$$x_{\min} = \frac{\lambda}{L}\sqrt{1+(2f/\#)^2} \tag{1}$$

where L is the number of phase levels[1]. In this case, the lenslets were square and 125 μm on a side and had a focal length of 1mm (for 850 nm light). Since, in this case, the minimum feature size that the fabrication process could achieve was ~ 1.2 μm, the 8 level inner part had a "diameter" of 150 μm, with the rest having four levels.

Consequently, at the ideal best only between 81% and 95% of the incident light was focused by the first order[2]. In theory, the rest of the incident light was sent into other higher orders. In practice, other losses such as mask misalignment (measured to be ~0.9 μm in the worst case for these lenslets), dust, and etch depth errors were present, further reducing efficiency. Additionally, Fresnel reflection losses could have been present since only one side of the lenslets substrate was anti-reflection-coated. However, two key parameters are the efficiencies of the first and zeroth orders, and this appendix describes measurements used to obtain them.

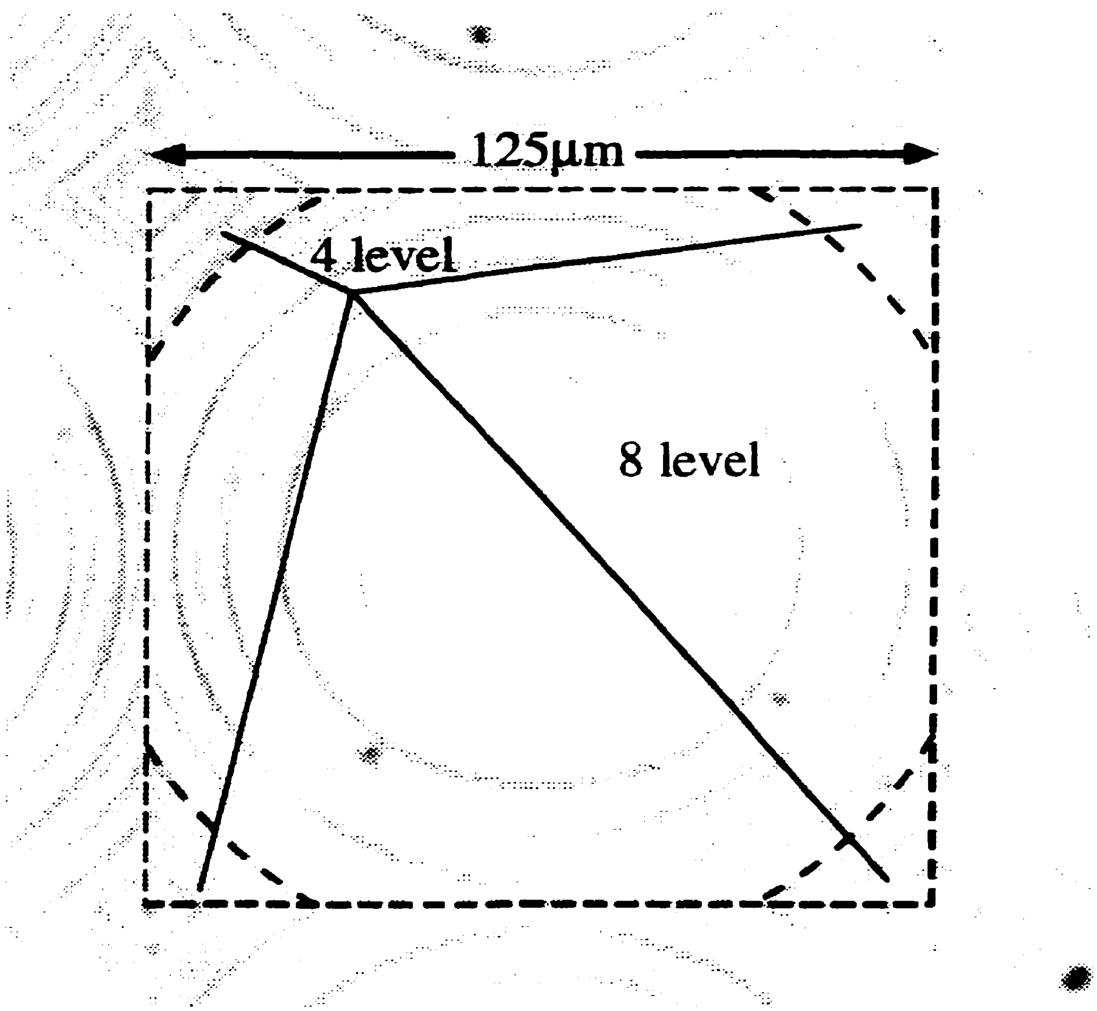

Figure A1: Separation between 8-phase level area and 4-phase level area in diffractive lenslet

AI.2 Measuring Efficiency of the First Order

Measuring the diffraction efficiency of diffractive lenses, especially closely spaced, short-focal length ones, is quite difficult, although measurements of the first order efficiency have been performed before on larger lenses [2]. Two different measurements were performed to obtain two specifications, namely the power contained in the first and zeroth order. These numbers were important for predicting the diffracted optical power during misalignment.

The first order was measured as follows. As shown in Figure A2a, an optical system consisting of two conventional lenses and lenslet A was built. The lenslet was placed a distance f_μ in front of the spot created by the second conventional lens.

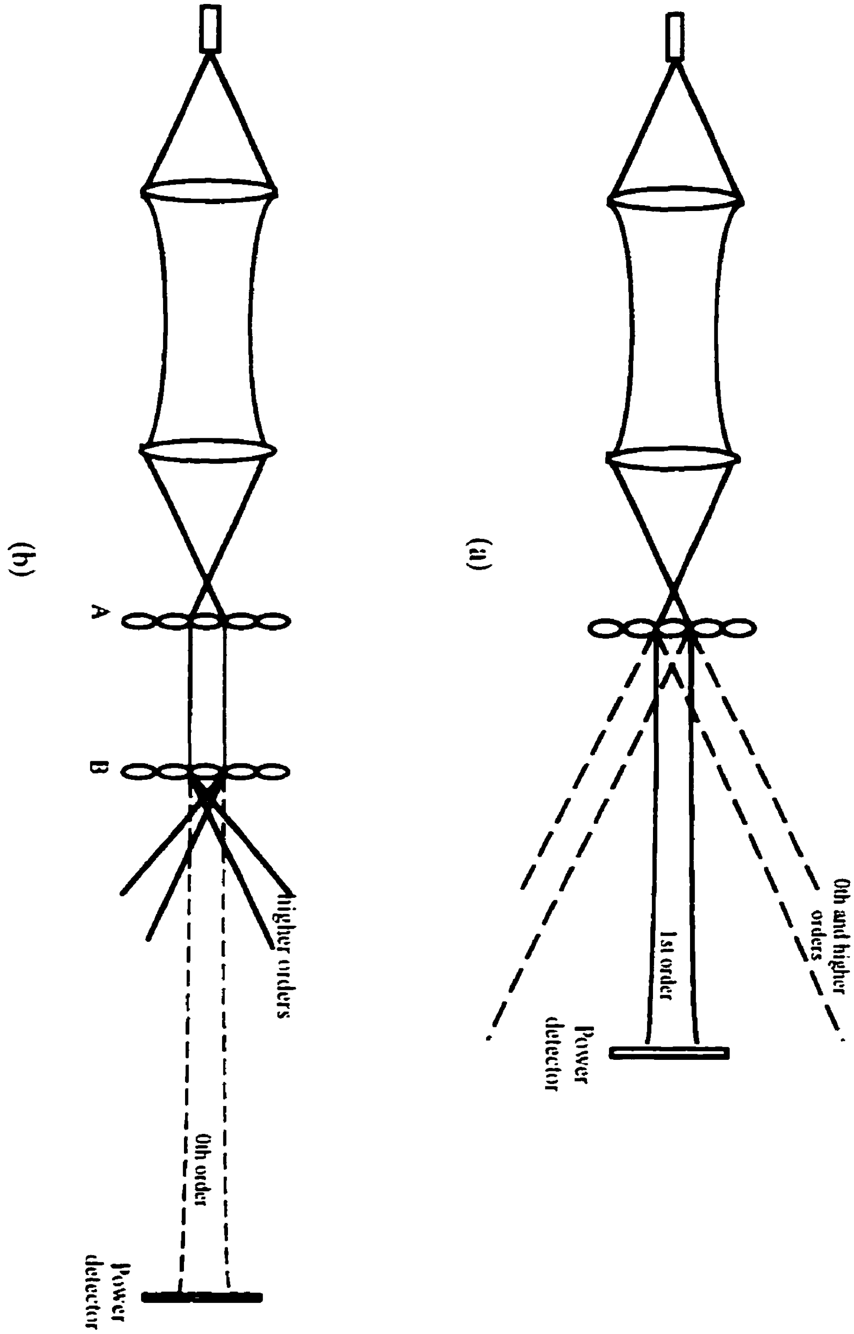

Figure A2 a) : Setup for measuring first order efficiency b) setup for measuring zeroth order efficiency

This simple system was designed such that well over 99 % of the incident light power was captured by the inner (8 level) of the diffractive lens. The light diffracted by the 1st order was measured by a power detector located over 150 mm away. and this measurement gave the efficiency of the first order for the inner part of the diffractive lens. It should be noted, however, that although the light diffracted by the zeroth order as well as those orders higher than the 1st was scattered away, some scattered light could nonetheless have impinged on the photodetector: this may have added a systematic error yielding efficiency measurements ~ 1% higher than the true value. Taking this factor and others such as Fresnel reflections off the substrates into consideration, the first order diffraction efficiency was found to be approximately 80%.

AI.3 Measuring Efficiency of Zeroth Order

The zeroth order, which is a function of fabrication errors such as etch depth, was measured using a two step process outlined in Figure A2b. In the first step, using lenslet A and with lenslet B not yet in the measurement rig, the power incident on the power detector - which this time was placed over 400 mm away -was measured. In the second step, lenslet B was inserted and the power at the distant power detector was once again measured. As can be seen in FigureA2b. only the light in the zeroth order could reach the distant power meter: the rest of the light was scattered into the 1st and higher orders. Taking into account losses due to reflections on the substrate, it was determined that the light power in the zeroth order represented 7 % of the incident power. The systematic error was estimated to be similar to the one in the first measurement.

AI.4 Overall Lenslet Performance

It was very difficult to measure the efficiency of the corner parts where only four phase levels were present. As such.the efficiency was deduced as follows. Since the eight phase level part had an efficiency of only 80% instead of the ideal 95%, it was estimated that the four level part had an efficiency of $(0.8/0.95) \times 81\% = 68\%$ where the 81% value is the efficiency for the ideal 4 level lens. In order to simplify calculations, it was desired to have one overall lens model instead of a piecewise-continuous one. As a result, a weighted sum of both was chosen, with the relative area of each part serving as the weighting factor. Geometric considerations indicate that the area of the 8 level region occupied~95% of the total lenslet area, with the rest in the four level part. This gave $0.95 \times 80\% + 0.02 \times 68\% = 79\%$ for the first order efficiency. To complete the model, it was assumed that a third of the remaining power went into a fifth order, with the rest scattering elsewhere to much higher orders and regions not of interest[3].

AI.5 References

1 F. B. McCormick, Ph.D. Thesis. "Optical and mechanical design issues in free-space optical interconnection and processing." Heriot Watt University (1993).

2 J. Jahns and S. J. Walker. "Two-dimensional array of diffractive microlenses fabricated by thin film deposition," *Applied Optics*, 28, pp. 931-936, (1990).

3 J. M. Miller. M. R. Taghizadeh. J. Turunen, and N. Ross, "Multilevel-grating array generators: fabrication error analysis and experiments," *Applied Optics*, 32, pp. 2519-2525 (1993).

On-Die Diffractive Alignment Structures for Packaging of Microlens Arrays with 2-D Optoelectronic Device Arrays

G. C. Boisset, *Member, IEEE*, B. Robertson, W. S. Hsiao, *Member, IEEE*, M. R. Taghizadeh, J. Simmons, K. Song, M. Matin, D. A. Thompson, and D. V. Plant, *Member, IEEE*

***Abstract*—A novel technique for aligning a microlens array to an electrically packaged optoelectronic device array is presented: reflective Fresnel zone plates (FZP's) are fabricated on the device die to provide registration spots during alignment. A proof-of-concept experiment in which an MSM array was aligned to a microlens array with an accuracy of better than 9 microns is described.**

I. Introduction

FREE-SPACE optical interconnects based on microlens technology promise to alleviate data throughput bottlenecks in future electronic computing systems [1], [2]. However, a major problem encountered in the construction of optical interconnects is the alignment of optoelectronic device arrays to microlenses. Current techniques addressing similar alignment problems include imaging fiducial alignment marks on the component substrate. However, to avoid lateral alignment errors incurred when imaging marks on different xy planes, additional components must be added [3], [4]. Other techniques in which microlenses are attached or defined during device fabrication also exist [5], [6].

This letter presents a new technique for aligning a microlens array to an optoelectronic device array: reflective diffractive structures fabricated on the device die provide registration spots during alignment. This technique can produce prealigned device/microlens packages which loosen alignment tolerance requirements for free-space optical interconnects.

II. Description of Technique

The objective is to align an array of microlenses of focal length f with respect to a packaged array of optoelectronic devices a distance d away from the microlenses, as Fig. 1 shows. The technique can yield precise alignment in x, y, and θ_z, and to some extent alignment in the other three degrees of freedom. There are three steps.

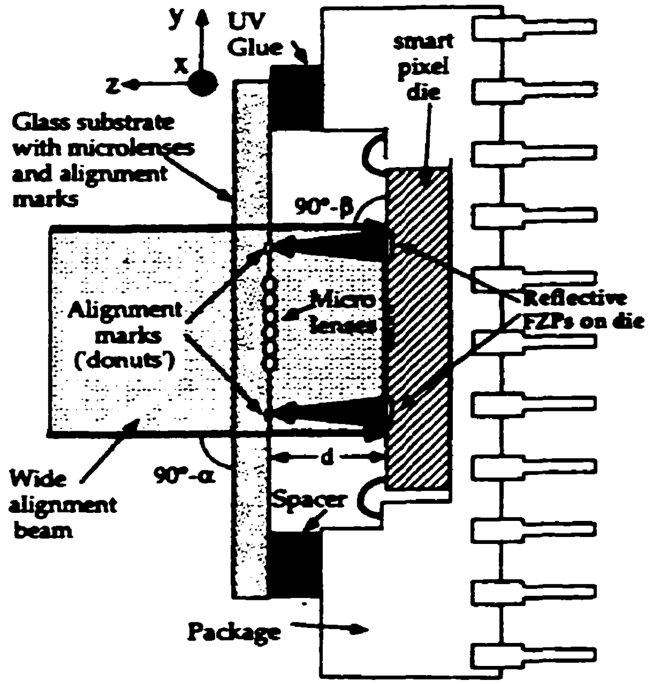

Fig. 1. Schematic of technique: reflective FZP's on device die focus light back onto alignment marks located on the microlens array.

The first step consists of laying out reflective FZP's of focal length $f_{fzp} = d$ on the edge of the device array, and laying out alignment marks at corresponding positions on the edge of the microlens array. In this experiment, FZP's are defined beside an array of metal semiconductor-metal (MSM) detectors, and corresponding marks ("donuts") are on the microlens substrate as Fig. 2(a) and (b), respectively, show.

In the second step, a wide, planar alignment beam with uniform irradiance distribution is generated as shown in Fig. 1 (the wide beam covers all FZP's). The microlens substrate is brought into the beam path, with the substrate perpendicular to the beam, and secured in place.

In the third step, UV glue is deposited on top of the package and the package is placed directly behind and moved into contact with the substrate. The alignment beam is then

Manuscript received February 2, 1996; revised March 20, 1996. This work was supported by a grant from the Canadian Institute for Telecommunications Research under the NCE program of the Government of Canada and the Nortel/NSERC Chair in Photonic Systems. The work of G. Boisset was supported by FCAR (cote. B2-05). The work of W. Hsiao was supported by the NSERC. The work of D. Plant was also supported by the NSERC (#OPG0155159) and FCAR (#NC-1415).

G. C. Boisset, B. Robertson, W. S. Hsiao, and D. V. Plant are with the Department of Electrical Engineering, McGill University, Montréal, PQ Canada.

M. R. Taghizadeh is with the Department of Physics, Heriot-Watt University, Edinburgh, Scotland.

J. Simmons, K. Song, M. Matin, and D. A. Thompson are with McMaster University, Hamilton, ON Canada.

Publisher Item Identifier S 1041-1135(96)05126-9.

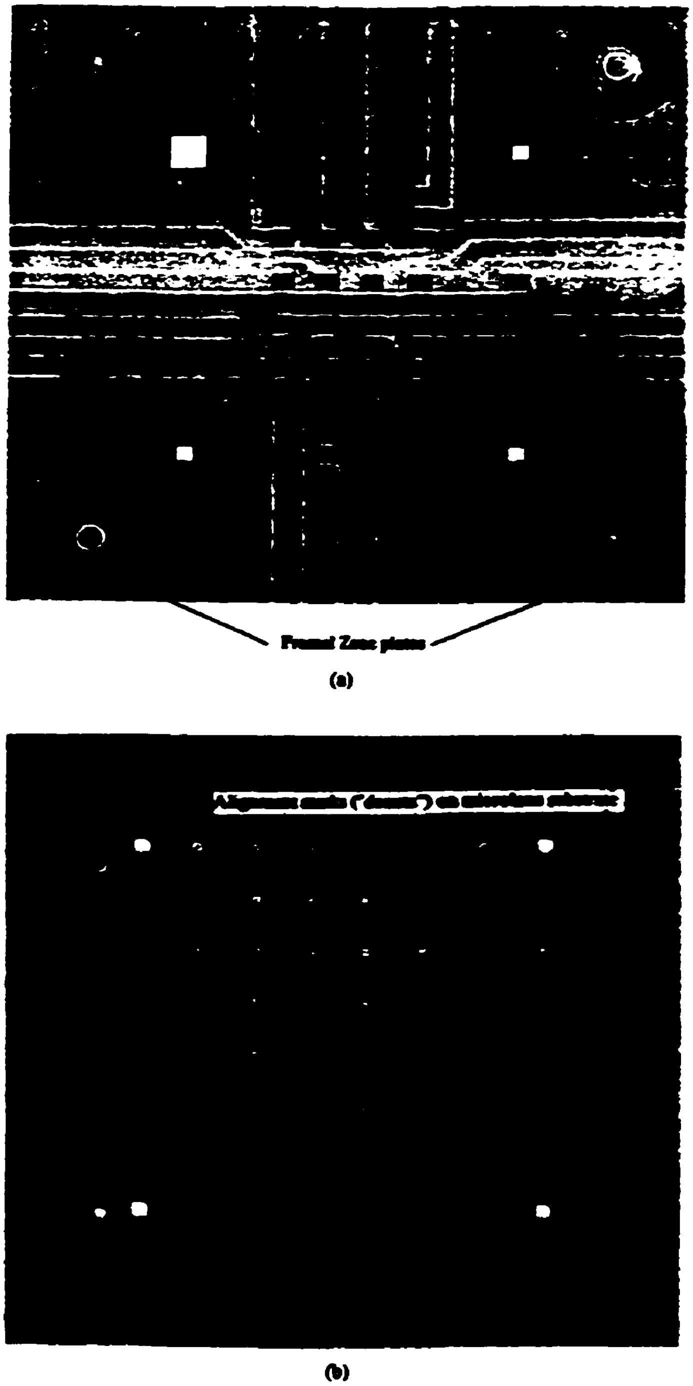

Fig. 2. (a) Reflective Fresnel zone plates on four corners of MSM die. (b) Alignment marks ("donuts") on microlens array substrate.

reflected off the FZP's and forms spots a distance f_{FZP} in front of the die. The package is then moved until the reflected spots from the FZP's coincide with the alignment marks on the microlens substrate, at which point the glue is UV cured. A spacer may be required between the package and the substrate.

III. Alignment Accuracy

Four main sources of errors affect this technique's lateral (xy) alignment accuracy: misalignment of FZP's relative to the optoelectronic device array during fabrication, misalignment of the alignment marks to the microlens array during fabrication, the effect of an angular tilt (α, $\beta \neq 0$ in Fig. 1) in the alignment beam on the position of the spots generated by the FZP's, and error in judging when the FZP spot is aligned to the alignment mark.

For operations in which the FZP's and the device array are defined in the same step, the error will be minimal and defined by the accuracy of the mask fabrication process. In most other processes, for example, when devices are flip-chipped onto metal pads on a die, the error can also be under one micron [5]. During microlens fabrication, the accuracy of the alignment mark position relative to the microlens array is determined by the mask aligner; conventional mask aligners routinely align to within 0.5–1 μm [7].

In Fig. 1, the angle between the die and the alignment beam is $90 - \alpha$. Since the interference pattern between the part of the alignment beam reflected from the substrate and that reflected from the die is used to determine the perpendicularity of the alignment beam to the die, a deviation from the normal of β between the alignment beam and the die will cause the spot generated by the reflective FZP's to be misaligned with respect to the die by approximately $\Delta = f_{fzp} \tan[2(\alpha^2+\beta^2)^{0.5}]$. For $f_{fzp} = 1$ mm, $\Delta < 1\,\mu$m if $2(\alpha^2+\beta^2)^{0.5} < 0.057°$.

Thus, in principle, a lateral alignment error of $\epsilon < 2\,\mu$m is achievable.

Two FZP's can yield rotational (θ_z) alignment information. For FZP's on diagonally opposite corners and a distance $\tau/2$ away from the array center, the θ_z error is under arctan (ϵ/τ). If this technique is also used for z alignment, the error is determined mainly by the depth of focus of the FZP's which is $\delta = \lambda/2(NA^2)$ [8], where NA is the FZP numerical aperture.

Other minor diffractive effects have been neglected in this analysis; these had negligible impact on the results below.

IV. Experimental Setup

The central 4 × 4 array of an 8 × 8 diffractive microlens array was aligned to a 4 × 4 MSM array using the above technique (MSM's were 50 μm × 50 μm with Ni–Pt–Au metallization on InP). These are shown in Fig. 2(a) and (b). The array pitch was 125 μm. The microlens glass substrate had nominal dimensions of 15 × 15 × 1 mm. Two binary amplitude FZP's (D_{FZP} = 295 μm) a distance τ = 1909 μm apart on diagonally opposite corners of the MSM array were defined; alignment donuts with an inner diameter of 25 μm were fabricated at corresponding places on the microlens substrate. Both the microlenses and the FZP's had a focal length of 1000 μm at λ = 850 nm. The MSM die was glued and wire bonded into a side brazed 22 pin dual in-line package. The average distance from the top of the die to the top of the package was ~451 μm (standard deviation = 20 μm), making a ~550-μm-thick spacer necessary. Fig. 3 shows the optical train which generated a flat beam with uniform irradiance. Only the central 1% of the light emerging from the fiber was captured by the ×40 microscope objective, ensuring a uniform irradiance distribution. A very flat beam was obtained by longitudinally moving the ×40 microscope objective until

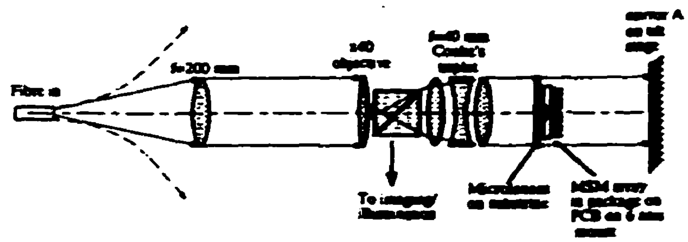

Fig. 3. Optical train for producing normally incident, flat, uniform irradiance beam.

Fig. 4. (a) Spot generated by FZP in upper right alignment mark ("donut"). (b) Microlens array deliberately misaligned by ~40 μm to show spot and donut separately.

the back focal plane of the $\times 40$ objective coincided with the front focal plane of the triplet. The beam flatness was measured with a shear plate interferometer and found to be better than $\lambda/10$ over the regions of the beam hitting the FZP's. Mirror A was then adjusted to reflect the incident beam back into the fiber. Standard interferometric techniques were used to ensure that the substrate was normal to the light beam. Afterwards the package was brought in as described in step 3 above.

V. Results

Interferometric measurements indicated that the angular errors were $\alpha = 0.09°$, $\beta = 0.09°$. Fig. 4 shows images of the FZP-generated spots in the donuts on the microlens substrate. Fig. 4(a) shows the spot in the donut on the upper right hand corner of the microlens substrate; a similar picture was obtained for the lower left spot. Fig. 4(b) shows the spot deliberately misaligned by ~40 μm and thus falling outside the donut. The large bright smear is due to the light from the illumination LED ($\lambda = 880$ nm) which was also focused by the reflective FZP. The LED was misaligned in order not to have the bright smear drown out the donut and alignment spot.

The measured diameter of the spot inside the donut was 12.5 μm (± 3 μm) and the spot was measured to be ~4 μm off center (this 4 μm error was due to the low resolution of the manual xyz stage used). Given the angular misalignments α and β, a further error of $\Delta = 4$ μm could have been introduced. Assuming a total error of 1 μm in mask alignment during various device fabrications, the total xy misalignment error was thus ~9 microns for this proof-of-concept experiment. This was verified by imaging the spots on the MSM's through a hybrid microlens-bulk lens relay. Additionally, first order calculations reveal that the 12.5-μm spot diameter corresponded to a 42-μm error in z alignment [8].

The alignment errors in future systems will be reduced by improving the orthogonality of the incoming beam and using more precise positioning equipment.

VI. Conclusion

By using on-die reflective diffractive structures, a smart pixel array was aligned to a microlens array in x, y, and θ_z. Further projects will involve on-die astigmatic FZP's for precise information on z misalignment, as in CD players [9]. These packaged devices will be used in experiments involving the analysis of optical crosstalk for detecting misalignment in larger systems [10].

References

[1] R. A. Nordin, F. J. Levi, R. N. Nottenburg, J. O'Gorman, T. Tanbun-Ek, and R. A. Logan, "A systems perspective on digital interconnections technology," *J. Lightwave Technol.*, vol. 10, no. 6, pp. 811–827, 1992.

[2] D. V. Plant, B. Robertson, H. S. Hinton, W. M. Robertson, G. C. Boisset, N. H. Kim, Y. S. Liu, M. R. Otazo, D. R. Rolston, and A. Z. Shang, "An optical backplane demonstrator system based on FET-SEED smart pixel arrays and diffractive lenslet arrays," *IEEE Photon. Technol. Lett.*, vol. 7, no. 9, pp. 1057–1059, 1995.

[3] M. S. Cohen, M. J. DeFranza, F. J. Canora, M. F. Cina, R. A. Rand, and P. D. Hoh, "Improvements in index alignment method for laser-fiber array packaging," *IEEE Trans. Comp., Packag., Manufact. Technol. B*, vol. 17, no. 3, pp. 402–411, 1994.

[4] J. M. Sasian and D. A. Baillie, "Simple technique for out-of-focus feature alignment," *Opt. Eng.*, vol. 34, no. 2, pp. 564–566, 1995.

[5] Y. C. Lee and N. Basavanhally, "Solder engineering for optoelectronic packaging," *J. Metals*, pp. 46–50, June 1994.

[6] K. Rastani, M. Orenstein, E. Kapon, and A. C. Von Lehmen, "Integration of planar microlenses with vertical-cavity surface emitting lasers," *Opt. Lett.*, vol. 16, no. 12, pp. 919–921, 1991.

[7] J. M. Miller, M. R. Taghizadeh, J. Turunen, and N. Ross, "Multilevel-grating array generators: Fabrication error analysis and experiments," *Appl. Opt.*, vol. 32, no. 14, pp. 2519–2525, 1993.

[8] W. J. Smith, *Modern Optical Engineering*. New York: McGraw-Hill, 1990.

[9] W. H. Lee, "Holographic optical head for compact disk applications," *Opt. Eng.*, vol. 28, no. 6, pp. 650–653, June 1989.

[10] G. C. Boisset, B. Robertson, W. Hsiao, H. S. Hinton, and D. V. Plant, "Detection of $x-y$ misalignment error using optical crosstalk in a lenslet-array-based free-space optical link," in *Conf. Proc. Optical Computing*, 1995, pp. 63–64.

Optomechanics for a four-stage hybrid-self-electro-optic-device-based free-space optical backplane

G. C. Boisset, M. H. Ayliffe, B. Robertson, R. Iyer, Y. S. Liu, D. V. Plant, D. J. Goodwill, D. Kabal, and D. Pavlasek

We present the design, fabrication, and testing of optomechanics for a free-space optical backplane mounted in a standard 6U VME backplane chassis. The optomechanics implement an optical interconnect consisting of lenslet-to-lenslet, as well as conventional lens-to-lens, links. Mechanical, optical, electrical, thermal, material, and fabrication constraints are studied. Design trade-offs that affect system scalability and ease of assembly are put forward and analyzed. Novel mounting techniques such as a thermal-loaded interference-fitted lens-mounting technique are presented and discussed. Diagnostic tools are developed to quantify the performance of the optomechanics, and experimental results are given and analyzed.

Key words: Optomechanics, diagnostics, alignment, optical backplane.

1. Introduction

Optical interconnects promise to alleviate the transmission bottlenecks that will appear in future computing systems as the demand for information throughput between processing elements reaches ever higher.[1] A major factor impeding progress in the field of optical interconnects is that of optomechanical constraints. Real systems will have to be designed to withstand the rigors of industrial settings if optical interconnects are ever to leave the research laboratory. Although the field of optomechanics and optical packaging has been studied for centuries[2] and is by now a well-established field with excellent references,[3–7] the field of optomechanics as applied to free-space digital optical systems is relatively new. The novel aspect of the optomechanics in this application is that the optics are used mainly to image large two-dimensional (2-D) arrays of beams. Several sophisticated digital free-space optical interconnect demonstrators have been described in the past,[8–11] along with optomechanics in such demonstrators.[12–15]

This paper analyzes the optomechanics of a four-stage hybrid bulk-lenslet free-space optical backplane demonstrator system nearing completion. The system is implemented in a unidirectional ring and comprises the optical interconnection of four hybrid-self-electro-optic device (-SEED) smart-pixel arrays. A hybrid combination of microchannel relays and conventional (bulk) relay lenses was used to interconnect the smart-pixel arrays. This system built on the previous demonstrator systems referenced above and introduces several new features, such as vertical mounting of the baseplate and installation of the system in a standard backplane chassis.

Additionally, a realistic system must remain operational even if roughly handled, and most electronic-computing systems today are exposed to mechanical vibrations originating from sources such as cooling fans blowing air over components; as the power consumption of components increases in future systems, these cooling considerations will become ever more important. As a result, future free-space optical interconnects will have to maintain their alignment and function in such a vibratory environment if they are to gain widespread acceptance. Moreover, diagnostic tools to quantify the optical misalignments, if any, caused by shock and vibrations will have to be devel-

---

G. C. Boisset, M. H. Ayliffe, B. Robertson, R. Iyer, Y. S. Liu, D. V. Plant, D. Kabal, and D. Pavlasek are with the Department of Electrical Engineering, McGill University, 3480 University Street, Montréal, Québec H3A 2A7, Canada. When this research was performed, D. J. Goodwill was with the Department of Electrical and Computer Engineering, University of Colorado, Boulder, Colorado; he is now with the Department of Interconnect Technology, Nortel, P.O. Box 3511, Station C, Ottawa, Ontario K1Y 4H7, Canada.

Received 11 December 1996; revised manuscript received 6 May 1997.
0003-6935/97/297341-18$10.00/0

oped. This paper also describes the design and implementation of an optomechanics diagnostic system.

The paper is structured as follows: In Section 2 we give an overview of key system aspects. In Section 3 we examine the bulk relay and the baseplate; in Section 4 we describe other modules. In Section 5 we explore the key issue of interfacing optoelectronics to optomechanics by use of a daughterboard. In Section 6 we describe a setup used to measure the performance of the daughterboard mounting technique. In Section 7 we give experimental results and follow it with a conclusion.

2. System Overview

The optical backplane was designed to implement a ring optical interconnection of four optoelectronic chips,[16] with each chip having 16 channels modulated at a maximum rate of 50 MHz. As a result, the peak theoretical bisection bandwidth of this demonstrator system was approximately 1.6 Gbits/s, which is comparable with middle-of-the-line backplanes available today.[17]

The principal optical-packaging and optomechanical objective was to interconnect optically four printed circuit boards within a standard 482.6-mm (19-in.) 6U VME[17] commercial backplane chassis. Fitting the system into the 6U chassis was a self-imposed design guideline to make the system mechanically compatible with many systems found in the field today.

An objective was also to separate the optics from the electronics so that, eventually, a user inserting a 6U circuit board into the backplane would see a conventional VME backplane environment—from a mechanical and electrical dc power perspective—while accessing the tremendous bandwidth offered by the free-space optical interconnect. In our system, this was accomplished by use of daughterboards and motherboards. The hybrid-SEED optoelectronic chips[16] were glued and wire bonded to the daughterboards residing in the optical layer; the daughterboards were then linked to the motherboards by means of a short, impedance-matched high-speed ribbon cable. As has been demonstrated previously,[18] this technique for in-

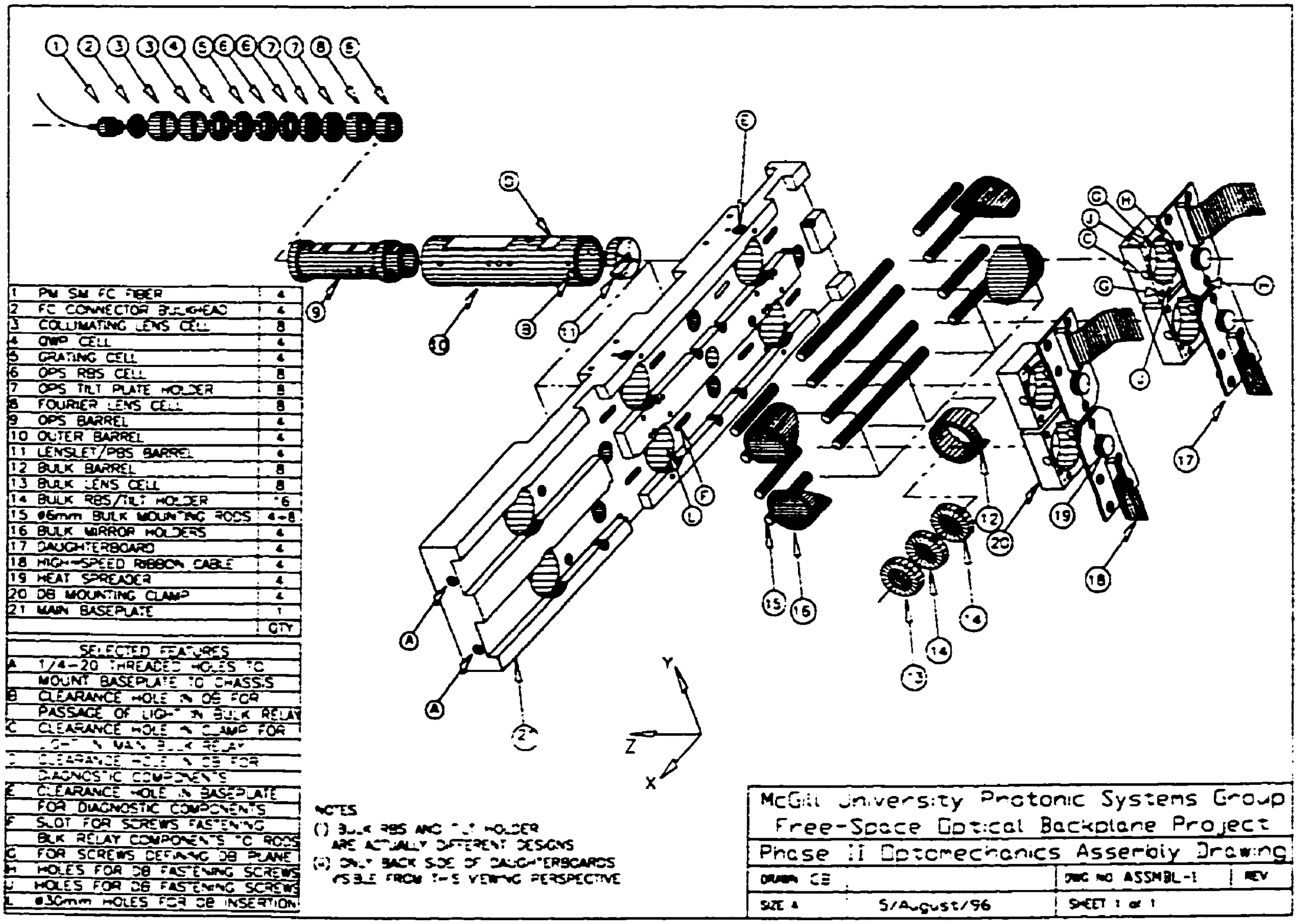

Fig. 1. Simplified 3-D system-assembly drawing. PM, polarization maintaining; SM, single mode; FC, fiber connected, QWP, quarter-wave plate; OPS, optical power supply; RBS, Risley beam steerer; PBS, polarizing beam splitter; Ø, diameter; DB, daughterboard; MB, motherboard; OB, outer barrel; BLK, bulk.

jecting electrical data from the motherboard into the optical backplane allowed for mechanical decoupling between daughterboard and motherboard while maintaining full electrical integrity between the two, provided the cable was short enough: An 8-cm length (~3-in.) was sufficient for the expected 50-MHz maximum clock speed, according to commonly used criteria for transmission-line integrity.[19]

System scalability was also a key goal. The demonstrated system occupied approximately the top half of the 6U chassis (which could therefore allow an identical system to occupy the bottom half) and featured expansion slots for interconnection of more boards if so desired. A simplified assembly drawing of the system is shown in Fig. 1. The system optomechanics had to accomplish the following tasks: (1) mechanically support the optics while respecting all tolerances demanded by the optical design, (2) support the packaged optoelectronics and interface them to the rest of the interconnect, (3) act as an interface between a commercially available electronic chassis and the rest of the system, and (4) integrate diagnostic optics and electronics for alignment and system characterization. The system as a whole had to be rugged, scalable, and easily assembled. The optomechanics were modularized as much as possible to facilitate assembly and alignment.

A key feature of this system was its three-dimensional (3-D) nature; to facilitate the discussions in this paper, it is necessary to define a frame of reference, which is shown at the bottom of Fig. 1. As can be seen, in this system the main relays that are based on bulk (conventional) optics and that implement the optical ring were in an x–y plane. However, the optical power supplies (OPS's), which illuminate the modulator chips with an array of cw power beams, as well as other relays such as the microchannels, were parallel to the z axis. Rotational directions are also defined. For example, θ_y is the angle of rotation about the y axis. Figure 2 shows a picture of the system.

A brief overview of the optical layout is now presented. Figure 3 shows an unfolded view of the overall four-stage system with one of the four OPS modules explicitly drawn. This unfolded view of the 3-D system is slightly misleading since the OPS's should actually be coming into the plane of the paper and the daughterboards should be parallel to the plane of the paper, not perpendicular, as is implied in the unfolded view.

A close-up of a hybrid stage-to-stage relay is shown in Fig. 4. Gaussian beam-propagation models were used in the design of the system. At each stage, lenslets were close to the smart-pixel devices to be able to collect the beams and reduce their numerical aperture, and bulk (conventional) lenses[20] relayed the beamlets from one stage to another. The lenslets reduced the numerical aperture of the beams relayed by the bulk lenses to less than 0.025. All lenslets were 125 μm $\times$ 125 μm eight-level diffractive structures with a focal length of $f_\mu = 768$ μm at $\lambda = 850$ nm. Lenslet array 1 (LA_1) consisted of alternat-

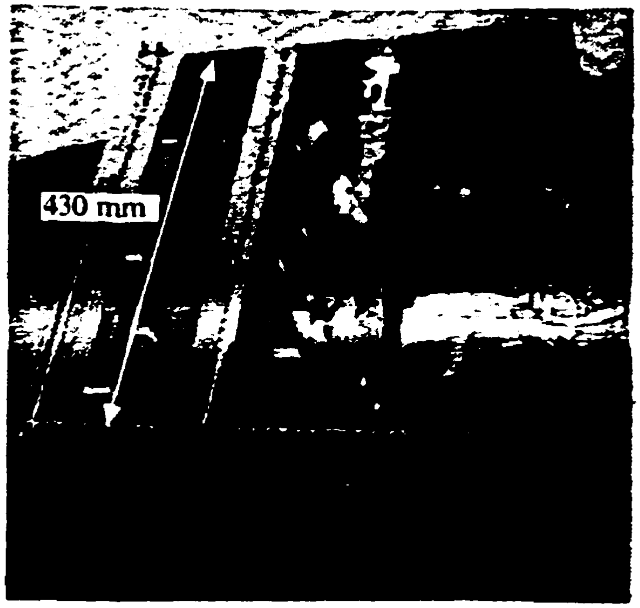

Fig. 2. Photograph of the system mounted in a standard 431-mm-wide (17-in.-wide) 6U VME chassis.

ing 1 $\times$ 8 lenslet strips and pixellated mirror strips 123 μm wide $\times$ 1 mm high. Lenslet array 2 (LA_2) consisted of an 8 $\times$ 8 array of lenslets. These are shown in Fig. 5. Additionally, alignment features were placed around the peripheries of the arrays.

The fiber-connected OPS generated an 8 $\times$ 4 array of right-hand circularly polarized cw beamlets at the power-array plane that was relayed by LA_1 and LA_2 to the smart pixel. The beamlets were then modulated by the chip, relayed through LA_2, and imaged by the bulk relay to stage 2. At stage 2, the beamlets were reflected by the polarizing beam splitter (PBS), then reflected off the pixellated mirror on LA_1, and finally imaged onto the receiver on board 2 by means of LA_2. The polarization components, namely the quarter-wave plates (QWP's) and the PBS were used for beam combinations, as discussed in Ref. 21. The optical microlens relay was designed to relay the beams using the maximum lens-to-waist configuration.[22] Tilt plates and Risley beam steerers (RBS's) were included for alignment purposes. The dimension of the array of beamlets was nominally 1.2 mm $\times$ 1.2 mm.

Space constraints were such that the aperture stop for the bulk interconnect lay between the PBS–QWP assembly and the RBS's at the entrance to the lenslet barrel (described below). This stop was 4.10 mm in diameter. To a first order this left an ~500-μm clearance between the edge of the outermost beamlet and the stop. As a result, any offset greater than 500 μm on the bulk interconnect would lead to considerable clipping of the outermost beamlet. However, as we show below, the alignment budget permitted only a smaller misalignment of 220 μm at the pixellated mirrors, since this was the maximum travel of the tilt plates.

This paper does not present a detailed analysis of the optical system. However, there were several crit-

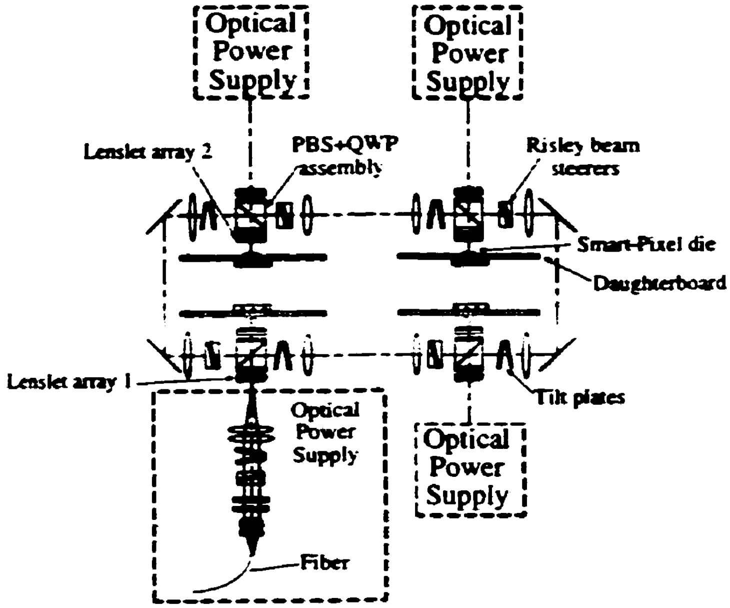

Fig. 3. Unfolded system optical layout.

ical and extremely tight optomechanical-alignment tolerances that influenced much of the design and must be given here. These tight tolerances were driven by the extremely small size of the multiple-quantum-well windows that all beams had to hit. The multiple-quantum-well windows were 20 μm × 20 μm (Ref. 16), and the beams incident on them had a nominal diameter (99% encircled power) of 19.5 μm. This situation imposed extremely tight tolerances, which are given in Table 1. Among other tolerances given, Table 1 indicates that the lateral-alignment (x–y) error between the microlens array and the smart-pixel device array had to be <1 μm to keep losses from misalignment to less than 1% optical power. Other demanding tolerances were the lenslet-to-lenslet alignment tolerances, key values of which are given in Table 2. As can be seen, the bulk interconnect tolerances (~220 μm) were much looser than the lenslet-device tolerances (~1 μm) or the lenslet-to-lenslet tolerances (~5 μm).

3. Baseplate and Bulk Relay

A. Baseplate Description

The baseplate was the central piece of the optomechanics and acted as the support structure for the entire optical–optomechanical layer. All other optomechanical and optical components were either attached to the baseplate or locked into barrels attached to the baseplate. The baseplate, a simplified sche-

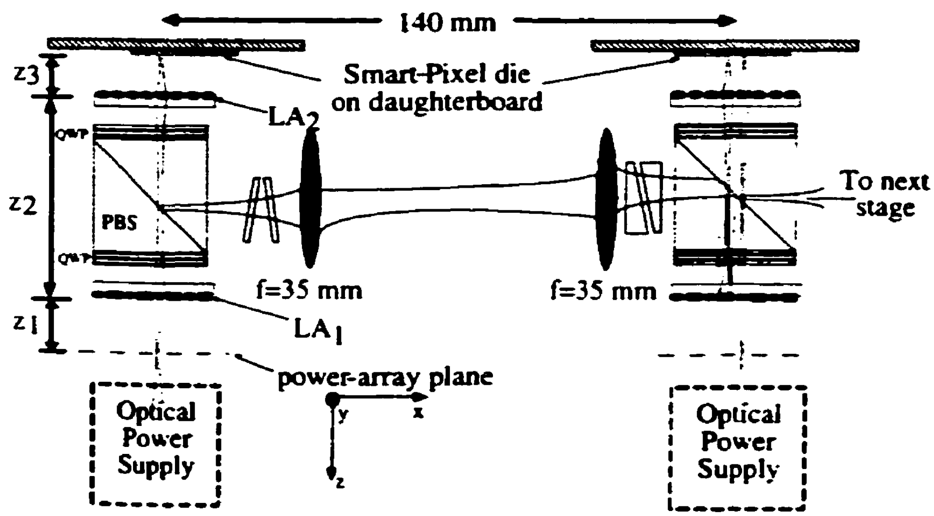

Fig. 4. Close-up of one board-to-board relay.

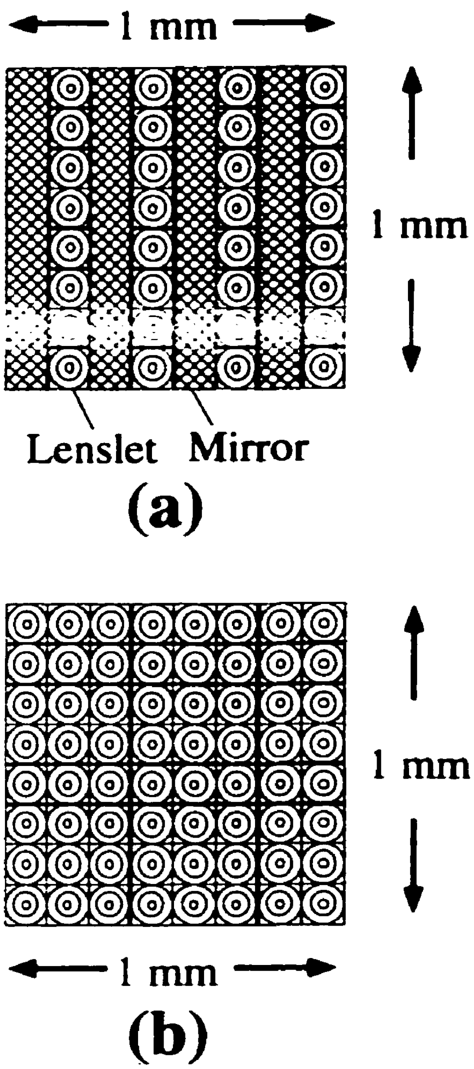

Fig. 5. Lenslet-array schematics: (a) lenslet array 1 (LA_1) and (b) lenslet array 2 (LA_2).

matic of which is shown in Fig. 6, was 431.8 mm (17 in.) long (the inside of the standard VME rack is 50.8 mm shorter than the outside because of mounting flanges), was mounted vertically into the chassis, and was bolted to the side panels of the chassis.

Previous free-space optical-switching demonstrator systems used aluminum or steel for baseplates, but it was determined that neither of these materials was suitable for production.[12] The baseplate for this system was made of magnesium AZ31B; the main reasons for choosing this metal were its ease of machinability, its lightness, and its low residual stress, which minimizes the need for stress relief when compared with other metals.[23] This type of metal has already been used in applications such as lens mounting.[24] Note that magnesium is softer than other frequently used materials: The Brinell hardness number (BHN) of magnesium is 82, compared with 95 for aluminum 6061-T6 or ~200 for 1080 steel (depending on drawing and other processes). This softness makes magnesium easier to machine but more easily dented,[25,26] which prompted the use of rods for

Table 1. Daughterboard Alignment Tolerances[a]

Degree of Freedom	Board Position and Tolerance to be Met	Board Position before Gluing	Board Position after Gluing
Δx (μm)	0 ± 1	0 ± 2	3.2 ± 3
Δy (μm)	0 ± 1	0 ± 2	-2 ± 3
z_3 (μm)	886 ± 15	887 ± 15	875 ± 15
Tilt θ_x	$0° \pm 0.5°$	$0.06° \pm 0.1°$	$0.55° \pm 0.27°$
Tilt θ_y	$0° \pm 0.5°$	$0.04° \pm 0.1°$	$0.18° \pm 0.14°$

[a]Tolerances for positioning of the smart-pixel die on the daughterboard with respect [illegible] columns 2–4 indicate (a) the positioning objective to be met for a <1% loss, (b) the measurement when the board is held at its nominal position by the positioning stage and is about to be glued to the optomechanics, and (c) the final position after the daughterboard is glued to the optomechanics and the stage is removed, respectively. The parameters Δx and Δy were measured 9 weeks after gluing; the other parameters were measured 4 days after gluing.

mounting the bulk optics (described in Subsection 3.C.2).

The main outer barrels, each one containing an OPS and a microlens relay, fit into the holes labeled L in Fig. 6, which were 30 mm in diameter. Of these six holes, four were used in the actual system (those at $x = 75$ mm and $x = 215$ mm); two others (at $x = 355$ mm) were kept for future system expansion.

Many holes and slots were included for diagnostic, assembly, and alignment purposes. Additionally, magnets were glued into holes machined at the back of the baseplate. They served to keep the bulk-mounting rods (described below) in place on the vertical baseplate during assembly, until the bulk components were bolted onto the rods.

B. Baseplate Machining and Characterization

Machining of the baseplate was performed as follows: The magnesium plate from which the baseplate was machined was clamped to the apron of a DRC 600 (Bridgeport) milling machine, and three 9-mm-deep main cuts in the y direction were made; these are the cuts that most affect baseplate bowing in θ_y. Most of the smaller clearance slots for the bulk-barrel screws were also machined at this time. A fly-cutter finish (with the cutter turning at 1200 rpm, a feed rate of 152 mm/min, and a cut depth of 125 μm) ensured a smooth surface for subsequent flatness measurements.

The flatness of the baseplate was measured in the main slots (in the x direction) along the two lines AA′ and CC′, as shown in Fig. 6. For performing these measurements, the baseplate rested on a granite

Table 2. Lenslet Alignment Tolerances[a]

Degree of Freedom	Position and Tolerance to be Met
LA_1 to LA_2 (x, y)	0 ± 5 μm
z_1	922 ± 15 μm
z_2	6.981 ± 0.15 mm

[a]Tolerances for lenslet-to-lenslet alignment as imposed by the optical design; z_1 and z_2 are as defined in Fig. 4.

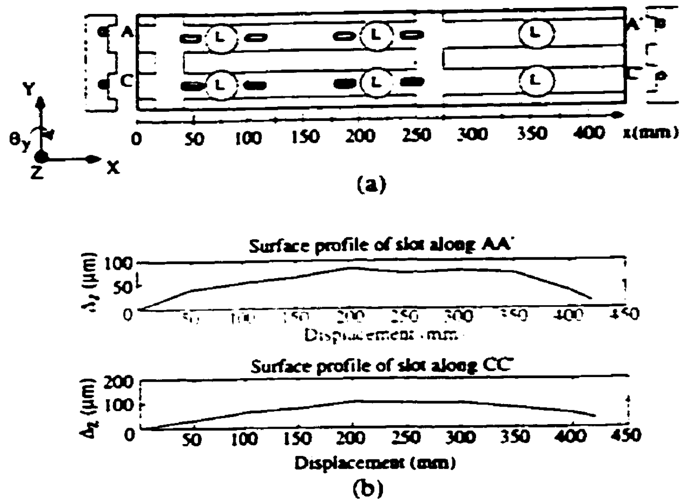

Fig. 6. (a) Sketch of the baseplate. (b) Surface profile of the baseplate along the slots.

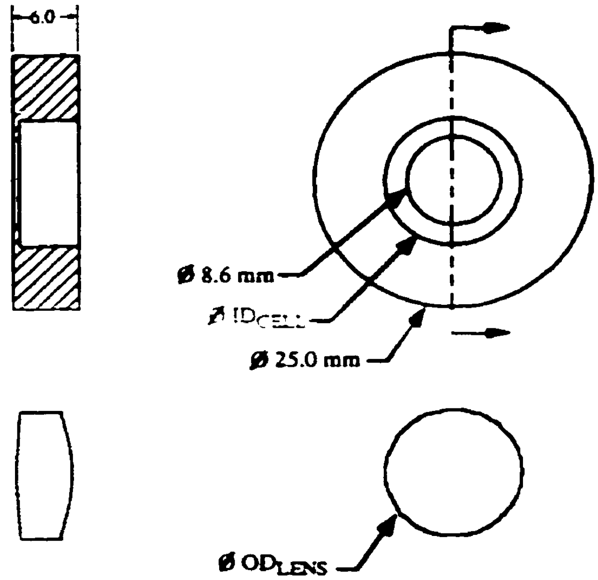

Fig. 7. Bulk lens and holder used for the FN1 interference-fitted lens holder. For an interference fit, $OD_{LENS} > ID_{CELL}$.

measuring slab and a level indicator was passed along the bottoms of the slots at approximately the place where the rods holding the bulk barrels made contact with the bottom of the slot. The maximum deviation was ~125 μm from one end of the baseplate to the other and was considerably less over the stretch (~50 < x < 275 mm) where the bulk relay actually resided. The use of rods (described below) for bulk mounting further helped reduce the effect of baseplate irregularities on the optical axis by averaging out surface irregularities. The repeatability of the flatness measurements was better than 10 μm.

These flatness values were well within the overall bulk interconnect alignment tolerance budget.

C. Bulk Barrel Assembly

The bulk lenses, RBS's, and tilt plates were mounted into their respective holders. Afterwards, as can be seen from the assembly drawing (Fig. 1), the mounted bulk lens and a pair of mounted steering elements (either a pair of RBS's or a pair of tilt plates), respectively labeled components 13 and 14 in Fig. 1, were inserted into a modular bulk barrel (component 12). This bulk barrel was then bolted to the baseplate.

1. Thermal Effects in Bulk Relay Lens Inner Mounting

Although many techniques exist for mounting lenses into cells,[3] none of these techniques left enough room to fit the bulk lenses and the steering elements (either RBS's or tilt plates) between the bulk turning mirror and the daughterboard. It was thus decided to forego any retaining ring and instead hold the lenses in their cells by use of the force of an interference fit between the outer diameter of the lenses, OD_{LENS}, and the inner diameter of the cells, ID_{CELL}, as shown in Fig. 7. In other words, $OD_{LENS} - ID_{CELL} = I$, where I is a positive number called the interference. Interference fits are frequently used in industry to maintain a constant bore pressure in hole–shaft assemblies; the difference between minimum and maximum values in the machining tolerances is kept small.[25]

The OD_{LENS} of the eight bulk relay lenses in the system were measured to be between 12.468 and 12.479 mm (±2.5 μm).

The use of interference fits posed several design challenges, most of them related to thermal issues. The first challenge was assembly. To first put the lens into the cell, we found that the easiest way was to heat the cell (but not the lens) to make it expand and then to insert the lens. As the cell cooled and shrank, the lens was held snugly.

Another challenge was the choice of material. The material chosen for the cell ended up being Delrin.[27] Its main drawback, namely, a high coefficient of thermal expansion CTE_{DEL} = 97 parts in 10^6/°C (ppm/°C), was compensated by its low cost, immediate availability, ease of machining, and low Young's modulus (in both compression and tension) of E_{DEL} = 2.76 GPa, which reduced the stress caused by thermal mismatch. In comparison, the numbers for the glass of the lens were similar to those of BK7: CTE_{LENS} = 7.1 ppm/°C and E_{LENS} = 81 GPa.

Using an interference fit with two such thermally mismatched materials can cause two main problems: (1) As the temperature T increases, the interference I decreases. Eventually, at T_{fall} the lens can simply fall out. (2) As T decreases, I increases, causing severe radial stress. This can lead to birefringence and possibly damage to the cell, the lens, or both.

Machining one different cell for each lens would have been prohibitively expensive, so one value of ID_{CELL} at 20 °C, ID_{CELL20}, was chosen for all cells. The basic criterion for computing the nominal value of ID_{CELL20}, was that, at a maximum operating temperature T_{max}, the interference should still lead to a FN1 interference fit (2.54 μm < I < 20.3 μm) for all

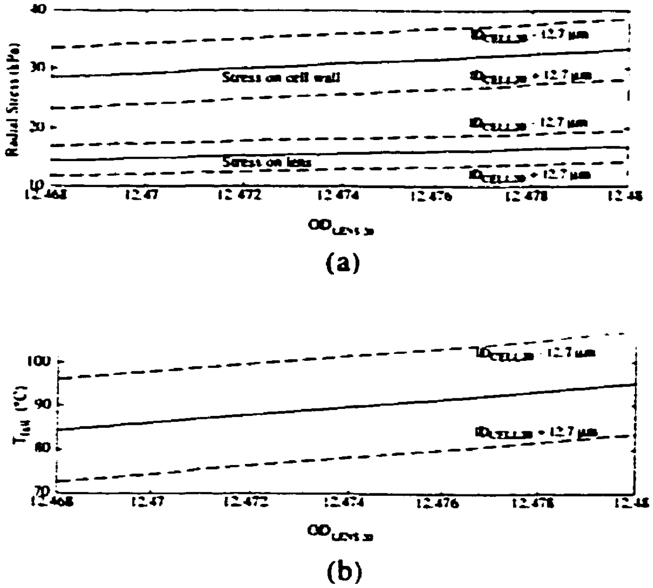

Fig. 8. (a) Curve relating the radial stress on the components to the lens outer diameter. (b) Curve relating the temperature at which the lens falls out to the lens's outer diameter.

lenses. This fit, described as a light drive fit, is used for permanent assemblies and produces a light assembly pressure.[25] The maximum operating temperature T_{max} was chosen to be 85 °C since this is the maximum tolerable case temperature for a commercial-grade Pentium Pro.[28]

The relations for calculating the radial stress in the lens, S_{RLENS}, and in the cell wall, S_{RCELL}, are[3]

$$S_{LENS} = \frac{(CTE_{DEL} - CTE_{LENS})\Delta T}{1/E_{LENS} + OD_{LENS}/(2E_{DEL}t_c)}, \qquad (1)$$

$$S_{RCELL} = \frac{(OD_{LENS})(S_{RLENS})}{t_c}, \qquad (2)$$

where the cell-wall thickness t_c is nominally 6.3 mm.

Given the above, ID_{CELL20} was calculated to be 12.397 mm, and Fig. 8 shows plots of the stresses on the cell and lens [Fig. 8(a)] and of T_{fall} [Fig. 8(b)] as a function of OD_{LENS}. The bands above and below each solid curve represent the effect of a machining error of ±12.7 μm on the value of ID_{CELL20}. It can be seen that a smaller cell inner diameter leads to greater stress and a greater T_{fall}. As a result, in the worst-case combination of lens tolerances and cell inner-diameter tolerances, the interference can fall to zero and the lens can fall out of the holder at 72 °C. At the other extreme worst case, the radial stress in the cell can reach 38 kPa, which is slightly over half of the 68-kPa nominal tensile strength of Delrin.[27] In all cases, calculations[3] revealed that the stress-induced birefringence was negligible.

Experimental validation was conducted on this technique. In the first experiment, the lens was mounted by use of the technique described above in this subsection. A beam was then passed through the lens, the cell with the lens in it was rotated, and the movement of the spot caused by the focused beam was observed in the focal plane. The spot traced out a circle with a radius of 3.5 μm (±1 μm). Since this passive-mounting technique cannot correct for defects within the lens, such as the intrinsic wedge angle or centering of the lens optical axis with respect to its mechanical axis, these have to be added to obtain a true picture of the centering accuracy. For the current lens, these additional factors could have added up to 10 μm to the radius of the circle traced out by the spot.[illegible] Consequently, this is a cheap and rapid technique for use only with good-quality, well-centered lenses; as a result, the technique demonstrates that the cost of lens mounting can be pushed back from the optomechanical assembler to the lens and cell fabricators.

In another experiment, a mounted lens with an outer diameter of OD_{LENS} = 12.469 mm at 20 °C was heated until the lens fell out. The lens did indeed fall out at T_{fall} = 100 °C ± 10 °C, showing that the technique worked as expected. This mounting process illustrates the compromises between ease of assembly, operating temperature, material selection, and tolerances that must be considered when designing and building optomechanical components.

2. *Bulk-Barrel Mounting*

After the bulk barrels were assembled they had to be mounted onto the baseplate in their proper positions. As with other similar systems,[8] slots were cut into the baseplate and the bulk barrels rested in these slots. However, given the vertical mounting and the rough handling the system was expected to receive in the chassis, the standard magnetic retaining techniques used in many other digital free-space optical interconnect demonstrations[8,10,11] were rejected; instead, all bulk-relay components (bulk barrels and mirrors) were bolted into the baseplate. Furthermore, the barrels were not in direct contact with the edges of the slots. Instead, hard, precision-ground stainless steel rods 6 mm in diameter were inserted into the slots and the components rested on the rods, as shown in Fig. 9. Such rods are cheap and readily available.[29] The outer-diameter tolerance of the above rods was +0 to −10 μm, and the outer diameters of the machined outer-barrel components were measured to have a deviation of ±10 μm from their nominal 30 mm.

Machining tolerances were the most important factor affecting the height of the optical axis. Other physical parameters were nonetheless studied, as they gave insight into the design. One of these parameters was the deformation of the barrels arising from the holding force exerted by the screws. If we assume that the screw threaded into the hole in the barrel can be modeled by a nut–bolt fastening, the holding force P exerted by the screw can be estimated to be[30]

$$P = T/(KD). \qquad (3)$$

For the 4-40 screw used, T is the installation torque (nominally 0.6 N · m for an 18-8 steel 4-40 screw), K is the torque coefficient (~0.15 for plated finish fas-

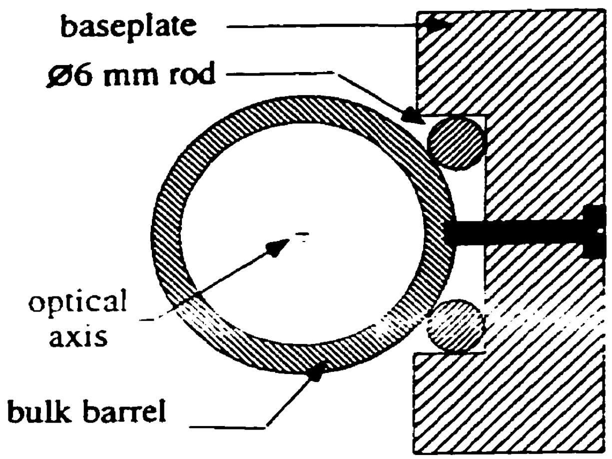

Fig. 9. Technique for mounting bulk-interconnect components onto a vertical baseplate. The bulk barrel has an inner diameter of 25 mm and an outer diameter of 30 mm.

teners), and D is the nominal screw diameter (2.79 mm for a 4-40 screw).[30] This yields $P = 1434$ N ($M = 1434$ N/9.8 = 146.3 kg).

This exerted force can damage the barrels, the rods, the baseplate, or any combination of these by causing indentations in the material. The most critical interface is between the barrel and the rods, and the damage to this interface can be estimated as follows. By use of the BHN's, the surface area A of the indentation in the barrel caused by the hard steel rods biting into the barrel can be approximated as[31]

$$A = 0.5 \times M/\mathrm{BHN}, \tag{4}$$

where the factor of 0.5 is due to the fact that each rod exerts only half the force on the barrel.

Using a value of BHN = 95 (Ref. 25) for the 6061-T6 aluminium used in the barrels means that the surface area A should be $0.5 \times 146.3/95 = 0.77$ mm^2. Further geometrical analysis indicates that, for a line contact of 13 mm (the length of the barrel) and a rod diameter of 6 mm, the drop in the height of the optical axis resulting from indentations is of the order of 1 μm, which is less than the machining error. This drop was further reduced by anodization of the barrels: Anodization increased the hardness of the barrels, thus reducing indentations in the barrels to negligible levels.

To summarize, the considerable forces involved in bolting the bulk barrels down onto the baseplate caused no significant damage to any component. It will be seen below, however, that the force involved in bolting a daughterboard to the optomechanics caused significant problems. Other forces, such as the force exerted between baseplate and rods, were spread over the length of the rods and as such could be neglected.

D. Bulk-Turning-Mirror Alignment

The optical system was a closed-loop ring system. As such, turning mirrors had to be installed at the four corners of the optical system to close this loop. Since errors in mirror alignment could be corrected only by the bulk RBS's and tilt plates, which had a wedge angle of 1° and a tilt angle of 10°, respectively, it was imperative that the mirrors be aligned as carefully as possible to reduce the travel requirements of the steering optics. Additionally, the mirrors had to be arranged so as to eliminate rotation of the 2-D array of beams.[32] In the overall system-assembly sequence, one of the first steps was mounting of the bulk turning mirrors onto the baseplate, as outlined in Fig. 10. This subsection describes the process.

Before assembly was started, all the mirrors were glued to their holders, which allowed for two degrees of freedom in tilt and rotation. Aligning the four mirrors into a loop presented a certain problem. In a system such as this, the slots in the baseplate can be used to locate the optical axis as it goes through four 90° turns in the loop. Apertures placed along the slots or along mechanical extensions of the slots can be used to define the optical axis; the further the apertures are from each other (i.e., the greater the lever arm), the better the optical axis can be defined.

It is therefore possible for one to align the mirrors by launching a reference beam that is known to be on axis and monitoring the reflected beam on an aperture far from the baseplate. However, this procedure works for only the first three mirrors; placing the fourth mirror closes the loop, and a lever arm longer than the baseplate cannot be used. For avoiding this problem, a technique involving a pellicle was used.

With no mirrors on the baseplate, a reference beam was launched down the barrel of the pellicle holder, at the end of which was fixed a 70/30 (transmissive–reflective) pellicle, as shown in Fig. 10. Seventy percent of the beam went through (beam T), and 30% was reflected toward position 1. Using customized alignment apertures on the baseplate and along the optical bench allowed the pellicle holder and incoming beam to be adjusted until they delivered a beam that was coaxial with the optical axis on the baseplate. The beam was parallel to the ideal bulk optical axis to within a few minutes and was less than 50 μm off axis. Afterward, bulk turning mirror 1, in its holder, was installed. After adjusting the mirror so that the reflected optical beam going toward position 2 was again parallel to and on the axis, mirror holder 1 was bolted. This procedure was repeated for mirrors 2 and 3. For the final mirror holder (4), the reflected beam R_1 was observed and the mirror holder was adjusted so as to minimize the angle β; mirror holder 4 was then bolted. The pellicle thus brought the reference beam off the baseplate and allowed for a lever arm to improve the accuracy of the alignment.

Figure 11(a) shows spots resulting from beams T, $R_1, R_2, R_3, \ldots$, which are projected onto a screen 3 m from the baseplate. This large (3-m) distance allows a lever effect to magnify the error in β. To obtain this picture, mirror 4 was deliberately misaligned; the actual alignment, which was much tighter ($\beta < 0.05°$), was similar to that shown in Fig. 11(b). This misalignment was sufficiently small for eventual correction by the bulk RBS's and tilt plates.

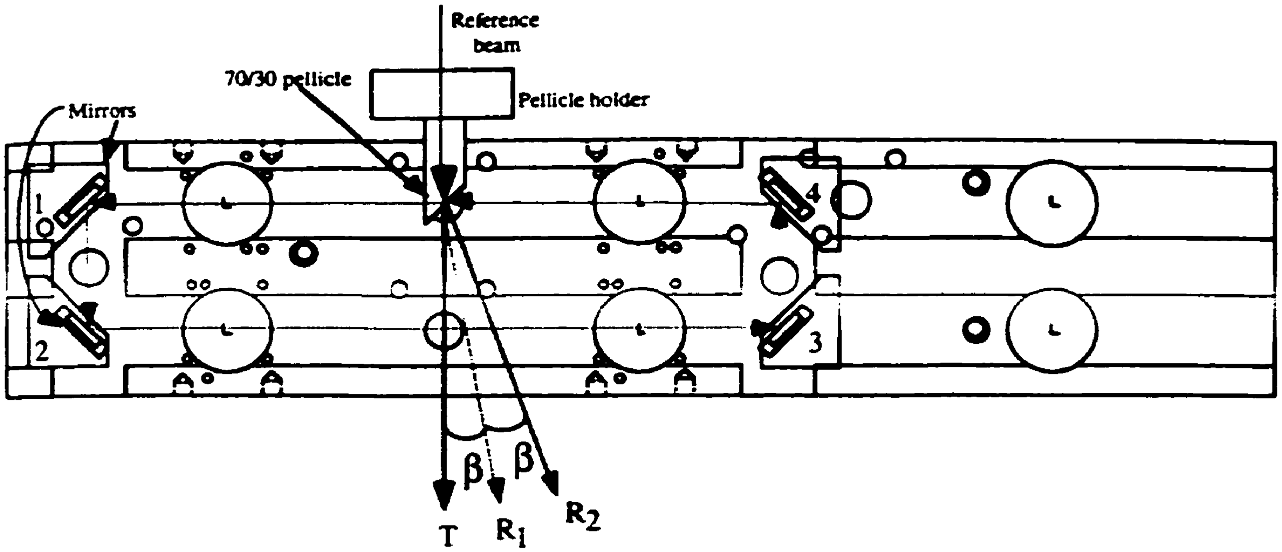

Fig. 10. Setup for mounting and aligning bulk turning mirrors on the baseplate.

4. Other Modules

This section covers the optomechanics associated with other key modules. It concludes with a first-order alignment-tolerancing analysis.

A. Lenslet–Beam-Splitter Barrel

A simplified drawing of the lenslet–beam-splitter barrel is shown in Fig. 12(a). To assemble the unit, we first aligned the PBS with the QWP's mounted on it (PBS–QWP) and then glued it inside the slot, as shown in Fig. 12(b). With a customized setup, the PBS was glued with an angular error of $\theta_y < 0.05°$. The lenslets were then glued to the faces of the barrel, as shown in Figure 12(c).

We met the demanding lenslet-to-lenslet alignment tolerances in (x, y) listed in Table 2 by building a separate prealignment and imaging rig. The tolerances in the spacing ($z_2 = 6.98$ mm; Fig. 4) between the lenslet arrays, as well as the relative tilt (θ_x and θ_y) between the lenslet arrays, were dictated by the machining tolerances, which were ± 10 μm for this case. These tolerances were well within those demanded by the optical design. When the lenslet–beam-splitter barrel assembly was complete it was inserted into the outer barrel; these components are pieces 11 and 10 respectively, in Fig. 1.

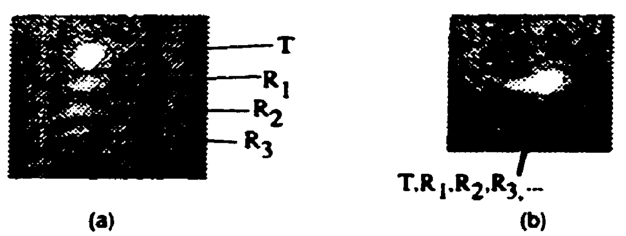

Fig. 11. Results of the alignment of the bulk turning mirror: (a) mirror 4 greatly misaligned and (b) mirror 4 at its optimum alignment.

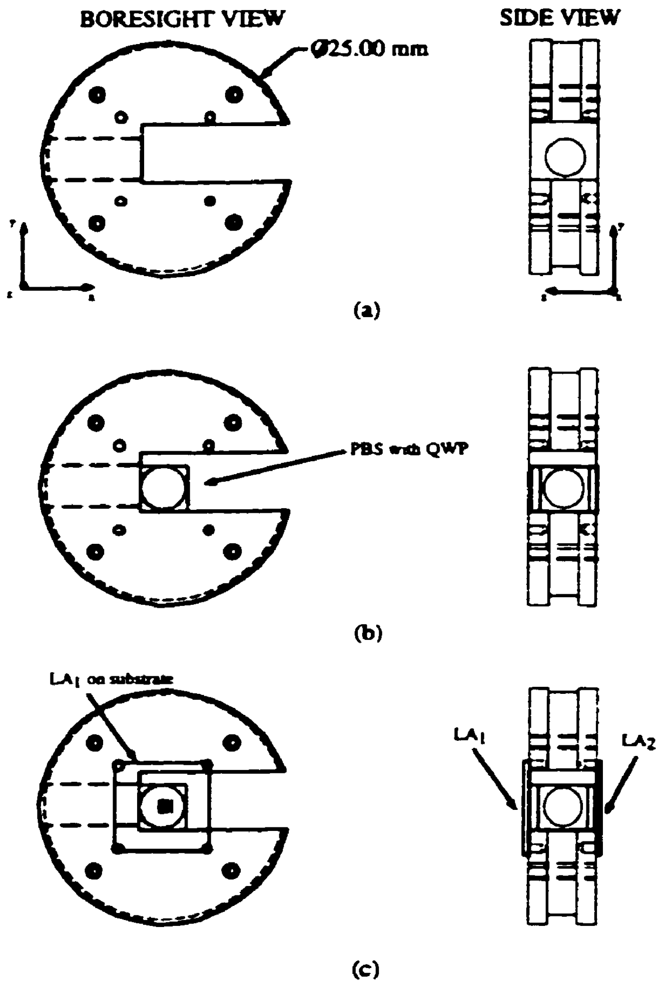

Fig. 12. (a) Lenslet–PBS barrel. (b) Lenslet–PBS barrel with the PBS mounted. (c) Lenslet–PBS barrel with the lenslets mounted.

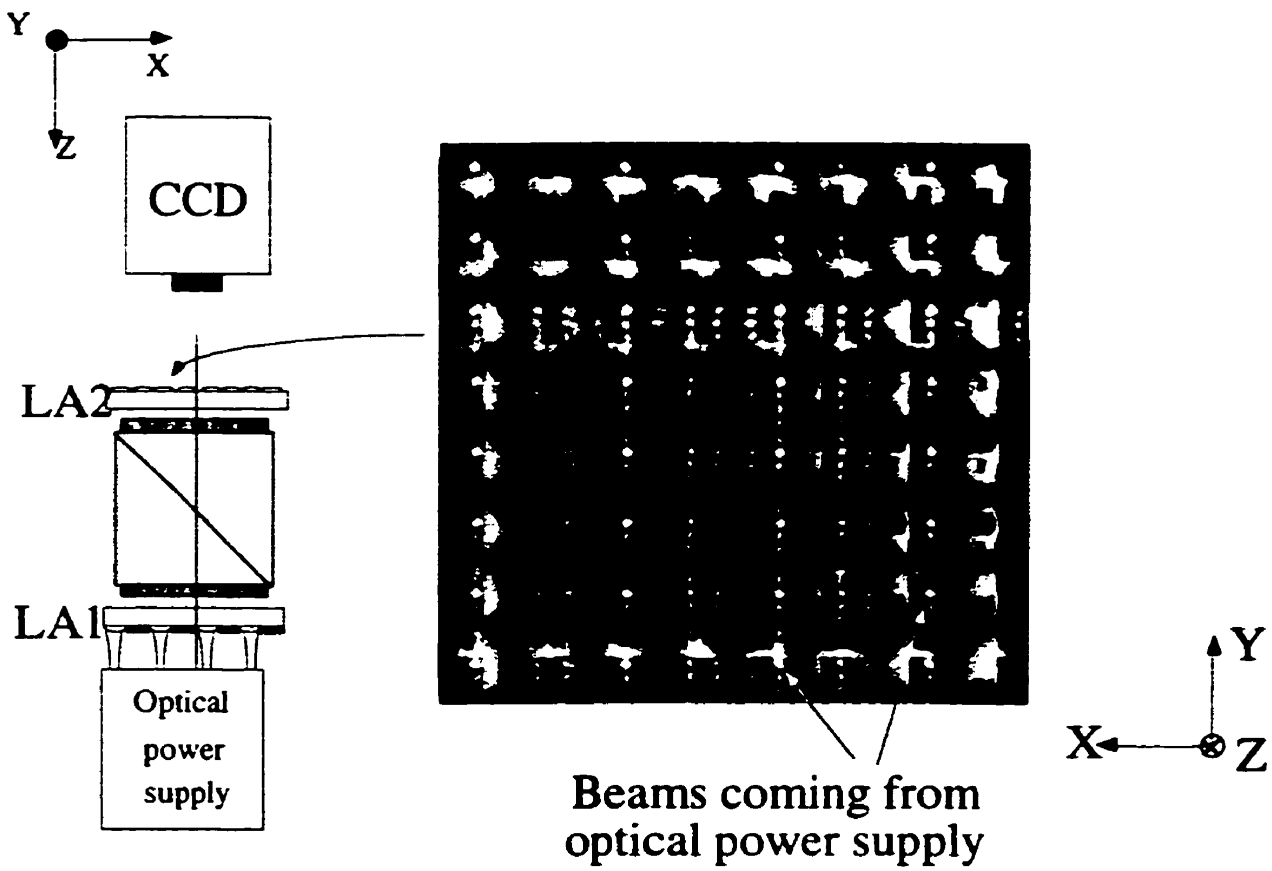

Fig. 13. LA_1 imaged by LA_2.

The optical microlens relay, which was designed to relay the beams by use of the maximum lens-to-waist configuration,[22] also exhibited another interesting characteristic: If we let z_2' (=5.41 mm) be the optical distance between actual LA_1 and LA_2 and z_3 (=886 μm) be the optical distance from LA_2 to the device plane, then $1/z_2' + 1/z_3 \approx 1/f_\mu$. As a result, each lenslet on LA_2 imaged a part of substrate 1 and relayed it to the device plane. These relayed images, with backillumination shown in Fig. 13, clearly indicate the strips of pixellated mirrors and lenslets on LA_1. In addition, the beamlets from the power-array plane clearly appear as bright spots coming from the lenslets. This qualitatively demonstrated that the lenslets were properly aligned and was of great help during system alignment.

B. Optical Power Supply

The OPS contained lenses to collimate the output from the fiber, a multiple-phase grating as a fan-out element, a Fourier transform lens pair, and additional components for beam-steering and polarization control. Each OPS barrel was 80 mm long. Each fully assembled OPS was prealigned separately and inserted into an outer-barrel assembly (components 8 and 10 in Fig. 1). At the end of this assembly sequence, therefore, each outer-barrel assembly contained a lenslet–beam-splitter barrel and an OPS. The outer barrels were then inserted into the baseplate. A full analysis of the OPS performance is the subject of another paper.[33]

C. Bulk-Interconnect Tolerancing

As shown in Fig. 4, the bulk interconnect had to relay the beams emerging from stage 1 onto the pixellated mirror of stage 2. The two bulk tilt plates, each 1.5-mm-thick SF10 (n = 11.71) glass at a 10° tilt, could each move the beam array approximately 110 μm at the pixellated mirror. By rotation of the tilt plates such that their individual contributions cancelled, it was possible to move the imaged beam array by 0 μm at the mirror plane; conversely, they could also be oriented such that they gave a total displacement of 220 μm at the pixellated mirror.

An ideal system would require no correction that was due to misalignment. In the present nonideal case, the following factors—mentioned in Section 4 above—contributed to misalignment, which had to be corrected by the tilt plates: machining errors affecting the outer diameter of the bulk barrels and the depth and width of the baseplate slots (~25 μm), the lens-centering error (~10 μm), rod deformation (~10 μm), baseplate-bow errors (~50 μm) from inserting the beam splitters into the outer barrels (~50 μm, total), and alignment errors in the bulk mirrors (~50 μm). To a first-order approximation, these errors could have caused a total alignment error of 90 μm (in quadrature addition) in addition to aberrations. This alignment error is corrected easily by the tilt plates.

5. Daughterboard Mounting Techniques

Mounting the daughterboards to the optomechanics was the most critical step of assembly since it involved interfacing the optoelectronics to the optomechanics. This section describes the various techniques implemented and the challenges that had to be overcome.

A. Procedure

This operation, which was performed four times, once for each daughterboard, was the most delicate of the entire assembly. The key components are outlined in Figs. 14(a) and 14(b) in a rear view and side view, respectively. In short, the daughterboard was attached to an interface piece called the daughterboard clamp, which was bolted to the baseplate.

The optical design specified that the smart-pixel device plane be $z_3 = 886 \pm 15$ μm away from the microlens array and that the x–y alignment error between lenslets and smart-pixel device windows be of the order of 1 μm, as shown in Table 1. These very tight alignment tolerances were required to reduce the loss of optical throughput resulting from daughterboard misalignment to below 1%. Misalignments greater than those given in Table 1 will cause a loss greater than 1%.

Since there were very few optoelectronic chips or lenslets available, it was decided that the step of gluing LA_2 to the device packaging would not be performed. Rather, a four-step assembly sequence was implemented. With the daughterboard mounting clamp already bolted to the baseplate, the objective was to align the daughterboard to the optomechanics and fasten it to the daughterboard clamp.

First, the device die was mechanically aligned, glued to the daughterboard to better than 150 μm of its nominal position,[34] and wire bonded. In the second step, light was launched into the OPS. The OPS RBS's were aligned such that the beams went through the microchannel relay and onto the plane where the optoelectronic devices were to be located.

In the third step, the daughterboard was coupled to a six-degree-of-freedom (6-DOF) precision-positioning system and aligned to the optical beams as follows. The daughterboard was adjusted in Δz, θ_x, and θ_y until a traveling microscope setup indicated that these three degrees of freedom were within the desired tolerance. When these three tolerances were achieved, three set screws emerging from holes in the daughterboard clamp (the holes labeled G in Fig. 14) were adjusted such that the set-screw tips just barely touched the front of the board. These three screw tips thus defined the proper plane of the daughterboard relative to the optomechanics. As a result, during the rest of this step the daughterboard never actually touched the clamp, but rather rested and slid on three points approximately 1 mm in front of the clamp. The θ_z accuracy then was verified by use of the imaging system. Finally, the highest contrast ratio of the modulated beams could be used to indicate the optimal x–y alignment of the beams to the device windows.

In the fourth step, after the tolerances in the six degrees of freedom were met, the daughterboard, which was still coupled to the six-degree-of-freedom stage and just barely in contact with the three screw tips, was fastened. The six-degree-of-freedom stage was subsequently decoupled from the daughterboard. This fourth step, namely fastening the aligned daughterboard to the optomechanics, was the most problematic of the entire system-assembly sequence. Two techniques were tried to fasten the board properly; they are described in Subsection 5.B.

B. Daughterboard Fastening Techniques

1. First Daughterboard Fastening Technique: Bolting

In this technique, three additional screws were used. Fastening screws with large heads were inserted into the clearance holes labeled H in Fig. 14 in the daughterboard and screwed into the holes labeled J in the clamp (the diameter of the fastening-screw heads was greater than that of the holes H so that the fastening-screw heads rested against the back side of the board). The fastening screws were then tightened so that the daughterboard did not simply rest on but rather was pressed very hard against the set-screw tips of step three above.

This technique proved to be very cumbersome and had fundamental problems. If the fastening screws were tightened too much, the daughterboard moved during tightening, causing the board to be bolted into an improper position. If, on the other hand, the holding screws were not sufficiently tightened, the board drifted over time. Experimental results indicating the drift are given in Subsection 7.B. Compromising between the two extremes in tightening the screws led to an unsatisfactory result in which the board moved slightly during tightening and drifted slightly afterwards. Consequently, the bolting technique was rejected.

2. Second Daughterboard Fastening Technique: Gluing

In this case, the board was glued to the set-screw tips. After a careful analysis of viscosity, holding force, and ease of curing, a glue from Loctite (No. 403) was chosen. With a syringe, the glue was gently applied to the three set-screw tips, which were just barely touching the daughterboard. This yielded satisfactory results, as the discussion below shows.

6. Mechanical Stability Experiments: Setup

This section describes the diagnostic setup used to measure the effect of mechanical vibrations and shock on the daughterboard x–y (lateral) alignment. Experimental results follow the setup description.

The measurement setup was as follows: In lieu of a smart-pixel die, a quadrant detector (QD) from UDT, Inc.,[35] as shown in Fig. 15, was glued and wire bonded

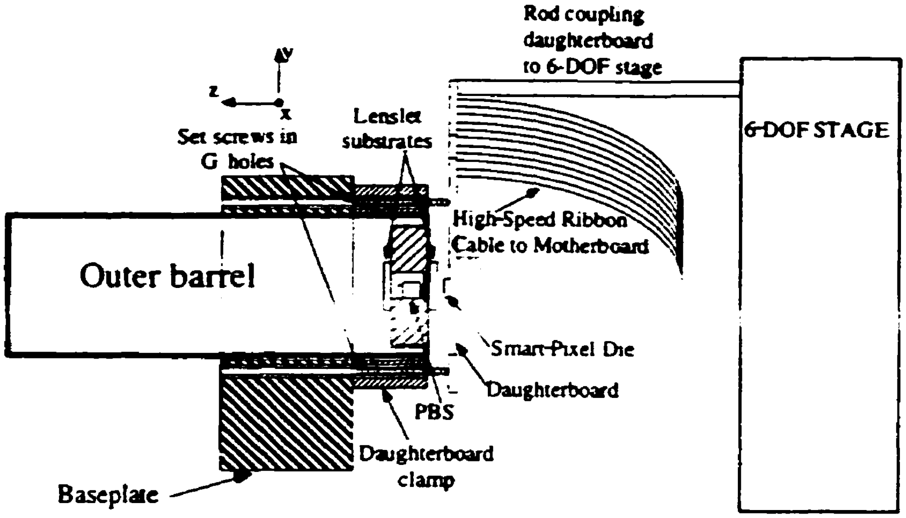

(a)

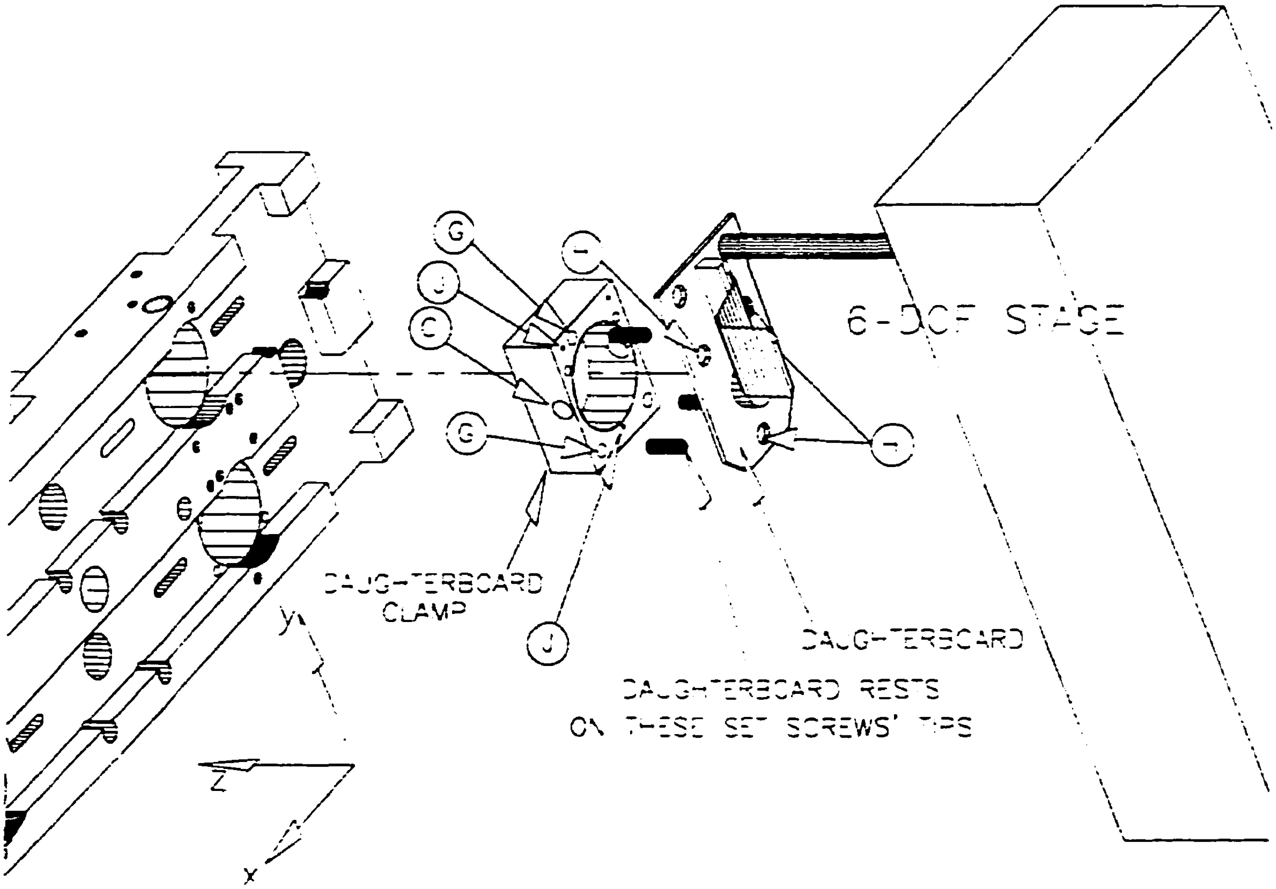

(b)

Fig. 14. (a) Side view of the daughterboard being mounted on the optomechanics. (b) Rear view of the daughterboard being mounted on the optomechanics.

to a daughterboard. Afterwards, one fiber-connected outer-barrel–lenslet–beam-splitter-barrel–OPS assembly, with all the components except the fan-out grating (held by piece 5 in Fig. 1) and the lenslets, was inserted into the baseplate according to the assembly procedure. The daughterboard with the QD was then aligned and fastened to the optomechanics by use of one of the techniques described in Subsections 5.B.1 and 5.B.2.

When light was launched into the OPS (with no

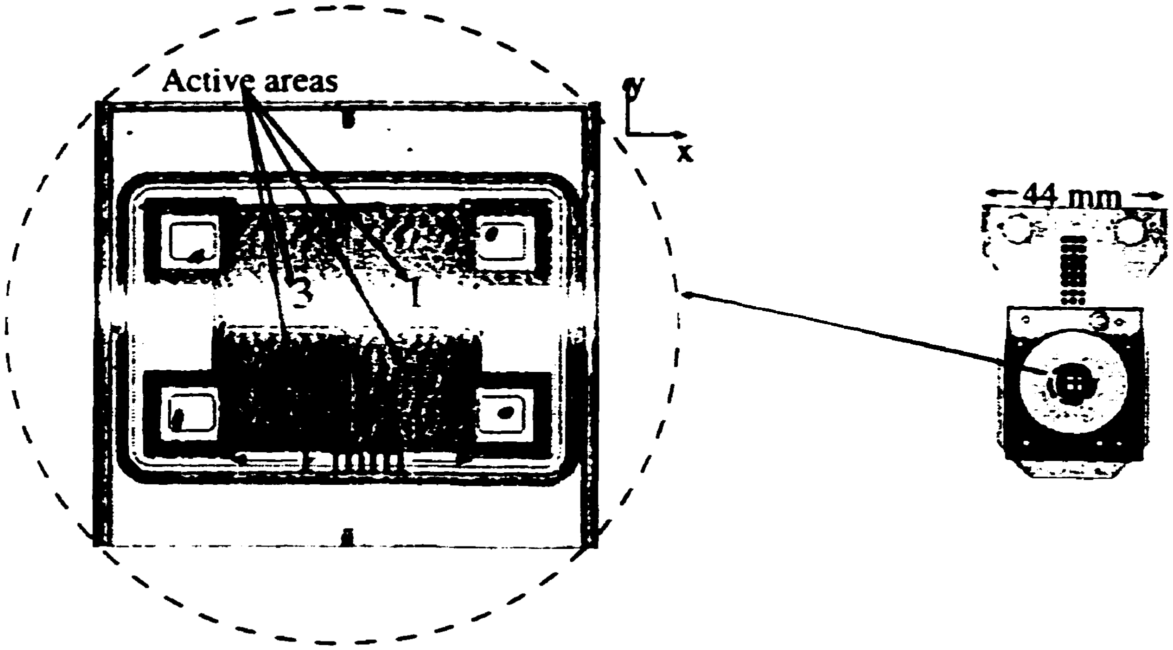

Fig. 15. Quadrant detector mounted on the daughterboard for alignment–diagnostic purposes.

fan-out grating), a single beam went through the OPS and impinged on the QD. At the QD, the beam had a nominal diameter of $3\omega = 1.02$ mm (99% encircled energy). The photocurrents generated by the four photodetectors, labeled 1, 3, 5, and 7 in Fig. 15, of the QD were fed by means of the high-speed ribbon-cable assembly to the dedicated alignment board. On the alignment board, each of the four signals was fed through a low-pass filter having a cutoff frequency of $f_{3dB} = 402$ Hz, buffered, and then finally fed to a Model Lab-NB A/D (analog-digital) board from National Instruments, which sampled each of the four voltages at 4096 samples/s. The low-pass filter was necessary to eliminate aliasing, among other problems associated with frequency. The setup for generating the alignment voltage V_1 is shown in Fig. 16. The three other setups for generating voltages V_3, V_5, and V_7 from their respective quadrants were analogous.

Further processing, such as the calculations required to obtain the Δx and Δy signals from the four sampled voltages, was performed in LABVIEW. For ensuring repeatable results regardless of optical power fluctuations, all misalignment calculations were normalized to the total optical power hitting the detector. For example, from the QD depicted in Fig. 15 it can be seen that

$$\Delta x = k\frac{(V_1 + V_7) - (V_3 + V_5)}{V_1 + V_3 + V_5 + V_7}, \tag{5}$$

where k is a calibration constant, which in this case was obtained experimentally. For this system, the calibration constant was such that the sensitivity was approximately 110 mV/μm for typical power levels. Figure 17 indicates that the system response was linear for a value of $\Delta x < 80$ μm.

7. Mechanical Stability Experiments: Results

The measurement system described in Section 6 was used to characterize many aspects of the optomechanics. This section gives the experimental results obtained.

A. Impact on System Alignment of Fiber Connector Insertion–Extraction

The field serviceability of the fiber-connected power supply was an advantage that this system offered. For this ease of connection to be of greatest use, however, it was imperative that the fiber easily be connected and disconnected without upsetting system alignment. The results of an experiment in which a new fiber with a fiber connector (FC) was connected to and disconnected from the receptacle on the FC bulkhead [part 2 in the assembly drawing (Fig. 1)]

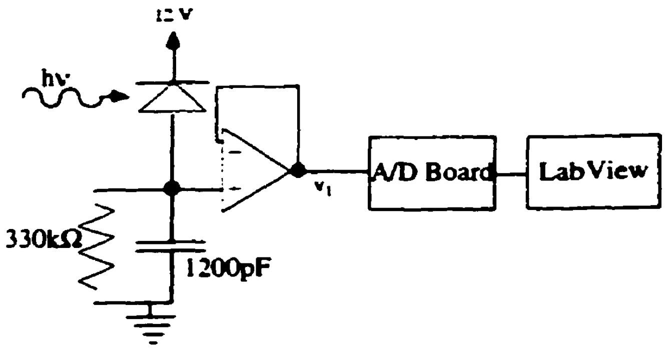

Fig. 16. Electronic setup for generating, buffering, and processing one QD signal.

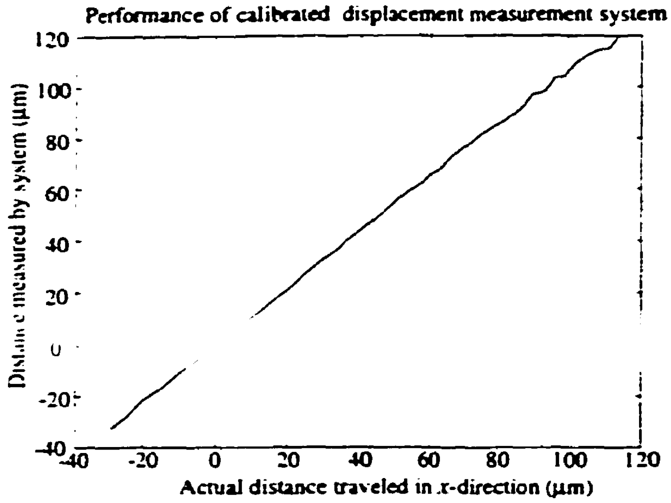

Fig. 17. Calibration and performance of the quadrant detector-based displacement measurement system.

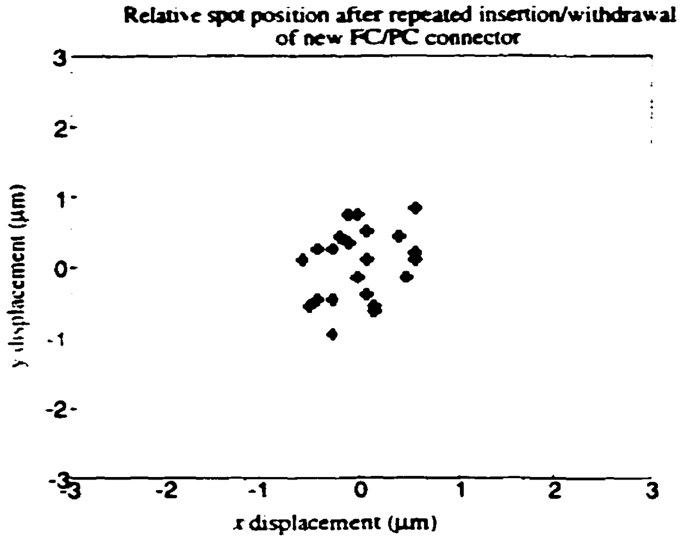

Fig. 18. Effect of repeated insertion–extraction cycles of a FC on the system alignment. Results indicate that inserting–removing the fiber does not affect system alignment to within a ±1-μm accuracy.

two dozen times within 5 min are shown in Fig. 18. As can be seen, the spot never moved at all, to within the measurement uncertainty of ±1 μm in this setup. This result is more than simple verification that a single-mode fiber connector has excellent repeatability: It indicates that system alignment was in no way affected either by the small shocks associated with fiber insertion or by the torque imparted to the outer barrel as the connector was hand tightened until the locking screw was snug. However, it should be noted that, if the connector was tightened extremely tightly, the spot did move by approximately 2 or 3 μm. Similar results were obtained for both daughterboard mounting techniques (bolting and gluing).

B. Measurement of Long-Term Drift of the Bolted Daughterboard

This experiment measured the long-term drift of the daughterboard after it was fastened by use of the bolting technique. The bolts were hand tightened sufficiently to hold the board snugly to its mounting clamp on the optomechanics; further tightening of the bolts might have been possible, but repeated experiments indicated that excessive tightening caused the board to move from its aligned position during system assembly.

After the daughterboard was bolted, a large (120 mm × 120 mm × 38 mm) industrial cooling fan typical of those mounted in conventional backplane chasses (Model 125DH 1LP11000 from ETRI, Inc.) was bolted to the VME chassis and mounted 50 mm away from the daughterboard. The fan was mounted beside the daughterboard and oriented such that it blew air directly onto the daughterboard. There was considerable clearance around the fan to allow for unimpeded air flow. The fan was fed 500 mA at 12 V dc (according to specifications), which made it rotate at ~3000 rpm (50 Hz). At this frequency, if the flow is unimpeded the fan is specified to blow 102 cfm (cubic feet per minute). The chassis was simply resting on a table and was not clamped down in any manner.

Every day for almost two weeks, with the fan always on at full power, the position of the daughterboard was measured. As can be seen from the results shown in Fig. 19, the daughterboard fell in the y direction by approximately 1 μm/day then stabilized after a week. The repeatability of these measurements was ±1 μm. As stated above, the poor long-term stability of the daughterboard bolting technique led to its rejection for system assembly.

C. Measurement of the Long-Term Drift of the Glued Daughterboard

This experiment measured the long-term drift of the daughterboard after it was fastened at $(x, y) = (0, 0)$ on day 1 by use of the gluing technique. Measurement results for x and y are shown in Fig. 20.

The most logical interpretation of the long-term drift results shown in Fig. 20 is as follows: The board was glued at (0, 0) ±2 μm and moved approximately 1 μm during curing. For more than 2 mos after curing the board never moved to within the measurement error, regardless of whether the ETRI 125DH fan in the setup described in Subsection 7.B was blowing air onto the daughterboard. Note that, after the glue had cured, decoupling the daughterboard from the motorized x–y–z stage or extracting–inserting the high-speed ribbon connector on the daughterboard produced no measurable misalignment. The final results are shown in Table 1. Note also that adjusting the RBS's in the OPS can compensate for small errors in x and y. In the case of this long-term drift measurement experiment, measurement repeatability was ±3 μm.

It should also be noted that, after the glue had cured (which took a few minutes), it left a slight

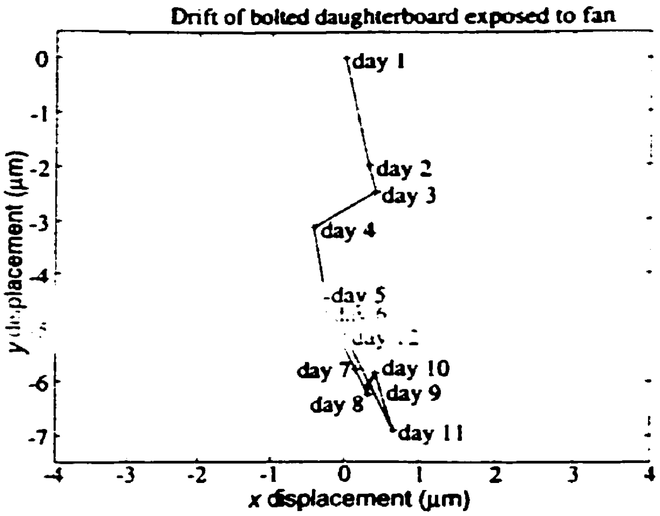

Fig. 19. Drift of a daughterboard fastened by use of the first (bolting) technique.

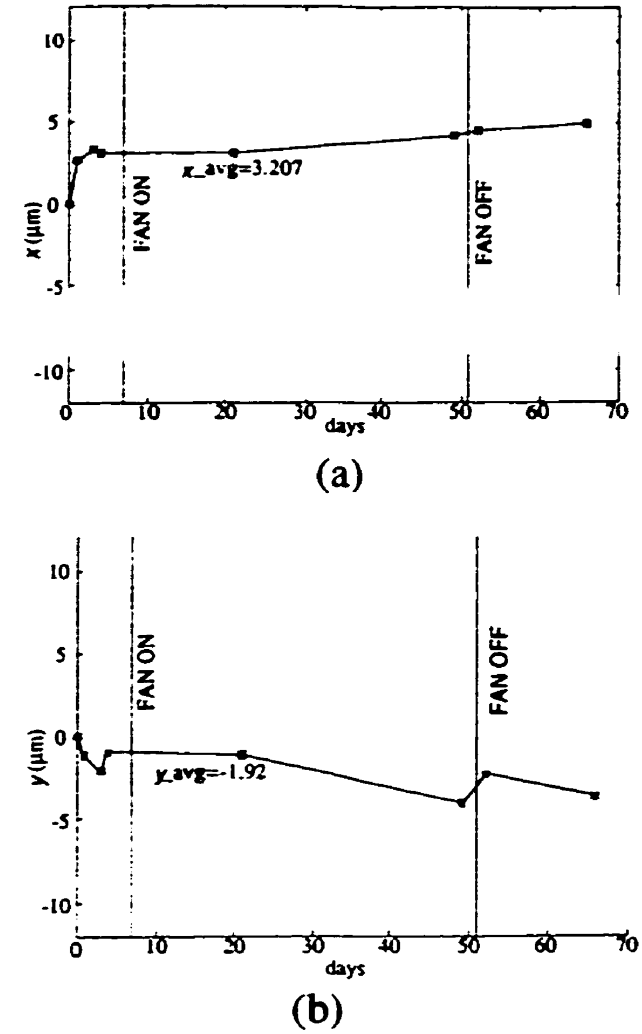

Fig. 20. Long-term drift of a daughterboard fastened by use of glue (second technique) measured across 9 weeks after gluing at day 0: (a) displacement in the x direction and (b) displacement in the y direction.

residue on some of the optics through which the broad alignment beam passed. However, this residue was subsequently measured to be extremely uniform over many millimeters; as a result, this residue had the effect of attenuating by only ~30% the light impinging on the quadrant detector. This attenuation did not affect the measured results since the calculations normalized all power received. A different glue that has no outgassing ("blooming") during curing or a different setup would eliminate this inconvenience.

D. Real-Time Measurements of Mechanical Vibrations of the Glued Daughterboard

Although the glued daughterboard when exposed to the large air currents generated by the fan did not move to within the measurement error over several months, it did exhibit a very interesting behavior when its real-time displacements were analyzed in the spectral domain. For analyzing the spectral behavior of the board's misalignment, fast Fourier transforms of the board's misalignment were performed with LABVIEW.

Figure 21(a) shows the results of the control experiment in which the ETRI Model 125DH fan was turned off. Other than the small spikes at low frequencies (<100 Hz) that are probably due to electrical interference the spectrum was generally quiet.

For the measurements shown in Fig. 21(b), however, the fan was turned on to full power as in previous experiments. In this case, spikes at 410 Hz and at subsequent integer multiples of this fundamental frequency can be discerned for Δx and are readily visible for Δy. The conclusion to be drawn is that the daughterboard mounting system has a mechanical resonance frequency of 410 Hz. This is very encouraging since it is almost an order of magnitude away from most cooling fans' 3000 rpm (50 Hz) rotational frequency; as a result, cooling fans should not cause this system to become mechanically unstable. More sophisticated modeling and measurement techniques obviously would yield more insight; this is a promising route for further research.

Even though the low-pass filter at the input-signal source had a half-power cutoff frequency of 402 Hz, the very slow (first-order) roll-off allowed signals in the 800 Hz range to be picked up, albeit with an attenuation of more than 50%.

The vibrations from the fan could have been coupled to the daughterboard in at least two main ways: (1) Since the fan was bolted to the chassis and the daughterboard was glued to the optomechanics, which were also ultimately bolted to the chassis, the fan's mechanical vibrations could have been coupled mechanically from the fan to the daughterboard by means of the chassis and optomechanics, or (2) since the powerful air flow was blowing straight onto the daughterboard and the electrical connector, the air flow itself could have caused the board to vibrate.

Experiments were conducted to determine which of these two alternatives was most responsible for the

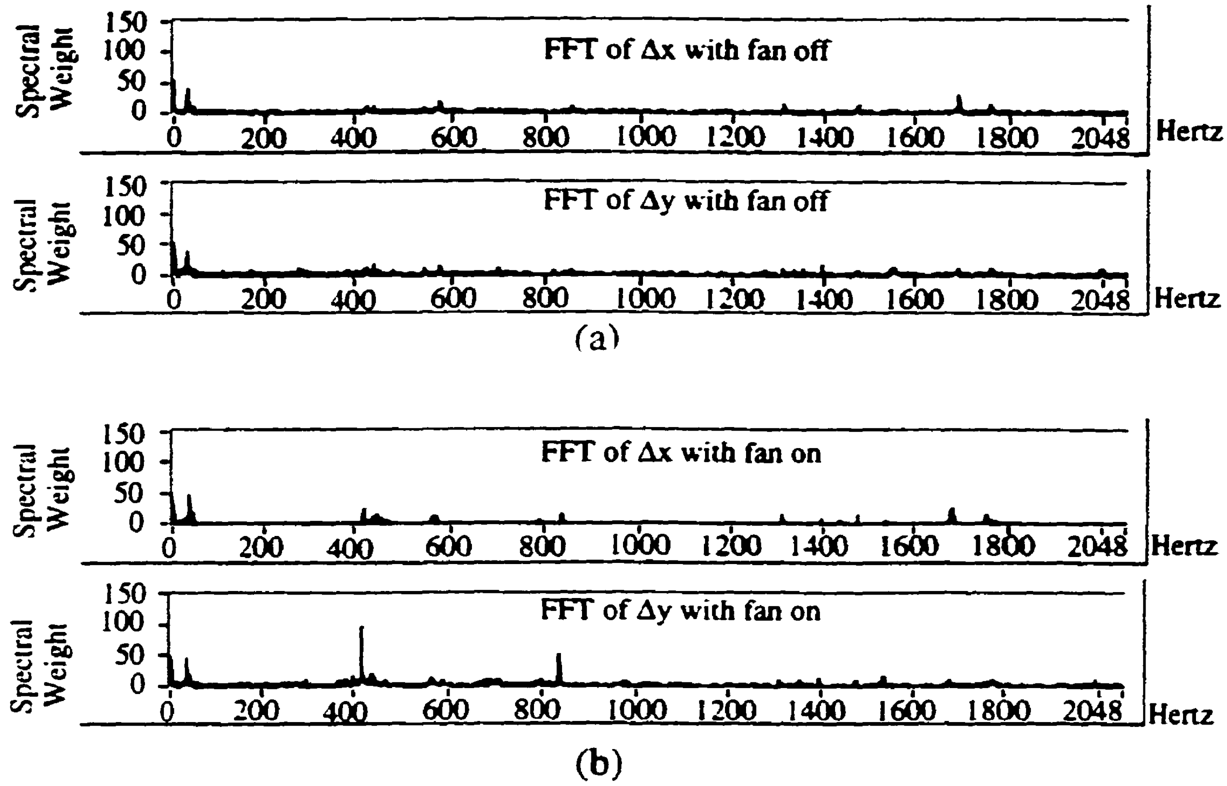

Fig. 21. Spectral behavior of the optomechanical misalignment (a) with the fan off and (b) with the fan on. The number of scans acquired was 4096 at a scanning rate of 4096 scans/s.

daughterboard vibration. In one experiment, the fan was placed in the same position and orientation as before but was attached to the table instead of to the chassis. As a result, the same air flow passed over the board but there was no direct mechanical coupling. In the other experiment, the fan was bolted to the chassis as before, but the air flow to the daughterboard was blocked by a stiff piece of cardboard. The results were inconclusive: Both experiments yielded a spectrum similar to the one shown in Fig. 21(b). More research must be performed in this area.

E. Daughterboard Positioning in Other Degrees of Freedom

The above measurements on daughterboard positioning address only two degrees of freedom: x and y. Of the four remaining degrees of freedom, three were considered critical: the errors in the tilts (θ_x and θ_y) and the error in z_3 (defined in Fig. 4). Given the small size of the array (8 × 4), a quick visual check before gluing was sufficient to ensure that daughterboard rotation (θ_z) was satisfactory.

With a traveling-microscope arrangement, measuring z_3 was accomplished by measurement of the distance from the edge of the daughterboard to the optomechanics and then subtraction of the known thickness of the die and its glue. Measuring the tilt was accomplished by measurement of z_3 at several positions along the daughterboard edge and use of simple geometrical relations to subtract from these readings a known tilt of the die with respect to the daughterboard. The results are summarized in Table 1.

F. Discussion of Results

The daughterboard mounting technique was labor intensive, and from Table 1 it can be seen that most objectives were probably not met. This is partly due to the extremely tight constraints that were imposed (the target value is for a 1% loss) and partly due to the novelty of the mounting technique, which is quite different from traditional slug-based techniques, given the system constraints. Although the system can still function with the results obtained, a certain number of conclusions can nonetheless be drawn from this work: (1) The interface between optoelectronics and optics is by far the most critical in any system of this nature. (2) A better way of aligning LA_2 to the optoelectronics, either by use of mechanical means or by prealignment of these components to each other before insertion, is necessary. (3) Once assembled, a system like this one is very stable (see Sections 6 and 7).

8. Conclusion

This paper has presented the first, to our knowledge, truly 3-D, vertically oriented, rack-mounted, multistage optomechanical system implementing a free-space optical interconnect. Additionally, the approach chosen can be scaled to much larger systems.

In this paper we have outlined some of the design trade-offs and issues to be faced when designing optomechanics for a free-space digital computing system. It was shown that optical constraints, machining tolerances, optoelectronic technology, electronic packaging, material parameters, thermal effects, and component availability all have a major influence on the optomechanics. Moreover, diagnostic techniques were developed and shown to yield considerable information on the status of the optomechanics. Finally, further avenues of research, such as a better understanding of vibration mechanisms, were proposed.

This research was supported by a grant from the Canadian Institute for Telecommunications Research under the National Centre for Excellence program of Canada and the Nortel/National Sciences and Engineering Research Council (Canada) (NSERC) Chair in Photonic Systems. In addition, D. V. Plant acknowledges support from NSERC (grant OGP0155159) and the Fonds pour la formation de Chercheurs et l'Aide à la Recherche (FCAR) under grant NC-1415. G. Boisset gratefully acknowledges funding from FCAR under grant cttee B2-05.

The lenslets were fabricated by M. Taghizadeh, Department of Physics, Heriot-Watt University (HWU), Edinburgh, Scotland. The authors thank J. Boka and D. Birdie from McGill and G. Smith from HWU for help during fabrication and characterization. The authors also thank the anonymous reviewers for their very helpful and thoughtful comments on the first submission.

References and Notes

1. R. A. Nordin, F. J. Levi, R. N. Nottenburg, J. O'Gorman, T. Tanbun-Ek, and R. A. Logan, "A systems perspective on digital interconnections technology," J. Lightwave Technol. **10**, 811–827 (1992).
2. G. Galilei, *Il Saggiatore* (Feltrinelli, Milano, Italy, 1656).
3. P. R. Yoder, *Optomechanical Systems Design* (Marcel Dekker, New York, 1993).
4. W. J. Smith, *Modern Optical Engineering: The Design of Optical Systems*, 2nd ed. (McGraw Hill, New York, 1990).
5. D. Vukobratovich, "Advances in optomechanics," in *Applications of Optical Engineering: Proceedings of OE/Midwest '90*, M. K. Dubiel, R. E. Gillespie, R. P. Guzik, and J. E. Pearson, eds., Proc. SPIE **1396**, 436–446 (1990).
6. D. O'Shea, "Annotated bibliography of optomechanical design," Opt. Eng. **25**, 1160–1170 (1986).
7. P. R. Yoder, ed., *Optomechanical Design*, Vol. CR43 of SPIE Critical Reviews Series (SPIE Press, Bellingham, Wash., 1992).
8. F. B. McCormick, T. J. Cloonan, A. L. Lentine, J. M. Sasian, R. L. Morrison, M. G. Beckman, S. L. Walker, M. J. Wojcik, S. J. Hinterlong, R. J. Crisci, R. A. Novotny, and H. S. Hinton, "Five-stage free-space optical switching network with field-effect transistor self-electro-optic-effect-device smart-pixel arrays," Appl. Opt. **33**, 1601–1618 (1994).
9. I. R. Redmond and E. Schenfeld, "A free-space optical interconnection network for massively parallel processing," IEEE LEOS Newsletter **9**, 10–13 (1995).
10. D. V. Plant, B. Robertson, H. S. Hinton, W. M. Robertson, G. C. Boisset, N. H. Kim, Y. S. Liu, M. R. Otazo, D. R. Rolston, and A. Z. Shang, "An optical backplane demonstrator system based on FET-SEED smart pixel arrays and diffractive lenslet arrays," IEEE Photon. Technol. Lett. **7**, 1057–1059 (1995).
11. S. M. Prince, F. A. P. Tooley, S. Wakelin, and M. R. Taghizadeh, "Implementation of optical perfect-shuffle module," Appl. Opt. **34**, 1775–1782 (1995).
12. J. L. Brubaker, F. B. McCormick, F. A. P. Tooley, J. M. Sasian, T. J. Cloonan, A. L. Lentine, S. J. Hinterlong, and M. J. Herron, "Optomechanics of a free-space switch: the components," in *Laser Interferometry IV: Computer-Aided Interferometry*, R. J. Pryputniewicz, ed., Proc. SPIE **1553**, 55–66 (1991).
13. F. B. McCormick, F. A. P. Tooley, J. L. Brubaker, J. M. Sasian, T. J. Cloonan, A. L. Lentine, R. L. Morrison, R. J. Crisci, S. L. Walker, S. J. Hinterlong, and M. J. Herron, "Optomechanics of a free-space photonic switching fabric: the system," in *Optomechanics and Dimensional Stability*, R. A. Paquin and D. Vukobratovich, eds., Proc. SPIE **1533**, 97–114 (1991).
14. J. M. Sasian, F. B. McCormick, R. Webb, R. J. Crisci, K. O. Mersereau, and R. P. Stawicki, "Design, assembly, and testing of an objective lens for a free-space photonic switching system," Opt. Eng. **32**, 1871–1878 (1993).
15. M. Mizukami, K. Koyabu, M. Fukui, and K. Kitayama, "Free-space optical module configuration using a guide-frame assembly method," Appl. Opt. **34**, 1783–1787 (1995).
16. D. R. Rolston, D. V. Plant, T. H. Szymanski, H. S. Hinton, W. S. Hsiao, M. H. Ayliffe, D. Kabal, M. B. Venditti, P. Desai, A. V. Krishnamoorthy, K. W. Goosen, J. A. Walker, B. Tseng, S. P. Hui, J. E. Cunningham, and W. Y. Jan, "A hybrid-SEED smart pixel array for a four-stage intelligent optical backplane demonstrator," IEEE J. Select. Topics Quantum Electron. **2**, 97–105 (1996).
17. IEEE Standard 1014-1987 for a Versatile Backplane Bus: VMEbus, IEEE ref. [1-55937-674-0] [SH11544-NYF] (Institute of Electrical and Electronics Engineers, New York, 1987).
18. D. V. Plant, B. Robertson, H. S. Hinton, M. H. Ayliffe, G. C. Boisset, W. Hsiao, D. Kabal, N. H. Kim, Y. S. Liu, M. R. Otazo, D. Pavlasek, A. Z. Shang, J. Simmons, K. Song, D. A. Thompson, and W. M. Robertson, "A 4 × 4 VCSEL/MSM optical backplane demonstrator system," Appl. Opt. **35**, 6365–6368 (1996).
19. S. Nimmagadda, J. Dillon, and A. Moncayo, "A 533-Mbits/sec/wire modular bus with single or double parallel termination," in *Proceedings of the 1996 Electronic Components and Technology Conference* (Institute of Electrical and Electronics Engineers, New York, 1996), IEEE ref. 0-7803-3286-5/96, pp. 974–983.
20. Lens 322286 (manufactured by the Spindler & Hoyer Corp., Göttingen, Germany).
21. H. S. Hinton, *An Introduction to Photonic Switching Fabrics* (Plenum, New York, 1993).
22. F. B. McCormick, F. A. P. Tooley, T. J. Cloonan, J. M. Sasian, H. S. Hinton, K. O. Mersereau, and A. Y. Feldblum, "Optical interconnections using microlens arrays," Opt. Quantum Electron. **24**, 465–477 (1992).
23. *Metals Handbook* (American Society for Metals, Materials Park, Oh., 1948), pp. 237–243.
24. P. R. Yoder, "Parametric investigation of mounting-induced axial contact stresses in individual lens elements," in *Optomechanical Design*, P. R. Yoder, V. L. Genberg, and D. Vukobratovitch, eds., Proc. SPIE **1998**, 8–19 (1993).
25. R. E. Green, C. J. McCauley, E. Oberg, F. D. Jones, H. L. Horton, and H. H. Ryffel, *Machinery's Handbook*, 25th ed. (Industrial Press, New York, 1996).
26. R. A. Flinn and P. K. Trojan, *Engineering Materials and Their Applications* (Houghton Mifflin, Boston, Mass., 1981).

27. *Properties of Polymer's Engineering Thermoplastics*, Pub. BR/ 5000-1 5/94 (Polymer Corp., Reading, Pa., 1994).
28. Data sheet 242769-001 (Intel Corp., Santa Clara, Calif., 1995).
29. See, for example, *Design Guide 101 Catalog*, (Nordex Inc., Danbury, Conn., 1991), p. 15A.
30. R. O. Parmley, *Standard Handbook of Fastening and Joining* (McGraw-Hill, New York, 1989), pp. 1–24.
31. H. O'Neill, *Hardness Measurement of Metals and Alloys* (Chapman & Hall, London, 1967), Chap. 2.
32. S. Wakelin, "Design and construction of a free-space digital optical information processor," Ph.D. dissertation (Heriot-Watt University, Edinburgh, Scotland, 1991).
33. R. Iyer, D. J. Goodwill, W. M. Robertson, D. V. Plant, G. C. Boisset, Y. S. Liu, B. Robertson, M. H. Ayliffe, and F. Lacroix, "Design, implementation, and characterization of an optical power supply spot-array generator for a four-stage free-space optical backplane," Appl. Opt. (to be published).
34. D. N. Kabal, G. Boisset, D. R. Rolston, and D. V. Plant, "Packaging of two-dimensional smart pixel arrays," in *Proceedings of the IEEE/LEOS Summer Topical Meeting on Smart Pixels* (IEEE Lasers and Electro-Optical Society, Picataway, N.J., 1996), paper ThA5.
35. Quadrant Detector: Spot 4D M1 [UDT Sensors, Inc. (formerly United Detector Technologies), Hawthorne, Calif., 1997].